

THÈSE

Pour l'obtention du grade de
DOCTEUR DE L'UNIVERSITÉ DE POITIERS
UFR des sciences fondamentales et appliquées
Institut de chimie des milieux et matériaux de Poitiers - IC2MP
(Diplôme National - Arrêté du 25 mai 2016)

École doctorale : Sciences pour l'environnement - Gay Lussac (La Rochelle)
Secteur de recherche : Chimie industrielle

Cotutelle : Université libanaise

Présentée par :
Hussein Sammoury

Synthesis of new zeolitic materials for hydroisomerization of n-alkanes by bifunctional catalysis to obtain medium distillates (C10-C14)

Directeur(s) de Thèse :
Ludovic Pinard, Joumana Toufaily, Yannick Pouilloux, Khalil Cherry

Soutenue le 28 novembre 2017 devant le jury

Jury :

Président	Tayssir Hamieh	Professeur, Université libanaise, Beyrouth
Rapporteur	Vasile Hulea	Professeur des Universités, École nationale supérieure de chimie de Montpellier
Rapporteur	Benoît Louis	Directeur de recherche CNRS, Université de Strasbourg
Membre	Ludovic Pinard	Maître de conférences, Université de Poitiers
Membre	Joumana Toufaily	Professeur, Université libanaise, Beyrouth
Membre	Yannick Pouilloux	Professeur des Universités, Université de Poitiers
Membre	Christophe Bouchy	Ingénieur de recherche, IFP énergies nouvelles, Lyon
Membre	Khalil Cherry	Maître de conférences, Université libanaise, Beyrouth

Pour citer cette thèse :

Hussein Sammoury. *Synthesis of new zeolitic materials for hydroisomerization of n-alkanes by bifunctional catalysis to obtain medium distillates (C10-C14)* [En ligne]. Thèse Chimie industrielle. Poitiers : Université de Poitiers, 2017.
Disponible sur Internet <<http://theses.univ-poitiers.fr>>

THESE

Pour l'obtention du Grade de

DOCTEUR DE L'UNIVERSITE DE POITIERS

(Faculté des Sciences Fondamentales et Appliquées)
(Diplôme National - Arrêté du 25 mai 2016)

Ecole Doctorale : Gay Lussac, Sciences pour l'environnement

Secteur de Recherche : Chimie des matériaux

Présentée par :

Hussein SAMMOURY

Synthesis of new zeolitic materials for hydroisomerization of n-alkanes by bifunctional catalysis to obtain medium distillates (C₁₀-C₁₄)

Directeurs de Thèse : **PINARD Ludovic**, Maitre de Conférence – HDR, Université de Poitiers
TOUFAILY Joumana, Professeur, Université Libanaise

Co-directeurs de Thèse : **POUILLOUX Yannick**, Professeur, Université de Poitiers
CHERRY Khalil, Maitre de conférence, Université Libanaise

Soutenu le 28 Novembre 2017 devant la Commission d'Examen

JURY

Rapporteurs : HULEA Vasile (Professeur de l'école Nationale Supérieure de Chimie de Montpellier)
LOUIS Benoit (Directeur de recherche, Université de Strasbourg, LaSyROC)

Examineurs : BOUCHY Christophe (Ingénieur de recherche, IFP énergies nouvelles)
HAMIEH Tayssir (Professeur, Université Libanaise)
CHERRY Khalil (Maitre de conférence, Université Libanaise)
PINARD Ludovic (Maitre de Conférence – HDR, Université de Poitiers)
POUILLOUX Yannick (Professeur, Université de Poitiers)
TOUFAILY Joumana (Professeur, Université Libanaise)



Université Libanaise

École Doctorale
Sciences et Technologies



Doctorat Université Libanaise

THESE de doctorat

Pour obtenir le grade de Docteur délivré par

L'École Doctorale des Sciences et Technologie

(Université Libanaise)

Spécialité : Chimie de matériaux

Présentée et soutenue publiquement par

SAMMOURY Hussein

28 Novembre 2017

**Synthesis of new zeolitic materials for hydroisomerization of n-alkanes
by bifunctional catalysis to obtain medium distillates (C₁₀-C₁₄)**

Directeur de thèse : **PINARD Ludovic et TOUFAILY Joumana**

Co-encadrement de la thèse : **CHERRY Khalil et POUILLOUX Yannick**

Membres du Jury

M. HULEA Vasile , Professeur, ENSCM, Montpellier, France	Rapporteur
M. LOUIS Benoit , Directeur de recherche, LaSyROC, Strasbourg, France	Rapporteur
M. BOUCHY Christophe , Ingénieur de recherche, IFP énergies nouvelles	Examineur
M. HAMIEH Tayssir , Professeur, MCEMA, Université Libanaise	Examineur
M. PINARD Ludovic , HDR, IC2mP, Université de Poitiers	Director
Mme. TOUFAILY Joumana , Professeur, MCEMA, Université Libanaise	Director
M. CHERRY Khalil , Docteur, MCEMA Université Libanaise	Co-director
M. POUILLOUX Yannick , Professeur, IC2mP, Université de Poitier	Co-director

Abstract

Two commercial nanocrystal *BEA zeolites with different textural properties and a microcrystal synthesized *BEA zeolite, were desilicated using different alkaline treatment; classical in presence of NaOH alone, or mixed with a pore directing agent. All parent zeolites and some selected desilicated samples were chosen for catalytic cracking of n-hexane, where no significant improvement of n-hexane conversion was observed after desilication.

To investigate the impact of desilication on the hydroisomerization of n-C₁₀, all parent and the some selected desilicated zeolites were transformed into their bifunctional form by platinum loading. The improvement of the textural properties by desilication using the different pore directing agents, was not always the cause behind an increase or decrease in the activity and selectivity of the catalyst, but rather was more the location of the Pt particles and their predicted distance from the acidic sites. However, there exists a synergetic effect between both the textural and bifunctional characteristics. Tests on the hydroisomerization of n-C₁₂ and n-C₁₄ to investigate the impact of chain length were done. In the nanocrystal series, a special phenomenon on n-C₁₂ appeared where the isomerization yield seemed to be less than that obtained on n-C₁₀ and n-C₁₄, suggesting that this would be due the confinement effect, which was shown to be more effective in case of n-C₁₂. The microcrystal series showed an improvement of the activity over all the catalysts in case of n-C₁₄ transformation in comparison with n-C₁₀, but a decrease in isomers selectivity as observed due to probable diffusional limitations within the zeolites' channels.

Key words: zeolite, n-hexane, hydroisomerization, diffusional limitations, hierarchization.

Résumé

Deux zéolithes nanocristaux de type *BEA commerciales avec de différentes propriétés texturales, et une zéolithe microcristaux de type *BEA qui a été synthétisée durant cette thèse, ont été modifiées par une desilication en utilisant de différents traitements alcalins. Toutes les zéolithes parentes et certaines désilicées ont été sélectionnées pour le craquage du n-hexane, où aucune amélioration significative de la conversion n'a été observée après la désilication.

Toutes les zéolithes parentes et quelques désilicées sélectionnées ont été transformés en leur forme bifonctionnelle par imprégnation du platine pour étudier l'impact de la désilication dans l'hydroisomérisation de n-C₁₀. On a constaté que l'amélioration des propriétés texturales par la désilication n'était pas toujours la cause d'une augmentation ou d'une diminution de l'activité et de la sélectivité du catalyseur, mais plutôt de la localisation des particules de Pt et leur distance prédite des sites acides. Cependant, il existe un effet de synergie positif entre les propriétés texturales et bifonctionnelles. Nous avons également étudié l'impact de la longueur de la chaîne dans l'hydroisomérisation de n-C₁₂ et de n-C₁₄. Un phénomène spécial dans le cas de n-C₁₂ est apparu, où le rendement d'isomérisation semblait inférieur à celui obtenu sur n-C₁₀ et n-C₁₄, ce qui suggère que cela résulte de l'effet de confinement. La série microcristaux a montré une amélioration de l'activité dans la transformation n-C₁₄ en comparaison avec n-C₁₀, mais une diminution de la sélectivité des isomères à cause des limites de diffusion potentielles.

Mot clés : Zéolithe, n-hexane, hydroisomerization, limitations diffusionnelles, hiérarchisation.

Acknowledgements

I would like to begin by expressing my gratitude to Dr. Ludovic Pinard for believing in my capabilities, for all the encouragement, for the consideration that he always expressed for me and for my work and for his kindness and attention.

To Professor Yannick Pouilloux, Professor Joumana Tufaliy, Dr. Khalil Cherry, I present my sincere thanks for their scientific and bureaucratic guidance, and for the availability throughout all these years. Without their interest and patience, this Ph. D. would not have been possible. Moreover, I present my thanks to Professor Tayssir Hamieh for all his contributions.

I wish to thank my lab co-workers of the IC2MP research lab for all the help you have given me during this thesis. A special thanks to all the friends that I have made, in particular to those with which I have shared my office, on the IC2MP during this thesis for their help, good spirit and for all the good memories from the times spent together.

To all the technicians who were part of this success, special thanks for your patience anyway.

To all my family and friends, thank you for being part of my life.

Most important, I am more than grateful to my dad and mom, to my sisters and brother, for the unconditional support and affection.

I would like to express my gratitude to the “Islamic Association for Guidance and Higher Education” for the financial support during my Ph. D.

Poitiers, 16 October 2017

Hussein Sammoury

Table of contents

List of Tables	i
List of Figures	iii
General Introduction	3
I Chapter I: Literature Review	11
1 Zeolites: History	11
1.1 Composition and structure	12
1.2 Porous structure of zeolites	14
1.3 Zeolite Acidity	14
1.4 Shape selectivity	16
1.5 Zeolites in catalysis	20
1.6 Beta zeolite (*BEA)	23
2 Hydroisomerization of alkanes	25
2.1 Reactions involved in hydroisomerization	26
2.2 Parameters influencing the hydroisomerization reaction	33
2.3 Limitations in Hydroisomerization	44
3 Hierarchical zeolites	46
3.1 Synthesis of hierarchical zeolites	47
3.2 Destructive pathways	49
3.3 Desilication	50
3.4 Impacts of desilication on the zeolite properties	54
4 Objective	62
II Chapter 2: Experimental procedures, techniques, and catalytic tests	67
1 Zeolites and catalysts preparation	67
1.1 Parent nanocrystal *BEA zeolites	67
1.2 Microcrystal *BEA synthesis and post-synthesis treatments	68
1.3 Bifunctional catalysts preparation	70
2 Techniques used for the physico-chemical characterization of the zeolites and their related catalysts	71
2.1 Study of zeolitic structure by X-ray diffraction (XRD)	71
2.2 Induced Coupled Plasma - Atomic Emission Spectroscopy (ICP-AES)	72
2.3 Nitrogen Physisorption	73

	2.4 Scanning Electron Microscopy (SEM)	81
	2.5 Transmission Electron Microscopy (TEM)	82
	2.6 Infrared spectroscopy.....	82
	3 Catalytic tests – n-alkane hydroisomerization.....	90
	3.1 Catalyst shape	90
	3.2 Chemical Product.....	90
	3.3 Experimental apparatus.....	90
	3.4 Catalytic test conditions.....	94
	3.5 Reactor Filling	95
	3.6 Chromatographic analysis.....	96
	4 Catalytic tests – n-hexane cracking	101
	4.1 Operating conditions.....	101
	4.2 Pilot plant flowsheet	102
	4.3 Results exploitation	103
III	Chapter III: Desilication of *BEA zeolites using different alkaline treatments: Impact on the catalytic cracking of n-hexane.....	109
	1 Introduction	109
	2 Catalysts characterizations.....	110
	2.1 Mass yields and crystallinity.....	111
	2.2 Crystals size of the zeolites.....	114
	2.3 Elemental composition	117
	2.4 Textural properties.....	119
	2.5 Acidic properties.....	123
	3 Catalytic performance in n-hexane cracking.....	126
	4 Conclusions	133
IV	Chapter IV: Impact of desilication of *BEA zeolites on the catalytic performance in hydroisomerization of n-C₁₀.....	139
	1 Introduction	139
	2 Catalysts characterizations.....	139
	2.1 Impact of desilication on zeolites' properties	140
	2.2 Bifunctional characteristics of the catalysts.....	142
	3 Catalysts activities.....	143

4	Reaction products and selectivity	148
5	Impact on the catalytic performance	157
6	Conclusions	160
V	Chapter V: Impact of desilication of *BEA zeolites on the catalytic performance in hydroisomerization of n-C ₁₀ , n-C ₁₂ & n-C ₁₄	165
1	Introduction	165
2	Catalysts activities and products selectivity	166
2.1	Catalysts of series 1	166
2.2	Catalysts of series 2	170
3	Catalytic performance	172
4	Conclusions	177
	General Conclusions	182
	Perspectives.....	185
	Annex.....	188
	Bibliographic references	193

List of Tables

Chapter I

Table I.1 Proposed polymorphs for *BEA zeolite family [97].	24
Table I.2 Relative β -scission rates for n-C ₁₀ transformation on Pt/HUSY catalysts at 405 K [120]. β -scission type B2 is taken as reference.	30
Table I.3 Summary of the advantages and disadvantages of the destructive and constructive approaches towards the synthesis of hierarchical zeolites [161].	48

Chapter II

Table II.1 Desilication conditions for P1 and P2 zeolites.	68
Table II.2 Molar compositions of the starting materials for MC synthesis.	69
Table II.3 Desilication conditions of MC.	69
Table II.4 Characteristics of reagents used.	90
Table II.5 Operating condition of n-hexane cracking.	101

Chapter III

Table III.1 Mass yield and relative crystallinity of all the	112
Table III.2 Crystallite average size of some selected zeolites.	115
Table III.3 Elemental composition of the zeolites.	117
Table III.4 Textural properties of the parent and desilicated zeolites.	120
Table III.5 Acidic properties of the zeolites of series 1-3.	124

Chapter IV

Table IV.1 Conditions of desilications on the different parent zeolites.	139
Table IV.2 Structural, elemental and acidic properties of parent and desilicated zeolites.	141
Table IV.3 Textural properties of the parent and desilicated zeolites.	141
Table IV.4 Bifunctional characteristic of all the catalysts.	142
Table IV.5 Activities of the different Pt content P1 catalysts measured at 230 °C.	144
Table IV.6 Activities of the different series 1 catalysts measured at 230 °C.	145
Table IV.7 Activities of the series 2 catalysts measured at 230 °C.	146
Table IV.8 Activities of the series 3 catalysts measured at 230 °C.	147

Table IV.9 Values of n_{Pt} / n_{H^+} ratio and turnover frequencies for all the catalysts.	147
Table IV.10 Kinetic constants calculated by Runge-Kutta method.	152
Table IV.11 Initial multi- to mono-branched isomers ratios, initial cracking to isomers ratios, and number of acidic steps involved during n-C ₁₀ transformation, on all the catalysts.	155

Chapter V

Table V.1 The n_{Pt} / n_{H^+} ratios, activity and TOF values of series 1 catalysts.....	167
Table V.2 The n_{Pt} / n_{H^+} ratios, activity and TOF values of series 2 catalysts.....	170
Table V.3 The corresponding kinetic constants of the different reaction steps during n-C ₁₀ , n-C ₁₂ and n-C ₁₄ transformations, calculated by Runge-Kutta method.	175

List of Figures

Chapter I

Figure I.1 Scheme of the tetrahedral assemblies of SiO_4 and AlO_4^-	12
Figure I.2 The 23 secondary construction units (SBUs) listed [14]. Each edge corresponds to a T-O bond. Their frequency of occurrence is indicated in parentheses.	13
Figure I.3 Formation of FAU, LTA and SOD structural zeolites from the same "sod" composite construction unit (CBU), passing through the combination of primary building units (PBU) into secondary units of Construction (SBU).	13
Figure I.4 Proton mobility in a zeolite.	15
Figure I.5 Parameters determining the acidic strength of the protonic sites.	16
Figure I.6 Reagent shape selectivity example in catalytic dewaxing. Adapted from [49].	17
Figure I.7 Product shape selectivity example in Toluene disproportionation [49].	18
Figure I.8 Transition state shape selectivity example in disproportionation of metaxylene [49].	18
Figure I.9 Favored adsorption configurations of a iso-paraffins over TON zeolite [39].	19
Figure I.10 "Window effect" example [54].	20
Figure I.11 *BEA zeolite representations.	23
Figure I.12 Structural defects of *BEA zeolite.	25
Figure I.13 Reaction mechanism of ethylene hydrogenation [105].	27
Figure I.14 Schematic representation of the carbenium (A) and three different configurations of carbonium (B) ions [28].	28
Figure I.15 Carbeniums stability. Heat formation values are taken from [106].	28
Figure I.16 Type A isomerization: R group migration (e.g. methyl) [28].	29
Figure I.17 Susceptible bonds to β -scission (R: H, CH_3 , C_2H_5) [28].	30
Figure I.18 Mechanism of cracking reaction through β -scission (R_n : H, CH_3 , C_2H_5 ...) [28].	30
Figure I.19 Schematic representation of the proposed classical mechanism [64].	32
Figure I.20 Schematic representation of n-heptane hydroisomerization over bifunctional Pt/Hzeolite catalysts [125].	32
Figure I.21 Effect of crystallite size on the physico-chemical properties of the zeolite: (1) the outer surface ($\times 0.01 \text{ m}^2/\text{g}$), (2) microporous volume (cm^3/g), (3) the relative contribution of external surface to the acidity of the zeolite [134].	35
Figure I.22 Effect of Pt concentration on n-hexadecane conversion.	38

Figure I.23 Isomers yield as a function of conversion over a Pt/H*BEA zeolite with different Pt loadings [82].	39
Figure I.24 Impact of the AF and HDF balance on the Pt/HY stability, activity and selectivity to isomers in n-decane hydroisomerization (250 °C, P _{atm} , H ₂ /C ₁₀ =9) [68]. Adapted from [49].	40
Figure I.25 Different series catalysts. Adapted from [82].	41
Figure I.26 TOF values of the catalysts series as function of the n _{Pt} / n _{H⁺} ratio. Adapted from [82].	42
Figure I.27 Controlled deposition of platinum (Pt) on the zeolite Y (fig. a) and the alumina component (fig. b) of Y/A extrudates. Pt particles are colored in yellow, zeolite Y in green, and alumina component in red. Adapted from [69].	43
Figure I.28 Comparison between hydroisomerization and hydrocracking of n-C ₆ – n-C ₁₀ paraffin over Pt/CaY catalyst [128].	44
Figure I.29 Hierarchical zeolite materials classification with their typical pore distribution [166].	46
Figure I.30 Brief overview on the various synthesis routes towards hierarchical zeolite materials. Adapted from [161].	47
Figure I.31 Dealumination of zeolites. Adapted from [19].	50
Figure I.32 Schematic representation of how Si/Al ratio dictates the formation of mesopores in ZSM-5 desilicated by NaOH [190].	51
Figure I.33 Hydrolysis of framework Si in alkaline medium. Adapted from [157].	52
Figure I.34 Comparison of desilication of zeolite in presence of organic (TPAOH, TBAOH) and inorganic (NaOH) species. Adapted from [191].	53
Figure I.35 X-ray diffraction patterns of parent and desilicated *BEA zeolite. Adapted from [162].	55
Figure I.36 X-ray diffraction patterns of parent and desilicated ZSM-5 zeolite. With treatments: AT (0.2NaOH), OT-4 (1M TPAOH, 300 min) and OT-3 (1M TPAOH, 480 min). Adapted from [191].	55
Figure I.37 Nitrogen adsorption isotherms (A) and pore size distribution (B) of parent and modified zeolites. Adapted from [164].	57
Figure I.38 TEM images of the parent Beta zeolite (a at 500 nm and a' at 200 nm) and Beta zeolite treated with 0.2 M NaOH (b at 500 nm and b' at 200 nm) and 0.2 M NaOH&TBAOH mixture (c at 500 nm and c' at 200 nm). Adapted from [162].	58
Figure I.39 TEM images of ZSM-5 zeolite before (A) and after (B) desilication. Adapted from [215].	59
Figure I.40 IR spectra of OH groups of parent ZSM-5 zeolite and its desilicated forms with different base concentrations. Adapted from [215].	60
Figure I.41 Silanol (3746 cm ⁻¹) and hydroxyl nests (3460 cm ⁻¹) in ZSM-5 zeolite. Adapted from [219].	61

Figure I.42 IR spectra showing the evolution of Brønsted and Lewis sites before and after desilication of USY, Beta and ZSM-5 zeolites. Adapted from [164].	61
-------------------------------------------------------------------------------------------------------------------------------------------------------------	----

Chapter II

Figure II.1 Platinum exchanged *BEA zeolites calcination program.	70
Figure II.2 Types of physisorption isotherms [217].	74
Figure II.3 Determination of the micropore volume of *BEA zeolite (CP811) through the DR method.	78
Figure II.4 Different types of t-plots: (a) nonporous solid; (b) mesoporous solid; (c) microporous solid and (d) micro- and mesoporous solid.	79
Figure II.5 T-plot example for *BEA zeolite (CP811).	80
Figure II.6 *BEA's OH stretching vibrations bands.	83
Figure II.7 Pyridine interaction bands ($1400 - 1700 \text{ cm}^{-1}$) of H*BEA zeolite (CP811) drawn at different temperatures.	84
Figure II.8 IR spectrum of CO adsorbed on Pt/H*BBEA (CP811).	87
Figure II.9 Accessible platinum sites determination (n_{Pt}) by CO adsorption followed by IR spectroscopy.	87
Figure II.10 H*BEA (CP811) structure bands.	89
Figure II.11 Different parts of the "Microactivity Effi" apparatus.	92
Figure II.12 Reactors and heating systems.	93
Figure II.13 Automatic six-port valves.	93
Figure II.14 Liquid-gas separator.	94
Figure II.15 Catalysts reduction program.	95
Figure II.16 Schematic view of the charged reactor with 0.2 – 0.4 mm catalyst particles.	96
Figure II.17 GC oven temperature program for the three reagents (n-C ₁₀ , n-C ₁₂ and n-C ₁₄) transformation products.	97
Figure II.18 Chromatogram examples of: a) n-C ₁₀ , b) n-C ₁₂ , and c) n-C ₁₄ hydroisomerization.	98
Figure II.19 Oven temperature program and analysis conditions of the GC.	102
Figure II.20 Pilot plant flowsheet.	102
Figure II.21 n-Hexane cracking chromatogram example.	103

Chapter III

Figure III.1 Variation of (a) mass yield and (b) crystallinity vs. total concentration of hydroxyl anions, and of (c) mass yield vs. crystallinity.	111
-----------------------------------------------------------------------------------------------------------------------------------------------------	-----

Figure III.2 XRD diffractograms of the selected zeolites of series: (1-3).....	112
Figure III.3 TEM microphotographs of P1, P2, MC, P1-D1, and P1-D2 zeolites, and Pt/P2-D6 catalyst.....	115
Figure III.4 Crystallites size distributions of the zeolite of series (1) and two zeolites of series (2).....	116
Figure III.5 TEM images of parent and desilicated zeolites of the microcrystal series (S3) at 100 nm scale.....	117
Figure III.6 Nitrogen sorption isotherms and there corresponding BJH curves of the selected zeolites of series: (1-3). The isotherms are shifted by 150 cm ³ /g.....	119
Figure III.7 Variation of porosity characteristics as a function of total concentration of hydroxyl anions.....	121
Figure III.8 Sheme shwoing the decrease of intercrystalline mesopore after desilication (series 1 zeolites).....	122
Figure III.9 Hydroxyl groups of the selected zeolites of series (1-3).....	123
Figure III.10 Variation of acidic properties of the different zeolites as function total concentrations of hydroxyl anions.....	126
Figure III.11 n-hexane conversion as a function of time-on-stream for the various catalysts of series: (1-3). ...	127
Figure III.12 Catalysts initial activities (a), ratios between final and initial activities (c), coke content (d) as a function of acidity, and ratios between final and initial activities as a function of coke content (b).	128
Figure III.13 Coke content as a function of acidity of the catalysts of the series: (1-3). The empty boxes correspond to the coke in the micropore, and the filled one in the mesopore.....	129
Figure III.14 Variation of paraffin (a) and olefin (b) products molar yield as a function of n-hexane conversion for all the selected catalysts.	131
Figure III.15 Ratios of initial paraffin to olefin (a) and normal to isomers (b) molar yields products as a function of n-hexane conversion for all the selected catalysts.	132
Figure III.16 Variation between initial (in black) and final (in red) “paraffin to olefin” (a) and “normal to isomers” (b) molar yields vs n-hexane conversion for all the selected catalysts.....	132

Chapter IV

Figure IV.1 n-C ₁₀ conversion as a function of temperature of the catalysts of series 1.	145
Figure IV.2 n-C ₁₀ conversion as a function of temperature of the catalysts of series 2.	146
Figure IV.3 n-C ₁₀ conversion as a function of temperature of the catalysts of series 3.	146
Figure IV.4 Yield in isomers (I) (a) and cracking (C) (b) products vs n-C ₁₀ conversion obtained over series 1 catalysts.....	149
Figure IV.5 Yield in isomers (I) (a) and cracking (C) (b) products vs n-C ₁₀ conversion obtained over series 2 catalysts.....	150
Figure IV.6 Yield in isomers (a) and cracking (C) (b) products vs n-C ₁₀ conversion obtained over series 3 catalysts.	151

Figure IV.7 Reaction scheme of n-C ₁₀ transformation.	152
Figure IV.8 Yield into monobranched (M), multibranched (B), isomers (I) and cracking (C) products. Experimental points (points) and theoretical curves (continuous lines) obtained from the kinetic model.	153
Figure IV.9 Cracking products distribution as a function of carbon number on the catalysts series: (1-3).	154
Figure IV.10 (a) Variation of initial C/I ratios, (b) variation of maximum isomers (I) yield; on the different catalysts as a function of n_{Pt} / n_{H^+}	156

Chapter V

Figure V.1 n-alkanes conversions vs temperature over series 1 catalysts.	167
Figure V.2 Yield in isomers over series 1 catalysts in the three n-alkanes transformations.	168
Figure V.3 Cracking products distribution over series 1 catalysts in the transformation of the three n-alkanes.	169
Figure V.4 n-alkanes conversions vs temperature over series 2 catalysts.	170
Figure V.5 Yield in isomers over series 2 catalysts in the three n-alkanes transformations.	171
Figure V.6 Cracking products distribution over series 2 catalysts.	172
Figure V.7 TOF values (a) and $n_{a,s}$ (b) vs carbon number for catalysts of series 1 and 2.	177

General Introduction

General Introduction

Zeolites are crystalline aluminosilicates that possess mono- or multidimensional microporous system. Many aspects of our daily life are related directly or indirectly to the interference of zeolites acting as molecular sieving materials. Being rich with unusual features, they are used in wide range of applications: adsorbents in fields as oil refining and petrochemistry, water and wastewater treatments, agriculture, in addition to their use as ion-exchangers and catalysts for catalyzing many industrial processes. They are known materials to have high surface area, which is in relation to their microporous structure. Moreover, their compositional flexibility and framework, physical and hydrothermal stabilities, cations that act as exchanging species, non-toxicity, and their accepted cost to benefit ratio, make them the most attractive candidates for these industrial applications.

The success of the zeolites in the industrial catalytic reactions is surely due to their micropores in which most of the catalytic sites are located and where the reactions take place. These materials consist of cages and channels whose sizes are very close to the usual organic molecules. Notwithstanding the positive effect induced by these micropores with respect to shape selectivity, they may still provoke negative impacts by lowering the rate of access of molecules into the crystals of the zeolites, and favor unwanted adsorption effects of the reactants or the products as they undergo the catalytic action. For example, in the hydroisomerization of n-alkanes, while short alkanes can rapidly diffuse in the micropore to undergo the reaction even deep inside the zeolite crystal, long alkanes will experience severe diffusion obstacles and will tend to react in a preferred undesired way on the active acidic sites located shortly after penetrating the pore. Hence, it was of much importance to seek after materials that withstand the bulky molecules without distorting the main objective.

Bulky molecules that cannot diffuse properly into the zeolite micropores might induce negative impact on the efficiency and activity in the media containing such substrates. These limitations have stimulated the researchers to follow up after new zeolitic structures. The discovery of ordered mesoporous materials (OMMs) that possess uniform mesopores with the pore size larger than that of micropores ($> 2\text{nm}$), however, was not serving as alternative strategy to the use of microporous zeolites owing to the fact that the former do not possess the

zeolite's properties as the acidity and hydrothermal stability. Other methodologies to minimize diffusion limitation and enhance catalyst effectiveness were followed. Synthesizing zeolites with larger micropores and decreasing the zeolite crystal size to reduce the intracrystalline diffusion path length, were two of the strategies used to overcome diffusional limitations. However, a more generally applied strategy to obtain materials with sufficient molecular transport properties is to synthesize hierarchical zeolites. These zeolites combine the primary micropore system and a secondary one that consists of mesopores (2–50 nm) inside the microporous zeolite crystals. These improved structures enhance diffusion of bulky reactants and products molecules into and out of the pores respectively. This makes the distance to the active sites shorter and thus facilitates adsorptive and catalytic reactions.

The synthesis of these zeolites can be achieved by two different ways, either by constructive pathways (bottom-up approaches) or by destructive ones (top-down approaches). The constructive pathways concerns the direct creation of the secondary porous system during the synthesis of the zeolite by introducing for example structural directing agents. In the other hand, the destructive pathway is a post-synthetic procedure that accounts to subject an already synthesized zeolite to treatments that target there pore structure thereby introducing mesoporosity. More details will be discussed about the destructive pathways, namely desilication, in the first chapter of this thesis. Nonetheless, the post-synthetic procedures may affect not only the pore system of the zeolite, but also the structural, compositional, acidic and as well the final catalytic performance of the catalyst. For that it is of much importance to be aware not to induce severe changes in the intrinsic properties of the zeolites by introduction some organic molecules that afford some protection to the zeolites crystals during their dissolution in the treatment solutions.

The catalytic dewaxing (or n-alkanes isomerization) of the long chain linear paraffin, presents itself as a model reaction to characterize the diffusion pathways inside the zeolitic channels. This dewaxing/hydroisomerization process occurs through the bifunctional mechanism that requires metallic and acidic functions. The catalysts used to catalyze such reactions are said to be bifunctional, associating both hydro-dehydrogenating (metallic) functions that are provided by a noble metal (e.g. platinum or palladium), and the acidic functions that are on the basis of zeolites like beta (BEA), MFI (ZSM-5), Y, etc. However, stopping the reaction of catalytic dewaxing or hydroisomerization is required before the paraffin to undergo cracking (hydrocracking), where cracking is pronounced more with high carbon

number paraffin. Therefore, it is important to use an adequate catalyst that possess catalytic properties that can further induce high selectivity towards isomerization products. The acidic support of these catalysts should possess high textural properties provided either by the small crystals (nanocrystals) or by the secondary pore system (mesopores) that can afford the shortening of the diffusional path length, hence, favoring the activity and the selectivity towards the desired products. Knowing also that the catalytic cracking of n-hexane is a model reaction to characterize the acidic sites of the zeolites, it can be also used to investigate about the diffusional pathways inside the zeolitic channels.

The aim of this work was firstly to synthesize a microcrystal *BEA zeolite which is a purely microporous zeolite, and further subject it to several desilication treatments to induce hierarchization to the structure, and to study the impact of desilication on the structural, elemental, acidic and textural properties of the zeolite. Moreover, it was challenge to apply the desilication post-synthesis modification by different alkaline treatments on an already hierarchical nanocrystal commercial *BEA zeolites, and study the impact on their global characteristics as well. This will be discussed in chapter 3 of this manuscript.

After transforming the selected parent and modified zeolites to their bifunctional form by impregnation of the noble metal, platinum, the second objective of this thesis was to study the impact of hierarchization of nano- and microcrystal *BEA zeolites on the catalytic performance in hydroisomerization of n-alkane (chapter 4). The impact platinum content on the activity of the catalyst and its selectivity towards isomerization was also studied (chapter 4).

The last objective was to study the impact of chain length on the catalytic performance of the requested catalysts in the hydroisomerization of n-C₁₂ and n-C₁₄, and if desilication would account for better performance of the catalysts by the improvement of the textural properties.

Chapter I

Literature Review

1 Zeolites: History

The history of zeolites really began with the discovery of a mineral (stilbite) by the Swedish mineralogist Crönstedt since 250 years ago, which (the mineral), due to its high water content, swelled when heated in a flame [1]. To this new family of minerals (hydrous aluminosilicates), he gave the name of zeolites derived from the Greek words zeo and lithos: the stone that boils. It is the advent of synthetic zeolites and simultaneously the discovery of large sedimentary basins that have allowed their use for many application.

Specialists in the synthesis of zeolites have been (and continue to be) particularly creative, due to the fact that only about forty different zeolites have been found in nature, while more than 180 have been synthesized. Moreover, the field of synthesis remains widely open, with theoretical considerations that suggest possible higher number of zeolite structures [2].

The first synthetic zeolites (called X, Y, and A) had quickly found applications in three major domains:

- Adsorption: Drying refrigerant gases and natural gas and for the separation n / isobutane on zeolite A (Isosiv process, 1959);
- Catalysis: Isomerization (1959) and cracking (1962) over zeolites X and Y;
- Ion-exchange: Replacement of polyphosphate pollutants in detergents (1974) by zeolite A.

Over the last 20 years, spectacular progress has been made with the synthesis of non-aluminosilicic microporous zeolites (silicoaluminophosphates [3], titanosilicates [4], etc.) and mesoporous zeolites [5,6]. The size of the channels of these mesoporous zeolites (≥ 2 nm) makes it possible to envisage their use for the transformation of very congested or bulky molecules. However, these solids generally do not have the appropriate active sites and therefore can't be used as such. Increasing the accessibility of zeolite active sites is an alternative widely exploited during the last two decades with the synthesis of nanocrystalline zeolites [7], or the delamination of zeolites into sheets [8]. An important research effort has been made to introduce zeolites into new fields: membranes, optoelectronics, functional nanomaterials, etc., but still their applications are limited to particular areas [9].

1.1 Composition and structure

Zeolites, also known as molecular sieves, are defined as microporous and crystallized solids belonging to the tectosilicate family. Their particular structure is related to the regular polymeric combination of primary building units (PBU), with tetrahedral geometry. Each oxygen atom, forming the vertices of these tetrahedra, is connected to two atoms of trivalent or tetravalent T elements (T = Si or Al) located in the center of the tetrahedron (O-T-O-T-O sequence, illustrated in Figure I.1): thus the O / T ratio is strictly equal to 2.

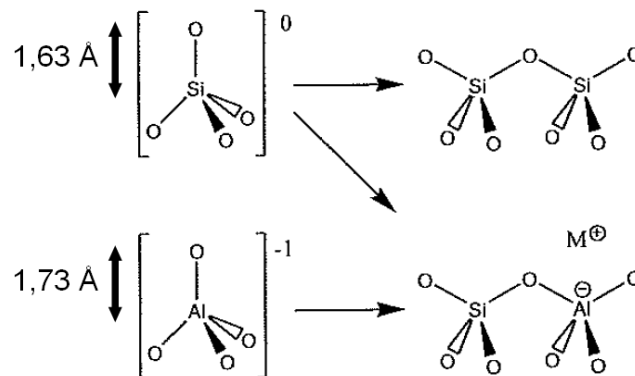
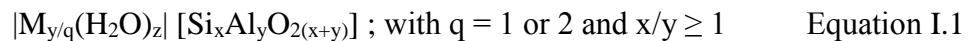


Figure I.1 Scheme of the tetrahedral assemblies of SiO_4 and AlO_4^- .

Zeolites in general have the following chemical formula:



Where M represents the alkaline (Na^+ , K^+) or alkaline-earth (Ca^{2+} , Mg^{2+}) cations, being the protons compensating the charges induced by the presence of trivalent AlO_4^- tetrahedra within the zeolite framework, q being the electronic charge of M, and z the quantity of water physisorbed.

The tetravalent tetrahedra SiO_4 has a zero electronic charge and therefore do not contribute to the overall load of the framework. The Si/Al atomic ratio that defines the intrinsic acidity of the zeolite is in all cases greater than 1. This is explained by an energy differential evaluated at 60 kJ/mol when two AlO_4^- tetrahedra are adjacent, compared with an alternation of AlO_4^- and SiO_4 tetrahedra [10]. This alignment is therefore less energetic: this is the Loewenstein rule [11].

Nowadays, “zeotypes” is the definition that has been extended to any crystalline mesoporous solid formed of silicon oxide where some of Si atoms have been replaced by

trivalent element atoms (Al, Fe, B, Ga, etc.), tetravalent (Ge, Ti, Zr, etc.) or even pentavalent element atoms (P, As) [12,13]. The combination of these secondary building units (SBUs) serve as reference units for classifying and describing the various structures of zeolites and their microporous networks. In 2007, 23 different SBUs were listed as demonstrated in Figure I.2.

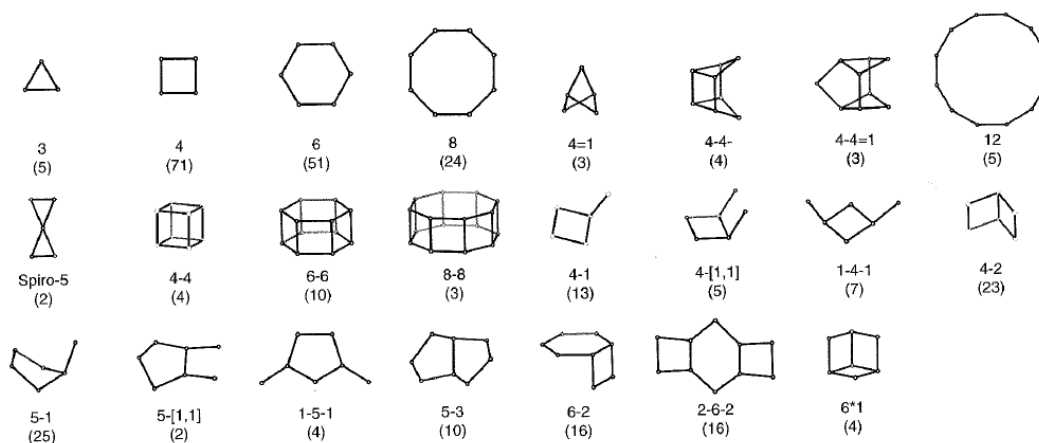


Figure I.2 The 23 secondary construction units (SBUs) listed [14]. Each edge corresponds to a T-O bond. Their frequency of occurrence is indicated in parentheses.

These SBUs can recombine with each other forming one of the 47 Composite Building Units (CBU), precursors of the zeotypes. Finally, the periodic assembly of these CBUs with other SBUs and / or CBUs leads to the formation of structures, characterized by a single porous network consisting of channels and cavities with calibrated morphologies and sizes (from 0.3 to 1.5 nm, up to 2.0 nm in the case of germanosilicates or metallophosphates) [15–17]. Figure I.3 illustrates these various steps.

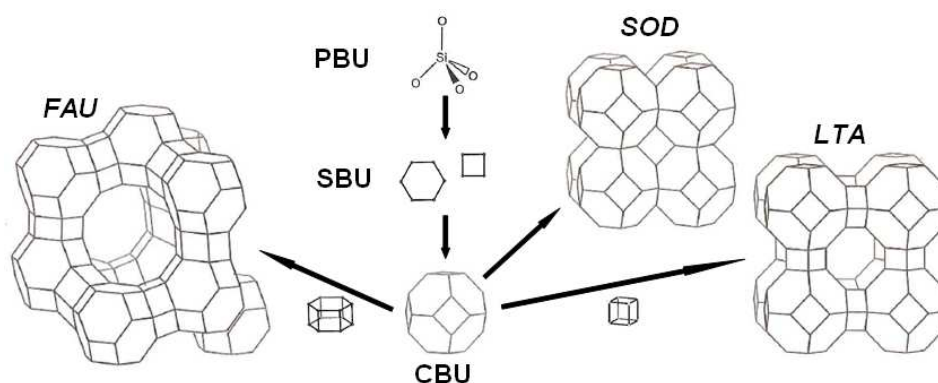


Figure I.3 Formation of FAU, LTA and SOD structural zeolites from the same "sod" composite construction unit (CBU), passing through the combination of primary building units (PBU) into secondary units of Construction (SBU).

For the moment, various structural zeolite types, natural or synthetic, have been discovered. Each of these structures is assigned a mnemonic code consisting of three letters and proposed by the Structural Committee of the International Zeolite Association (IZA). An asterisk is added to the mnemonic code in the case of a zeolite structure with structural defects and a dash is placed following this code to indicate that the structure of the zeolite is interrupted. The IZA structure commission (IZA-SC) describes around 232 zeolite structures by 2016. Regular updates can be found on the IZA website (<http://www.iza-structure.org/databases/>).

1.2 Porous structure of zeolites

The use of zeolites in catalysis is linked to the presence of acid sites in their porosity (protonated zeolites). The size of the pores is also an important factor because only those products whose kinetic diameter is in line with that of the pores will be formed. Moreover, since the catalytic adsorption / desorption processes involve the diffusion of molecules through the pores of the zeolite, only the opening pores containing at least 8 oxygen atoms O or 8 T atoms (T = Al, Si) allow this diffusion. Zeolites are classified into 3 main categories according to their porosity:

- Small pore zeolites (8MR): the opening of the pores (diameters of 0.30 - 0.45 nm) is delimited by 8 atoms (O or T) (e.g. LTA, SAPO-34).
- Medium pore zeolites (10MR): the pore opening (diameters 0.45 - 0.60 nm) is delimited by 10 atoms (O or T) (e.g. MFI, ZSM-22, MCM-22).
- Large pore zeolites (12MR): the opening of the pores (diameters of 0.60 - 0.80 nm) is delimited by 12 atoms (O or T) (e.g. FAU, MOR, *BEA).

The comparison of the pore openings of the zeolites with the kinetic diameter of the molecules (e.g. n-butane 0.43 nm, isobutane 0.50 nm, benzene 0.585 nm, etc. [18]) clearly shows that zeolites can be used for molecular sieving. It should be noted, however, that these dimensions depend on temperature, which increases both the flexibility of the organic molecules and the "respiration" of the network and the pore mouth of the zeolites.

1.3 Zeolite Acidity

It is agreed that the transformation of the hydrocarbons occur on the protonic sites rather than Lewis sites. The latter do not intervene directly in these reactions, but can increase the acid strength of neighboring proton sites. The origin of this protonic acidity is associated to the

negative charge on the AlO_4^- tetrahedra that form the zeolite framework. In acid catalysis, the activity of a zeolite obviously depends on the number of proton sites and their activity. The activity of proton sites depends on their location (accessibility), their strength (the stronger the site, the more active it is), and sometimes their concentration. [19]

The protonic acidity of the zeolites arises mainly from bridged hydroxyls: $\text{Al}(\text{OH})\text{Si}$. However, other hydroxyl groups are present, generally created by zeolites' dealumination during their pretreatment: silanol groups, hydroxylated EFAL species (extra-framework Aluminum species), etc. These hydroxyl groups sometimes have an acidic force sufficient to start certain catalytic reactions. [19]

The protonated oxygen atom, which is connected to an Al atom in the zeolite structure, forms three different bonds. A positive charge is observed then because of an excess bond on the oxygen atom. However, the high electronegativity of the oxygen atom provokes a displacement of the hydrogen electrons towards the first, leading to a transfer of the positive charge to the hydrogen atoms. This process gives the O-H bond a weak ionic character that can be easily subjected to breakage. Therefore, the Brønsted acid sites are at the origin of the proton that can have a large mobility over the zeolite structure as shown in Figure I.4 [19–22].

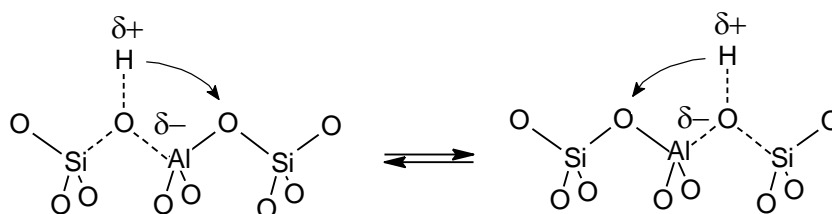


Figure I.4 Proton mobility in a zeolite.

The maximum number of protonic acid sites (bound to bridged hydroxyls) is equal to the number of framework aluminum in the tetrahedral position. Since the aluminum atoms can't be adjacent to each other taking into account that Al-O-Al bond is much too unstable in the framework (Lowenstein rule), the maximum number of proton sites is that obtained for the lowest Si/Al ratio which is equal to 1 (8.3 mmol of H^+ per gram of zeolite [19]). However, no pure protonic zeolite can be prepared with this low Si/Al framework ratio. For this Si / Al ratio but also for higher ones, the actual number of protonic sites is smaller than the theoretical number obtained. This is due to an incomplete proton exchange of cations and dehydroxylation or even dealumination phenomena during the activation of the zeolite at high temperature (500-

550 °C) before its use in any catalytic test. The parameters that affect the acidic strength are illustrated in Figure I.5 below:

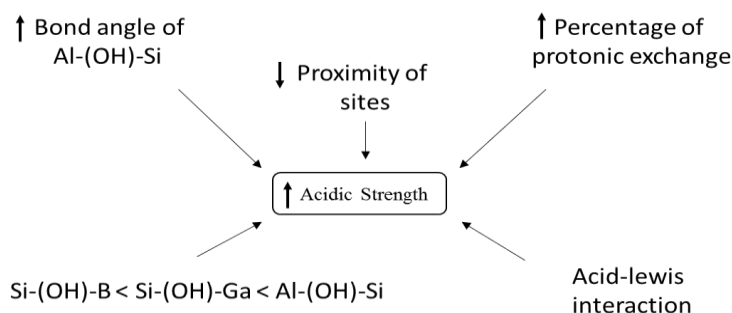


Figure I.5 Parameters determining the acidic strength of the protonic sites.

In other words, it is said that the acidic strength of the protonic sites depends on the rate of exchange of the alkaline cations of the zeolite, and it increases as might be expected with the percentage of exchange. However, at approximately 100% exchange rate, this increase in acid strength seems to arise not only due to the creation of very strong protonic acid sites but also due to the increase in the acid strength of the protonic sites itself that are already present in the zeolite [23].

Moreover, the EFAL species (octahedral or tetrahedral aluminium atoms) generated through dehydroxylation and dealumination [19,20,24], together with the tri-coordinated Al located in the structural defects are responsible for the Lewis acidity in the zeolites. Lewis acid sites can be found in several types in the zeolitic structures: Al^{3+} , AlO^+ , $\text{Al}(\text{OH})^{2+}$, $\text{AlO}(\text{OH})_3$, $\text{Al}(\text{OH})$, Al_2O_3 (neutral Al), $\equiv\text{Si}^+$ (silicate species) [25–27].

1.4 Shape selectivity

The catalytic reactions over zeolites occur mainly within their intra-crystalline porous systems, where the major part of the active catalytic sites is located. Consequently, the size and shape of the zeolites' cages, channels and pore apertures, can highly influence the diffusion of the molecules, entry and exit of reactants and products respectively, as well as disturb the formation of some intermediate compounds (bulky molecules) or transition states in some reaction mechanisms. This "shape selectivity" plays an important role in the zeolite industrial application [19,24,28–32]. It has become the basis of many industrial processes in oil refining and petrochemical processes [33]. Conversion and product yields can be influenced by a simple

change in the zeolites pore architecture. Furthermore, the zeolite structure can be selected in order to favour or prevent a desired reaction.

Three theories of zeolite shape selectivity are widely accepted and the other five are less acknowledged [34]. The reactant, product and transition state shape selectivity mechanisms are widely accepted theories as been proven in literature [32,35,36]. On the contrary, the other theories are still subjects of debate: pore-mouth / key-lock shape selectivity [37–40], molecular traffic control [41–43], inverse shape selectivity [44,45], “nest effect” [41,46], and the “window effect” [47,48].

1.4.1 Reagent shape selectivity

This mechanism distinguishes between different competing reactants. It is based on the molecular size exclusion at or very near the pore mouth. Consequently, only a portion of the reactants can, in an easy way, access the active sites located inside the pores of the zeolite [34]. Therefore, this type of shape selectivity depends on the pore geometry of the zeolite structure. One example of this mechanism is on the selective catalytic “dewaxing” of branched paraffins over ZSM-5 zeolite [37] (Figure I.6).

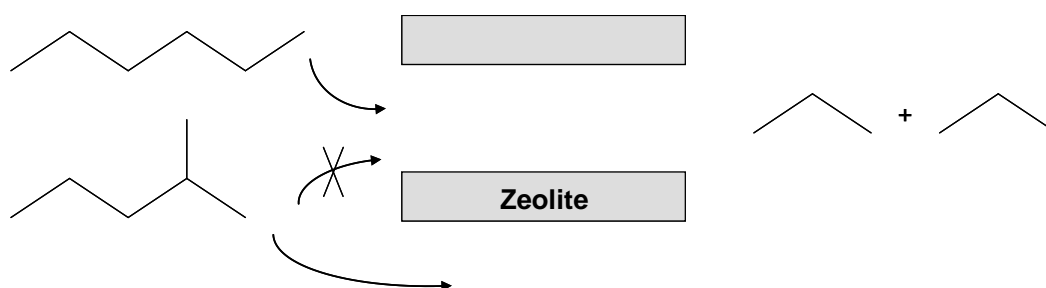


Figure I.6 Reagent shape selectivity example in catalytic dewaxing. Adapted from [49].

1.4.2 Product shape selectivity:

This mechanism refers to the case where the pore diameter is small enough to interfere on the product molecules of the reaction exiting the pores. Therefore, even if large molecules are formed in cages or channel intersections, these can only exit the zeolite structure if they are small enough to diffuse out of the zeolite’s pore aperture [34]. An example of this mechanism is the selective toluene disproportionation for the production of para-xylene [50,51] (Figure I.7).

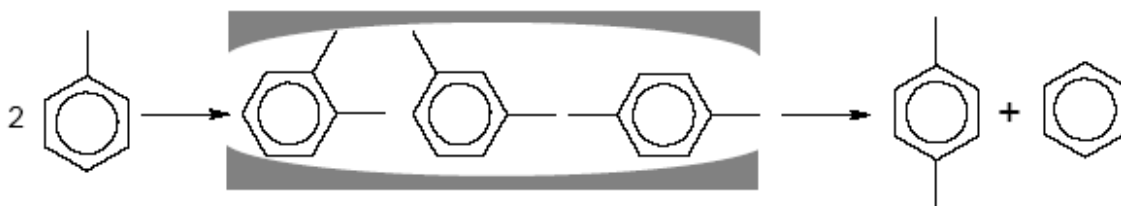


Figure I.7 Product shape selectivity example in Toluene disproportionation [49].

1.4.3 Transition-state shape selectivity

The current mechanism belongs to reactions where the geometry of the pores around the active sites endures steric constraints on the transition state [35]. Thus, the pore size causes formation inhibition of unstable transition states or reaction intermediates [46].

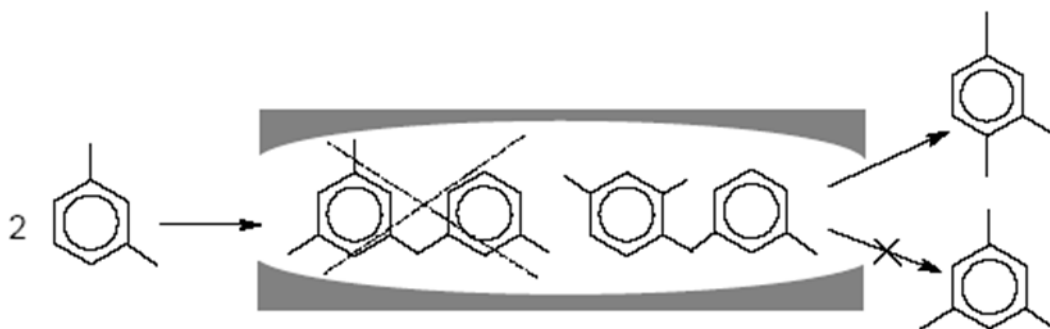


Figure I.8 Transition state shape selectivity example in disproportionation of metaxylene [49].

1.4.4 Pore-Mouth / Key-Lock shape selectivity

This mechanism is concerned only in the interactions between the n-/iso-alkane and the zeolite pore over one-dimensional zeolite with non-intercepting medium pore zeolites [31,39,40]. In the hydroisomerisation reaction, this theory explains the high selectivity of such catalysts towards the formation of monobranched isomers. Figure I.9 shows schematically the possible adsorption configurations of long chain paraffin over the medium pore TON zeolite.

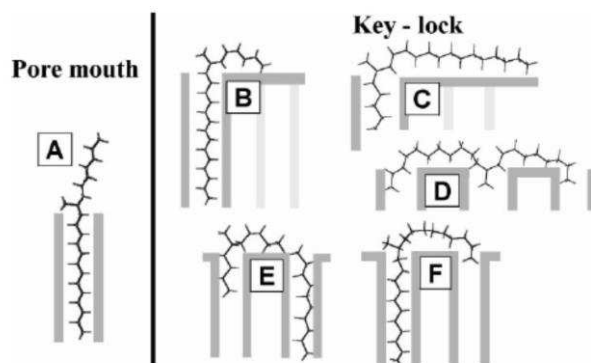


Figure I.9 Favored adsorption configurations of a iso-paraffins over TON zeolite [39].

According to this mechanism, only the linear paraffins are able to enter the zeolite structure due to the small pore sizes of the zeolite used. Consequently, monobranched isomer formation is favored, but once the isomerized form of the paraffin is formed, it will be less able to access the zeolite framework once more. Note that in the pore mouth mechanism, the molecules enter and exit from the same pore aperture, i.e. they do not exit from the other extremity of the pore.

1.4.5 Molecular traffic control

This theory is concerned specifically in the molecular sieves where two or more different pore systems with different diameters intersect. It considers the case where one of the molecules can easily diffuse on both pore systems and a second species can only diffuse on one of the pore systems [52]. Therefore, reactants that enter by one pore system can be converted in the molecular sieve and diffuse out through an alternative pore system. ZSM-5 is an example of zeolite structure of this theory [41,53].

1.4.6 Inverse shape selectivity

This mechanism theory seeks to explain the preferential adsorption of large molecules within the zeolite pores [34,44,45].

1.4.7 Window effect

The “window effect” refers to the variations of the diffusivity of the n-paraffins on the molecular sieves with increasing carbon number (Figure I.10).

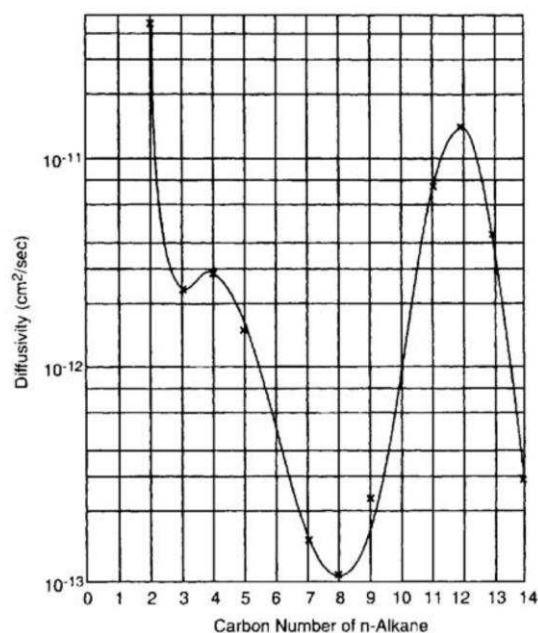


Figure I.10 “Window effect” example [54].

1.4.8 Nest effect

This theory was proposed to point for the shape selectivity changes in non-shape selective active sites on the crystallites external surface. The theory suggests that the acid sites located within cavities formed by the terminal of the pore at the surface level, are able to provide different shape selectivity than those inside the pore itself [34]. For example, in submicron crystals, if the external surface sites have the same catalytic behavior as the intracrystalline sites, or maybe more active than them, then the shape selectivity could be changed by these surface sites [55].

1.5 Zeolites in catalysis

Each type of zeolite can be obtained with a wide range of composition, even by direct synthesis and / or by post-synthesis treatments (exchange, dealumination, desilication, etc.). In addition, various compounds can be introduced into the pores of these zeolites or even synthesized therein (ship in a bottle synthesis). This explains why zeolites can be used as in many industrial processes that impose the presence of acidic, basic, acid-base, redox, bifunctional catalysts. However, the main applications are based on acid (monofunctional) and bifunctional catalysis. [19]

1.5.1 Monofunctional catalysis on zeolites

Most of hydrocarbon reactions and many transformations of functional compounds are catalyzed only by the acidic sites of the zeolites [19]. Many examples exist in literature that show the utilization of only a monofunctional zeolite (H-zeolite). Etherification of glycol have been reported to take place over H-*BEA and MFI (H-ZSM-5) zeolites [56]. The use of acidic zeolites were also seen to be catalyzing a Friedel-Crafts alkylation processes (over H-*BEA) [57], molecules cracking processes (over H-*BEA) [58,59], as well as dehydration processes (H-ZSM-5, H-*BEA, H-USY) [60], etc.

1.5.2 Bifunctional catalysis on zeolites

The catalysts responsible for catalyzing such mechanisms comprise a hydro/dehydrogenation function (HDF) represented by a metal, and an acidic function (AF) provided by the acidic support [61]. Zeolites, silicoaluminophosphates (SAPO), mesostructured and amorphous silica alumina, represent the acidic functions. Tungstated- and sulfated-zirconia, modified tungsten and molybdenum carbides and oxides [62], in addition to heteropolyacids [63], are also forms of acidic supports.

The HDF may be represented by noble metals (Pd, Pt) or non-noble transition metals (Mo, W, Co, Ni) [64]. Several studies were carried out to investigate the values of obtained conversion and selectivity with the indicated noble metals [65–67]. They were also found to be effective in the hydroconversion of LTFT waxes (low temperature Fischer-Tropsch) [64].

These bifunctional zeolitic catalysts are used in various industrial processes: isomerization of light and heavy alkanes, hydrocracking processes, dewaxing, aromatization of alkanes, isomerization of the aromatic C8 cut, etc. The HDF components associated with the zeolite can be very different and located in different positions:

- well-dispersed noble metals (Pt, Pd, etc.), being located in the pores of the zeolites, e.g. Pd/HFAU [68], or deposited on another support, e.g. PtAl₂O₃/HY catalysts used for hydroisomerization of heavy alkanes [69];
- Generally mixed metal sulphides deposited on alumina, e.g. hydrocracking catalysts NiMoS / Al₂O₃-HFAU;
- Metal oxides, e.g. Ga₂O₃ combined with an HMFI zeolite in the aromatization of light alkanes, the dehydrogenating sites being formed by a complex process in the first reaction moments [70].

Bifunctional catalysis reactions involve a succession of catalytic steps of hydro/dehydrogenation, rearrangement, cracking, etc., that result sometimes in the formation of small quantities of intermediates. These have to migrate from HDF sites to AF sites (and vice versa), this migration being in some cases the kinetic limiting step of the reaction.

1.5.3 Hydroisomerization reactions over zeolites

Due to the convenient acidic and shape selectivity properties of zeolites, they are often used to catalyze the hydroisomerization reactions. Zeolites like, BEA, MOR, TON, MFI and FAU, are often used for this purpose [64,71].

As referred, the small acid site density as well as its strength are important to improve the isomers selectivity. Nonetheless, the molecular shape selectivity governed by the zeolite pore system can highly intervene. The use of medium pore zeolites, e.g. ZSM-22 (TON zeolite), improves the catalysts selectivity towards monobranched isomers [31,37,72–74] through the Pore-Mouth / Key-Lock shape selectivity mechanism described in section 1.4.4. However, low activities are exhibited due to the nature of the mechanism, where only active sites located at the pores entrance and external surface of the zeolite framework are accessible for reaction [75,76]. Consequently, it is more preferred to use high external surfaces when using medium pore zeolites.

The use of large pore size zeolites allows the full access to all the available active sites within the pores, and therefore yields higher activities exhibited with the catalysts [77]. The lack of molecular shape selectivity enables the formation of multibranched isomers and can cause further cracking steps. The higher potential to cracking of molecules in the large pore zeolites is directly linked to the higher probability for the reagent to find an accessible acidic site. Therefore, the reduction of the acid sites density and their strength as well, will induce the selectivity towards isomers, but may reduce the catalyst activity in the same time. Another strategy can be efficient by reducing the molecules residence time inside the framework of the zeolite (small diffusion pathway), thus reducing the probability of these to be more in contact with the active sites. High external surface zeolites possess high meso- and macropore volumes, thus they enable a quick exit of the reaction products from the framework of the zeolite.

Among the large pore zeolitic structures, *BEA zeolite is one of the most used in the hydroisomerization catalytic processes [78–82]. This zeolite, has proven to be quite active in

hydroisomerization, as well as being easy susceptible to synthesis post-synthesis procedures in order to decrease the products residence time inside the framework.

1.6 Beta zeolite (*BEA)

The interest in Beta zeolite has grown steadily in recent decades. Indeed, it possesses certain characteristics, e.g. large pore structure and large cavities that result from the interconnection of its channels, in addition to its controllable acidity, make it a good candidate to perform in heterogeneous catalysis, playing the role of an additive for the reactions of FCC (Fluid Catalytic Cracking) [83], hydroisomerization reactions [78,84–87], as well as for organic chemistry reactions [88,89].

1.6.1 Structure of Beta zeolite

The *BEA type zeolite is an aluminosilicate compound which was synthesized for the first time in 1967 by Wadlinger, Kerr and Rosinski [90], from an aluminosilicate gel in a basic medium (NaOH) and in the presence of tetraethylammonium cation. The silica / alumina ratio of the framework of this zeolite is between 10 and 200 [88]. Before the knowledge of its structure in 1988 [91], Martens had classified this zeolite as a large-pore zeolite [92]. Its channel network is in fact the interconnection of two channel systems, one monodimensional and the other two-dimensional. Respectively, the first is parallel to the axis $\langle 100 \rangle$ and has channel openings of 12 tetrahedra ($7.6\text{-}6.4\text{\AA}$). As for the second, it is parallel to the axis $\langle 001 \rangle$ and consists of sinusoidal channels with pore openings of 12 tetrahedra ($4.5\text{-}5.5\text{\AA}$) [93] (Figure I.11).

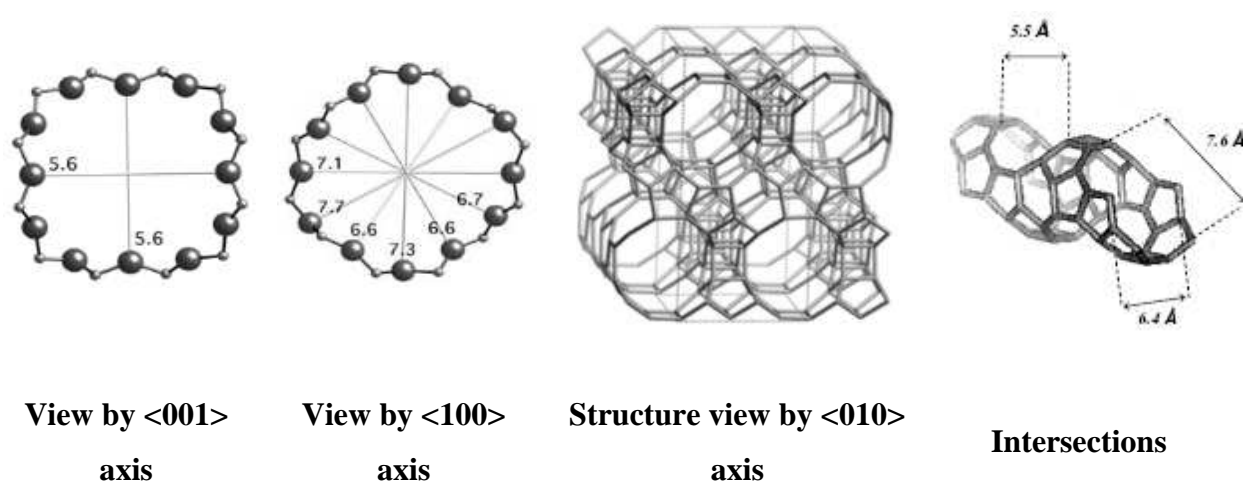


Figure I.11 *BEA zeolite representations.

Due to its complexity, the structure of the beta zeolite was only elucidated 21 years after its discovery, simultaneously by two teams: Newsam et al. (1988), and Higgins et al. (1988) [94,95]. Structural determination is the result of information provided by high resolution electron microscopy, X-ray diffraction and computer-aided modeling. *BEA zeolite results from the intergrowth of two neighboring structures (polymorphs), each provided with a three-dimensional system of 12-tetrahedron-formed pores. One of the structures is of tetragonal symmetry (polytype A), and the other is of monoclinic symmetry (polytype B) [93,96]. The different polymorphs proposed are given in Table I.1.

Table I.1 Proposed polymorphs for *BEA zeolite family [97].

Polymorph	Space group	Crystal unit parameters	Type of 12 MR channel
A (BEA)	P4 ₁ 22 ou P4 ₃ 22	a = b = 1,26 nm c = 2,64 nm	2 linear 1 sinusoidal
B	C2/c	a = b = 1,79 nm c = 1,43 nm $\beta = 114,8^\circ$	2 linear 1 sinusoidal
C_N (BEC)	P4 ₂ /mmc	a = b = 1,28 nm c = 1,30 nm	3 linear
C_H	P2/c	a = b = 1,79 nm c = 1,43 nm $\beta = 114,8^\circ$	2 linear 1 sinusoidal
D_N	P2/m	a = b = 1,28 nm c = 1,38 nm $\beta = 108,4^\circ$	3 linear

1.6.2 Structural defects of *BEA zeolite

Most of the defects discovered are due to inter-growth of different phases and stacking defects [98,99]. The observation of a large number of silanol groups in the *BEA zeolite could not be explained for many years, but it has been proposed that when two stacks occur within the same layer, the structures of the two polymorphs are incapable to connect at the extremities, leading to the formation of abnormal pores which can accommodate silanol groups. This type of defect is observed along the axis $\langle 100 \rangle$.

Figure I.12 shows the two polymorphs A and B of the *BEA zeolite and illustrates the formation of structural defects. The HRTEM images, recorded along the direction $\langle 100 \rangle$ of the *BEA zeolite, show the existence of numerous double pores of a size approximately equivalent to that of a pore at 17 MR or 15 MR (Figure I.12-a). Figure I.12-b shows the presence of pore at 12 MR (large white dots) surrounded by pores at 4, 5, and 6 MR (small white dots). It was found that the two polymorphs A and B intersect together and form numerous defects arranged in a disordered manner.

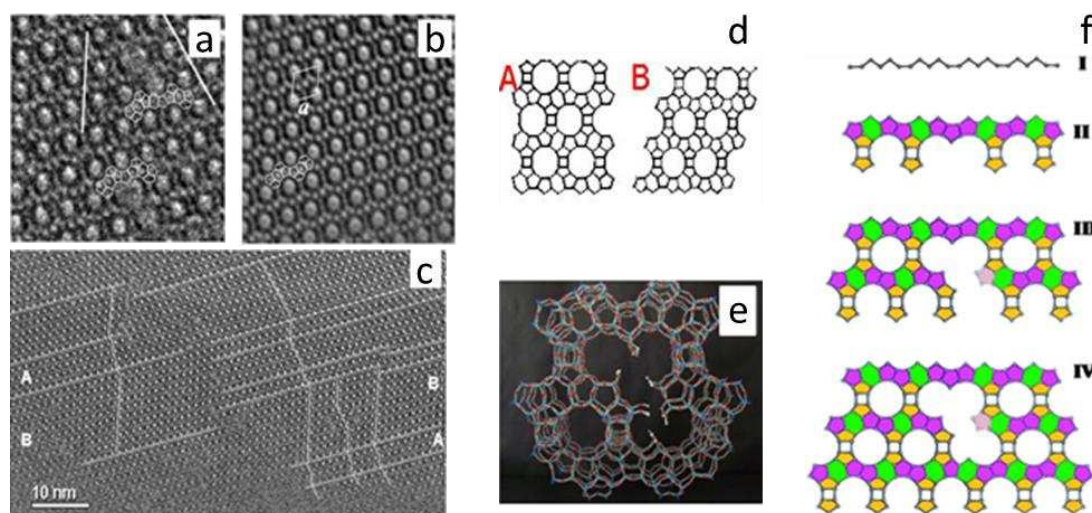


Figure I.12 Structural defects of *BEA zeolite.

Figure I.12-f illustrates the crystal growth sequence suggestion, indicating how defects are formed and how construction units adopt different orientations at defects (similar subunits are stained with the same colors). When the two polymorphs meet, they are unable to connect to form normal pores. Many open links are created on the wall of these defective pores (Figure I.12-f), on which silanol groups can be connected.

2 Hydroisomerization of alkanes

The hydroisomerization of n-alkanes contributes to the quality of diesel fuels and oils [100]. The issue behind dewaxing of diesel fuels and oils by means of hydroisomerization, i.e. to transform them from linear to branched alkane chains (mainly monobranched chains), is to improve the cold properties of these materials. This is called the isodewaxing process [19]. The isoparaffinic nature of these molecules are considered high quality diesel fuels [101,102]. They exhibit outstanding properties indispensable for a better engine performance: high cetane

number, low or no sulfur, nitrogen and aromatic emissions, which reduces the pollution caused by the engine's emissions [64].

2.1 Reactions involved in hydroisomerization

Two different types of active sites are required for the hydroisomerization process to take place. The acidic function (AF) represented by the zeolite support, and the hydro/dehydrogenating function (HDF) represented by the metallic element [19,24,28,64,103]. Elementary reactions occur on these functions separately, but when combined together, they form the bifunctional mechanism which is responsible to hydroisomerize the linear paraffins.

2.1.1 Metallic function reactions

The reactions that take place on the metallic function are of high importance for this bifunctional mechanism, being responsible for the first reaction step (as will be discussed later). The dehydrogenation and the hydrogenation reactions consist in the alkane transformation into its corresponding alkene and vice-versa. Other reactions like hydrogenolysis (cleavage of a C-C bond) and the skeletal isomerization of hydrocarbons, can occur on these functions [104]. However, no deep details on these reactions will be discussed due to the minimal impact accompanied by them.

As the hydrogenation and the dehydrogenation are in fact inverse reactions, the description will be focused only on the hydrogenation reaction mechanism.

The particular metallic function reaction that takes place in this bifunctional mechanism is the hydro/dehydrogenation reaction. The hydrogenation reaction consists in the saturation of a double bond with hydrogen. It is considered a highly exothermic reaction. Consequently, this reaction is thermodynamically favoured at low temperatures and high pressures. On the other hand, in order for such a reaction to take place, the catalyst should require a metal, e.g. platinum. The role of the catalyst is then the activation of the hydrogen so that the reaction can take place. This is due to the fact the thermal breakage of the H-H bond is energetically unapproachable. An example is given on the hydrogenation of ethylene molecule in Figure I.13.

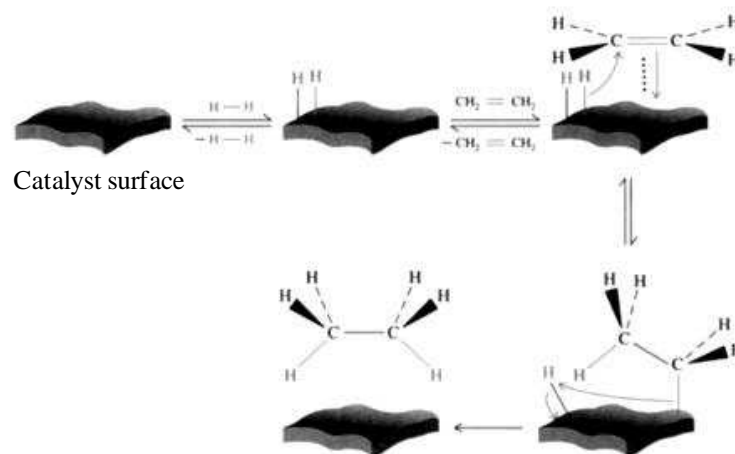


Figure I.13 Reaction mechanism of ethylene hydrogenation [105].

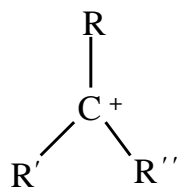
2.1.2 Acidic function reactions

The acidic sites of a zeolite are capable of inducing several chemical reactions. Cracking, isomerization, oligomerization, hydrogen transfer, alkylation, etc., are examples of such reactions [28,104]. These reactions happen through the activation of the hydrocarbon, even by the addition or by subtraction of a proton or a hydride / halogen, respectively. The Brønsted acid sites are then responsible for the protonation of the hydrocarbon [19,28,106–108], and the Lewis sites perform the hydride / halogen subtraction [28,104,109–111]. Regardless of the type of acid site used in these reactions, the activation of the hydrocarbon always results from the formation of a carbocation.

2.1.2.1 Carbocation chemistry

The hydrocarbon transformation over the acidic function of the catalyst occurs through the formation of carbocations as reaction intermediates [19,112,113]. Here are two different types of carbocations: the carbenium ion, which is the most common possessing a positively charged ion on a three-coordinated carbon atom (Figure I.14-A); and the carbonium ion which represents a positively charged ion but with a five-coordinated carbon atom (Figure I.14-A) [28,104,114].

A



B

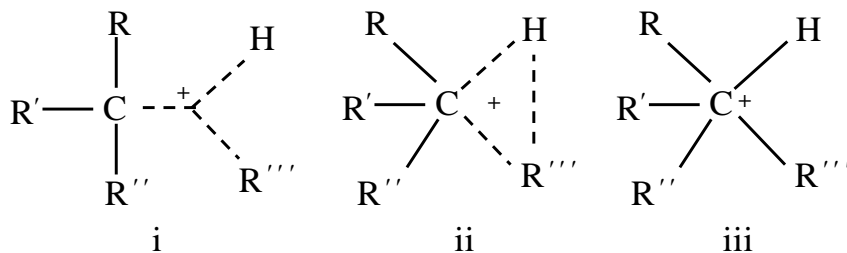


Figure I.14 Schematic representation of the carbenium (A) and three different configurations of carbonium (B) ions [28].

The carbocation stability is also a parameter to take into account when considering the possible formation of an intermediate, as the hydrocarbon transformation via highly unstable carbocation is very unfavored. Several factors may affect the stability of carbocations. For example, the presence of a double bond near the charge or an electron attractor group on the molecule, can highly stabilize the carbocation [28]. Moreover, a counter ion or polarizing solid (e.g. zeolite) near the molecule may also play a role in stabilizing the carbocation [28]. However, one rule can be generalized to summarize all forms: as much as the substitution degree of the carbon containing the positive charge is higher, as much the stability of the carbocation will be. Indeed, the occurrence of a carbocation on a carbon with three substitution groups (tertiary carbocation) is more likely to be formed than on a carbon with only one substitution group (primary carbocation) (Figure I.15).

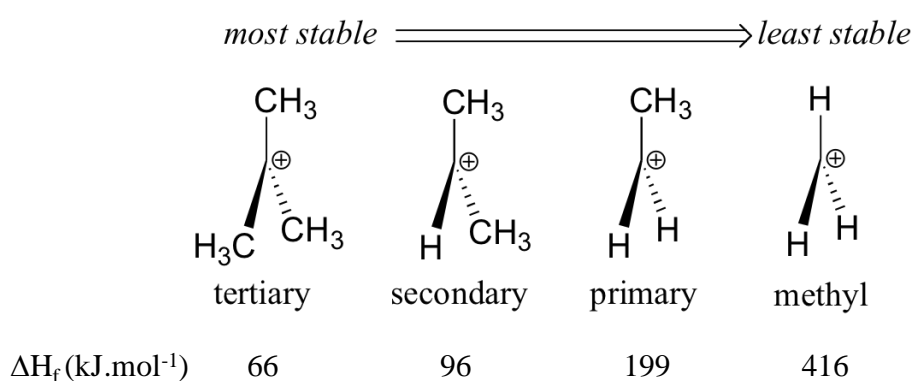


Figure I.15 Carbeniums stability. Heat formation values are taken from [106].

The figure shows also the values of the energy (heat) required to form these carbenium ions. Less energy is required to form the tertiary carbenium ion intermediate, which makes it the easiest to be formed in competition with the others.

2.1.2.2 Isomerization

The formation of the carbenium is followed by its transformation through isomerization. This reaction occurs intramolecularly in these molecules. The isomerization reaction can take place through two different types:

Type A isomerization, where the structure of the carbenium ion remains unchanged, and occurs by the migration of a negatively charged alkyl group (R^-) to one or two positions way [115], as described in Figure I.16.

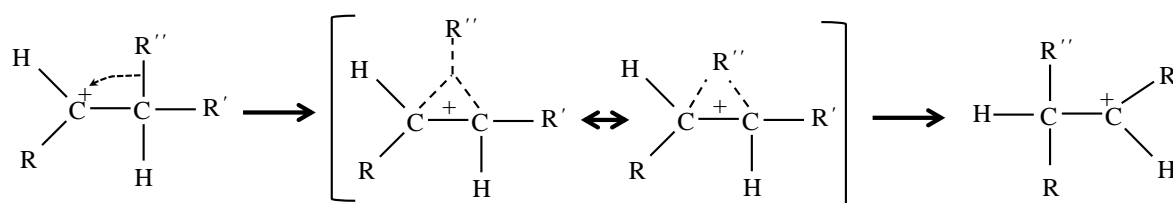


Figure I.16 Type A isomerization: R group migration (e.g. methyl) [28].

It is important to know that the migration rate of the alkyl group highly depends on the nature of the carbocation before and after migration to take place, e.g. Tertiary \rightarrow Tertiary \gg Tertiary \rightarrow Secondary.

Type B isomerization is defined when the transformation of the hydrocarbon occurs through the formation of a cyclic carbocation. It is characterized by an increase or decrease of the branching degree. In this case, the transformation is very unlikely since the isomerization of a linear into branched carbocation requires the formation of primary carbenium ion as an intermediate.

2.1.2.3 Cracking

The cracking reaction is defined by the scission of a C-C bond. From a thermodynamic view, this reaction is favored at high temperatures and low pressures due to the increase in the entropy and due to the endothermic nature of it [19,63]. Two cracking mechanisms exist on acid catalysts: the β -scission and protolytic cracking. Both of these mechanisms require the formation of carbocations as intermediates [19,28,104,116–119].

β -scission mechanism is defined by the promotion of the scission of a C-C or C-H bond in a carbenium ion just located in the β position of the positively charged carbon (Figure I.17).

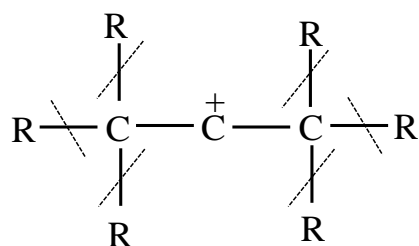


Figure I.17 Susceptible bonds to β -scission (R: H, CH₃, C₂H₅) [28].

The β -scission corresponds to the electrophilic attack by the C-C bond located in β position of the positive charge (Figure I.18). This leads to the cleavage of the molecule into two parts to form smaller carbocation and an olefin.

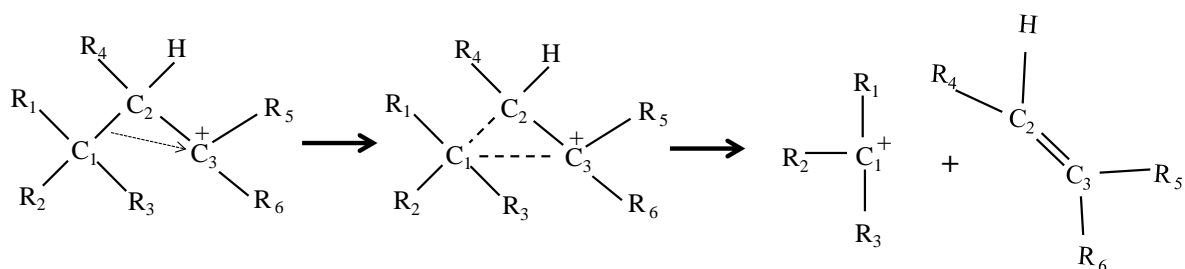


Figure I.18 Mechanism of cracking reaction through β -scission (R_n: H, CH₃, C₂H₅...) [28].

Like in isomerization, the nature of the carbenium ion before and after the scission is directly related to the reaction rate. The relative reaction rates of the different types of β -scission for the n-decane cracking on the bifunctional Pt/HUSY catalyst are presented in Table I.2.

Table I.2 Relative β -scission rates for n-C₁₀ transformation on Pt/HUSY catalysts at 405 K [120]. β -scission type B2 is taken as reference.

Transformation	Relative rate
Type A (Tertiary \rightarrow Tertiary)	1050
Type B1 (Secondary \rightarrow Tertiary)	2.8
Type B2 (Tertiary \rightarrow Secondary)	1.0

Type C (Secondary → Secondary)	0.4
Type D (Secondary → Secondary)	≈ 0

On the other hand, the **protolytic cracking** which occurs through the Haag-Dessau mechanism, is defined by the direct protonation of an alkane with the formation of a carbonium ion [104,119]. The formed unstable intermediate will collapse forming a carbenium and a smaller alkane (or hydrogen molecule) [63,119]. This mechanism becomes evident only at temperatures around 800 K or higher [104,119].

No further details will be provided about this mechanism since it requires higher temperatures than needed during the hydroisomerization reaction, taking into consideration that the latter performs at milder conditions to avoid as much as possible cracking reactions.

2.1.2.4 Other acidic reactions

Several reaction may take place over the acidic sites through acid catalysis, e.g. oligomerization and other reactions. However, the relevance of these reactions is ignored therefore will not be discussed. Nonetheless, reactions like coke formation or hydride transfer have no impact on the desired reaction, thanks for the presence of strong hydrogenation sites.

2.1.3 Bifunctional mechanism

The combination between the hydro/dehydrogenating functions (HDF) and acidic functions (AF) reaction, was proved since long time to be in fact the basis of this bifunctional mechanism [28]. This bifunctional mechanism that explained the different steps of the hydroisomerization reaction, was proposed by Weisz in the 50's [121–123].

Weisz's bifunctional mechanism proposal considers that the HDF and AF have an independent catalytic action. Nonetheless, each one of these functions has a complementary action to the second function. According to the classical reaction mechanism proposed, the hydrocarbon is dehydrogenated through the HDF action to form its corresponding alkene, where the latter diffuses to the AF where will be transformed into a carbocation that undergoes several possible transformations like: skeletal rearrangement, β -scission, cyclization, etc. The resulting intermediates diffuse back to the HDF to be hydrogenated into saturated

hydrocarbons. The schematic representation of this reaction mechanism can be seen in Figure I.19.

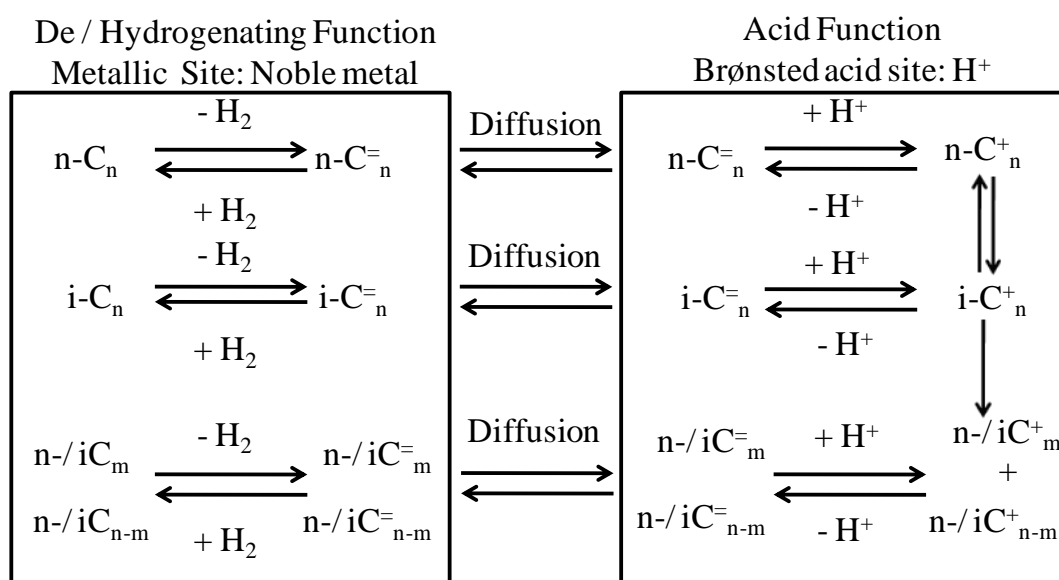


Figure I.19 Schematic representation of the proposed classical mechanism [64].

This mechanism is discussed more in details in literature. Seven successive steps are covered during this model reaction, 3 of which are chemical and 4 of which are physical. The chemical steps involve the hydro/dehydrogenation steps being catalyzed over the metallic sites, and the skeletal rearrangement for the reaction intermediates being catalyzed on the acidic sites. The physical steps require the diffusion of the molecules (alkanes and alkenes in gaseous phase) along the zeolite channels from Pt to H⁺ sites and vice versa [124–126]. This mechanism is illustrated in the next figure (Figure I.20) showing the application of this model reaction in n-heptane transformation over Pt/Hzeolite catalysts [125].

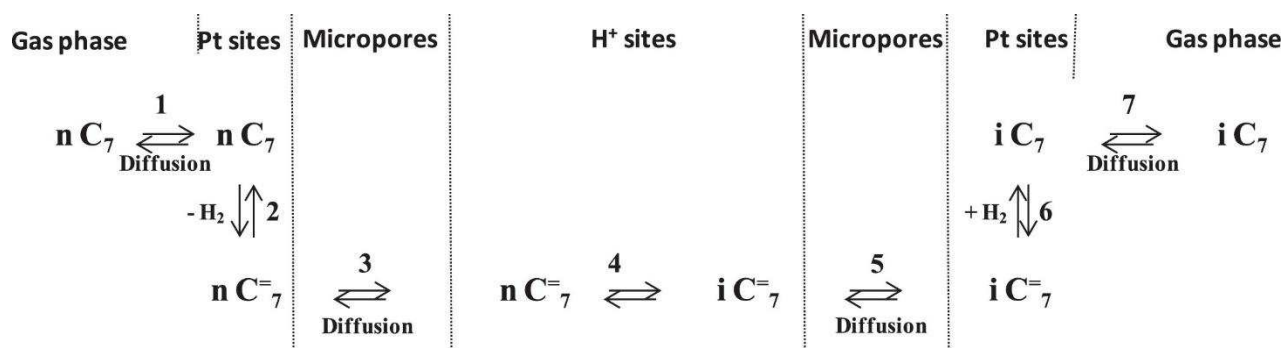


Figure I.20 Schematic representation of n-heptane hydroisomerization over bifunctional Pt/Hzeolite catalysts [125].

However, as proposed by Weisz, the olefin transfer between the active sites could be the reaction limiting steps, thus reducing the activity of the bifunctional catalyst and its selectivity toward mono-branched isomers [122]. To avoid any transfer limitations for these olefins, the HDF and AF active sites should be close enough. This is the “intimacy criterion” proposal. However, to obtain an ideal catalyst, the balance between the HDF and AF active sites should be taken into consideration so that the HDF are enough in quantity to feed the AF sites with the olefins [127]. However, many other parameters to be discussed further, play a crucial role in impacting directly the hydroisomerization reaction in terms of activity and selectivity of the bifunctional catalyst.

2.2 Parameters influencing the hydroisomerization reaction

Many parameters have been widely discussed in literature to define the ideal bifunctional catalyst that exhibit the optimal properties that permits to obtain optimal catalytic performance in the hydroisomerization reaction. Weitkamp considered that the ideal bifunctional catalysis is obtained above certain value of the balance between the HDF and AF, where the activity depended more on the acidic activity, with the acidic step being the rate determining step [128]. However, Guisnet et. al had shown on bifunctional zeolite catalysts that when the activity is no longer depending on the hydrogenating function, there is still an evolution in stability and selectivity to reach a plateau only at much higher values of the ratio between the hydrogenating and acidic activities [129]. The ideal catalyst was defined after the catalyst in which the apparent reaction pattern of alkane transformation is identical to that of alkene intermediate conversion [19].

Nonetheless, besides the independent influence of each of the HDF and AF sites, the synergetic influence is also taken into account (e.g. intimacy criterion, $n_{a,s}$, etc.), in addition to the textural properties, as well as the chain length effect, etc.

2.2.1 Influence of textural properties

2.2.1.1 Porosity

If the pore opening of the zeolite is small enough, the catalyst exhibits good isomerization selectivity for the conversion of n-paraffins [71]. The zeolites of medium pore size favor the formation of branched monomethyl isomers. In general, the selectivity to branched monomethyl isomers increases as porosity decreases, while branched mono-ethyl and mono-propyl isomers,

which are more sensitive to hydrocracking, are obtained on large pore and large cavity zeolites [71].

Several studies were performed on Pt/ZSM-22 catalyst in the hydroisomerization of long chain n-paraffins and were observed to obtain significant results in isomerization products [39,40,130]. The low cracking tendency of the iso-paraffins, via the β -scission mechanism, on this zeolite is explained by the limited penetration of these molecules into the openings of the micropores.

The effect of porosity was also observed in a study carried out by Taylor et. al on a mixture of n-C₁₆ and i-C₁₉ with equal molar fractions [131]. According to the authors, only transformation of n-C₁₆ was observed on the medium pore zeolites catalysts (Pd/SAPO-11 and PD/ZSM-5). On the contrary, large-pore zeolites like Beta (BEA), mordenite (MOR) and USY (FAU), had shown low activity for n-C₁₆ conversion until the complete conversion of i-C₁₉.

In another study in 2008, Soualah et al. have proven the effect of the porous structure of zeolites on activity and selectivity towards isomers products [78]. The study was done on large (*BEA) and medium pore zeolites (ZSM-5 and MCM-22) in the hydroisomerization of long-chain n-alkanes. Whatever the chain length was, the acidic sites of the three dimensional porous structure in the *BEA zeolite was more accessible to the paraffins than the acidic sites of the small diameter straight channels of ZSM-5 and MCM-22. This permitted higher activity exhibited with *BEA zeolite catalyst than ZSM-5 and MCM-22. Moreover, the large channels of *BEA zeolite, in addition to the smaller crystallites' size (20 nm for *BEA and > 100 nm for the other zeolites), allowed rapid diffusion of the molecules, and promoted as a consequence the formation of monobranched products with limited cracking [78]. However, the case with the small porous system of the other two zeolites was not the same, where cracking products were the major products obtained to the blockage of the intermediates inside the pores [78].

An attempt to improve the molecular diffusion of the olefin intermediates in the pores of a nanocrystal *BEA zeolite was performed recently in 2013 by Batalha et al. [81]. The nanocrystal *BEA zeolite with an ignored mesopore volume (0.08 cm³/g), was less selective to the isomers products in the hydroisomerization of n-hexadecane. The agglomeration of the zeolitic crystals seemed to obstacle the diffusion of the molecules in and outside the pores, and lead to high residence time inside the pores and consequently provoked cracking reactions to occur. However, the direct germination of this zeolite on α -alumina surface prevented the

agglomeration of its nanocrystallites without affecting the acidic and textural properties. The composite catalysts in this study were seen to be more active and selective than the *BEA nanocrystal zeolite [81]. This was attributed to better diffusion of the molecules in and outside the pores of the zeolitic phase, which lead to decrease the residence time inside the pores and avoid secondary reactions including cracking [81].

2.2.1.2 Crystallite size effect

The size of the crystallites has a great effect on the hydroisomerization selectivity and the distribution of the cracking products [132,133]. Decreasing crystal size in the nanometric range <100 nm produces substantial changes in the physicochemical properties of the zeolite, especially on the outer surface, microporous volume [132,133], and the fraction of acid sites on the outer surface of the crystals [134]. The variation of these properties are shown in Figure I.21. This decrease most likely affects the performance of zeolite-based catalysts in various ways, including altering the activity through changes in the relative contributions of "internal and external" acid sites [135].

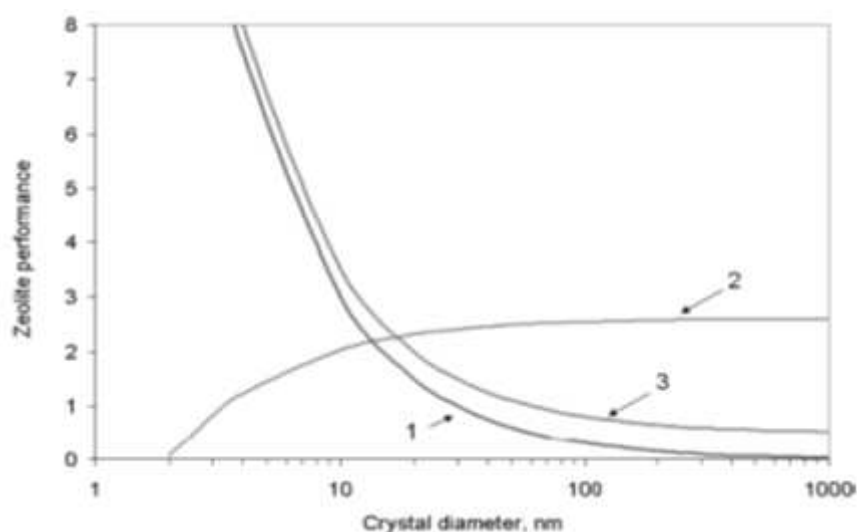


Figure I.21 Effect of crystallite size on the physico-chemical properties of the zeolite: (1) the outer surface ($\times 0.01 \text{ m}^2/\text{g}$), (2) microporous volume (cm^3/g), (3) the relative contribution of external surface to the acidity of the zeolite [134].

Since the effect of the crystallite size of the zeolites cannot be predicted theoretically, experimental evaluation is necessary for a better understanding of the catalytic reactions and for the formulation of requirements for the design of optimal zeolitic catalysts.

Arribas et al. [136] studied the influence of the crystallite size of a *BEA zeolite on the conversion of n-heptane. They obtained an iso-heptane yield of 90% and 70% respectively on the small (nanometric order) and large crystallites of the zeolite beta. This higher selectivity to iso-heptane selectivity was explained by lessening the path length of the molecules through these crystallites, improving their diffusion and thereby minimizing cracking reactions.

Very good catalytic performances were observed for the isomerization of n-heptane using platinum supported by *BEA nanocrystals [137]. This experimental result can be explained by two factors: the Brønsted acid sites considered to be weaker than those of mordenite, and a faster diffusion of the branched isomers through the small crystallites (10-20 nm) of the *BEA zeolite, leading to a reduction in the cracking rate [138].

During their work on the hydroisomerization of n-hexadecane, Razika et al. [139] have shown that initial activity of Pt/HBEA catalysts increased with increase of crystal size from 0.02 to 10-15 μm . However, this activity was seen to decrease after deactivation of the catalysts to 90% on the large crystals, but was maintained on the small crystals (0.02 μm). The yield into isomers was also seen to be higher on small crystal sizes than on larger ones. This was explained by the probable subsection to several transformations (transformation of mono- to multibranched isomers and the later to cracking products) on the accepted quantity of acidic sites on large crystals, before being hydrogenated on the next Pt site. The few acidic sites on the small crystals before encountering another Pt site reduces the probability to be transformed into multibranched isomers and to cracking [139].

In 2013, Kim et al. [140] studied the effect of the zeolite crystal thickness of Pt/MFI nanosheets on the hydroisomerization of n-heptane. The study showed that the decrease of the crystal thickness from 300 to 2 nm improved the selectivity toward i-C₇ products by a factor of 2.2, assuming that the low selectivity of the bulk zeolite might be due the diffusion limitations of the branched isomers. Moreover, a study was done by Verheyen et al. in 2013 [141] on the MFI nanosheets in comparison with a reference ZSM-g zeolite, in the hydroconversion of n-C₁₀, noting that the selectivity to isomers products was more on the nanosheets of lowest thickness (2 nm).

Recently in 2016, Amir et al. [142] discussed the impact of downsizing of *BEA zeolite crystals on activity and selectivity in the hydroisomerization of n-hexadecane. In order to obtain an “ideal” bifunctional catalyst, it was not only the well balance between the HDF and AF sites,

but rather the decrease of the zeolite crystal to the nanometric scale in order to minimize the residence time of the intermediates within the zeolite crystals [142]. It was observed that the downsizing of the crystal sizes had a positive impact on the activity of the catalyst and selectivity towards isomers products, However, the extreme downsizing as in the case of a nanosponge *BEA zeolite, there was a loss in activity despite that the selectivity towards isomers was maximal. This was attributed to the low acidity of the nanosponge that caused low activity and consequently a low TOF value.

2.2.2 Influence of acidity

Several zeolites were tested in the hydroisomerization of n-hexadecane by Park et al. [143]. The acidic strength as well as the catalytic activities of the 0.5%Pt/catalysts varied in this order: Pt/ZSM-5 > Pt/Beta > Pt/ZSM-22 > Pt/Y > Pt/SAPO-11. For a conversion of n-hexadecane from 37 to 45%, the selectivity to isomerization products decreased in the following order: Pt/Y (75.7%) > Pt/SAPO-11 (67%) > Pt/beta (50.7%) > Pt/ZSM-22 (31.2%) > Pt/ZSM-5 (15.6%). The high selectivity of the Pt/Y catalyst is directly related to the low acidity and the good dispersion of the platinum.

The effect of the acidity of the zeolite on the hydroisomerization of n-hexadecane was also examined by Carati et al. [144], on two forms of Pt exchanged beta zeolite (borosilicate form: BOR-beta and boroaluminosilicate form: Al-BOR-Beta). The Pt/BOR-Beta zeolite shows better selectivity in isomerization products compared to conventional Beta zeolites. The introduction of small quantities of aluminum into the Beta zeolite (Al-BOR-Beta) leads to an increase in the acid sites of the catalyst, which by turn lead to a decrease in the selectivity of isomerization products.

An approach to control the number of acid sites in zeolites is the dealumination of the zeolite by acid extraction and/or heat treatment in the presence of water vapor [144]. In a further work, Apelian et al. [145,146] tested Beta and mordenite zeolites, treated with oxalic acid and exchanged with platinum (0.48 and 0.43%, respectively) in the production of lubricating oil from a commercial wax. The authors note an improvement in the lubricant yield over the treated zeolites compared to the untreated ones. The beta zeolite have reached better isomers yield amongst the tested catalyst. According to the authors, this result may be due to the higher surface area and the lower catalytic activity in Pt/Beta cracking compared to Pt/mordenite [145,146].

The effect of Na exchange of a H*BEA zeolite on the activity and selectivity of the Pt bifunctional catalyst was studied in the hydroisomerization of n-hexadecane by Razika et al. [147]. The exchange by sodium ions of the protonic sites of the parent H*BEA zeolite lead to the decrease of the Brønsted acid sites of the zeolite. The parent Pt/H*BEA seemed to be more selective toward cracking products than isomers products. This was suggested to be due to a rather high protonic acidity (448 $\mu\text{mol/g}$). The proton exchanged zeolite by Na^+ ions was shown to be more selective toward isomers products. The acidity of this zeolite (Pt-Na-H*BEA) decreased to 329 $\mu\text{mol/g}$, but, however, this decrease had a negative impact on the activity were it was shown to decrease during the n-C₁₆ transformation. The selectivity of this catalyst toward the isomers products was very similar to that reached by Pt-HZSM-22 (80%) in n-C₁₆ transformation, but its activity was still 2.5 times higher [147].

2.2.3 Effect of metal concentration (Pt)

In a study done in 1996 by Keogh et al. [148] about the effect of the Pt concentration for activated sulfated zirconia catalysts in the conversion of n-hexadecane, the results showed that the conversion of n-hexadecane increases with the increase of the Pt concentration to a percentage of 0.6% (Figure I.22) where the conversion was optimal. The conversion of n-hexadecane appears to be 76.1% at this Pt concentration, but a decrease is then observed at higher concentrations. This figure shows the evolution of n-hexadecane conversion with the increase of Pt concentration.

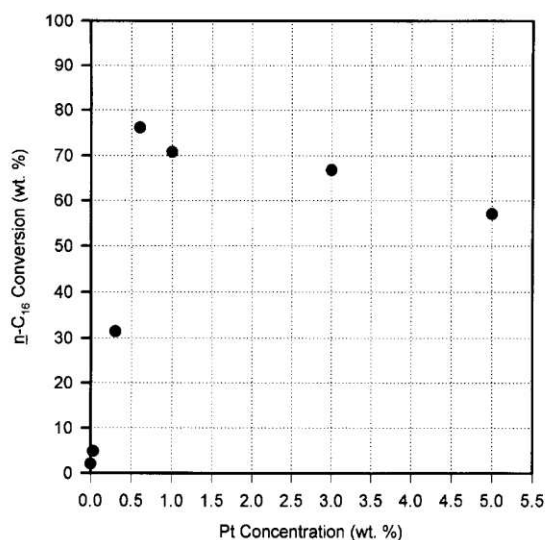


Figure I.22 Effect of Pt concentration on n-hexadecane conversion.

Recently in 2013, Batalha et al. [82] studied the effect of Pt concentration on the activity and selectivity in the hydroisomerization of n-hexadecane. The Pt concentration varied in this order: 0.2, 0.5, 1.0, 1.5% of Pt. The results have shown that starting from 1% of Pt there is no more evolution neither in activity nor in the selectivity towards isomers. The maximum activity per Brønsted acid sites (TOF) and isomers yield were obtained starting from 0.5%, and were found to stay constant with Pt increase (with TOF = 30 h⁻¹ and isomers yield of ca. 50%) [82]. The figure below (Figure I.23) shows the evolution of the isomers yield as Pt concentration increases.

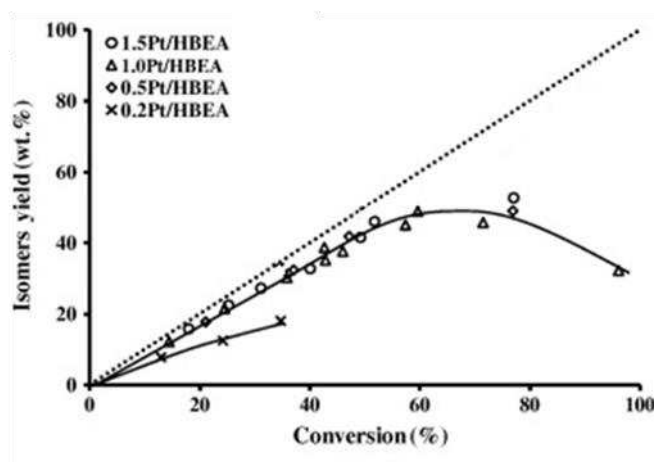


Figure I.23 Isomers yield as a function of conversion over a Pt/H*BEA zeolite with different Pt loadings [82].

2.2.4 Synergetic effect of HDF and AF sites

2.2.4.1 Balance between HDF and AF sites (n_{Pt} / n_{H^+})

The activity, selectivity and stability of bifunctional Pt/zeolite catalysts depend essentially on the balance between the number of accessible metal sites (n_{Pt}) and the number of acid sites (n_{H^+}) represented by the n_{Pt} / n_{H^+} ratio. The relationship between the n_{Pt} / n_{H^+} ratio and the performances of the Pt/HY catalysts was established in the hydroconversion of the n-decane by Alvarez et al. [68]. Figure I.24 shows the evolution of the activity, stability and selectivity of the catalysts with the ratio n_{Pt}/n_{H^+} .

The activity changes with the n_{Pt}/n_{H^+} ratio as provided for by the bifunctional mechanism. Thus, for low values of n_{Pt}/n_{H^+} (< 0.03), the metallic sites are not sufficient enough for the acid sites to be used optimally. The hydrogenating function is the rate limiting steps

then. However, when the metallic function is sufficient ($n_{Pt}/n_{H^+} > 0.03$), the activity reaches its maximum and does not change any more forming a plateau after this value. Therefore, the acidic steps responsible for the transformation of the intermediates are then the rate limiting steps.

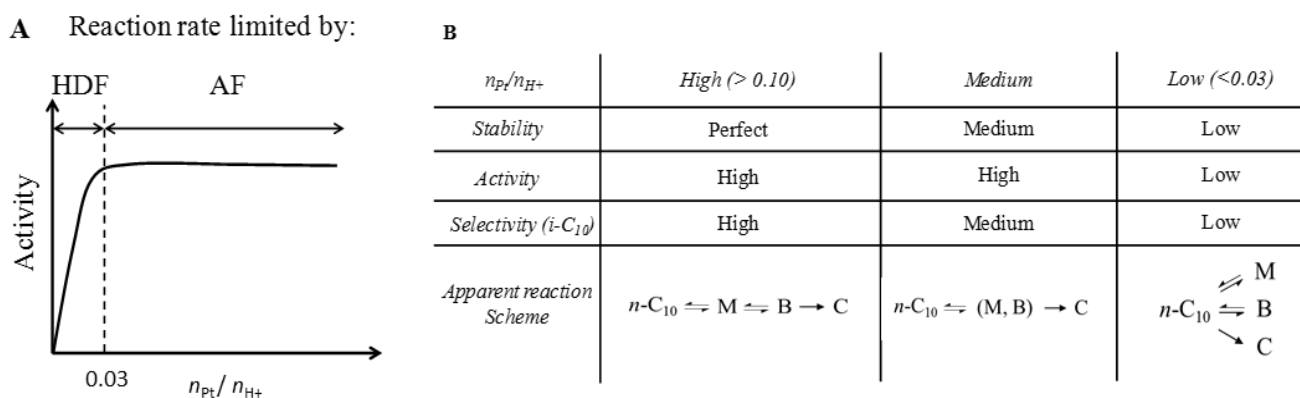


Figure I.24 Impact of the AF and HDF balance on the Pt/HY stability, activity and selectivity to isomers in n-decane hydroisomerization (250 °C, P_{atm} , $H_2/C_{10} = 9$) [68]. Adapted from [49].

The stability of the catalyst is directly linked to the acid sites possessed by the zeolitic support. When the number of acid sites is too large ($n_{Pt}/n_{H^+} < 0.1$), the catalyst deactivates by coke. Indeed, the olefinic intermediates can react successively on several acid sites before reaching a hydrogenating site. These intermediates will therefore not only be isomerized and / or cracked, but additionally will also be condense, forming heavy carbon compounds, which, by limiting the access of the reactive molecules to the acidic sites, will gradually decrease the activity of these sites. As a result, the catalyst activity will be diminished.

The selectivity of the catalyst toward the desired products is also influenced by the balance between the HDF and AF sites. When $n_{Pt}/n_{H^+} < 0.03$, all the products obtained (isomers and cracking products) are apparently primary. They come either from the direct transformation of olefins, or from successive isomerizations and cracking on the acid sites during their transport stage. In the 0.03-0.1 range, cracking becomes a consequence of isomerization. The number of metallic sites becomes too large to give branched olefin intermediates an opportunity to adsorb onto new acid sites and crack. However, for $n_{Pt}/n_{H^+} > 0.1$, each olefinic intermediate undergoes only one transformation during its diffusion between two hydrogenating sites: isomerization in mono-branched products. These isomers are then successively transformed

into multi-branched isomers and cracked products. These catalysts are referred to as "ideal hydroisomerization and hydrocracking catalysts". In this case, an additional parameter was introduced to define an "ideal bifunctional catalyst". This parameter is defined by the number of acidic steps ($n_{a,s}$) involved in the transformation of the olefinic intermediates (rearrangement or cracking) along their diffusion between two Pt sites [82,149].

However, the preceding discussion was meant with the observations on n-decane transformation. In their work, i.e. Batalha et al. [82], similar behavior was observed with a little difference in defining the range of the ratio, in the hydroisomerization of n-hexadecane over three catalysts series. Series 1 catalysts was defined by Pt/H*BEA agglomerates with different Pt loadings (0.2, 0.5, 1.0, 1.5%), series 2 was defined by intimate mixture of Pt/alumina (Pt/A) and H*BEA with different loadings of these two, and series 3 was defined by a physical mixture of Pt/A and H*BEA with different loadings as in series 2 (Figure I.25). In the previous work of Guisnet et al.[19,129,150], they concluded that a n_{Pt}/n_{H^+} ratio of at least 0.03 was required to obtain a maximum catalyst performance in the hydroconversion of n-decane. However, the catalytic results obtained with the Batalha et al. [82], clearly showed that a minimum n_{Pt}/n_{H^+} ratio of 0.02 was enough for the catalysts to attain a maximum activity without any deactivation (Figure I.26), i.e. by the initial increase in the performance until reaching the ratio of 0.02, to attain after a nearly constant variation (plateau). This difference was easily explained by the higher reactivity of n-hexadecane at lower temperature (220 °C in comparison to 250 °C with Guisnet et al.), and the higher hydrogen pressure (30 bars).

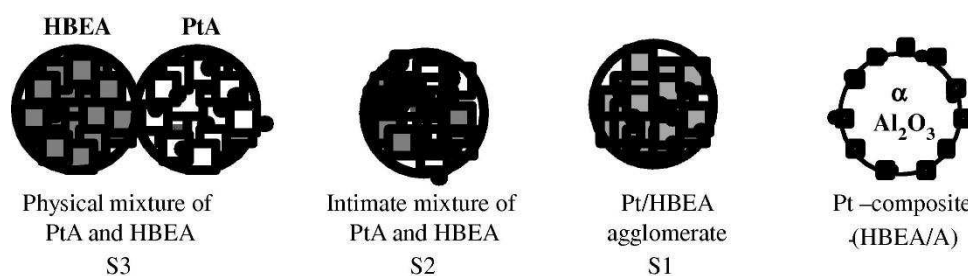


Figure I.25 Different series catalysts. Adapted from [82].

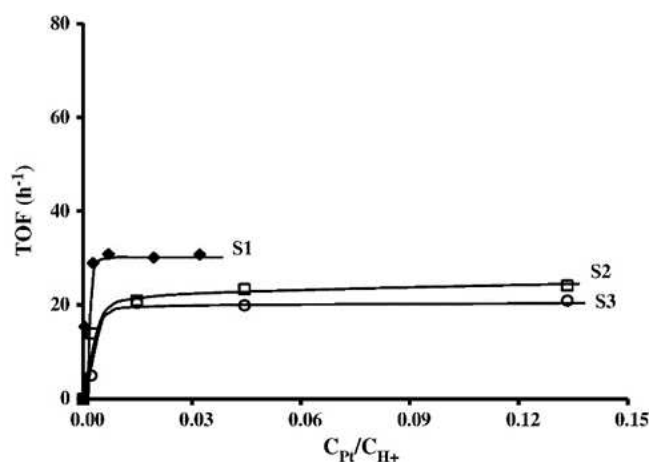


Figure I.26 TOF values of the catalysts series as function of the n_{Pt} / n_{H^+} ratio. Adapted from [82].

Besides the activity, the selectivity toward the isomers products was increasing with the increase in the ratio between HDF and AF sites. The result in series 1 follows this manner to certain Pt loading (0.5%) and then maintains constant the products yield into isomers, as shown in Figure I.23. In series 2 the trend was more clear with the increase of the HDF to AF ratio. Series 3 catalysts maintained low selectivity anyway [82].

The effect of n_{Pt}/n_{H^+} was also seen to influence the additional parameter mentioned before that defines the “ideal bifunctional catalyst” ($n_{a,s}$). In the same work accompanied by Batalha et al. [82], the increase in the ratio had a positive influence in the number of acidic steps involved in the transformation of the intermediates, where the latter was seen to decrease despite the lower impact in case of series 2 and 3, but the impact was clearly more observed on series 1 catalysts.

2.2.4.2 The intimacy criterion

It is in too much importance to determine the proximity between the HDF and AF sites. From a logic point of view, as much as the distance between the two functions sites increases, as much as the probability of the olefin intermediates is more susceptible to rearrangements and cracking procedures. The far proximity thus induces lower selectivity to isomers products.

This issue was also studied in the same work discussed before [82]. The proximity between HDF and AF functions increased in the following order: PtA + H*BEA (S3) < PtA + H*BEA (S2) < Pt/H*BEA (S1). Nonetheless, the selectivity towards isomers was also seen to

increase in the same manner. This indicates that as much as the proximity between the active sites is closer, as much as the intermediates are less susceptible to cracking procedures. However, this suggestion was contradicted two years after, very recently in 2015, by Martens et al. [69]. In their work, the utilization of a large pore zeolite Y mixed with an alumina binder was chosen to investigate the effect of nanoscale intimacy between the two active sites (HDF and AF). It was found that when the Pt particles were in the closest position to the acidic sites (impregnated on the zeolite Y) (Figure I.27-a), the feed components were obliged to diffuse into the micropores where the Pt particles are located, leading to longer residence time within, which increases the probability of these intermediates to be cracked. In the contrary, when the metal particles were located on the alumina binder but not on the zeolite (Figure I.27-b), the olefin intermediates formed were easily diffusing through the wide pores of the binder to the zeolite Y, where isomerization process is more dominant than cracking. Therefore, the optimal location for the metal function should not be in the micropores of the zeolites to establish the most convenient proximity, but rather on the surface of the crystals or inside the mesopores of the zeolite [133,151].

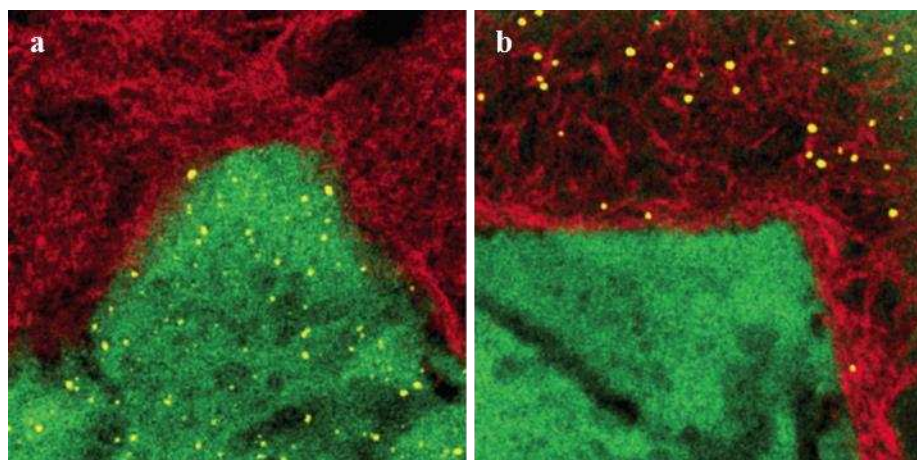


Figure I.27 Controlled deposition of platinum (Pt) on the zeolite Y (fig. a) and the alumina component (fig. b) of Y/A extrudates. Pt particles are colored in yellow, zeolite Y in green, and alumina component in red. Adapted from [69].

2.2.5 Effect of chain length

The tendency for cracking of the branched n-paraffin increases with the hydrocarbon chain length as well as the degree of branching. The cracking of n-paraffin requires more carbon atoms (at least 7 C atoms) than isomerization requires (at least 4 C atoms). Thus, pentanes and

hexanes can be readily isomerized than cracked. For paraffin having a number of carbon atoms greater than 6, there is competitiveness between cracking and isomerization [152]. Figure I.28 summarizes the results obtained by Weitkamp on the isomerization and cracking of paraffin from n-C₆ to n-C₁₀ over a bifunctional Pt/CaY catalyst [128]. The figure confirms also that there is competition between isomerization and cracking showing that isomerization takes place at lower temperatures. This confirmation is in agreement with the work done by Sie et al. [152].

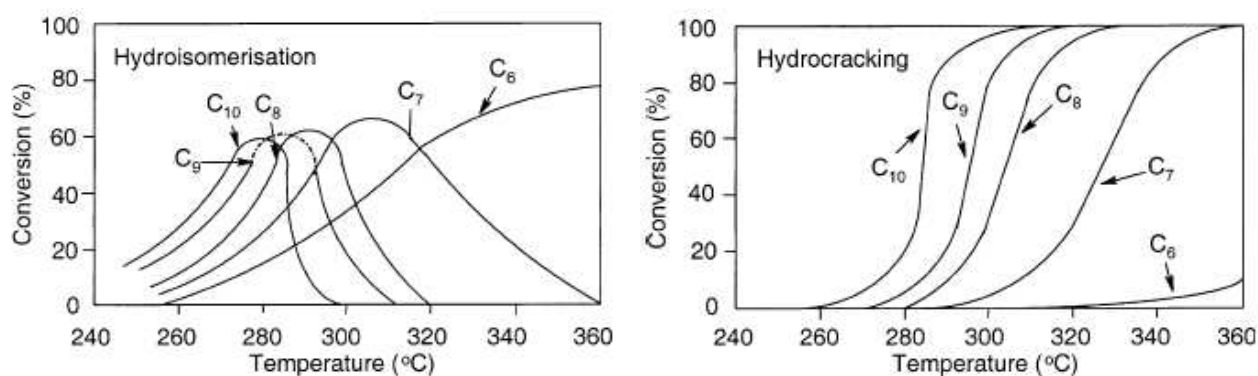


Figure I.28 Comparison between hydroisomerization and hydrocracking of n-C₆ – n-C₁₀ paraffin over Pt/CaY catalyst [128].

The effect of carbon chain length on the hydroisomerization reactions was also addressed by Calemma et al. [61,153]. The hydroconversion of n-C₁₆, n-C₂₈, n-C₃₆ and n-C₄₄ was tested by an amorphous silica alumina exchanged with 0.3% platinum. The selectivity towards isomers showed a decrease as a function of chain length and with increasing conversion levels. In 2008, Soualah et al. [78] reported a similar behavior upon the hydroisomerization of n-C₁₀, n-C₁₄ and n-C₁₆ over three bifunctional catalysts (Pt/H*BEA, Pt/HMCM-22, and Pt/HZSM-5) exchanged with 1% of Pt. The results confirmed the previous suggestions that the isomers yield is decreasing with the increase in carbon chain length. In addition, the activity was also seen to decrease with chain length. However, Martens et al. [69], showed recently the same drawback of activity and isomers production as chain length increased from n-C₁₀ to n-C₁₉ and i-C₁₉, but, however, the catalysts were seen to be more active on the iso-paraffin.

2.3 Limitations in Hydroisomerization

In the hydroconversion of hydrocarbons, certain drawbacks are observed due to diffusional restrictions associated with non-convenient pore size [19,82,149,154,155]. For

example, the loss in isomers selectivity in the hydroisomerization of n-alkanes may not be favored over catalysts possessing low textural properties. It is easy to imagine that the loss of selectivity in this case is closely linked to the residence time of the reaction intermediates within the porous network [156]. The long time contact within the pores of the zeolite, i.e. long time contact with the acidic sites, may subject the intermediates to several acidic steps like rearrangements and further cracking. Decreasing the residence time makes it possible to overcome these limitations and may have a significant effect on the catalytic performance.

Two main strategies have and still being used to overcome these limitations, even to reduce the zeolite crystal size to the nanometer scale, or to introduce secondary pores with diameters larger than 2 nm (meso- or macropores), to give respectively nanosized and hierarchical zeolites [157]. These improved zeolites structures enhance the diffusion of bulky molecules into and out of the pores. This shortens the distance to the active sites and reduces the residence time with them and facilitates adsorptive and catalytic reactions [157].

The use of nanozeolites with crystal sizes < 100 nm can overcome diffusional limitations [157]. They possess properties that result in longer lifetimes, higher activities and better performances. The large surface areas they have, the more accessible active sites and shorter diffusion path lengths, as well as the well-controlled surface properties, are, in addition to more others, factors behind the improved overall catalytic performance [158–160].

In the other hand, the hierarchical zeolites can be generated by the introduction of a further porosity range via post-synthesis modifications of the zeolite crystallites. These post-synthesis modifications are classified as “top-down” or “destructive” [161] approaches, they consist of a selective extraction of the metallic atoms (Si or Al) from the network. The simplicity of the implementation of demetallation techniques, their limited cost and their low environmental impact, made it possible to industrialize these processes.

Targeting the porous network of the zeolite and, thus, improving its textural properties, have a significant influence on the residence time of the reaction intermediates within the pores. As has been discussed in literature, post-synthesis methods to obtain hierarchical zeolites, e.g. “desilication”, have shown a positive impact on the activity of the catalysts and their selectivity towards the desired products, i.e. their catalytic performance [56,162–165].

3 Hierarchical zeolites

The hierarchical zeolites combine the catalytic power of the micropores with the facilitated access and improved transport consequence of a complementary mesopore network [166–168]. This makes the use of the zeolite based catalysts more effective. They are considered alternative zeolites to overcome the drawbacks observed in several catalytic transformations. In fact, such materials have high external surfaces [169,170], which means the ability of more active sites to perform the reaction, enhancing therefore the activity of the reaction. Moreover, the large pores equipped within these zeolites reduces the residence time of the reaction intermediates within the framework structure, lessening by that the undesired secondary reactions as cracking.

Hierarchical zeolites are divided into three different material types as shown in Figure I.29: hierarchical zeolite crystals, zeolites with nanosized crystals and supported zeolites crystals. The pore size distribution associated to each type (in the same figure), confirms always the presence of micropores with the additional meso- or macropores depending on the type. However, the synthesis of these hierarchical zeolites is carried out through different techniques to be discussed.

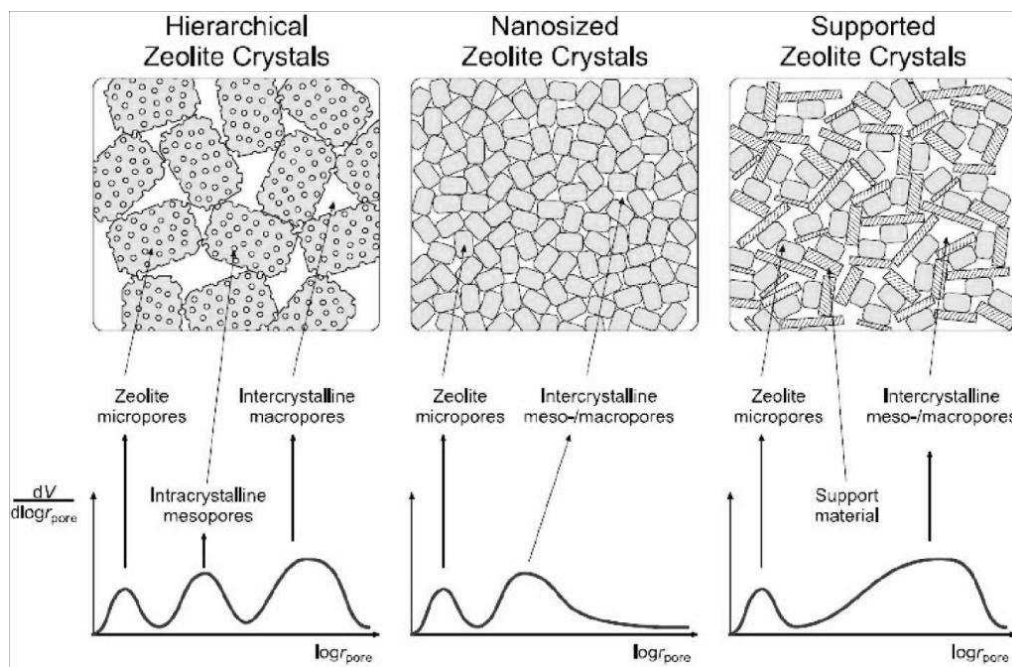


Figure I.29 Hierarchical zeolite materials classification with their typical pore distribution [166].

3.1 Synthesis of hierarchical zeolites

Different strategies can be used to prepare hierarchical zeolite materials with combined micro- and mesoporous networks [167,171–173]. The preparation could be done even through structure breaking or so-called “destructive” modification pathways and approaches, or through structure building or so-called “constructive” pathways [161]. Structure breaking is concerned by the modification of the microporous structure through mesopores inducement by post-synthesis treatments. The second pathway covers direct or two-step synthesis routes that use multiple templates or small zeolite-based building blocks such as seeds or nanocrystals, which give rise to mesopores associated with the micropores of the zeolite [161]. Figure I.30 below summarizes the various synthesis approaches.

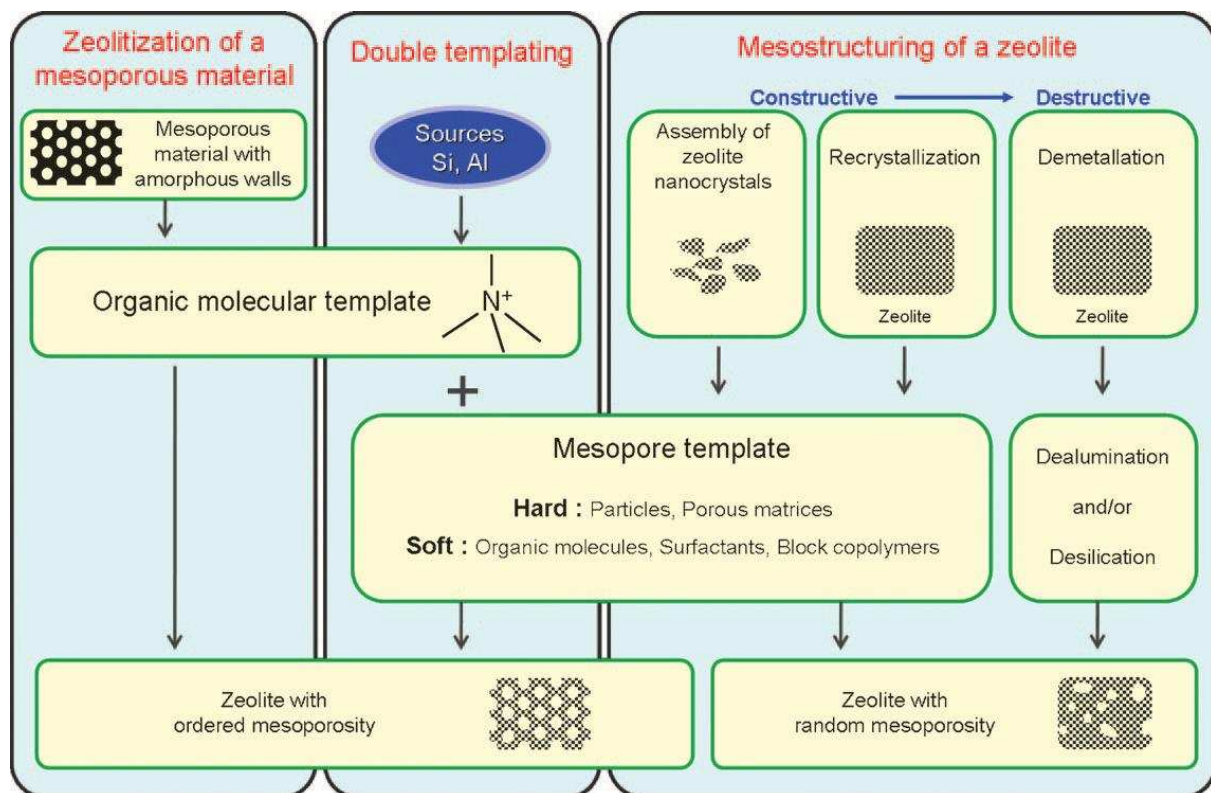


Figure I.30 Brief overview on the various synthesis routes towards hierarchical zeolite materials. Adapted from [161].

3.1.1 Destructive versus constructive pathways

Applied zeolites in industry that combine the micro- and mesoporous network are principally synthesized by post-treatment modifications. Certain pathways as dealumination and desilication, have been proposed for mesopore introduction [161]. Much promise is held

by these processes, thanks to its low cost requirements, simplicity, and reported important results concerning final material characteristics, in addition to no major HSE concerns (Health/Safety/Environment issues).

In the other hand, enormous progress over the last years has been followed in the synthesis and characterization of the hierarchical zeolites that comprise structured mesoporosity obtained through constructive methods. However, the high amounts of the organic materials used in such synthesis approaches, and consequently their high cost, is a real problem as it marks a major drawback on a large industrial scale. The high operating conditions associated with presence of large quantities of organic molecules used, are considered highly inconvenient and may be behind the release of effluent gases that may cause environmental problems. In addition to detrimental effect on the final framework structure caused by high applied temperatures. These concerns get in the way of the eventual industrializing of the constructive synthesis methods, and, consequently, their effective application in industry is somehow limited [161]. Table I.3 summarizes the advantages and disadvantages associated to the destructive and constructive approaches towards hierarchical zeolites synthesis.

Table I.3 Summary of the advantages and disadvantages of the destructive and constructive approaches towards the synthesis of hierarchical zeolites [161].

	Formation route	Production cost	HSE issues	Hydrothermal stability	Flexibility in Si/Al
Destructive	Dealumination	Low	No	High	Medium
	Desilication	Low	No	High	Little
Constructive	Zeolitization of mesoporous material	High	Yes	Low	Medium
	Soft templating	Medium/High	Yes	Medium/High	Yes
	Hard templating	High	Yes	High	Yes
	Mesostructuring of zeolites	High	Yes	Medium/High	Yes

As said previously, the low production cost, with the negligible HSE concerns, in addition to the higher hydrothermal stability associated with the destructive routes towards hierarchization of zeolites, makes them more advantageous over constructive methods.

3.2 Destructive pathways

The introduction of mesopores into the zeolite crystals by destructive post-synthetic treatments can be achieved through selective extraction of atoms from the zeolitic framework. As zeolites are considered aluminosilicates, the most two studied destructive techniques are dealumination and desilication processes. Herein will be a brief look on the different destructive dealumination pathway, with more attention given to techniques performed by means of desilication by alkaline treatments in the next section.

Dealumination: One of the post-synthetic treatments is dealumination of the zeolite framework. It consists in extracting the aluminum from the zeolite framework by hydrolysis of the Al-O-Si bonds through calcination [174–176], steaming [161], acid leaching [177,178], or other chemical treatments [161]. Originally, the dealumination treatments were done to control the concentration and the strength of the acid sites by increasing the Si/Al ratio of low-silica zeolites [161]. The defects created in the structure of the zeolite during the removal of aluminum atoms are then at the origin of a partial collapse of the framework, thus generating mesopores (Figure I.31). During some thermal treatments, and depending more on the thermal conditions and zeolite type, the mobility of aluminum species increases, where part of them is removed from the framework to form extra-framework aluminum (EFAL). A mild acidic treatment is necessary after to dissolve the EFAL species to establish finally the micro- and mesoporous network without further extraction of more framework aluminum atoms. Dealumination treatments require perfect control of the operating conditions (concentration, pH, temperature) in order to generate mesopores without the collapse of the zeolitic structure.

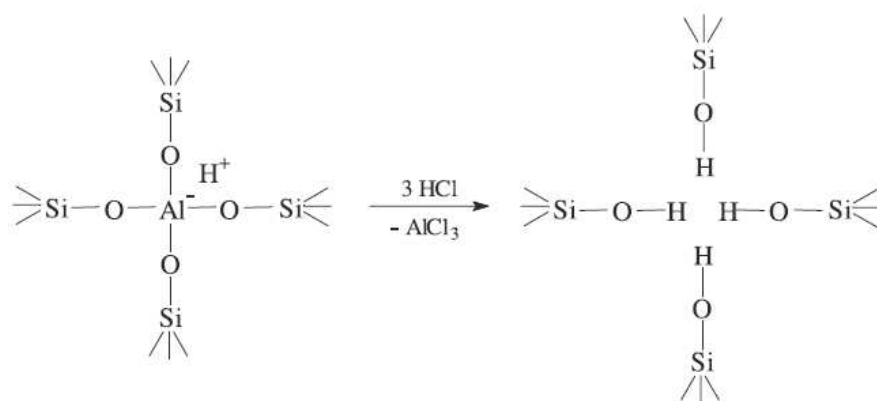


Figure I.31 Dealumination of zeolites. Adapted from [19].

However, besides the positive effects and the simplicity of this treatment, negative aspects are also observed. For example, partial amorphisation of the zeolitic framework which leads to a decrease in the relative crystallinity and lowering the amount of active sites as well as their blockage by amorphous debris [179]. Moreover, the introduction of mesopores is not fully controllable and are obtained in a random or/and non-optimized way [180,181]. Furthermore, for dealumination to be effective and induce sufficient amount of vacancies that form the mesopores, a minimum amount of Al species is required [182].

3.3 Desilication

Another well-known demetallation approach for generating mesopores is through the selective extraction of silicon from the zeolite framework by treatment with an aqueous alkaline solution [183–185]. This method was first reported in 1992, when it was shown that treating a conventional zeolite crystals with an alkaline solution resulted in a selective extraction of Si from the framework [183]. It has been known since long time that this technique yields lower Si/Al ratios with small changes in framework acidity [186–189]. The desilication method can be used effectively for the introduction of mesopores when the Si/Al ratio of the parent material is in a certain range. An optimal Si/Al range of 25-50 has been found to lead to a well-controlled formation of mesopores in ZSM-5 zeolites [167,190–192]. As suggested by Cizmek et al. [189], the charge on lattice Al prevents the extraction of the Si neighbors from the zeolite framework. Therefore, for high concentrations of Al, i.e. low Si/Al ratios, the extraction of Si is too much limited. However, when the Si/Al ratio of the parent zeolite is high (> 50), no selective extraction takes place due to excessive Si removal, consequently, no selective mesopore

formation (large meso- and macropores) as shown in Figure I.32. However, it has been known that this range is apparently applicable for other zeolites studied than ZSM-5 [161,190].

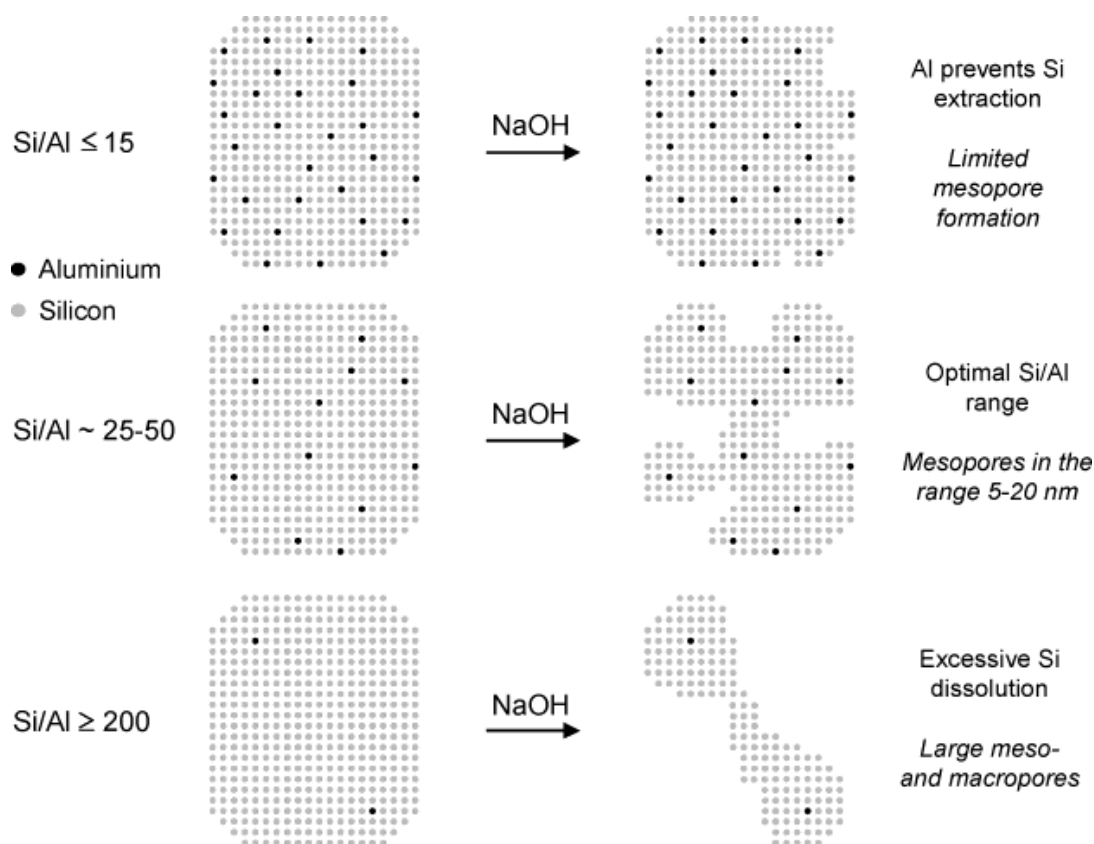


Figure I.32 Schematic representation of how Si/Al ratio dictates the formation of mesopores in ZSM-5 desilicated by NaOH [190].

The classical desilication treatments are performed in the presence of strong inorganic bases (e.g. NaOH, Na₂CO₃, NaAlO₂, KOH, LiOH, etc.) [157,161]. The developed porosity seems to be obtained by preferential extraction of Si atoms from the framework due to hydrolysis in the presence of HO⁻ anions (Figure I.33), where the Si atom becomes five-bonded after HO⁻ attack, and then by a second mechanistic step, by the action of H₂O molecules, the silicon is extracted from the framework in the form of Si(OH)₄ normally [193]. The vacancy left by this extraction is attributed to the porosity developed hereafter. However, the pore directing role of framework aluminum is sometimes behind the extraction of dissimilar silicon containing species of different size in the various zeolites. Fragment X stands even for the hydroxyl group in case of monomeric species or for a siloxane chain for polymeric entities (Figure I.33).

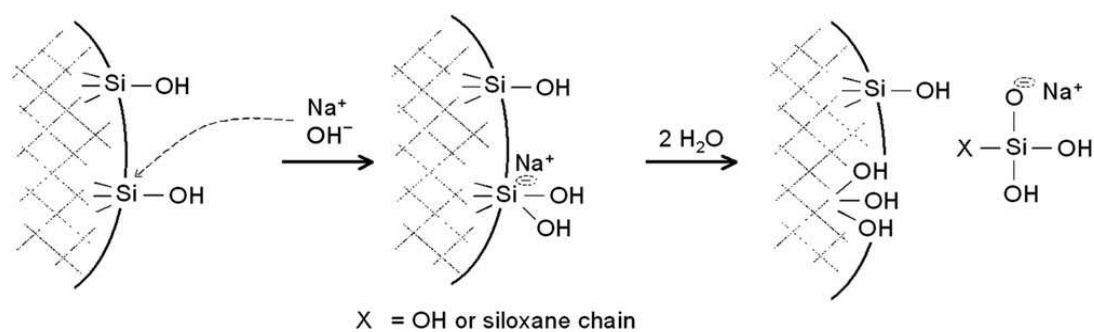


Figure I.33 Hydrolysis of framework Si in alkaline medium. Adapted from [157].

Besides the desilication by inorganic bases, hierarchical zeolites combining the micro- and mesoporous network were prepared by desilication of the parent zeolite in aqueous solution of organic based compounds such as tetrapropyl- and tetrabutylammonium based organic compounds. However, these organic compounds are less reactive and less selective towards the dissolution of silicon than inorganic solutions [161]. To be more effective, these treatments require more elevated temperatures and/or longer desilication durations for the formation of important mesoporosity which allows high control of the dissolution process. Moreover, the direct use of only organic hydroxides produced directly the protonic form of the final mesoporous product after calcination, without any need for ion-exchange with NH_4NO_3 species. This is only in case there is no incorporation with the inorganic species, e.g. NaOH , where ion-exchange is necessary to eliminate the Na^+ cations from the zeolite framework. It was shown that tetraalkylammonium based organic compounds when dissolved, produce the tetraalkylammonium cations (TMA^+ , TEA^+ , TPA^+ or TBA^+) that are usually used as structure-directing agents during the synthesis of zeolites. They are well known to largely protect the zeolite crystal by interacting preferentially with the surface to stabilize the structure and hinder the attack of HO^- anions by steric effect [194]. Therefore, these organic structural agents (pore directing agents) are considered promising variant to the classical treatments, as they preserve way better the intrinsic properties of the zeolite, for example microporosity and crystallinity [195–197], in addition to better conservation of the mass yield after desilication [157]. Figure I.34 shows the difference between desilication in presence of inorganic species (e.g. NaOH) and in presence of organic ones (e.g. tetraalkylammonium hydroxides). The figure illustrates how the tetraalkylammonium cations adhere to the surface of the zeolite and protects it against HO^- attack, leading to a lower extent in material loss, preserving way better the properties of the zeolite. It is also seen in the figure that the Si/Al ratio decreased more in

presence of inorganic species (from 42 in starting material to 26 in desilicated one), while the effect was less in the one desilicated in presence of organic species (from 42 to 36).

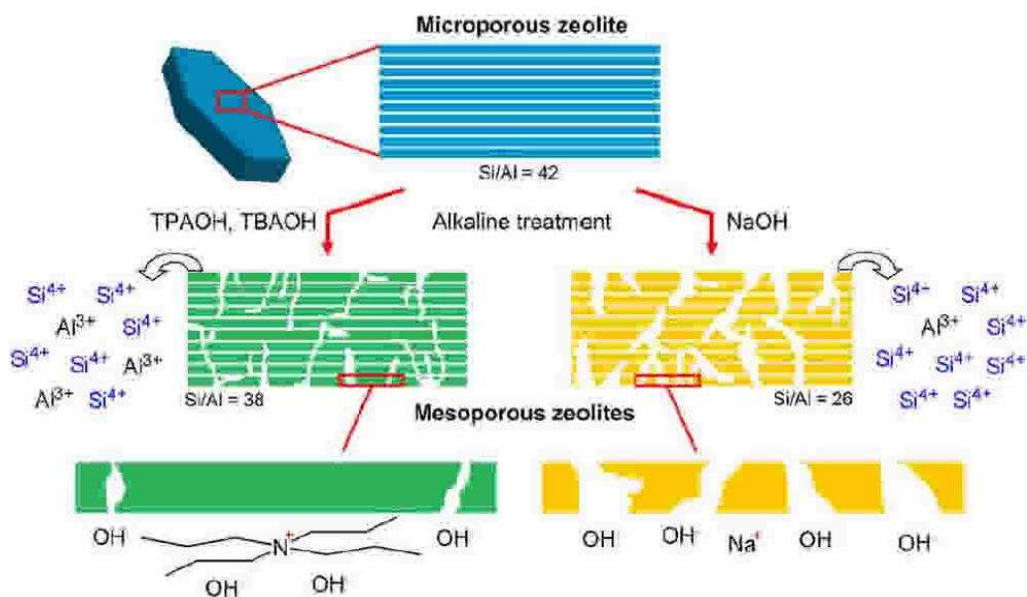


Figure I.34 Comparison of desilication of zeolite in presence of organic (TPAOH, TBAOH) and inorganic (NaOH) species. Adapted from [191].

This post-modification method was firstly applied to the average pore MFI zeolite (ZSM-5) [198,199], but later on was extended on wide range of zeolites: MOR [200–202], MTW [203,204], ITQ4 [205,206], BEA [207–210], TON [170,211], and small pore zeolites (e.g. CHA) [212], etc. The diffusion path of these obtained hierarchical pore zeolites, was constituted of microporosity interconnected by a mesoporous network [213]. However, among the reported zeolites subjected to such alkaline treatments, beta zeolites were more susceptible to Si extraction, i.e. mesoporosity development, since the Al species in beta zeolites are not stable as in MFI, FER, and MOR zeolites [207,214], and therefore cannot moderate Si extraction. In all cases, it is generally accepted that the Al atoms in the AlO_4^- negatively charged tetrahedra, protect the Si atoms against HO^- attack [162]. In beta zeolites, the surface is poorer in Al atoms than the bulk, which makes this type of zeolite more prone to Si extraction from the surface [162]. Unlike ZSM-5, the surface zone is highly enriched with the AlO_4^- tetrahedral, which makes it more resistant to desilication in basic solutions [215].

3.4 Impacts of desilication on the zeolite properties

The main issue behind the proposal of such treatments as said before is the introduction of mesopores as auxiliary network to the already existing micropores. Nevertheless, these treatments had shown to influence the properties of the modified parent zeolite, where the elemental, textural, acidic, and the catalytic properties are highly affected post to these treatments. An overview on these effects will be further discussed.

3.4.1 Impact on zeolitic structure

The X-ray diffraction patterns always show the preservation of the zeolite structure characteristics of the parent material after post-modification via desilication. But, however, in the majority of the cases, a decrease in crystallinity is observed. To compare the crystallinity before and after desilication, relative crystallinities were calculated by estimation from the diffraction peaks intensities, considering the crystallinity of the parent material to be 100% crystalline [216].

In a study done by Tarach et al. [162], the structural characteristics of the *BEA zeolite was seen not to show any change, thus indicating the preservation of the parent's structure after desilication (Figure I.35). However,, it was seen that in presence of the inorganic species (NaOH), the relative crystallinity decreased to 66%, indicating that NaOH leads to partial amorphization of the zeolite. Nevertheless, the crystallinity was recovered again in a solution containing organic compounds (TBAOH) to 100%. The role of these organic species, as said before, is to protect the surface of the crystal and prevent material loss and debris formation. In another study by Abello et al. [191], no change in the peaks position in the XRD patterns was observed in ZSM-5 zeolite before and after desilication, which indicates the preservation of the parent's zeolitic structure characteristics. Figure I.36 below shows also that the desilication with NaOH alone (AT curve), causes more loss in crystallinity than when desilicated in presence of TPAOH (OT-3 and OT-4 curves), in comparison to the parent zeolite's curve (P curve). This was revealed by the decrease more or less in the intensities of the peaks relative to the parent's ones.

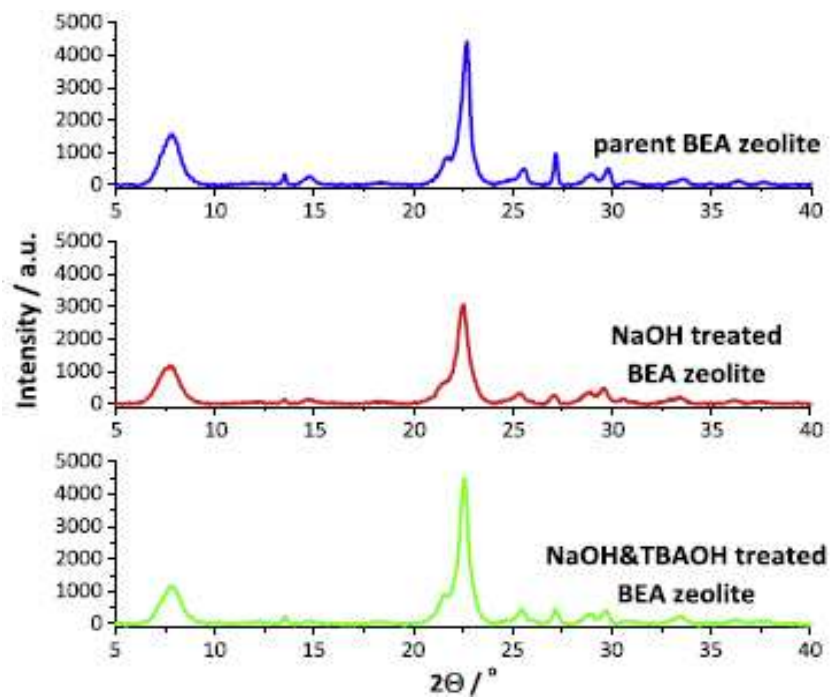


Figure I.35 X-ray diffraction patterns of parent and desilicated *BEA zeolite. Adapted from [162].

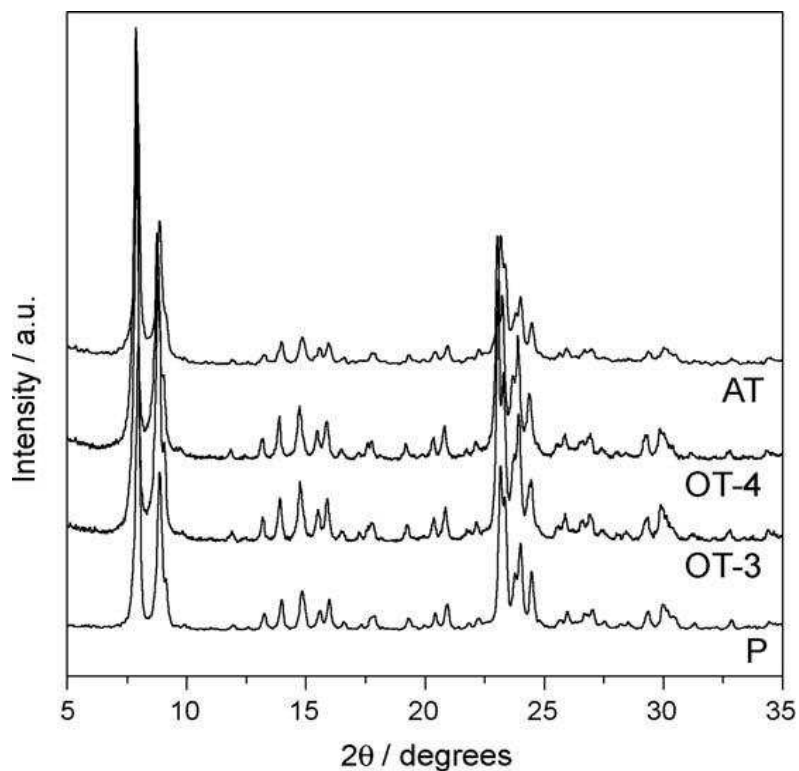


Figure I.36 X-ray diffraction patterns of parent and desilicated ZSM-5 zeolite. With treatments: AT (0.2NaOH), OT-4 (1M TPAOH, 300 min) and OT-3 (1M TPAOH, 480 min).

Adapted from [191].

3.4.2 Impact on chemical composition

It is known that during the process of creating mesopores by means of desilication, it's the Si atoms being extracted predominately. However, it is both Si and Al atoms are removed from the framework, where the Al atoms re-aluminate again on the external surface of the zeolite [193]. The removal of Al atoms is, however, not that much considered at low concentrations of the alkaline solution.

Sadowska et al. [215] studied the effect of NaOH concentration on the chemical composition, and its consequences on the Si/Al ratio upon the desilication of ZSM-5 zeolite. The ratio was shown to decrease more and more as the NaOH concentration increased. However, it was shown also that the percentage of extracted Al was negligible (0.5, 2 %) at low NaOH concentrations (0.1, 0.2 M), but it was more pronounced (elevated to 18, 62 %) when the concentration was more than the double (0.5, 1.0 M). In the other hand, upon the desilication of the same zeolite in presence of protective organic species (TBAOH), the Si/Al ratio was seen to decrease but in a lower extent in comparison with desilication by NaOH alone. Moreover, the percentage of extracted Al was also lower in this case [215].

The studies reported by Tarach et al. [162] and Abello et al. [191], reveal also the same aspect. The studied showed that the Si/Al ratios decreased after desilication by NaOH alone, but the decrease was reduce upon incorporation of the organic species. This reduced influence reflects the protective effect of the organic species on the chemical composition of the zeolite.

3.4.3 Impact on textural properties

The main objective of the constructive and destructive pathways is to reduce the diffusional pathways of the molecules within the pores of the zeolites. This is achieved by targeting its textural properties even by introducing mesopores as auxiliary porosity to the micropores, or by decreasing the crystal sizes to the nanometric scale (< 100 nm). Upon the route covered by desilication destructive pathways, it was not only the mesopores being influenced, the micropores, external and BET surfaces were also affected, in addition to the size and shape of the zeolite crystal in some cases.

Figure I.37-A below shows the nitrogen sorption isotherms of three desilicated zeolites: ZSM-5, beta and USY, where P stands for parent and M for modified zeolite after alkaline treatment. The adsorption curves show always that the adsorbed volume is increased at high relative pressure, a significance for creation of mesopores. As well known, when there is no

elevation of the curve at high relative pressure, i.e. where there is a plateau conservation, it means the material is considered to be microporous exhibiting type I isotherm [217]. This is clearly seen in USY (P) zeolite in the figure below. However, after desilication, this material seems to have an elevation in the curve at high relative pressure. The type of isotherm it exhibits now is type II isotherms [164], which correspond to mesoporous industrial adsorbents [217]. This aspect is also seen in ZSM-5 zeolite where it was purely microporous before the treatment, and became micro- and mesoporous zeolite after desilication. However, the beta zeolite in this case was already possessing mesopores, but the more attracting is that the already existing mesopores seem to adsorb more nitrogen volume after desilication, a sign of increase in the mesoporous volume. Moreover, part B of the figure shows the pore size distribution in the parent and modified zeolites. It is shown that the three zeolites exhibit mesopores after desilication with different diameter distributions which are all > 2 nm (typical of mesoporous solids [217]). Beta (M) zeolite possessed also a bimodal distribution of pores, reflected by the centering of the peaks at 7.5 and 25 nm.

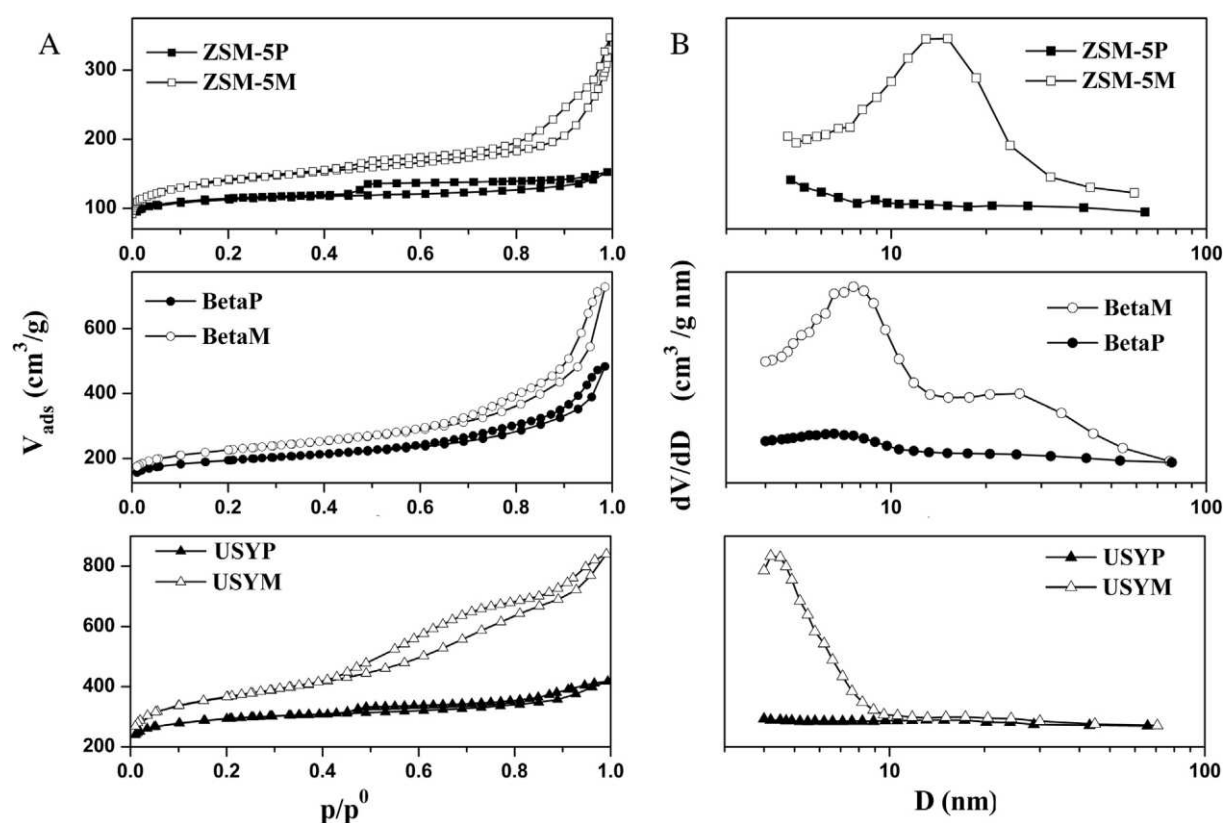


Figure I.37 Nitrogen adsorption isotherms (A) and pore size distribution (B) of parent and modified zeolites. Adapted from [164].

To investigate deeply the impact of desilication on the textural properties, it is important to discuss quantitatively the textural parameters before and after desilication. It was seen in this study, that the mesoporous surface, BET surface and total pore volume have increased after the alkaline treatments, knowing that the BET equation cannot be held on microporous solids and to a lesser extent on mesoporous materials according to several hypotheses [218]. The more important is to preserve the micropore volume unchanged. This was seen in ZSM-5 zeolite, but in a less extent in USY (from 0.359 to 0.289 cm³/g) and beta zeolites (from 0.199 to 0.190 cm³/g) [164].

In another study by Tarach et al. [162], it was seen the usage of NaOH alone caused more drop in micropore volume (from 0.18 to 0.10 cm³/g) than in presence of NaOH and TBAOH (from 0.18 to 0.14 cm³/g) during the treatment of a beta zeolite. This indicates the protective effect of these organic molecules. Moreover, Figure I.38 shows the morphology of the crystals before (a and a') and after desilication by NaOH alone (b and b') and NaOH+TBAOH (c and c'). It is well observed that the samples treated with NaOH&TBAOH show a more uniform mesopore network spreading through the whole zeolite particle, while the treatment with NaOH alone results in -as said- core-shell particle [162], in which the mesopores are located at the crystallite's external surface, while the inner part remains almost unmodified.

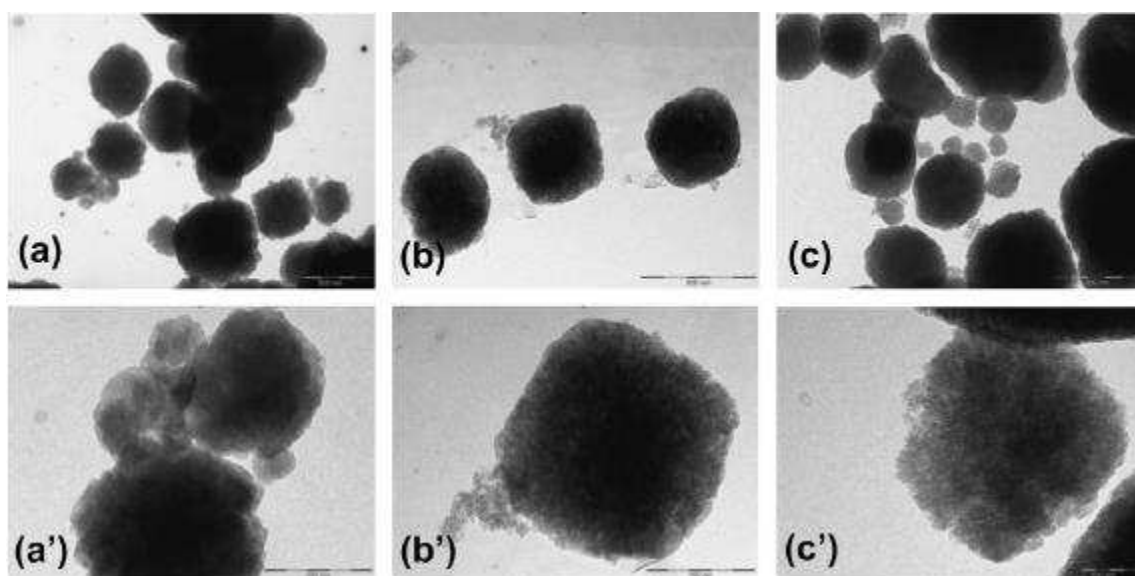


Figure I.38 TEM images of the parent Beta zeolite (a at 500 nm and a' at 200 nm) and Beta zeolite treated with 0.2 M NaOH (b at 500 nm and b' at 200 nm) and 0.2 M NaOH&TBAOH mixture (c at 500 nm and c' at 200 nm). Adapted from [162].

In the study performed by Sadowska et al. [215], it shows that the crystallites of ZSM-5 zeolite show the formation of the mesopores after desilication, as illustrated by the TEM images in Figure I.39.

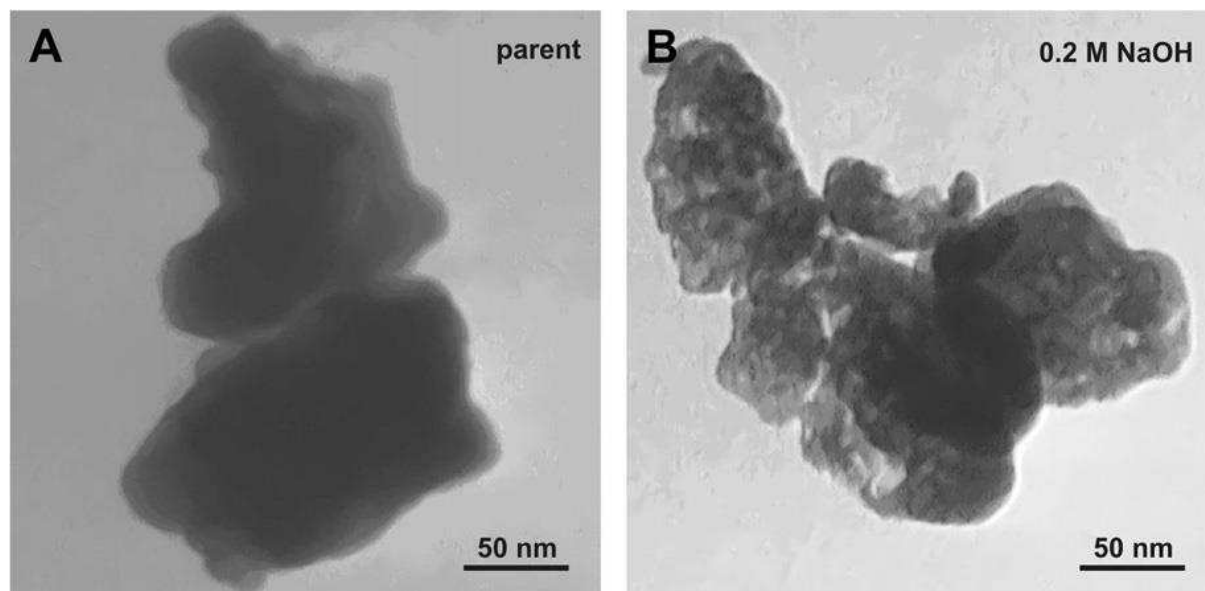


Figure I.39 TEM images of ZSM-5 zeolite before (A) and after (B) desilication. Adapted from [215].

3.4.4 Impact on acidity

Four bands are usually observed in the IR region that correspond to the vibration of OH groups with different configurations (e.g. ZSM-5). The band at 3740 cm^{-1} corresponds to the Si-OH groups on the crystallites external surface (Figure I.40), or on the mesoporous surface if mesopores were already existing. The increase in such a band is attributed to the formation of mesopores and increase in its volume and surface [162]. However, at high base concentrations, this band may decrease, pointing to a destruction of the pore system of the zeolite due to the severe base concentration [215]. The highly acidic groups that are presented by the Si-OH-Al groups, peaked at 3610 cm^{-1} , may increase upon desilication due to the selective extraction of Si, which is concurrent with the decrease in the Si/Al ratio. It is important to note that high basic concentrations may induce Al extraction also, causing a decrease in the corresponding acidity (Figure I.40). The hydroxyl nests (Figure I.41), possessed in microporous solids, that appear at $3400\text{-}3500\text{ cm}^{-1}$ region, are referred to Si-OH defects bonded by hydrogen that is bonded to the framework oxygen [215]. Gil et al. [203] and Holm et al. [219] reported the disappearance of these groups upon desilication. Therefore, it may be concluded that these

defect sites are the places the most incurred to the attack of the base, due to the probable least stable Si atoms that are bonded via oxygens (low Si atoms stability due to absence of Al in neighborhood), to other three Si atoms and to the OH in defects, being removed easily by NaOH treatment.

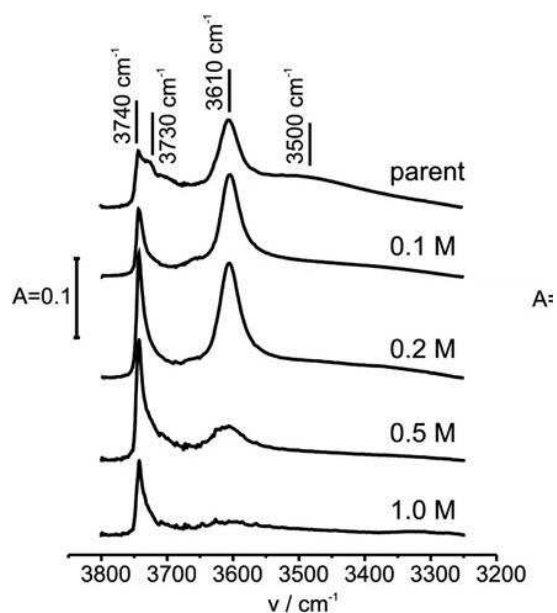


Figure I.40 IR spectra of OH groups of parent ZSM-5 zeolite and its desilicated forms with different base concentrations. Adapted from [215].

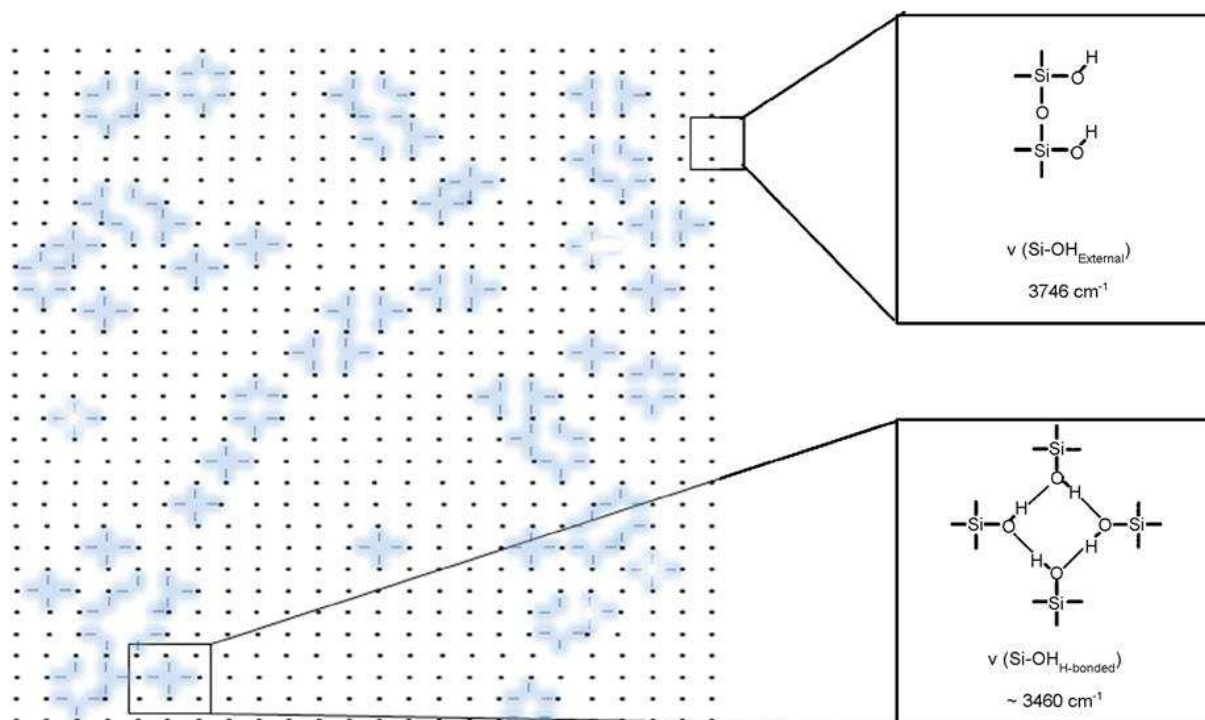


Figure I.41 Silanol (3746 cm^{-1}) and hydroxyl nests (3460 cm^{-1}) in ZSM-5 zeolite. Adapted from [219].

Furthermore, it is possible to determine qualitatively and quantitatively the Brønsted and Lewis acid sites from IR spectra after pyridine adsorption at different temperatures. Bands at 1545 and 1637 cm^{-1} correspond to Brønsted acidity (PyH) and bands at 1455 and 1622 cm^{-1} correspond to Lewis (PyL) sites, in addition to the band at 1490 cm^{-1} attributed to pyridine adsorbed on both Brønsted and Lewis sites [220,221]. Studies showed that desilication tend to decrease both acidities [163,222]. This was seen to be reflected by the decrease in the peaks' intensities at 1545 and 1455 cm^{-1} (corresponding to most common Brønsted and Lewis acidities respectively) as in Figure I.42. It was suggested that desilication causes the removal of strong acid sites through dissolution of the zeolite framework and the disappearance of aluminum in the tetrahedral coordination position [222]. However, an increase in the Brønsted acid sites could also be seen due to the decrease in the Si/Al ratio, pointing, as generally accepted, to an increase in the Al concentration [162]. Lewis acid sites increase could also be observed due to a redistribution in the strength of Lewis acid sites within the sample [221] (ZSM-5M zeolite in Figure I.42).

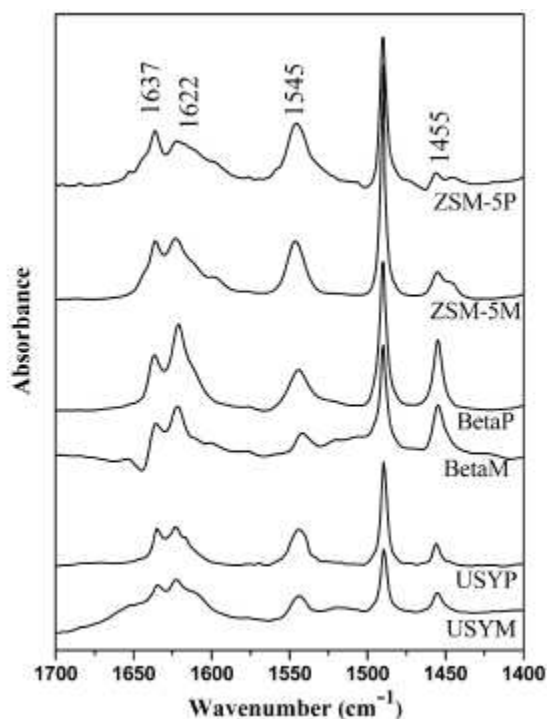


Figure I.42 IR spectra showing the evolution of Brønsted and Lewis sites before and after desilication of USY, Beta and ZSM-5 zeolites. Adapted from [164].

3.4.5 Impact on catalytic performance

As well said, the objective of hierarchization is to reduce the diffusion path length which by turn lessens the diffusional limitations exhibited within small pore sized zeolites. The lower the diffusion path length, the lower the time contact between the intermediates and the active acidic sites, in particular, the Brønsted sites. In the conversion of methanol to hydrocarbons studied by Liu et al. [223], the hierarchized porous zeolite Beta was seen to exhibit larger conversion capacity, with faster reaction rate and a remarkably longer lifetime when comparing to the conventional zeolite Beta. Moreover, the hierarchical ZSM-5 and Beta zeolites with inter/intra-crystalline mesoporosity had shown excellent activity and selectivity in the synthesis of wide range of aromatic and heterocyclic ketones, as in the work reported by Kore et al. [224]. It was suggested by this team that there was high accessibility of the reactant molecules to the acid sites located at the pore-mouth or inside the channels, which enhanced the diffusion of the reactants as well as products after desorption through the inter-crystalline mesopores [224].

In the hydroisomerization of n-alkanes, lower activities and selectivities toward isomers products are observed with small pore sized zeolites [78,211]. In a study done by Martens et al. [78,211], it was seen that the hierarchization of ZSM-22 zeolite by means of desilication, had registered a remarkable effort in improving the activity of the catalyst and the selectivity towards isomers product in the hydroisomerization of n-decane, n-nonadecane and pristane. Some hydrocarbons are also known to readily isomerize, e.g. monoterpenes. These molecules have also been studied using hierarchical zeolites [225,226]. In these studies, ZSM-12 zeolite was desilicated in NaOH alkaline treatment to produce a ZSM-12 zeolite with a mesoporous network. This mesoporous material was found to have enhanced activity in comparison with the conventional ZSM-12 zeolite in the isomerization of α -pinene.

4 Objective

While no much studies have been reported on the catalytic performance of hierarchical *BEA zeolites in the hydroisomerization reactions of n-alkanes, we tend in our work to go deep in this issue, and try to investigate the impact of hierarchization on the activity and isomers selectivity of the related catalysts. The work will be consisting of several tasks. One of the tasks is to synthesize a microcrystal *BEA zeolite that possess only micropores in its pore system, and subject it to several post-modifications by means of desilication in presence of inorganic and organic hydroxyl compounds. The impact of desilication of the microcrystal *BEA zeolites

on their structural, textural, acidic and catalytic performance properties in the hydroisomerization of n-C₁₀ and n-C₁₄, will be investigated and discussed. Moreover, another task will be accomplished by the attempt to subject two commercial mesoporous *BEA zeolites that possess both the micro- and mesoporous network, to desilication treatments also in presence of inorganic and organic hydroxyl compounds, seeking for additional mesoporosity that may enhance more and more the diffusional pathways of the olefin intermediates within the pores. As in the first task, the impact of desilication will be investigated on the zeolites' properties, and their catalytic performance in the hydroisomerization of the desired n-alkanes.

Chapter II

Experimental Part

1 Zeolites and catalysts preparation

1.1 Parent nanocrystal *BEA zeolites

Two commercial nanocrystal *BEA zeolites were used in the different catalytic tests to be discussed later in this chapter. The first *BEA zeolite referenced CP811, denoted by P1, where “P” stands for parent, was supplied by PQ Corporation. The second parent *BEA zeolite referenced CP814E, denoted by P2, was supplied by Zeolyst Company. Despite of the fact that they are both commercial *BEA zeolites, but they still have some differences in the elemental, textural, and acidic properties. The structural and different physico-chemical properties will be presented and discussed in chapter III.

Both zeolites were subjected to alkaline treatments to induce some textural modifications seeking for a solution to the diffusion limitations found within the zeolites’ porous structure. The treatments were said to be post-synthesis treatments, i.e. top-down approaches were used to modify the zeolite structure. Among the variable post treatments found in literature, the most recent one was desilication, and was as used method in the work presented.

P1 zeolite was desilicated by the classical way, in presence of NaOH alone, and by the alternative way in presence of a solution mixed of NaOH and tetrapropylammonium bromide (TPABr. P2 zeolite was desilicated in solutions of NaOH alone, solutions of NaOH and tetrabutylammonium hydroxide (TBAOH), and solutions of NaOH and tetrapropylammonium hydroxide (TPAOH). The mixtures’ concentrations as well as the molar fractions of the tetraalkylammonium based pore directing agents were varied to study their effects on the zeolite properties. The desilicated samples of P1 will be denoted by P1-Dn (with n the number of desilication performed), and will be referred to series 1 zeolites. Similarly, The desilicated samples of P2 will be denoted by P2-Dn (with n the number of desilication performed), and will be referred to series 2 zeolites, as seen in Table II.1.

After each desilication, the suspension was cooled down in an ice-bath, filtered and washed with distilled water to reach neutral pH. The Na⁺ species were exchanged by NH₄⁺ through a threefold successive ion-exchange treatments, with a 0.5M NH₄NO₃ solution, at 80 °C for 1 hour. The final powders were calcined at 550 °C for 6 hours, and the mass after calcination was measured to determine the yield of each desilication reaction, represented by the following equation:

$$Y (\%) = \frac{m_f}{m_i} \times 100 \quad \text{Equation II.1}$$

where,

Y is yield of desilication;

m_f is the final mass after desilication;

m_i is the initial mass before desilication.

The conditions of desilications as solutions, concentrations, of P1 and P2, are reported in Table II.1, knowing that all reactions were performed at 65 °C for 30 minutes.

Table II.1 Desilication conditions for P1 and P2 zeolites.

Sample	[NaOH] (M)	DPA	[DPA] (M)	[HO ⁻] (M)	R (TBAOH molar ratio)
P1	-	-	-	-	-
P1-D1	0.2	-	-	0.2	-
P1-D2	0.2	TPABr	0.2	0.2	-
P2	-	-	-	-	-
P2-D1	0.1	-	-	0.1	-
P2-D2	0.2	-	-	0.2	-
P2-D3	0.5	-	-	0.5	-
P2-D4	0.15	TBAOH	0.1	0.075	0.2
P2-D5	0.225	TBAOH	0.025	0.1	0.04
P2-D6	0.202	TBAOH	0.134	0.13	0.385
P2-D7	0.12	TBAOH	0.2	0.13	0.625

1.2 Microcrystal *BEA synthesis and post-synthesis treatments

Besides the nanocrystals and the effects of desilications on its properties and catalytic performance (to be discussed later), a microcrystal *BEA zeolite was synthesized to make the same investigation processes, based on the procedure mentioned in literature [227]. The synthesis was finalized in accordance to the molar compositions presented in Table II.2.

Table II.2 Molar compositions of the starting materials for MC synthesis.

Compounds	SiO₂	Al	TEAOH	HF	H₂O
Molar composition (mol)	1	0.033	0.573	0.573	7.033

The synthesis was carried by adding the amounts of aluminum (Al), tetrethylammonium hydroxide solution (TEAOH) and tetraethoxysilane (TEOS), to a teflon beaker. The mixture was kept under stirring for two days at room temperature. After two days the amounts of water and hydrofluoric acid (HF) were added and the mixture was mixed well. The teflon beaker was then put in an autoclave and the later was transferred into an oven. The mixture was allowed to crystallize at 170 °C for 14 days. The final suspension was collected from the beaker, filtered, washed several times to insure no more impurities and to reach neutral pH, then dried and calcined at 550 °C for 6 hours. The final product was denoted by “MC”, an abbreviation of the term: microcrystal.

The protonic form of the MC *BEA zeolite obtained finally after calcination, was subjected to three desilication treatments. The solutions used were a) NaOH solution, b) a solution of NaOH and TPABr, and c) a solution of NaOH and TBAOH. The desilicated forms were also ion-exchanged and calcined using the same procedures followed previously with the nanocrystals desilications. The desilicated samples of MC will be denoted by MC-Dn (with n the number of desilication performed), and will be referred to series 3 zeolites (Table II.3 Desilication conditions of MC).

The conditions of desilications as solutions, concentrations, time and temperature, of the microcrystal *BEA zeolite, are reported in Table II.3, with the same time and temperature followed in series 1 and 2.

Table II.3 Desilication conditions of MC.

Series 3	[NaOH] (M)	DPA	[DPA] (M)	[HO⁻] (M)	R
MC	-	-	-	-	-
MC-D1	0.2	-	-	0.2	-
MC-D2	0.2	TPABr	0,2	0.2	-

MC-D3	0.12	TBAOH	0.2	0.13	0.625
-------	------	-------	-----	------	-------

1.3 Bifunctional catalysts preparation

All the parent and desilicated zeolites used in the hydroisomerization catalytic tests, were transformed into their bifunctional form by the impregnation of platinum (Pt). The impregnation was based on the ion exchange principle using the $\text{Pt}(\text{NH}_3)_4(\text{NO}_3)_2$ salt. The exchange was performed during 24 hours under continuous stirring at room temperature. NH_4NO_3 salt was added to supply the mixture with NH_4^+ , respecting the molar ratio between NH_4^+ and Pt to be 100. The ratio between the volume of the water and the mass of the zeolite ($V_{\text{H}_2\text{O}} / m_{\text{zeolite}}$) was equal to 50 mL.g^{-1} . After the exchange, the zeolite was filtered, washed and dried at $100 \text{ }^\circ\text{C}$ over night. Finally, the dried sample was calcined under air flow of 150 mL.min^{-1} , following the temperature program present in Figure II.1.

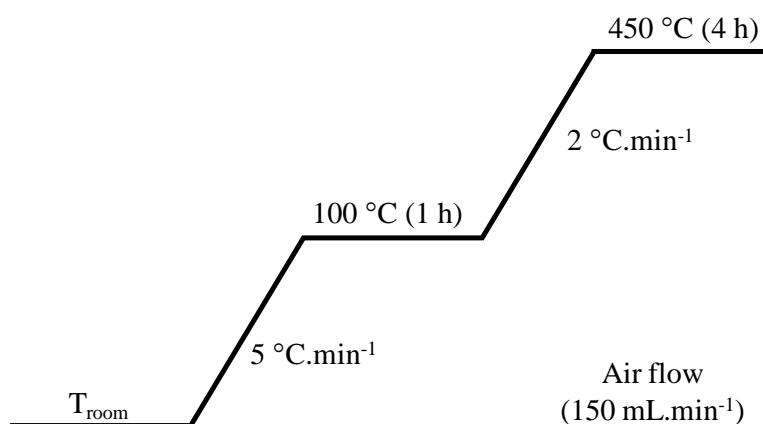


Figure II.1 Platinum exchanged *BEA zeolites calcination program.

In series 1, the balance between the metallic and acidic sites was studied by the impregnation of different platinum loadings: 0.44, 0.98, 1.1 and 1.5 wt. percentage of platinum. The metal loadings of the desilicated forms of P1 and of series 2 catalysts contained approximately 1.5 wt. percentage of Pt to insure obtaining a well-balanced catalyst. Series 3 catalysts contained less amounts of Pt loading, despite the effort made to impregnate 1.5% wt. of Pt. But unexpectedly, the loading was 0.75% in MC and 1.0% in its desilicated forms. Hereafter, these catalysts will be called xzeolite, where “x” represents the platinum loading wt. %, and “zeolite” represents the parent (P) or desilicated (D) zeolite.

2 Techniques used for the physico-chemical characterization of the zeolites and their related catalysts

2.1 Study of zeolitic structure by X-ray diffraction (XRD)

2.1.1 Principle

The X-ray powder diffraction patterns were determined to seek information about the crystalline phases existing on the parent and desilicated materials before being tested to check if they still maintain the *BEA zeolite characteristics. It was also important to use the integration of the peaks' areas for each desilicated material to estimate the crystallinity percentage in comparison with the parent material (considered to be 100% crystalline). Moreover, through the Scherrer method, the resulting diffractograms helped to estimate the size of the crystal size of the microcrystal synthesized zeolite. In addition to that, the associated XRD software can be used to determine the Miller indices of the different crystalline phases accompanied with each sample.

The crystalline bodies can be considered as assemblies of atomic planes, called reticular planes, separated by a characteristic distance, the inter-reticular distance (d_{hkl}). When an X-ray beam irradiates a crystalline material, it is reflected by a family of planes with a Miller's index (h k l) encountered at a certain angle, called the Bragg angle (θ). The X-rays diffracted during the angular scanning of the surface of the sample are collected by a detector. Each diffracted peak thus corresponds to an angle θ which can be connected to the inter-reticular distance according to the Bragg's law:

$$2d_{hkl} \times \sin\theta = n \times \lambda \quad \text{Equation II.2}$$

where,

d is the distance between two Miller index planes;

λ is the X-ray wavelengths;

n is the diffraction orders;

and θ is the incident angle of the X-ray beam (Bragg's angle).

2.1.2 Experimental procedure

All the XRD patterns were obtained on a D5005 BRUKER AXS diffractometer using a $\text{CuK}\alpha$ radiation ($\lambda=1.5406 \text{ \AA}$) as incident beam, obtained by summing a copper anode to a tension of 40 kV and an intensity of 30 mA. The $\text{CuK}\beta$ radiation and the eventual fluorescence were eliminated by a graphite monochromator.

The acquisition method ranged from 5 to 60 $^{\circ}2\theta$ on all the samples including the parent, the desilicated, and the synthesized materials as well.

2.1.3 Scherrer method

As said before, to estimate the average crystallite size, the Scherrer method was used. The corresponding Scherrer equation (equation II.3) was applied to the most intense peak, which in case of the *BEA zeolite (microcrystals only) corresponds to 22.4 $^{\circ}2\theta$ (Miller index 3 0 2).

$$D = \frac{K\lambda}{FWHM \cdot \cos \theta} \quad \text{Equation II.3}$$

where,

D (\AA) is the crystallite size;

K is the shape factor (typically 0.9);

λ (\AA) is the incident x-ray radiation wave length;

FWHM (rad) is the full width at half maximum of the peak;

and θ (rad) is the incidence angle or Bragg's angle [228].

2.2 Induced Coupled Plasma - Atomic Emission Spectroscopy (ICP-AES)

The compositional weight of Pt, Si, Al and Na, allowed the determination of the total Si/Al ($\text{Si}/\text{Al}_{\text{total}}$) ratio of the pure *BEA samples before and after desilcations, was obtained by the elemental analysis with the aid of atomic emission spectrometry (ICP-AES) on a Perkin Elmer Optima 2000 DV.

2.2.1 Principle

Inductive plasma emission spectrometry (ICP-AES) is based on the formation of plasma in a rare gas stream. The liquid sample is nebulized then transferred to the plasma (Argon). It undergoes various stages of decomposition, atomization and ionization, leading to the

excitation of atoms and ions. After excitation, the atoms contained in the sample emit light with a characteristic wavelength. The light is transmitted via the optical system to a detector which allows dosing. A prior calibration of the element to be assayed makes it possible to quantify it.

2.2.2 Experimental procedure

The analysis was carried out in an argon plasma using a Perkin-Elmer OPTIMA 2000DV spectrometer. The sample is diluted in aqueous solution and then vaporized using a plasma to measure the emission intensity of a radiation characteristic of the element to be assayed.

2.3 Nitrogen Physisorption

The textural properties were determined by nitrogen physisorption technique. It was possible to obtain several samples characteristics through this technique, such as: surface area, external surface, pore volume and pore size distribution.

2.3.1 Experimental procedure

The experimental data on the nitrogen adsorption-desorption isotherms were obtained by using a Micromeritics ASAP 2000 apparatus. The samples were first outgased for 1 h at 90°C then at 350°C for at least 4h. After, the nitrogen isotherm was determined at -196 °C.

2.3.2 Isotherm classification

Besides to all the properties that the nitrogen physisorption technique provides us with, the isotherm itself allows to classify the type of the material studied through the observation of the isotherm type. The majority of the physisorption isotherms are included into the six types as shown in Figure II.2.

Type I – This type of isotherm corresponds to adsorption in gaseous phase on microporous solids. It is typical of single-layer adsorption, with saturation when the layer is completely filled. This is the most frequent case encountered for zeolites and activated carbons. It demonstrates a relatively strong interaction between the adsorbate and the adsorbent, and is reversible over the entire pressure range. A decrease in the diameter of the micropores results in both the increase in the adsorption energy and a decrease in the relative pressure at which the filling of the microporous volume occurs. The narrow range of relative pressure necessary to reach the plateau is an indication of the narrow pore size distribution. In addition, the fact that this plateau is almost horizontal indicates that the external surface is very weak. Type I (a) isotherms are for materials with micropores smaller than 1 nm diameter, while Type I (b)

isotherms are for those with a larger pore size (up to 2.5 nm). The mesoporous materials whose pore size is between 2 and 2.5 nm are thus included in the type I isotherm (b).

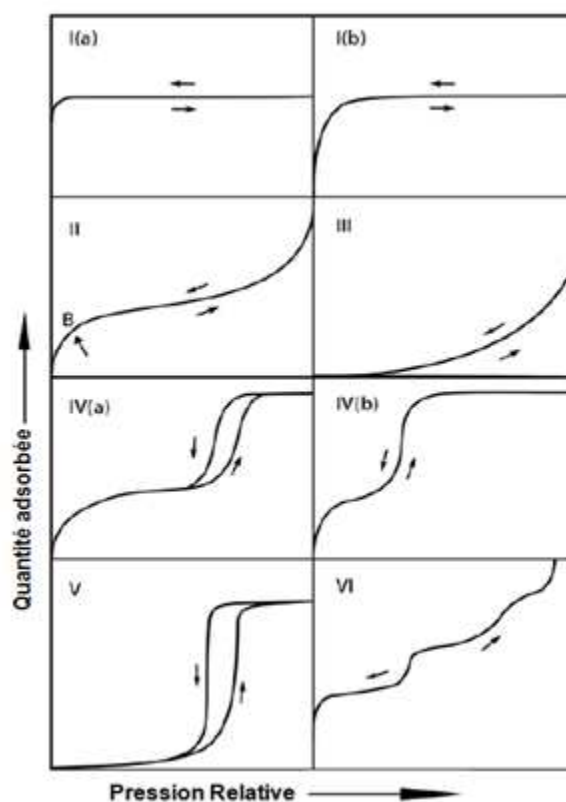


Figure II.2 Types of physisorption isotherms [217].

Type II – This isotherm results from multilayer adsorption on an open surface and are characteristic of nonporous and macroporous materials. Point B in an indication to the stage at which monolayer coverage is complete and multilayer adsorption is about to begin. They may exhibit the hysteresis phenomenon.

Type III – These isotherms with a convex curvature are rare and characterize very weak adsorbate-adsorbent interactions.

Type IV – Very typical type IV isotherms (a) are characteristic of mesoporous materials, and generally exhibit a hysteresis phenomenon: this indicates the presence of mesopores where the adsorbate is found in its condensed form. These isotherms are characteristic of strong molecular interactions. Type IV isotherms (b) are concerned with materials whose mesopores are cylindrical or conical in shape.

Type V – This isotherm type is uncommon and related to the Type III isotherm in the measure that the adsorbent-adsorbate interaction is said to be weak, but still it is obtained with certain porous adsorbents. Type V isotherms with convex curvature are also quite rare. They indicate a lower adsorbate-adsorbent interaction, and the appearance of a hysteresis is related to the presence of mesopores.

Type VI – These types are due to a multi-layer adsorption process on materials with orientation on a particular crystal face (multilayer adsorption on a homogeneous non-porous surface). Argon or krypton on graphitized carbon blacks are the most popular examples of this type of isotherm obtained at liquid nitrogen temperature.

2.3.3 Specific Surface – BET surface

The Brunauer, Emmett and Teller equation (BET) [229], which is an extension of the Langmuir equation [230] was used to estimate the specific surface area of the zeolitic materials. Therefore, the values obtained for the “specific surface” through the BET equation will be then designated by BET surface (S_{BET}).

In order to get the value the BET surface it was needed to calculate first the amount of gas needed to fill the monolayer (v_m). The following equation was used to fit the experimental data to, thus obtaining the monolayer and the BET surface after.

$$\frac{\frac{P}{P_0}}{v\left(1-\frac{P}{P_0}\right)} = \frac{C-1}{v_m \cdot C} \cdot \frac{P}{P_0} + \frac{1}{v_m \cdot C} \quad \text{Equation II.4}$$

where,

P, pressure at equilibrium (mmHg), on zeolites: $P/P_0 < 0.1$;

P_0 , saturation pressure (mmHg);

v, quantity of adsorbed gas (mol);

v_m , quantity of monolayer gas (mol);

C, BET constant.

However, as said in the literature review, the BET equation cannot be held for microporous materials and a in lesser extent to mesoporous ones according to several hypotheses [218].

The BET constant (C) depends on the molar heat of adsorption of the first layer on the surface of the material (E_1) and the molar heat of liquefaction of the diazote (E_L). Strong adsorbent-adsorbate interactions are characterized by a high value of the constant C. The exponential equation of this constant is presented by equation below:

$$C = \exp\left(\frac{E_1 - E_L}{RT}\right) \quad \text{Equation II.5}$$

Once the v_m was determined, the BET surface was obtained by using the following equation:

$$S_{BET} = v_m \cdot \sigma(N_2) \cdot N_A \quad \text{Equation II.6}$$

where,

S_{BET} , BET surface ($m^2 \cdot g^{-1}$);

v_m , quantity of monolayer gas (mol);

$\sigma(N_2)$, Nitrogen surface area ($16.2 \times 10^{-20} m^2$);

N_A , Avogadro's number ($6.022 \times 10^{23} mol^{-1}$).

2.3.4 External surface

The external surface (S_{ext}) includes the external surface of crystals and the area of mesopore, was obtained through the t-plot method to be described below.

2.3.5 Pore Volume

The pore volume of the analyzed sample was also determined by nitrogen physisorption. It was also possible to classify the samples pore volumes according to their sizes into three different categories [217]:

- i. Macropores: greater than 50nm (not detected with nitrogen physisorption);
- ii. Mesopores: between 2 and 50nm;
- iii. Micropores: less than 2nm;

Moreover, the micropores can be also divided into ultra-micropores (less than 0.8 nm) and super-micropores (between 0.8 and 2 nm).

2.3.5.1 Total pore volume

It is important first to determine the total pore volume through the volumic amount of nitrogen adsorbed on the sample needed to attain a relative pressure (P/P_0) of 0.97. It is calculated according to the following relation in the next equation:

$$V_{Total} = \frac{M \cdot V_{ads}}{V_M \cdot \rho_{liq}} \quad \text{Equation II.7}$$

where,

V_{total} , total pore volume ($\text{cm}^3 \cdot \text{g}^{-1}$);

M, molar weight of nitrogen gas ($28 \text{ g} \cdot \text{mol}^{-1}$);

V_M , molar volume ($22414 \text{ cm}^3 \cdot \text{mol}^{-1}$);

ρ_{liq} , density of liquid nitrogen ($0.808 \text{ cm}^3 \cdot \text{g}^{-1}$).

2.3.5.2 Micropore volume ($\emptyset < 2 \text{ nm}$)

The method proposed by Dubinin and Raduskhevitch enables the determination of the volume of all the pores with less than 2 nm (V_{micro}) [231]. This method considers that instead of filling the pore layer by layer, it is done by capillary condensation, and according to this point the following equation can be derived:

$$\log(V) = \log(V_{micro}) - \frac{BT^2}{\beta} \left[\log^2 \left(\frac{P}{P_0} \right) \right] \quad \text{Equation II.8}$$

where,

V, pore volume ($\text{cm}^3 \cdot \text{g}^{-1}$);

V_{micro} , micropore volume ($\text{cm}^3 \cdot \text{g}^{-1}$);

B, constant;

T, isotherm temperature (K);

β , adsorbate affinity coefficient;

P, pressure at equilibrium (mmHg);

P_0 , saturation pressure (mmHg);

The linear equation $\log(V) = f \left[\log^2 \left(\frac{P}{P_0} \right) \right]$ allows to determine V_{micro} by the extrapolation of the linear curve part between $\left[\log^2 \left(\frac{P}{P_0} \right) \right] = 2$ and 6, as shown Figure II.3.

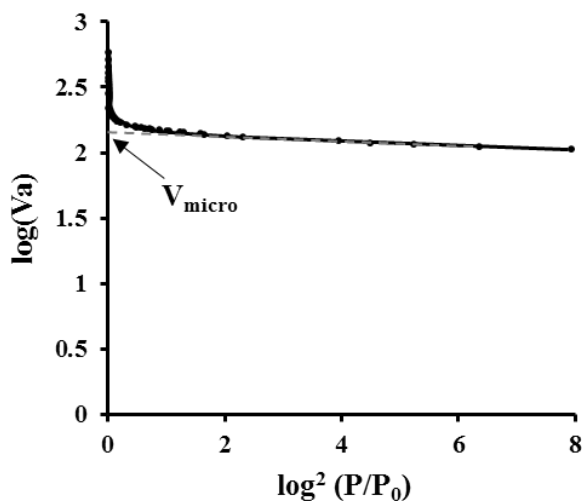


Figure II.3 Determination of the micropore volume of *BEA zeolite (CP811) through the DR method.

2.3.5.3 Ultra micropore volume ($V_{\text{ultra}} - \text{\AA} < 0.8 \text{ nm}$)

The t-plot method was used to calculate the ultra-micropore volume ($\text{\AA} < 0.8 \text{ nm}$) once the micropore volume was determined. Figure of t-plot (Figure II.4) illustrates different types of t-plots, which represents graphically the adsorbed volume (V_{ads}) against the statistical thickness of the adsorbed layer (t). For nonporous materials (a), a straight line passes through or very close to the origin. In materials possessing mesopores (b), the plot shows a deviation from the straight line at high nitrogen relative pressures, whereas for microporous materials, deviations take place at low nitrogen relative pressures (c) [232–234]. In some zeolitic materials possess both micro- and mesopores, their t-plot therefore fits to that presented in d.

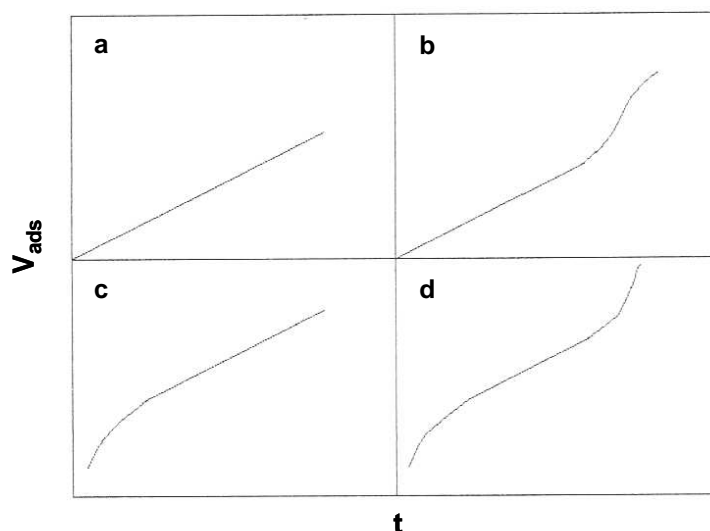


Figure II.4 Different types of t-plots: (a) nonporous solid; (b) mesoporous solid; (c) microporous solid and (d) micro- and mesoporous solid.

Different mathematical models (Halsey, Harkins-Jura, Broekhoff-de Boer) were suggested to obtain the statistical thickness of the adsorbed layer (t), depending on the studied solids [232–234]. In our case, case of zeolites, it was demonstrated that the Harkins-Jura isotherm was the suitable one [235]. Consequently, the equation represented by the Harkins-Jura isotherm is as follows:

$$t = \sqrt{\frac{13.99}{0.034 - \log\left(\frac{P}{P_0}\right)}} \quad \text{Equation II.9}$$

where,

t , thickness of the adsorbed layer (Å);

P , pressure at equilibrium (mmHg);

P_0 , saturation pressure (mmHg).

In microporous solids (c, d), at low relative pressures (low t values) and after the complete filling of the micropores volume that occurs, a linear region appears in the plot. It is possible then to determine the ultra micropore volume (V_{ultra}) and the external surface (S_{ext}), from the interception at $t=0$ and the slope of the straight line respectively, as shown in Figure II.5. As said before, it should be taken into consideration that the value of external surface comprises both the external surface of crystallites and the mesopore area.

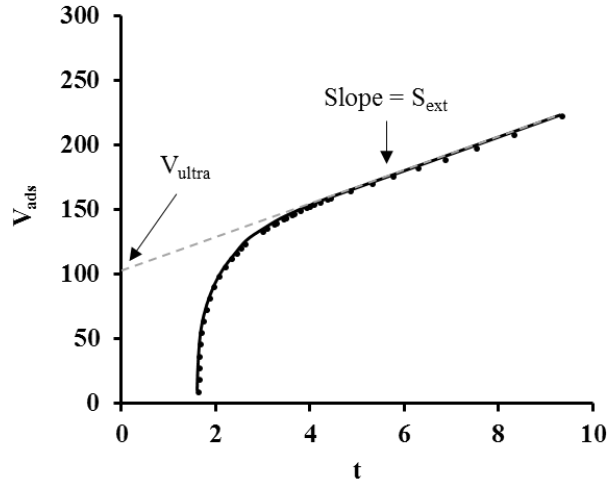


Figure II.5 T-plot example for *BEA zeolite (CP811).

2.3.5.4 Mesopore volume ($2 < \text{\AA} < 50 \text{ nm}$)

The mesopores volume was finally the difference obtained between the total pores volume (V_{total}) and the micropore volume (V_{micro}).

2.3.6 Mesopore size distribution

The BJH method (Barret, Joyner and Halenda) [236] was used to obtain the pore size distribution. This method describes the adsorption-capillary condensation process that takes place inside the mesopores [232]. In the capillary condensation region ($P/P_0 > 0.4$), the increase in pressure causes the thickening of the layer adsorbed on pore walls, as well as capillary condensation in pores having a core (empty pore space) size r_c defined by the Kelvin equation as follows:

$$\ln\left(\frac{P}{P_0}\right) = -\frac{2\gamma V_M \cos\theta}{RT r_c} \quad \text{Equation II.10}$$

where,

P , pressure at equilibrium (mmHg);

P_0 , saturation pressure (mmHg);

γ , surface tension (N_2 : 8.85 m.Nm^{-1});

V_M , molar volume (N_2 : $22414 \text{ cm}^3.\text{mol}^{-1}$);

θ , contact angle;

R, gas constant;

T, temperature (K);

r_c , radius for cylinder pores.

By assuming the pore geometry, it is possible to calculate the contribution of a thickness of the adsorbed film to the total adsorption and the core volume. Therefore, from these results and from the assumed pore geometry it is possible to transform the core volume and core size into pore volume and pore size respectively. Finally, the mesopore size distribution can be determined by following the isotherm step by step in the range $0.4 < P/P_0 < 0.97$.

2.4 Scanning Electron Microscopy (SEM)

The SEM was used to observe the morphology of the samples. It was also possible through this technique to determine the crystals sizes of all *BEA samples. Its principle is based on the detection of the secondary electrons emerging from the surface of a sample under the impact of a very thin primary electron beam that sweeps the observed surface. These secondary electrons are collected and allow reconstruction of an enlarged image of the surface after certain scanning duration.

2.4.1 Experimental procedure

The samples morphology and size of crystals were determined through scanning electron microscopy (SEM) performed on a FEG-SEMJEOL microscope (JSM 5600-LV model). In order to be analyzed the samples were dispersed on a double face carbon adhesive tape that was deposited on a microscope slide and finally were covered with a carbon layer.

2.4.2 Particle size distribution

The SEM images were used to obtain the *BEA crystals particles size distribution. This was performed by measuring the size of at least 500 different particles with the help of ImageJ software.

2.4.3 Average particle size

Once the particle size distribution is determined, the average particle size can be determined by this arithmetic formula.

$$D_p = \frac{1}{n} \sum_1^n d_{p_i} \quad \text{Equation II.11}$$

where,

D_p , average particle size;

n , number of particles;

d_{pi} , size of the particle i .

2.5 Transmission Electron Microscopy (TEM)

The TEM technique was also used to observe the morphology of the crystals of the parent, desilicated and synthesized *BEA zeolites.

2.5.1 Experimental procedure

The morphology of the samples was determined by transmission electronic microscopy (TEM) using a Philips CM 120 microscope equipped with a LaB₆ filament. To prepare the sample, a small drop of a suspension in ethanol was put on a gold grid (Au) and after that the solvent was evaporated.

2.5.2 Platinum particles average size and distribution

The platinum particles size distribution and average size were obtained through the same methodology used in scanning electron microscopy (SEM).

2.6 Infrared spectroscopy

The infrared spectroscopy experiments were done using a Fourier Transform Infrared spectroscopy (FT-IR) apparatus. In the work reported, this technique was used for the following purposes:

- To study the hydroxyl (OH) stretching vibrations bands in the range of 3500 – 3800 cm⁻¹ IR region.
- To use the probe molecules pyridine and CO, for the quantification of the samples acid sites density and platinum dispersion respectively.
- To determine the framework Si/Al ratio of the *BEA zeolite through the use of the zeolite structure bands.

2.6.1 Stretching vibration bands of hydroxyl groups (OH)

In general, the hydroxyl groups of zeolites and acid catalysts are often associated to the Brønsted acidity. Their vibrations generate IR adsorption bands in 3500 and 3800 cm⁻¹ IR

region. The quantification of the density of the hydroxyl groups acidity is not possible, since when the Brønsted acid sites density increases, the O-H bond weakens thus decreases the OH frequency [237]. On the other hand, the O-H bond also depends on the location of the hydroxide group, which means the pore structure and presence of an extra-framework phase. Therefore, the comparison of these groups between zeolites is not possible, as well as between OH groups in case located on different environments inside the same sample [237].

2.6.1.1 Experimental procedure

All the experiments were done in a quartz IR cell equipped with CaF₂ windows, connected to vacuum as well as precised atmospheric systems, in addition to a temperature controlled oven. The catalyst was pressed prior to analysis into a self-supported 2 cm² wafer (0.5 ton) that weighed between 10 and 30 mg. The sample is then placed in the IR cell and was calcinated over night at 450 °C under air flow (60 mL.min⁻¹). Following the calcination, the sample was outgased (10⁻⁵ bar) during 1 h at 200 °C, after which finally an IR spectrum was taken.

The figure below (Figure II.6) shows the example of a *BEA zeolite OH stretching vibration bands, where:

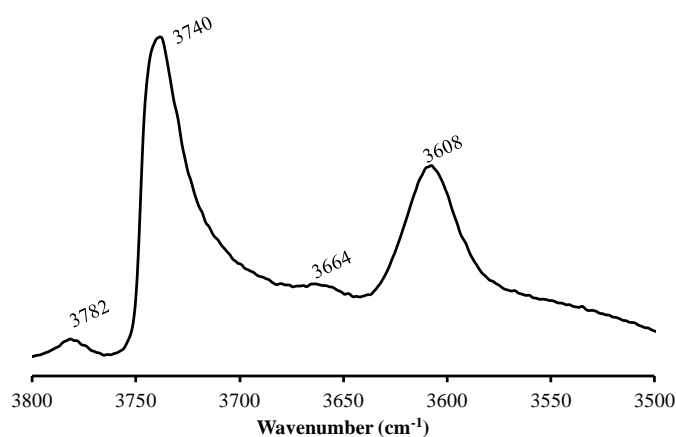


Figure II.6 *BEA's OH stretching vibrations bands.

- The band at 3782 cm⁻¹ refers to hydroxylated monomeric EFAL species and framework defects with Lewis acidity [238].
- The most intense band at 3740 cm⁻¹ corresponds to the silanol groups (Si-OH) which are similar to those of silica and with a very weak acidity [237,239], [240]. Sometimes two bands may overlap. The first band from 3730 to 3740 cm⁻¹ which is attributed to the internal Si-OH and the second band at 3745 cm⁻¹ attributed to external Si-OH [241,242].

- The band at 3664 is ascribed to the Al-OH hydroxyls. They refer to the aluminum those that does not make part of the zeolite framework [14], [243].
- The band at 3608 cm^{-1} is ascribed to bridging OH groups that are responsible for the Brønsted acidity [237,239].

2.6.2 Determination of Brønsted and Lewis acidity

To determine the acidity of some materials like oxides and zeolites, pyridine is widely used as a molecule to probe these materials [239,244,245]. The interactions between the pyridine molecule and the material's acid sites are responsible for the appearance of several bands in the IR spectra. These bands appear in the 1400 – 1700 cm^{-1} IR region. The bands at 1490, 1545 and 1640 cm^{-1} are attributed to the formation of pyridinium ions on the Brønsted sites (PyH^+) and those at 1455, 1490 and 1600-1630 cm^{-1} are attributed to the coordination of the pyridine on the Lewis sites (PyL) [237,246]. The corresponding spectrum is shown below in Figure II.7.

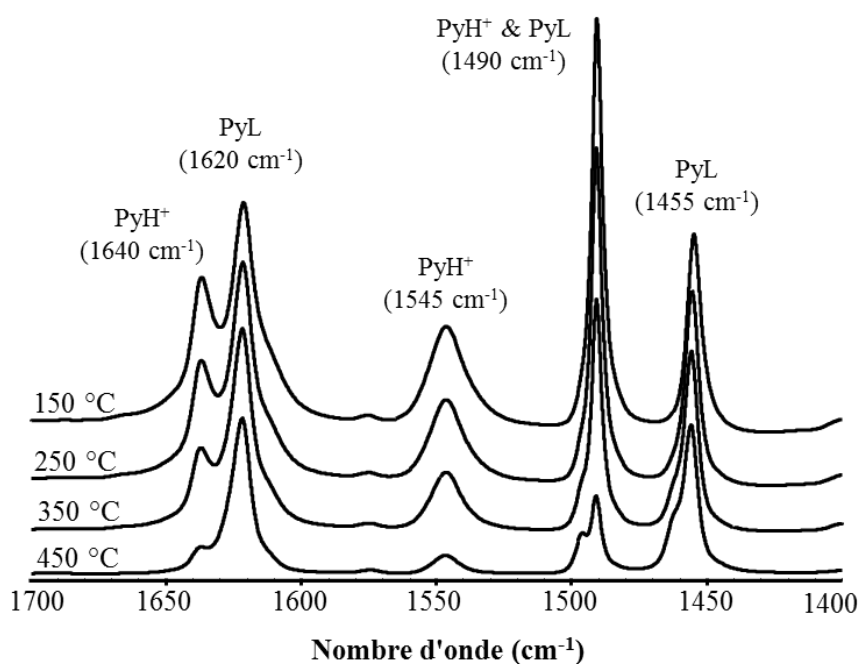


Figure II.7 Pyridine interaction bands (1400 – 1700 cm^{-1}) of H*BEA zeolite (CP811) drawn at different temperatures.

The integration of the areas under the bands at 1545 and 1455 cm^{-1} enables the determination of the Brønsted and Lewis acid site density as explained bellow.

2.6.2.1 Experimental Procedure

All the experiments were done in a quartz IR cell equipped with CaF₂ windows, connected to vacuum as well as precise atmospheric systems, in addition to a temperature controlled oven. The catalyst was pressed prior to analysis into a self-supported 2 cm² wafer (0.5 ton) that weighed between 10 and 30 mg. The sample is then placed in the IR cell and was calcinated over night at 450 °C under air flow (60 mL.min⁻¹). Following the calcination, the sample was outgassed (10⁻⁵ bar) during 1 h at 200 °C, after which an IR spectrum was taken. The sample was then cooled to 150°C and subjected to exposure of 1.5 mbar pyridine pressure during 5 min and once again outgassed (10⁻⁵ bar) in order to eliminate the physisorbed pyridine probing molecules. A spectrum was then recorded at 150°C after 1 hour followed by three other spectra taken at 250, 350 and 450 °C with 1 hour gap between every spectrum. This enables to have further understanding of the acid sites strength. The characteristic spectra of the adsorbed pyridine at each temperature were, consequently, obtained by difference with the reference spectra taken at 200 °C.

All the spectra were determined on a THERMO NICOLET 6700 FTIR spectrometer between 1000 and 4000 cm⁻¹ IR region with a resolution of 2 cm⁻¹ and 64 analyses per spectrum).

As explained before, the pyridine interaction with a support enables to determine both Brønsted and Lewis acid site densities on this support. This is achieved through the correlation between the 1455 and 1545 cm⁻¹ bands integrated absorbance and, respectively, the Lewis and the Brønsted acid sites density given by a modified Lambert-Beer law, which ultimately results on the following equation:

The Lambert-Beer law allows the calculation of the acid sites densities by fitting the values of the integrated bands at 1455 and 1545 cm⁻¹ of the the Lewis and the Brønsted acid sites respectively, in the following equation:

$$c = \frac{A.S}{\epsilon.m} \quad \text{Equation II.12}$$

where,

c, Brønsted or Lewis acid site density (μmol.g⁻¹)

A, Wafer surface area (2 cm²);

ε, molar absorption coefficient (ε_B = 1.13; ε_L = 1.28)

m, wafer weight (g)

S, are under integrated peak ($\text{cm}^2 \cdot \text{mol}^{-1}$).

2.6.3 Platinum dispersion determination

The carbon monoxide adsorption followed by FT-IR spectroscopy enables to estimate the amount of metallic sites on some catalysts. The bond between the platinum and the CO molecules as proven to be linear, consequently, only one CO molecule is adsorbed by accessible platinum atom [25, 84]. Moreover, this interaction generates a stretching band, around 2080 cm^{-1} , that can be used to determine the amount of accessible platinum atoms [85, 86].

2.6.3.1 Experimental Procedure

All the experiments were carried out in a quartz IR cell equipped with CaF_2 windows, connected to vacuum and atmospheric systems, as well as temperature controlled oven. Prior to analysis, the catalyst was pressed into a self-supported wafer 2 cm^2 (0.5-2 ton) that weighted between 10 and 20 mg. Once placed in the IR cell the sample was reduced over night at $450 \text{ }^\circ\text{C}$ under hydrogen flow ($60 \text{ mL} \cdot \text{min}^{-1}$). After, the sample was outgased (10^{-5} bar) during 2 h. Finally, the sample was cooled to room temperature, thus finishing the pre-treatment.

The reference spectrum was taken at room temperature under vacuum (before CO introduction). All spectra were taken in a 1000 to 4000 cm^{-1} range on a THERMO NICOLET 5700 FTIR spectroscopy (resolution: 2 cm^{-1} , 64 analysis per spectrum). Then, precise amounts of CO were introduced in the IR cell, using a calibrated volume ($V = 0.9837 \text{ mL}$), until complete sample saturation. Between, each CO injection an IR spectrum was recorded. The characteristic spectra of the adsorbed CO molecules were, consequently, obtained by difference against the reference spectra.

2.6.3.2 Accessible platinum sites (platinum dispersion)

As it was said before, the interaction between the CO molecules and the platinum atoms generates a stretching band that can be observed by IR spectroscopy. In the particular case of platinum, the adsorption band appears around 2080 cm^{-1} representing the CO molecules linearly connected to the CO. Additionally, another less intense band may be observed around 1850 cm^{-1} representing the bridged CO bonds, as shown on Figure II.8.

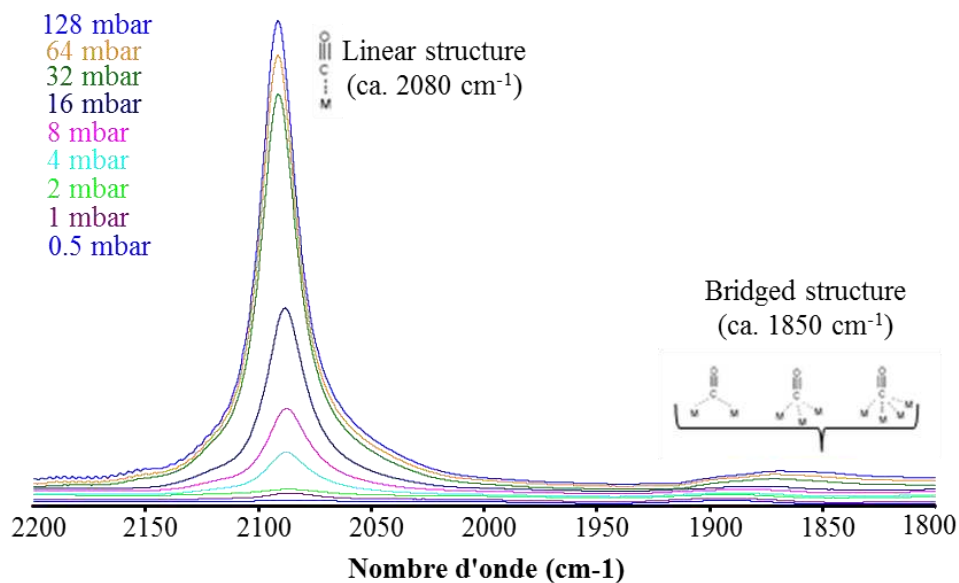


Figure II.8 IR spectrum of CO adsorbed on Pt/H*BBEA (CP811).

The evolution of the 2080 cm^{-1} band surface with the amount of CO introduced in the IR cell allowed to determine the amount of accessible platinum sites (n_{Pt}), as shown on Figure II.9, considering that each CO molecule was only adsorbed on a single metal site (linear structure).

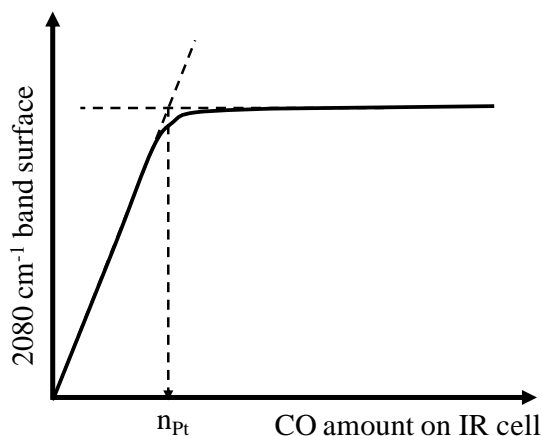


Figure II.9 Accessible platinum sites determination (n_{Pt}) by CO adsorption followed by IR spectroscopy.

Once determined the n_{Pt} amount it was possible to determine the platinum dispersion (D) on the analyzed sample by using the following equation:

$$D = \frac{n_{Pt} \cdot M}{Pt(wt)} 100 \quad \text{Equation II.13}$$

where,

D, platinum dispersion (%);

n_{Pt} , accessible platinum atoms (mol.g^{-1});

M, platinum molar weight (195 g.mol^{-1});

Pt(wt), sample platinum loading (g.g^{-1}).

After the platinum dispersion determination it was possible to estimate the platinum particles size, assuming that these were under a cubic form (typical for platinum particles). Consequently, the platinum particle average size (d) is given by the following equation:

$$d = 5.10^6 \frac{M}{\rho.D.S} \quad \text{Equation II.14}$$

where,

d, platinum particle average size (nm)

M, platinum molar weight (195 g.mol^{-1});

D, platinum dispersion (%);

ρ , platinum metal density (21.45 g.cm^{-3})

S, platinum's metal surface ($\text{cm}^2.\text{mol}^{-1}$)

2.6.4 Zeolite structure bands

The bands are attributed to the vibrations of the T-O (T = Si, Al), which adsorb between 400 and 1300 cm^{-1} . However, these result from the vibration of the whole zeolitic structure and not only a single bond [90]. Some of these bands frequencies have been proven to depend linearly on the amount of framework aluminum. Therefore, they can be used for the determination of zeolite framework Si/Al ratio.

2.6.4.1 Experimental procedure

The zeolite structure bands were measured on a THERMO NICOLET 5700 FTIR spectrometer in a 500 to 1300 cm^{-1} range (resolution: 2 cm^{-1} , 64 analysis per spectrum).

Due to the high absorbance of the zeolitic structure bands, the zeolite ($\approx 2\text{wt.}\%$) was dispersed in potassium bromide (KBr), which did not absorb on the same range. The resulting

powder was pressed ($\approx 7 \text{ ton.cm}^{-2}$) into a self-supported wafer, which was directly analyzed without further treatment.

2.6.4.2 Framework Si/Al ratio

The zeolite framework aluminum content (N_{Al}) was determined by using the following equation found in [247]:

$$N_{Al} = \frac{(1099.1 - \nu)}{3.337} \quad \text{Equation II.15}$$

where,

N_{Al} , framework aluminum content;

ν , wavenumber of the band near 1090 cm^{-1} (Figure II.10).

The framework aluminum content N_{Al} is referent to the *BEA zeolite chemical formula $Al_{N_{Al}}Si_{64-N_{Al}}O_{128}$ [194, 264]. Therefore, the framework Si/Al ratio is given by Equation II.16.

$$Si/Al_{framework} = \frac{(64 - N_{Al})}{N_{Al}} \quad \text{Equation II.16}$$

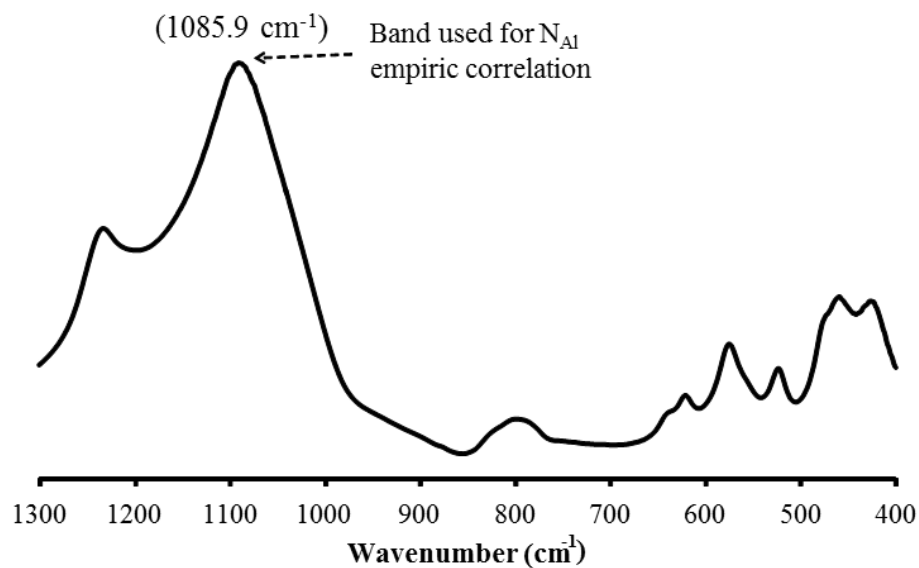


Figure II.10 H*BEA (CP811) structure bands.

3 Catalytic tests – n-alkane hydroisomerization

The following section will describe all the important parameters for the different n-alkane (n-C₁₀, n-C₁₂ and n-C₁₄) hydroisomerizations including the experimental procedure.

3.1 Catalyst shape

The direct use of catalyst under the powder form may lead to various engineering problems. The lack of interspace between the powder particles may cause some pressure problems, and serious threats may rise due to the possibility of the powders to be dragged into the pilot lines. Consequently, the catalyst powders were pressed under a pressure of 6 ton.cm⁻², crushed then sieved to obtain particles between 0.2 – 0.4 mm. The size preserved has already proven to cause no any diffusional limitations [248].

All the catalysts used in our case in all the hydroisomerization reactions, undergo the same procedures prior to any test.

3.2 Chemical Product

The catalytic tests only required the use of each chemical product alone, no need for incorporation of any other product as a solvent. The characteristics of n-decane, n-dodecane and n-tetradecane are reported in Table II.4.

Table II.4 Characteristics of reagents used.

Reagent	Chemical formula	T _F (°C)	T _B (°C)	Density (cm ³ /g)	Supplier	Purity (%)
n-tetradecane	C ₁₄ H ₃₀	5.5	253	0.762	Acros Organics	99.9
n-dodecane	C ₁₂ H ₂₆	-9.6	216	0.75	Fischer	99.9
n-decane	C ₁₀ H ₂₂	-30	174	0.73	Scientific	99.9
					Sigma Aldrich	

3.3 Experimental apparatus

The n-alkanes hydroisomerization reactions were performed in two fixed bed reactors located inside the “Microactivity Effi” apparatus. The Microactivity Effi reactor is probably the

most advanced worldwide modular laboratory system for measurement of catalytic activity and for the study of the yield and kinetics of chemical reactions. It is produced by PID Eng&Tech.

PID Eng&Tech, is a worldwide leading company at sector of Microreactors for Catalytic studies. This instrument has been developed as a standard unit that can be adapted to whatever performance is needed for catalytic testing through different configurations and options.

The Microactivity Effi is a compact reactor that is completely automated. It is equipped with cutting-edge process control technology in the market. This enables the user to program a series of experiments from the computer, even on the network, and obtain real-time results with the highest degree of reproducibility and accuracy.

This equipment has been designed to save time and resources at both, catalyst development stage and factory report process during catalyst screening.

This apparatus (shown in Figure II.11) comprises the following main parts:

- Liquid feed systems.
- Reactors and heating system.
- Automatic six-port valves.
- High pressure Liquid/Gas separators.
- On-line analysis system.
- Independent safety levels separate from PC. User-defined functions for alarms.
- PC with User-friendly software with real time supervision and program recipes Distributed control.

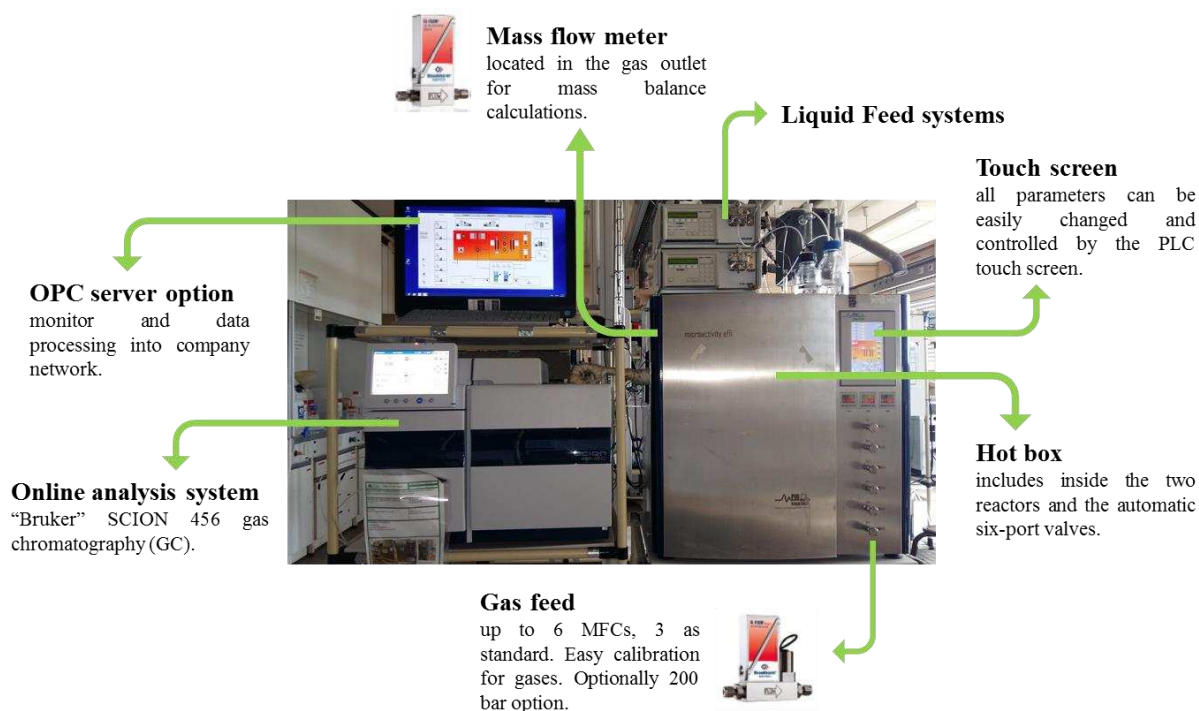


Figure II.11 Different parts of the "Microactivity Effi" apparatus.

3.3.1 Liquid feed systems

There exists up to 2 HPLC pumps (0.02 – 5 ml/min). It consists of heating option up to 90 °C for heavy liquids. In addition to a syringe pump for very low and accurate flow (from 0,01 µL/min).

3.3.2 Reactors and heating systems

Two SS316 tubular reactors, with 9.1 mm. internal diameter, with easy loading of up to 3.3 ml. catalyst. A thermocouple connected inside the oven is placed directly in the catalyst bed (Figure II.12).

The maximum working reactor temperature is up to 1100°C ± 1°C, it depends on the reactor material. In our case being SS316 as standard: 9,1 mm ID x 300 mm length, with a 20 µm porous plate. All the layout inside the hot box made with hot air convector. The maximum temperature held is up to 200°C ±1°C.

The apparatus is also associated with a maximum working pressure up to 100 ± 0.1 bar. Based on micrometric servo-controlled valve design.



Figure II.12 Reactors and heating systems.

3.3.3 Automatic six-port valves

These valves are present for different purposes. It acts as a liquid-gas separator valves, and as an up/down flow selector.

They are also responsible to take the product into the reactor that contains the catalyst, where the reaction takes place at the desired reaction temperature. It can also allow the product to skip the reactor and take them into analysis directly (mainly for blank tests to check for impurities). Figure II.13 below shows the location and external view of the valves.

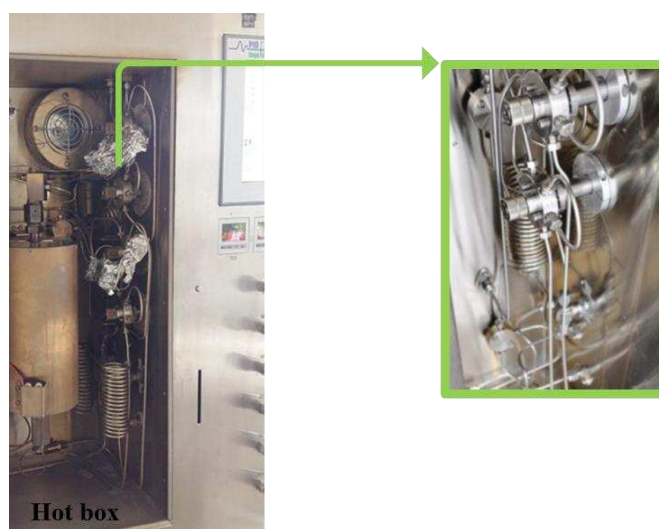


Figure II.13 Automatic six-port valves.

3.3.4 High pressure Liquid/Gas separators

The liquid-gas separator shown in Figure II.14 is associated with a capacitive level sensor that detects very low dead volume (less than 1 ml.). It allows real time results without accumulation. The level controlled valve (LCV) is based on micrometric servo-controlled valve.

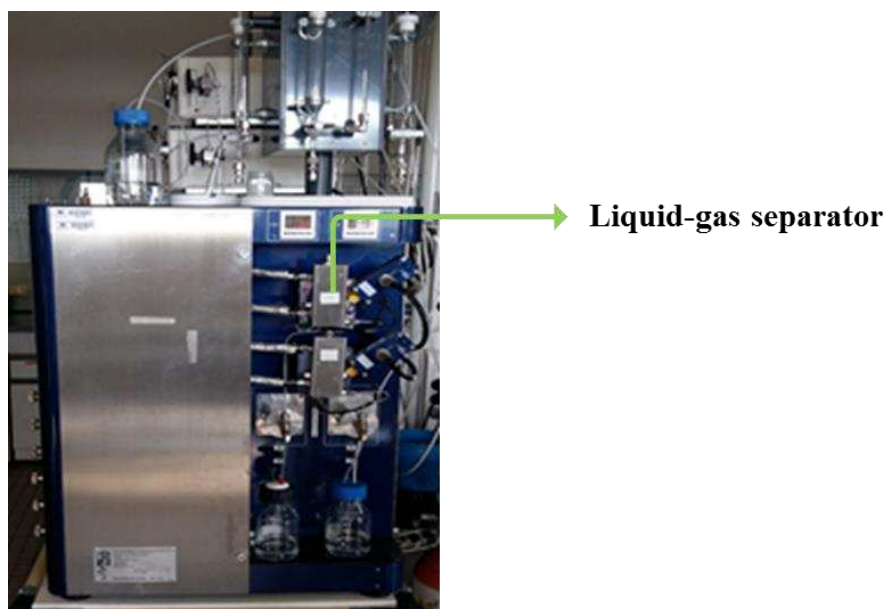


Figure II.14 Liquid-gas separator.

3.3.5 On-line analysis system

The reaction products were analyzed on-line using a “Bruker” SCION 456 gas chromatograph (GC) equipped with a Flame Ionization Detector (FID), placed just left to the “Microactivity effi” apparatus.

3.4 Catalytic test conditions

The transformation of n-alkanes were carried out under the following conditions: temperature = 200-300°C, total pressure = 10 bar, H₂/n-C_x molar ratio = 7 and WHSV (weight hourly space velocity) = 38-95 h⁻¹. In order to obtain different conversion values, the temperature was varied in the range mentioned above in operating conditions, while the flow rate of the reagent (n-alkane) was kept constant during its complete conversion. Before use, the catalysts were reduced in situ under hydrogen flow of 50 ml/min at 450°C according to the following program (Figure II.15):

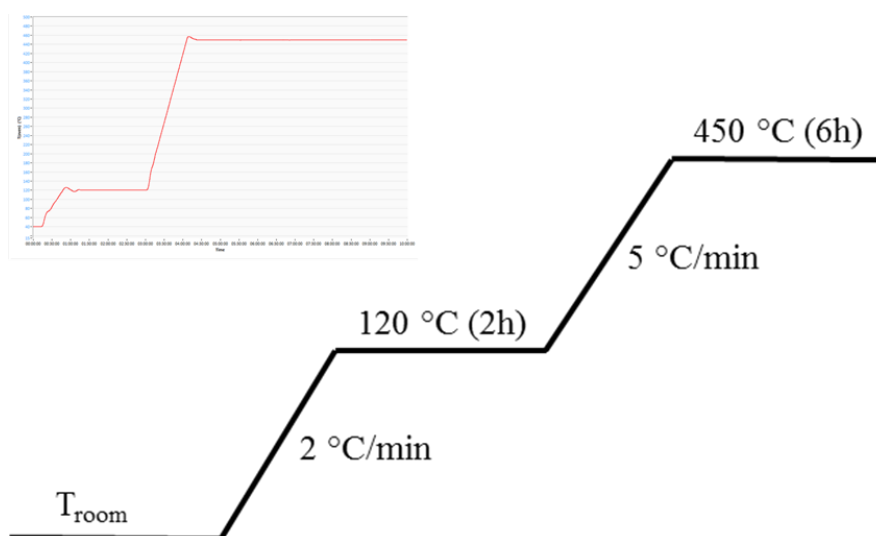


Figure II.15 Catalysts reduction program.

3.5 Reactor Filling

Once the catalyst particles are under the form of 0.2-0.4 mm, every catalyst was mixed with SiC (Carborundum – VWR; 0.25 mm particle size) so as to achieve a total weight of 500 mg. This procedure avoids preferential paths and always ensure the same catalyst bed height. As shown in Figure II.16, this mixture (Catalyst + SiC) was placed at the center of the reactor, between the glass cotton wool. In order to decrease the empty volumes inside the reactor, glass beads were added under and above the catalytic bed as seen in the figure.

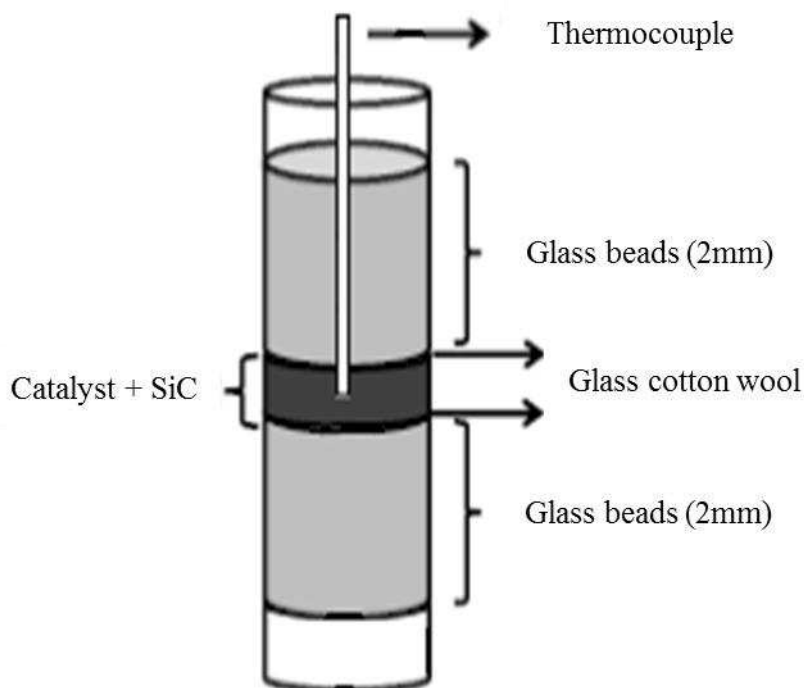


Figure II.16 Schematic view of the charged reactor with 0.2 – 0.4 mm catalyst particles.

3.6 Chromatographic analysis

As said before the reaction products analysis were performed on a “Bruker” SCION 456-GC equipped with an FID. In order to well separate the reaction products, a capillary column with the following characteristics was used:

- Length: 50 m;
- Internal diameter: 0.25 mm;
- Stationary phase: Nonpolar fused silica;
- Film thickness: 0.5 μm .

3.6.1 Analysis conditions

The GC analysis was made under the following conditions:

- Vector gas: Hydrogen;
- Capillary column flow: constant pressure of 10 psi;
- Split ratio: 20;
- Injector temperature: 50 $^{\circ}\text{C}$;
- Detector temperature: 300 $^{\circ}\text{C}$;

➤ Oven temperature program (Figure II.17):

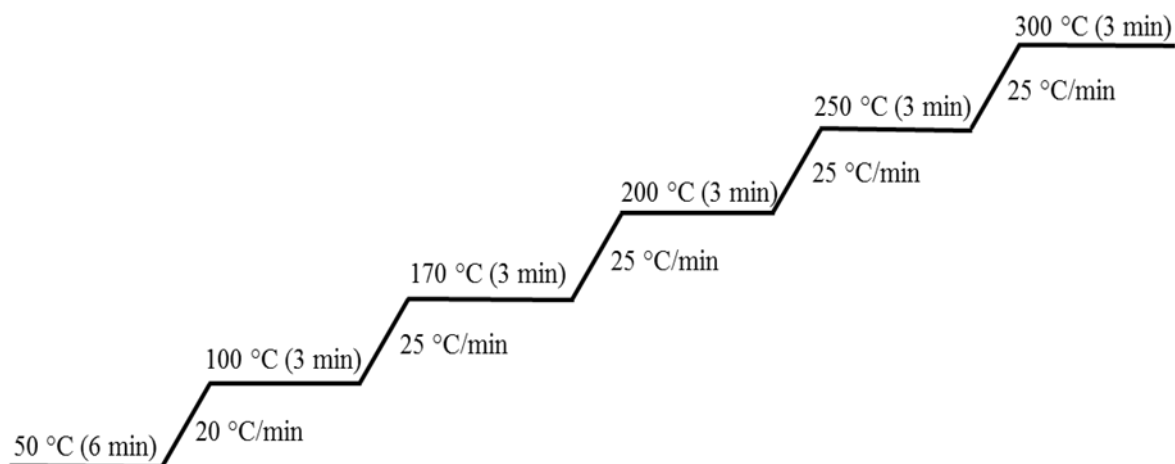


Figure II.17 GC oven temperature program for the three reagents (n-C₁₀, n-C₁₂ and n-C₁₄) transformation products.

3.6.2 Product identification

High amount of products resulting from the n-alkanes hydroisomerization process were produced. The reaction products were separated into three main different groups: Cracking products (C), multibranched isomers products (B) and monobranched isomers products (M). Three examples of chromatograms corresponds to n-C₁₀, n-C₁₂ and n-C₁₄ hydroisomerization products with the identified groups are shown below in Figure II.18.

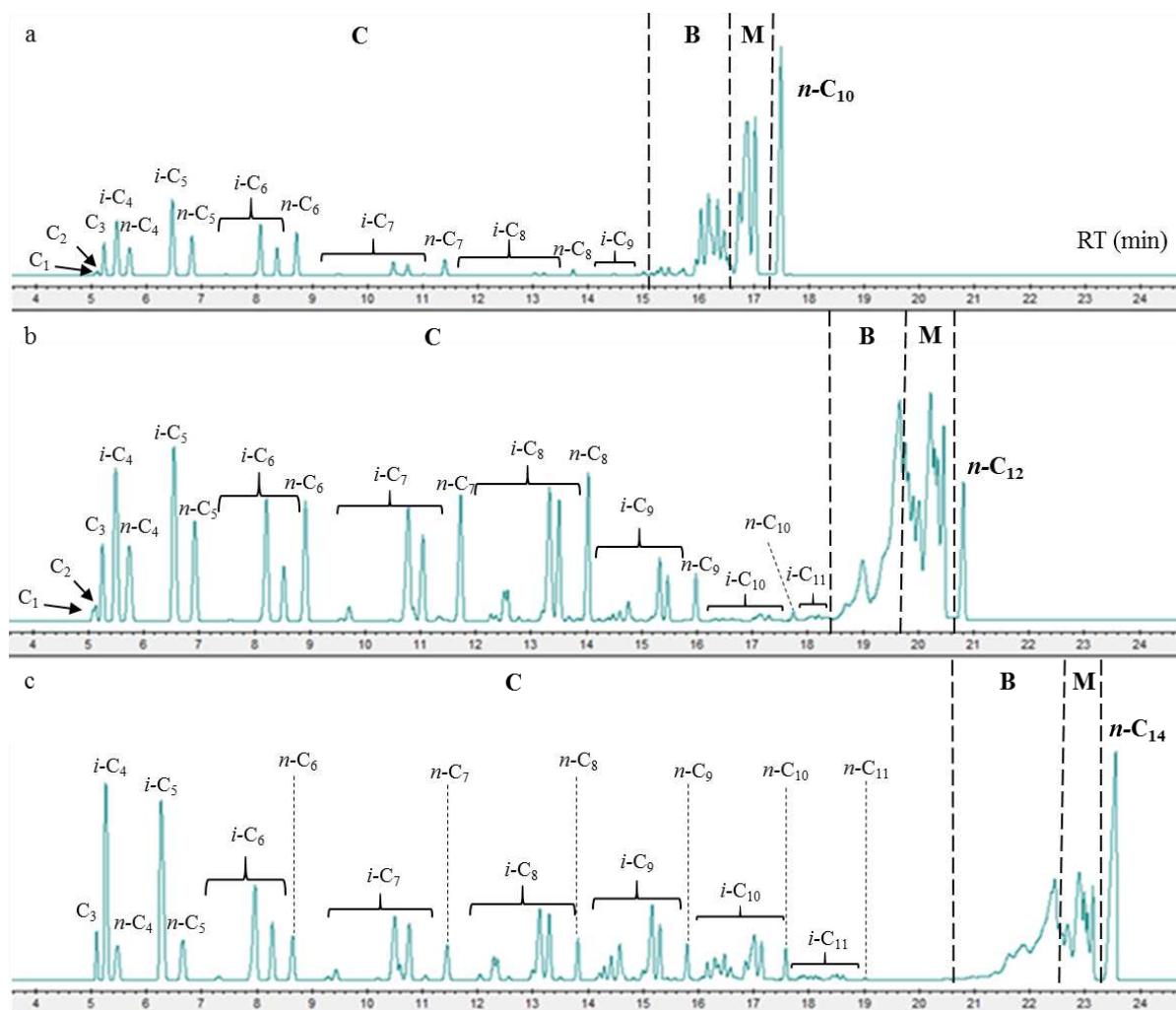


Figure II.18 Chromatogram examples of: a) $n\text{-C}_{10}$, b) $n\text{-C}_{12}$, and c) $n\text{-C}_{14}$ hydroisomerization.

The multi- and monobranching isomers products carry always the same carbon number as was the starting material. The cracking products are a result of cleavage of C-C bond, thus the carbon number is always lower than that of the starting material. In case of $n\text{-C}_{10}$ hydroisomerization, $n\text{-C}_9$ cracking product is not well identified since it may overlap with the multibranching isomers (B). Similarly, in $n\text{-C}_{12}$ and $n\text{-C}_{14}$ hydroisomerizations, $n\text{-C}_{11}$ and $n\text{-C}_{13}$, respectively, are also not well identified. However, in the example given on $n\text{-C}_{14}$, C_1 and C_2 cracking products, as well as their corresponding complementary C_{12} and C_{13} cracking products respectively, show no peaks, a sign of absence of hydrogenolysis side reactions. This aspect may also be observed in case of $n\text{-C}_{10}$ and $n\text{-C}_{12}$ hydroconversions, where C_1 and C_2 products, and their corresponding complementary cracking products may not appear due to the same reason.

3.6.3 Chromatogram results exploitation

The data resulting from the n-alkane hydroisomerization chromatograms allowed determining the following parameters: n-alkane conversion; catalyst activity; Turn-Over-Frequency (TOF); and products mass and molar yield.

3.6.3.1 n-Hexadecane conversion (x)

The n-alkane conversion (x) defined by the ratio between the amount of reactant before and after reaction, is given by the following equation:

$$x = \left(1 - \frac{a_{nC_x}}{\sum_i a_i}\right) * 100 \quad \text{Equation II.17}$$

Where,

x, n-alkane conversion (%);

a_{nC_x} , n-alkane (nC_x) peak area;

a_i , all the peaks areas.

3.6.3.2 Catalyst activity (a)

The equation below allows the calculation of the catalyst activity:

$$a = \frac{D_{nC_x}}{m} * \frac{x}{100} \quad \text{Equation II.18}$$

Where,

a, catalyst activity ($g_{nC_x} \cdot g_{cat}^{-1} \cdot h^{-1}$);

D_{nC_x} , n-alkane liquid flow (g/h);

m, catalyst weight (g);

x, n-alkane conversion (%).

3.6.3.3 Turn-Over-Frequency (TOF)

The TOF represents the activity per Brønsted acid site and is given by the following equation:

$$TOF = \frac{a}{M * n_{H^+}} \quad \text{Equation II.19}$$

Where,

TOF, Turn-Over-Frequency – activity per Brønsted acid site (h^{-1});

a, catalyst activity ($\text{g}_{\text{nCx}} \cdot \text{g}_{\text{cat}}^{-1} \cdot \text{h}^{-1}$);

M, n-alkane molar weight ($\text{g} \cdot \text{mol}^{-1}$);

n_{H^+} , catalyst Brønsted acid site density ($\text{mol} \cdot \text{g}_{\text{cat}}^{-1}$), determined by pyridine adsorption followed by IR at 150°C (see section 2.6.2 of this chapter).

3.6.3.4 Products mass and molar yield (Y)

The mass yield of a certain product or products group (mainly monobranched, multibranched and cracking products), is given by the following equation:

$$Y_i = \frac{\sum_j a_j}{\sum_i a_i} * 100 \quad \text{Equation II.20}$$

Where,

Y_i , product or group of products mass yield (wt.%);

a_j , product or group of products peak area;

a_i , all the peaks areas.

On the other hand, the products molar yield was determined taking into consideration that the FID signal intensity was proportional both to the amount and the carbon number of the detected molecule, and was given by the following equation:

$$Y_i = \frac{\sum_j \frac{a_j}{c_j}}{\sum_i \frac{a_i}{c_i}} * 100 \quad \text{Equation II.21}$$

Where,

Y_i , product or group of products molar yield (mol%);

a_j , product or group of products peak area;

a_i , all the peaks areas;

c_i , c_j , molecule carbon number.

4 Catalytic tests – n-hexane cracking

The cracking of n-hexane is a reaction which requires high acidity (activation energy E). It is used as a model reaction to characterize the acidity of zeolites.

4.1 Operating conditions

The catalytic tests were carried out in an assembly consisting of a quartz reactor with fixed bed with a descending flow placed in a three-zone furnace. The temperature of the bed is checked by a thermocouple (Chrome-Nickel) placed at the same height where the catalyst is present. The upper part of the reactor is provided with a coil, which makes it possible to prolong the residence time of the reactant in the furnace, thus ensuring its vaporization before reaching the catalytic bed. As for the lower part, it is linked to an automatic storage valve (10 loops) and a 6-way electric valve which allows their injection in chromatography.

Before each test, the materials are pretreated in situ under N₂ at 540 °C overnight. The n-hexane (Sigma Aldrich > 99% purity) is then injected with a Metrohm 725 Dosimat infuser after dilution in dinitrogen. The standard operating conditions are shown in Table II.5 below.

Table II.5 Operating condition of n-hexane cracking.

n-hexane transformation	
Reaction temperature (°C)	540
Pressure (bar)	1
Contact time (g.mol.h⁻¹)	1.3
N₂/n-C₆ (molar ratio)	9

The reaction products are injected manually into a "VARIAN 450" gas chromatography equipped with a capillary column (Al₂O₃/KCl: 50 m, diam. = 320 μm) and a FID flame ionization detector. The temperature program of the furnace of the column and the conditions of analysis (detector and injector) are presented in the following diagram:

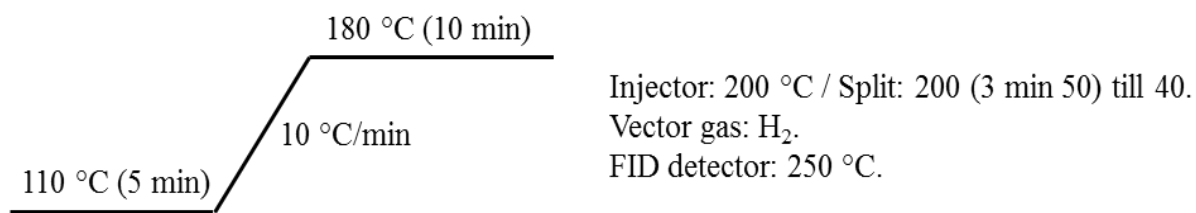


Figure II.19 Oven temperature program and analysis conditions of the GC.

4.2 Pilot plant flowsheet

All the reactor outlet lines, as well as the storage and injection valves, are heated to about 200 °C in order to avoid condensation of the products. The overall layout of the assembly is shown in the diagram below (Figure II.20):

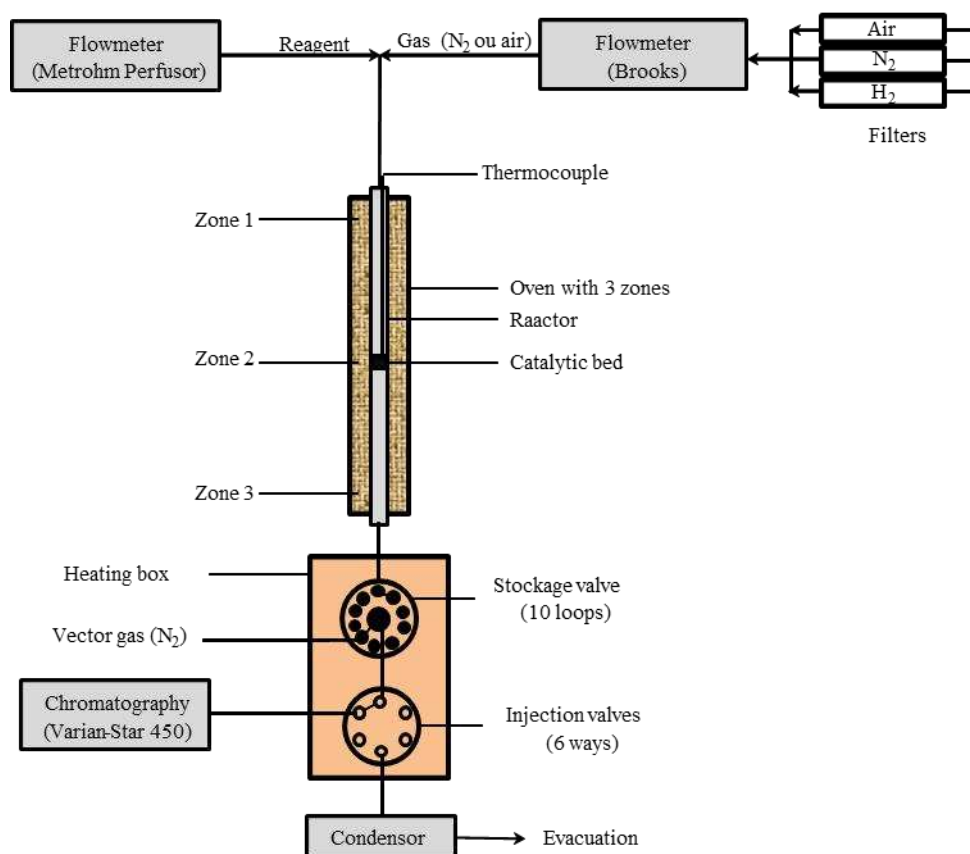


Figure II.20 Pilot plant flowsheet.

4.3 Results exploitation

The n-hexane cracking chromatograms allowed determining the following parameters: n-hexane conversion; catalyst activity; Turn-Over-Frequency (TOF); and products mass and molar yield. One example of these chromatograms is present in Figure II.21.

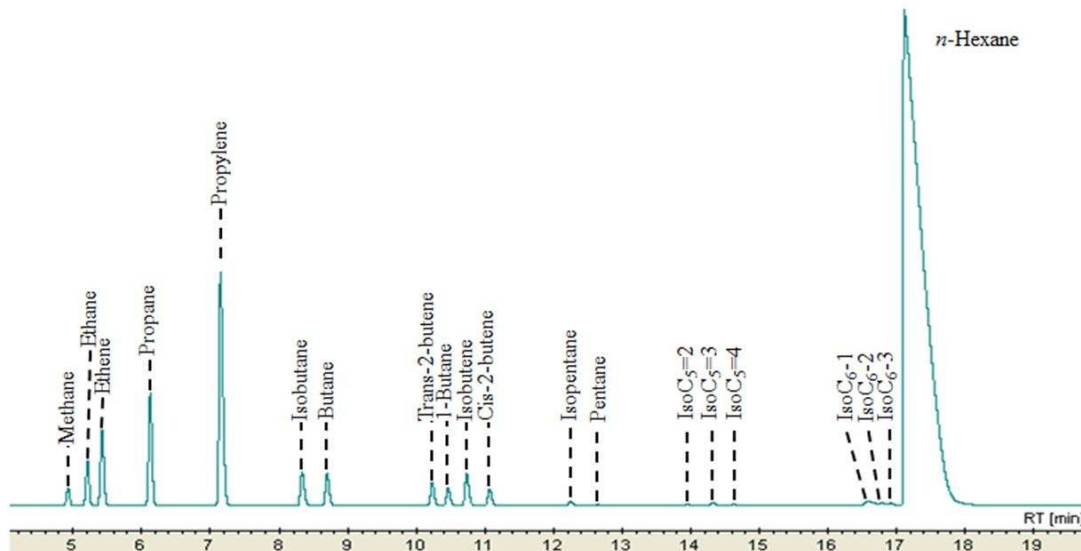


Figure II.21 n-Hexane cracking chromatogram example.

4.3.1 n-Hexane conversion (x)

The conversion (x) of n-hexane defined by the ratio between the amount of reactant before and after reaction, is given by the following equation:

$$x = \left(1 - \frac{a_{nC_x}}{\sum_i a_i}\right) * 100 \quad \text{Equation II.22}$$

Where,

x, n-hexane conversion (%);

a_{nC_x} , n-hexane (nC_x) peak area;

a_i , all the peaks areas.

4.3.2 Catalyst activity (a)

The equation below allows the calculation of the catalyst activity:

$$a = \frac{D_{nC_x}}{m} * \frac{x}{100} \quad \text{Equation II.23}$$

Where,

a, catalyst activity ($\text{mol.g}_{\text{cat}}^{-1}.\text{h}^{-1}$);

D_{nCx} , n-hexane liquid flow (mol/h);

m, catalyst weight (g);

x, n-hexane conversion (%).

4.3.3 Turn-Over-Frequency (TOF)

The TOF represents the activity per Brønsted acid site and is given by the following equation:

$$TOF = \frac{a}{n_{H^+}} \times 1000000 \quad \text{Equation II.24}$$

Where,

TOF, Turn-Over-Frequency – activity per Brønsted acid site (h^{-1});

a, catalyst activity ($\text{mol.g}_{\text{cat}}^{-1}.\text{h}^{-1}$);

n_{H^+} , catalyst Brønsted acid site density ($\text{mol.g}_{\text{cat}}^{-1}$), determined by pyridine adsorption followed by IR at 150°C.

4.3.4 Products mass and molar yield (Y)

The mass yield of a certain product is given by the following equation:

$$Y_i = \frac{a_j}{\sum_i a_i} * 100 \quad \text{Equation II.25}$$

Where,

Y_i , product mass yield (wt.%);

a_j , product peak area;

a_i , all the peaks areas.

The molar yield is calculated using the following relation:

$$Y_i = \frac{n_i}{\sum n_j} * 100 \quad \text{Equation II.26}$$

Where,

Y_i , product molar yield (mol %);

a_j , product molar weight given by: $n = a_j / M$, with M molar mass of the product;

n_j , summation of molar weights of all products.

Chapter III

Desilication of *BEA zeolites using different alkaline treatments: Impact on catalytic cracking of *n*-hexane

1 Introduction

The promising properties of hierarchical zeolites, as known materials to be combining the microporous network with an auxiliary mesoporous one, have issued great effort to improve the catalytic performance of these zeolite [249–252], as it was shown to induce better diffusion, exhibit higher activity, selectivity and lifetime [253–256]. Researchers have tried to industrialize these zeolites through destructive approaches, i.e. post-synthesis procedures, to enhance their catalytic performance, especially those associated with diffusional limitations [56,162,163,165,214]. However, in particular with *BEA zeolites, post-synthesis treatments were applied on both types of porous structure: i) purely microporous *BEA zeolites to introduce mesoporosity [56,162,165,257], and on ii) *BEA zeolites comprising micro- and mesoporous network with the attempt to increase their mesoporous content [163,164,214,258].

Desilication by alkaline treatment is one of the most widely applied methods recently to induce mesoporosity, taking into account its simplicity and efficiency [196,259–261]. It is a controlled silicon extraction from the zeolite framework in alkaline aqueous solution [162]. Desilication applied in presence of NaOH is the classical way of desilication. Nonetheless, it leads to dissolution of both Al and Si species, but, however, the removed Al species realuminate on the external surface of the zeolite, thus lowering the final material Si/Al ratio [258]. The organic structural agents (pore directing agents) like tetraalkylammonium based organic compounds, were known to be promising variants to the classical treatment, as the intrinsic properties of the zeolite are way better preserved, e.g. microporosity and crystallinity [195–197]. This definitely seems to rely on the affinity of these compounds to the zeolite surface [262], and how they can direct the attack of HO⁻ anions. However, the utilization of the desilication approach for introducing or increasing mesoporosity to *BEA zeolites structures, had shown to have a positive impact on their activity and selectivity, i.e. their catalytic performance [56,162–165,214].

The catalytic cracking of n-hexane is one of the most important routes that focuses on the production of light olefins (ethylene, propylene and butene), which are used as significant raw materials in the chemical industry like production of polymers and alkyl benzenes [263–265]. Due to their properties as intrinsic acidity, variety of frameworks and managed pore structures, acidic zeolites are the most catalysts used broadly in the catalytic cracking of n-hexane, with HZSM-5, H-Beta and HY zeolites the most extensive studied catalysts for this reaction [266–

269]. However, due to the presence of narrow intracrystalline micropores, molecules suffer some diffusional limitations within the channels of such zeolites, highly affecting the catalysts activity, selectivity and lifetime [270–273]. Altering the porosity system of these microporous zeolites is one of the strategies followed to recover back their activity and selectivity in the desired reaction. The generation of mesopores hereafter by subjecting the zeolites to alkaline treatments for example, results in the formation of the hierarchical zeolites that can provoke facile access to the active sites and reduces catalyst deactivation.

The objective in this work is to study the impact of desilication of already hierarchical nanocrystal *BEA zeolites and a synthesized microcrystal *BEA zeolite (purely microporous), on the structural, elemental, textural and acidic properties of these zeolites. It is also meant to study if the increased mesoporous content (in the hierarchical series) or the introduced mesopores (in the microcrystal series) would account to any improve in the catalytic activity and selectivity of the catalysts in the catalytic cracking of n-hexane.

2 Catalysts characterizations

It is meant to investigate the impact of desilication on the zeolites' different characteristics as a function of total concentration of HO^- anions, sourced either by NaOH alone, or by the company of NaOH and TBAOH when used together. When the treatment is composed of NaOH and TPABr, it is only the HO^- anions sourced by NaOH that are measured. In figure 1, different colors are present. The black color refers to the samples of series 1, the red color to the samples of series 2, and the green to the samples of series 3. The white filled points are the samples desilicated by NaOH, the shaded ones are the samples desilicated with NaOH and TPABr, and the filled ones are the samples desilicated by NaOH and TBAOH. All the previous specification are presented as follows:

- ▲ Series 1 zeolites (\triangle by NaOH, \blacktriangle by NaOH+TPABr);
- Series 2 zeolites (\circ by NaOH, \bullet by NaOH+TBAOH);
- Series 3 zeolites (\square by NaOH, \blacksquare by NaOH+TBAOH, \boxtimes by NaOH+TPABr).

2.1 Mass yields and crystallinity

The percentage yield of the different samples was calculated by dividing the final mass after desilication treatment, to the initial mass of the corresponding parent zeolite before treatment, multiplied by 100.

Figure III.1-a shows the general decrease of the yield with HO^- increase for all the desilicated samples, an observation that resembles that obtained with Verboekend et al. [274]. Verboekend reported that high Si/Al zeolites (MFI in their case) showed more pronounced reduction in yield even at lower concentrations of HO^- , but as for lower Si/Al zeolites, it was seen that higher concentrations were required to dissolve the Si species and induce intracrystalline mesopores. In our case, the case of *BEA zeolites, starting from 0.2M of total concentration of HO^- anions was enough to cause a loss of around 35% of the starting material (% yields are reported in Table III.1). Nonetheless, in the microcrystal *BEA series, the Si/Al ratio was higher than that in the nanocrystals (series 1 & 2), but still at low concentrations (0.13M of HO^-), the loss of material was more pronounced (to ca. 50% of starting material), due to more dissolved Si species of higher Si/Al series (series 3).

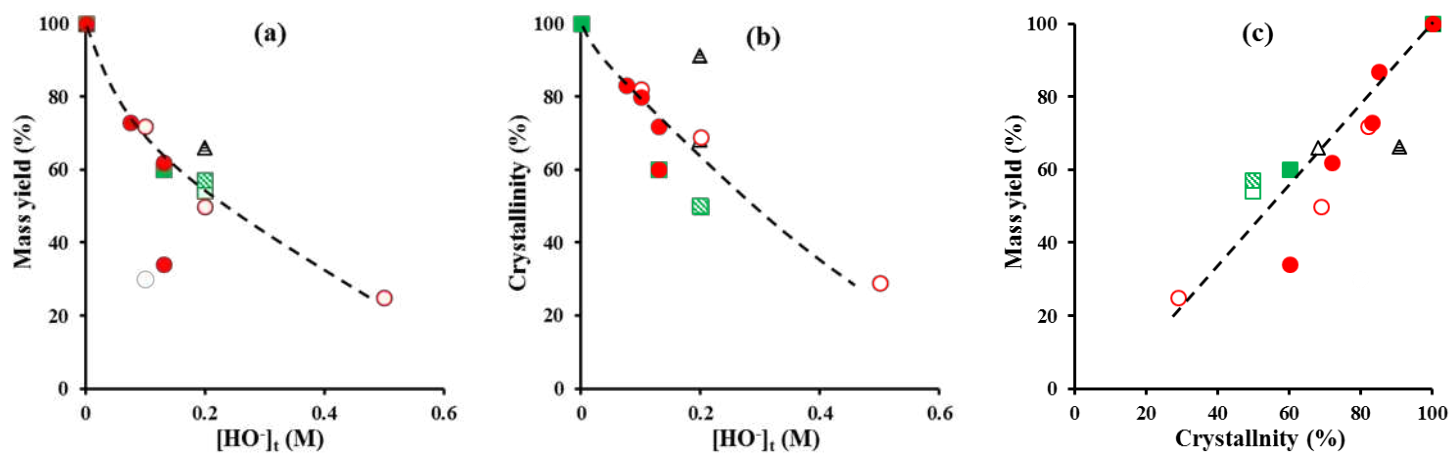


Figure III.1 Variation of (a) mass yield and (b) crystallinity vs. total concentration of hydroxyl anions, and of (c) mass yield vs. crystallinity.

The diffractograms shown in Figure III.2, show also the preservation of the characteristics of *BEA zeolite structure, no matter what the series is. Note that only the diffractograms referring to the catalysts used in the catalytic tests are shown in the related figure.

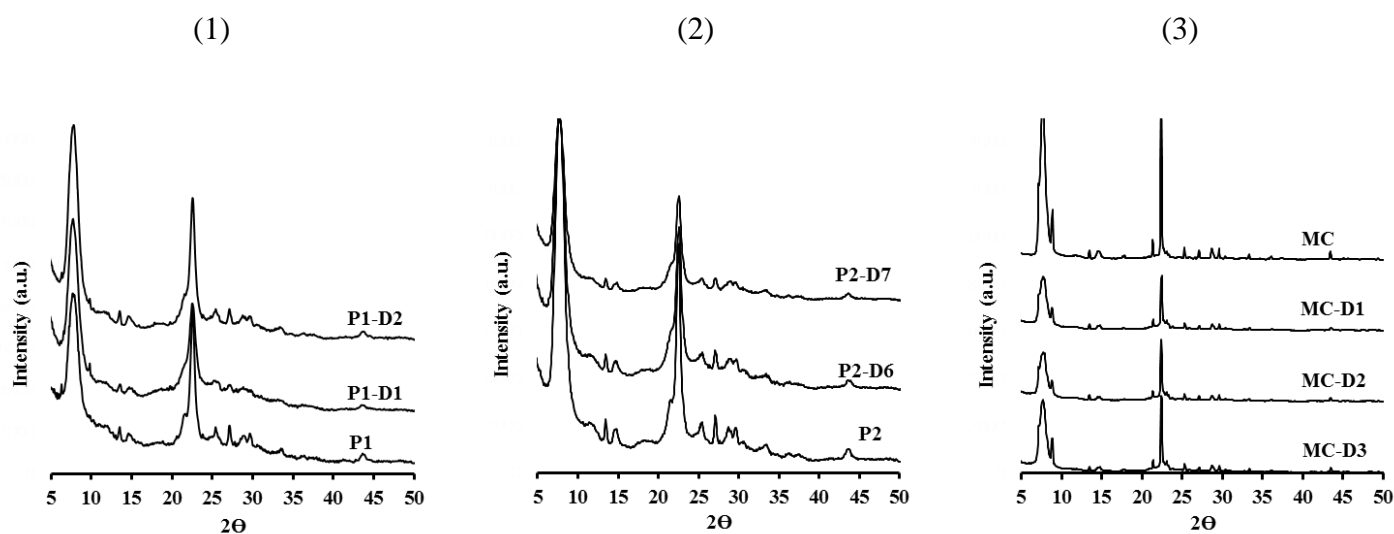


Figure III.2 XRD diffractograms of the selected zeolites of series: (1-3).

Table III.1 records the % of crystallinity of the desilicated samples in comparison with their parent material (considering the parent zeolite 100% crystalline) that are represented also as a function of $[\text{HO}^-]$, in Figure III.1-b. The percentage of crystallinity was calculated by determining the area under the X-ray pattern of the desilicated sample, then dividing it by that of the parent's material, multiplying finally by 100.

Table III.1 Mass yield and relative crystallinity of all the zeolites of series: (1-3)

Sample	Mass Yield (%)	% Crystallinity
P1	100	100
P1-D1	66	68
P1-D2	66	91
P2	100	100
P2-D1	72	82
P2-D2	50	69
P2-D3	25	29
P2-D4	73	83
P2-D5	-	80

P2-D6	62	72
P2-D7	34	60
MC	100	100
MC-D1	54	50
MC-D2	57	50
MC-D3	60	60

Figure III.1-b shows that a general decrease in the crystallinity was also observed as $[\text{HO}^-]_t$ increased. The % crystallinity of P1-D1 (68%) desilicated by NaOH alone, in comparison with their parent zeolite, seems to be recovered after the company with the tetrapropylammonium ions (TPA^+) sourced by the TPABr pore directing agent, as seen in P1-D2 (91%). This signifies the protective effect of the TPA^+ ions to the zeolite surface provided by the adhesion affinity characteristic [275,276]. The loss to ca. 30% of crystallinity due to NaOH treatment as shown with P1-D1 has already been reported [208,216], where it was assumed that NaOH leads to partial amorphization of the zeolite's structure.

In series 2 zeolites, P2-D1, P2-D2 and P2-D3 zeolites, seem to have a clear crystallinity decrease with $[\text{HO}^-]_t$ as shown in Table III.1. However, the TBA^+ ions in the other samples of this series seem not to have a clear effect on the protection to the zeolite's surface, due to the low concentrations used, e.g. P2-D4, P2-D5. Nonetheless, amongst these two zeolites, it is shown that the crystallinity is decreasing with $[\text{HO}^-]_t$, as the very low molar ratio of TBAOH was also decreasing, leading to a lower protection. Amongst this series, comparing P2-D4 and P2-D5 with P2-D1, the total concentrations of HO^- anions in the formers are slightly lower than P2-D1, and though the crystallinity, signifying that the action of TBA^+ ions here is somehow neglected due to their low concentration as shown in (Table II.1). As the $[\text{HO}^-]_t$ increased in case P2-D6 and P2-D7, the crystallinity decreased more, noting that decreasing also the molar ratio of TBAOH in P2-D7, leads to more loss in crystallinity, signifying also the protective effect of the TBA^+ ions as that of TPA^+ ions.

Series 3 zeolites, the microcrystal *BEA series, is more reactive with the attack of hydroxide anions, owing to the high Si/Al ratio in this series, which highlights on the lacked zeolite's self-protection offered by the neighboring Al atoms [277]. The influence of aluminum

species on the structure stability after desilication have been discussed in literature [277]. It is accepted that the Al atoms in the AlO_4^- tetrahedral protect the neighboring Si atoms just near them against the attack of HO^- anions. The lack of Al effect is seen by the more loss of crystallinity to around 50%, where Si atoms are more prone to extraction in the case of high Si/Al zeolites [162]. However, in case of MC-D3, the crystallinity increases again to 60%, thanks to the lower $[\text{HO}^-]$ used in this treatment. A linear relation in

Figure III.1-c arises between the percentage yield and percentage crystallinity indicating the direct proportionality between the structural destruction and the loss of the material.

2.2 Crystals size of the zeolites

To study more the effect of the pore directing agents, the TEM images in Figure III.3 allowed the estimation of the crystallites size reported in Table III.2 by counting around 200 particles for the investigated zeolites (except for MC that was estimated by Scherrer method), as we have reported that in our work [278].

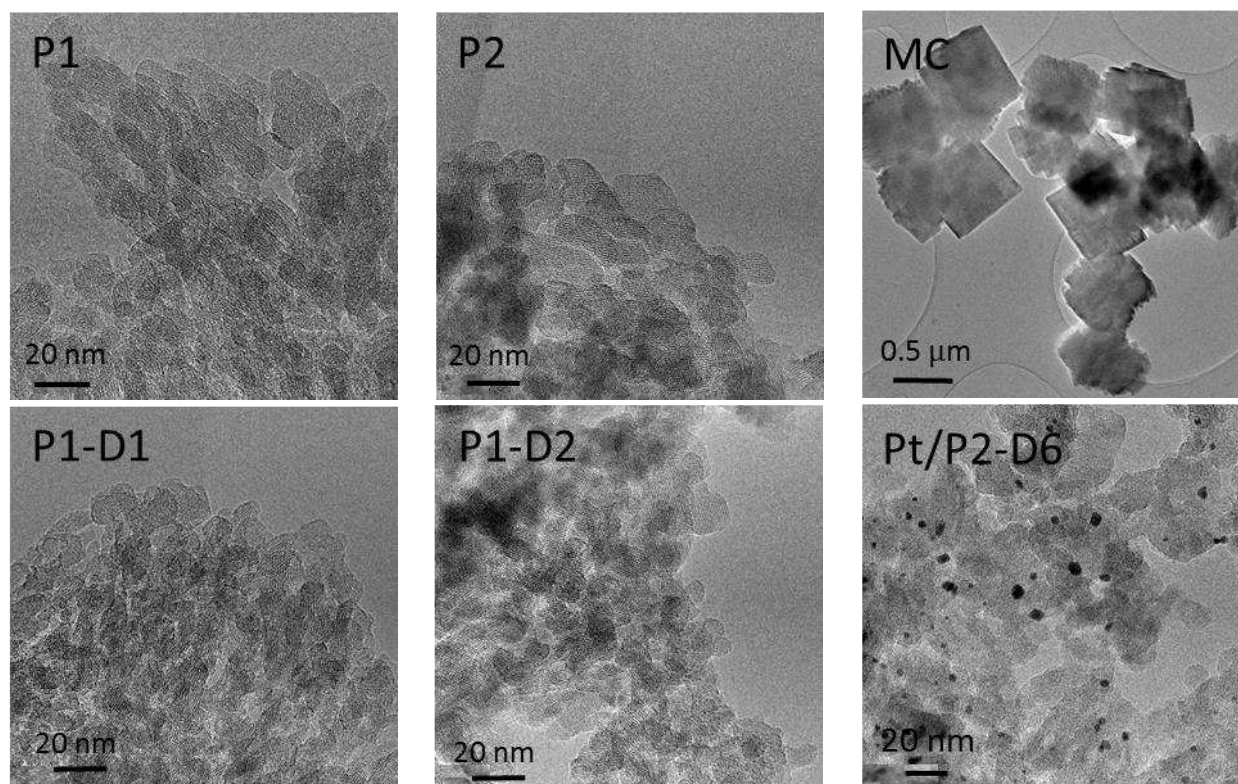


Figure III.3 TEM microphotographs of P1, P2, MC, P1-D1, and P1-D2 zeolites, and Pt/P2-D6 catalyst.

Table III.2 Crystallite average size of some selected zeolites.

Zeolites	Crystal size (nm)
P1	20
P1-D1	13.5
P1-D2	14.9
P2	20
P2-D6	19.6
MC	780
MC-D1	-
MC-D2	-
MC-D3	-

The TEM images revealed that the average crystal size of P1 and P2 zeolites was ca. 20 nm (Table III.2). More TEM images are provided in the annex of this thesis. This was also reflected by the bar graphs of the crystal size distributions (Figure III.4), where it shows that there is domination in the 17.5-20 nm range. The desilication of P1 by NaOH alone (P1-D1), leads to a decrease of the crystal size to ca. 13.5 nm, by NaOH and TPABr to 14.9 nm (P1-D2), which was also reflected in the bar graphs where there is a domination in the 10-15 nm range in P1-D1, and in 12.5-15 nm range in P1-D2 (Figure III.4). The decrease in nanocrystal size in P1-D1 is suggested to be referred to the attack of the HO⁻ anions along the surface of the zeolite. This aspect was also revealed in P1-D2 but in a lower extent, which could be attributed to the adhesive characteristics of TPA⁺ cations as said above. However, as reported by Verboekend et al. [262], such cations are partially dispersed in the solution, and as a result they are not completely adhered to the zeolite surface. This permits the attack of HO⁻ anions to be partially oriented along the crystallite surface and partially through the bulk of the zeolite.

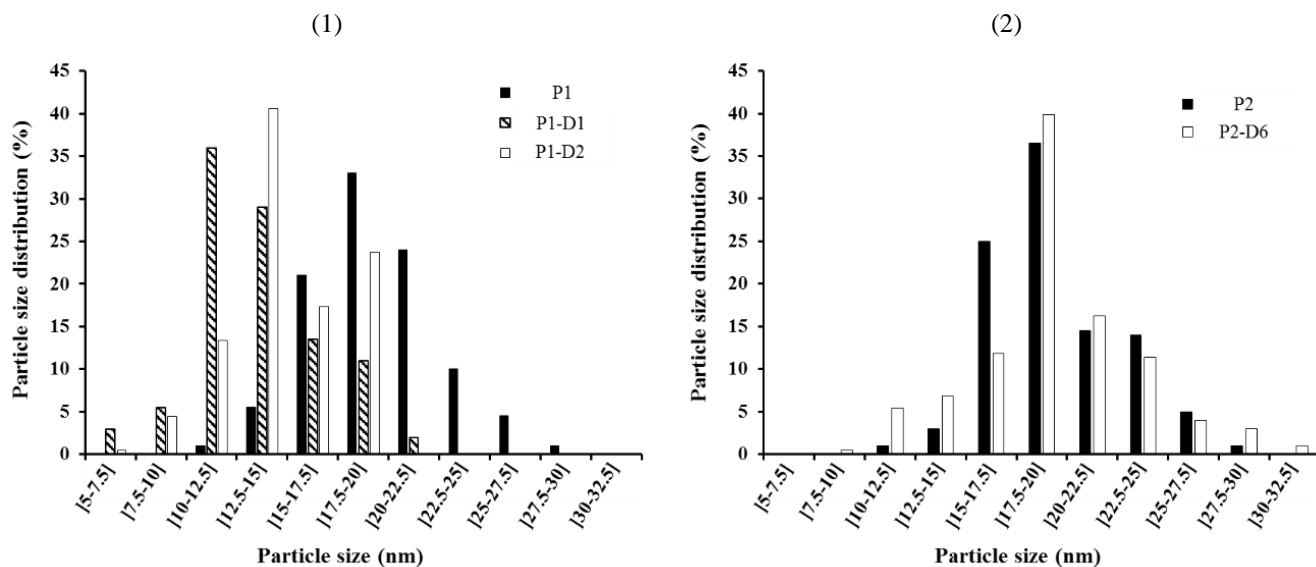


Figure III.4 Crystallites size distributions of the zeolite of series (1) and two zeolites of series (2).

In the other hand, no clear decrease in the crystal size in P2-D6 (19.6 nm), as reflected also by the dominating range of the crystal size distribution between 17.5-20 nm, which may be attributed to the probable stronger affinity of the TBA^+ cations to the zeolite's surface [262]. Note that the TEM image provided for P2-D6 zeolite is for its corresponding catalysts impregnated by Pt that was studied in the hydroisomerization reactions of this research (chapters IV and V).

From Scherrer equation and with the aid of the diffractogram related to MC, the crystal size of this synthesized zeolite was estimated to be 760 nm (Table III.2), as also revealed in the TEM image (700-800 nm) of MC. After desilicating MC by NaOH alone, the crystal seems to be deformed losing by that the initial shape of the crystal as shown for MC-D1 (Figure III.5), which is attributed to the attack of the HO^- anions starting from the surface of the crystal. However, the company of the pore directing agents seem to preserve way more the initial form of the parent's crystal as in MC-D2 and MC-D3 (fig. 2), due to the protection of the crystal's surface by the action of the pore directing agents, followed by the attack of the HO^- anions through the bulk of the crystal.

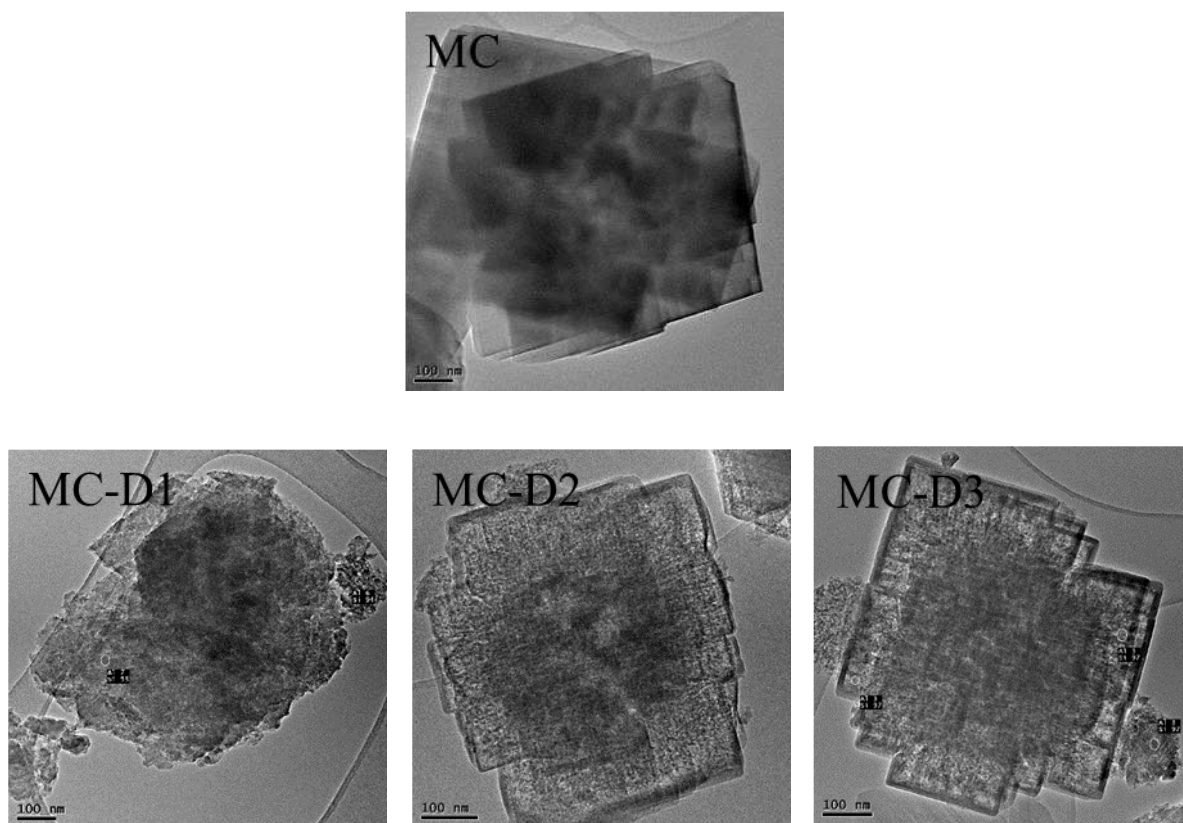


Figure III.5 TEM images of parent and desilicated zeolites of the microcrystal series (S3) at 100 nm scale.

2.3 Elemental composition

Table III.3 shows the total Si/Al ratios of the zeolites and those of the framework composition.

Table III.3 Elemental composition of the zeolites.

Sample	Si/Al _{total}	Si/Al _{fw}
P1	12.0	15.0
P1-D1	7.6	32.9
P1-D2	9.0	26.4
P2	11.8	20.0
P2-D1	9.8	18.4
P2-D2	7.7	10.5
P2-D3	7.2	7.2

P2-D4	9.7	15.6
P2-D5	-	15.5
P2-D6	8.6	18.0
P2-D7	8.4	23.5
MC	35.0	23.0*
MC-D1	26.8	16.4
MC-D2	28.9	14.5
MC-D3	29.1	16.2

* Same synthesis protocol used by Astafan et al. [142].

The total Si/Al ratio was seen to decrease in all the desilicated samples, in agreement with the concept of desilication [56,162,163,262,279]. Again, as seen in series 1 zeolites, NaOH alone caused more drop in the total Si/Al ratio (7.6) than that obtained after treatment with TPABr (Si/Al = 8.9), a significance of the protection influence provided by the TPA⁺ ions right here. In series 2 zeolites, upon desilication by NaOH alone (i.e. P2-D1, P2-D2 and P2-D3 zeolites), the Si/Al ratio was seen to be more reduced continuously with [HO⁻] increase. However, the addition of TBAOH as shown for zeolites P2-D6, P2-D7, afforded an additional protection to the structure, where the TBAOH played a similar role as that for TPABr, and caused less drop in the ratio (from 11.8 in P2 to 8.6 and 8.4 in P2-D6 and P2-D7). Less extensive desilication of the parent *BEA zeolites in presence of the quaternary ammonium ions (TPA⁺ and TBA⁺ ions) is assigned the protective influence of these ions of the zeolite structure. Such observations were seen in literature when organic pore directing agents were used and compared with inorganic alkaline bases as NaOH [162,280]. Note that the total Si/Al ratio decreased in P2-D4 similarly as in P2-D1, where the [HO⁻]_t were very slightly different, with as said before, the interference of TBA⁺ ions is not too much effective due to low concentration. In the microcrystal series, the same manner of silicon extraction was observed, where it was more pronounced in presence of NaOH (Si/Al ratio dropped from 35 to 26.8) as in MC-D1, and less pronounced in presence of the quaternary ammonium ions directing agents (Si/Al ratio dropped from 35 to ca. 29), as in MC-D2 and MC-D3. The drop in the framework Si/Al ratio in this series (from 23 to almost around 15), reveals also the high drop in crystallinity amongst this series. This confirms again the easy extraction of Si species in the higher total Si/Al zeolite due to the lack of the Al atoms that provide structural protection.

2.4 Textural properties

Figure III.6 shows the nitrogen adsorption isotherms of the zeolites investigated in the catalytic cracking of n-hexane only. From these isotherms, we were able to calculate the micro- and mesopore volumes of the different zeolites, as well as the external and specific surface areas, as reported in Table III.4

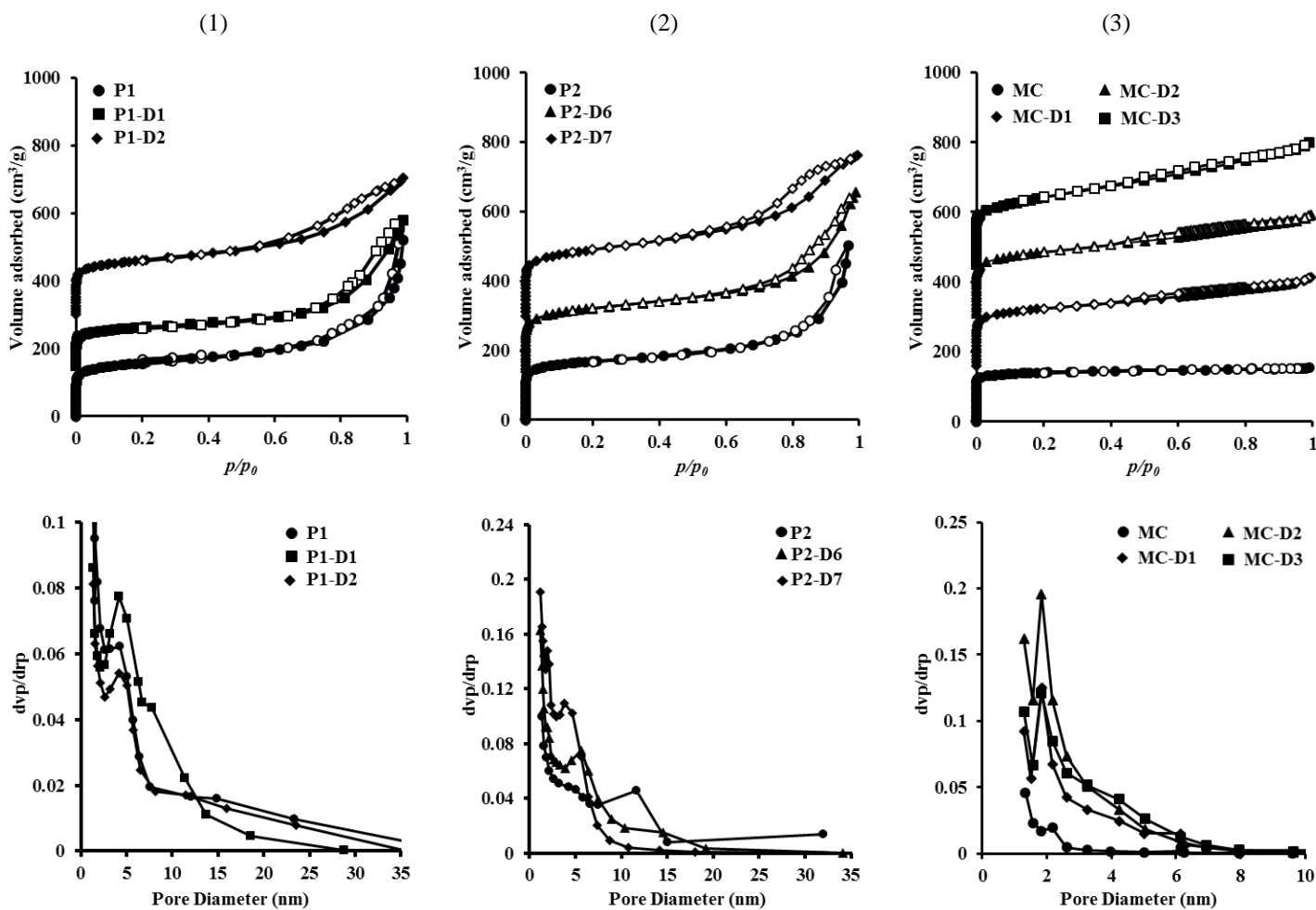


Figure III.6 Nitrogen sorption isotherms and there corresponding BJH curves of the selected zeolites of series: (1-3). The isotherms are shifted by $150 \text{ cm}^3/\text{g}$.

Figure III.7-a displays the relative micropore volumes of the desilicated samples with respect to their parent ones, as a function of total concentration of HO^- anions. A clear decreasing trend was observed with $[\text{HO}^-]_t$ except in P1-D2 which reflects the clear preservation of microporosity due to the presence of TPA^+ cations [164]. P1-D1 showed a reduction in the micropore volume from 0.22 to $0.16 \text{ cm}^3/\text{g}$, which is consistent with the higher degree of

amorphization (loss of crystallinity) of the zeolite structure after desilication [163,214,257,280].

Table III.4 Textural properties of the parent and desilicated zeolites.

Sample	V_{micro} (cm³/g)	V_{meso} (cm³/g)	S_{BET} (cm²/g)	S_{ext} (cm²/g)
P1	0.22	0.58	577	254
P1-D1	0.16	0.50	401	156
P1-D2	0.22	0.44	576	297
P2	0.20	0.54	605	176
P2-D1	0.19	1.03	592	206
P2-D2	0.16	1.14	639	309
P2-D3	0.08	0.97	415	238
P2-D4	-	-	-	-
P2-D5	0.19	0.62	611	216
P2-D6	0.18	0.61	572	208
P2-D7	0.16	0.55	635	300
MC	0.21	0.02	502	125
MC-D1	0.15	0.25	574	274
MC-D2	0.16	0.29	617	276
MC-D3	0.16	0.38	655	330

In the zeolites of series 2, the micropore volume decreased extensively with [HO⁻] in P2-D1, P2-D2 and P2-D3. This was also consistent with the degree of lost crystallinity of these three samples, where severe alkaline media in the case of P2-D3 kept only ca. 29% of the crystal phase of the zeolite, leading to ca. 71% of debris formation. However, the company of the TBA⁺ cations (P2-D4 to P2-D7) was shown not to preserve the microporosity, since similar amounts of total HO⁻ concentrations were used as in P2-D1 (where NaOH was used without any of the protecting agents), but have shown no impact.

In series 3 zeolites, the effect of desilication was more pronounced relative to the nanocrystal series, no matter what was the treatment used. The micropore volumes could not be preserved by the action of the quaternary ammonium cations. This may be explained by the external surface area exhibited in the parent MC of this series. In comparison with the

nanocrystals, the external surface area of MC is half that of the nanocrystal ones. Moreover, at the microscopic level, the interaction of the quaternary ammonium cations with the external surface will be lower than that at the nanoscale. Consequently, the affinity of these cations to the surface will be less pronounced in the MC zeolite, and will have a very weak protective effect. This was reflected in the amorphization (to ca. 40-50%) and debris formation after desilication, as well as the decrease in the micropore volumes even in presence of these cations.

Figure III.7-b shows the variation of the normalized microporosity of the zeolites in terms of crystallinity, as a function of $[\text{HO}^-]_t$. A horizontal straight line is obtained which attributes the preservation of the *BEA structure characteristics after desilication. This implies that in most cases the pore directing agents had no influence on the micropore volume (as clearly seen in series 2 zeolites), but the direct influence was on the crystallinity by which in its turn affects the microporosity [163,214,257,280].

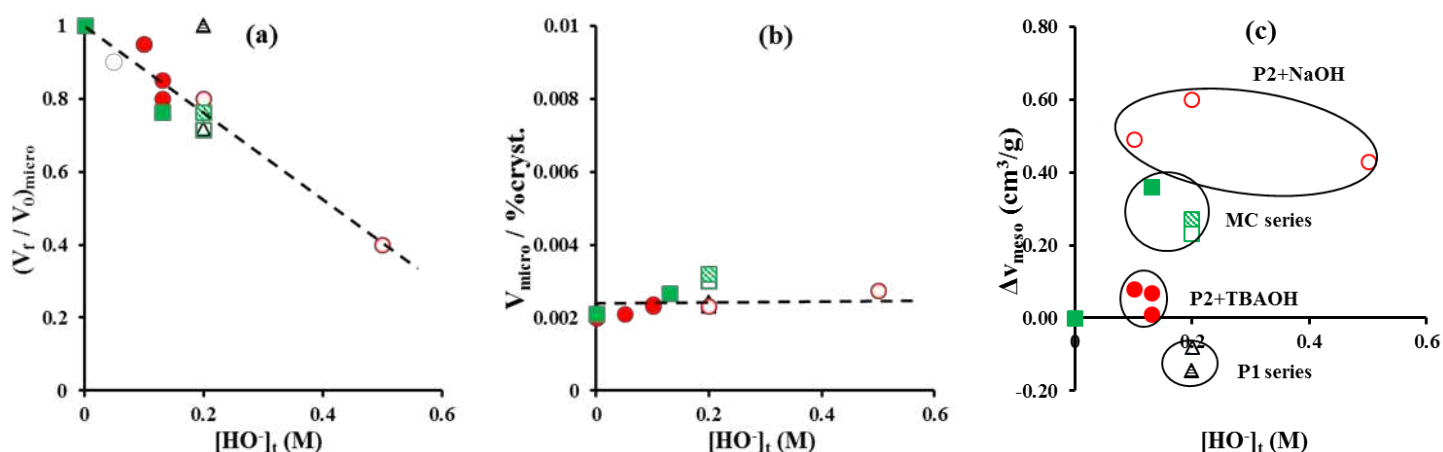


Figure III.7 Variation of porosity characteristics as a function of total concentration of hydroxyl anions.

Figure III.7-c shows the difference in the mesopore volume between that of the desilicated sample and its parent zeolite. Four regions were assigned in the current image. The region that corresponds to the P1 series (series 1), show non-surprisingly a negative difference. The isotherms of series 1 zeolites display lower N_2 uptake for the desilicated samples at high relative pressure, a sign of mesopore reduction. Despite of the attempt to increase more the mesopore volume within these zeolites, but the result wasn't though. As assumed before, the attack of the HO^- anions was said to be along the surface crystals, by which it caused a reduction in these crystals. Because of crystal reduction, certain portion of the intercrystalline mesopore volume

was missed, due to the following aspect that when the crystals are reduced, they will be more compact over each other and thus the volume of the voids in between them will decrease. This observation is explained more in Figure III.8.

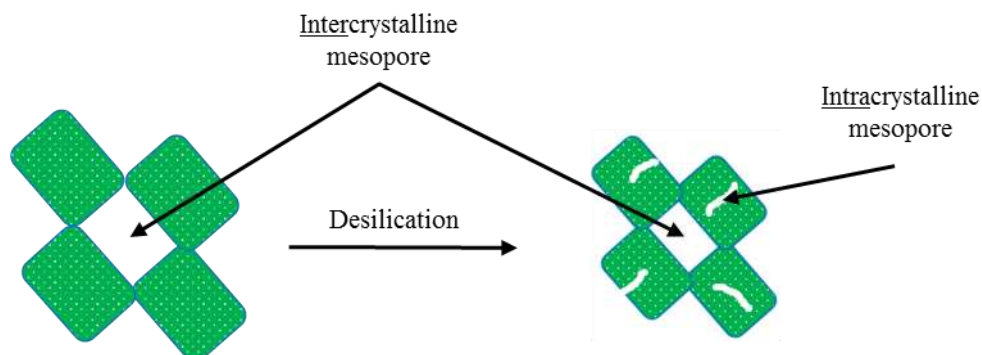


Figure III.8 Scheme showing the decrease of intercrystalline mesopore after desilication (series 1 zeolites).

Moreover, the hysteresis loop displayed for P1-D2 is a sign of mesopore organization; this leads us to confirm again that the HO^- attack was occurring via two ways, along the crystallites surface and through the bulk of the zeolite introducing also some intracrystalline mesopores. Consequently, the attack through the bulk have just organized the pores, while that along the surface was more effective by reducing the size of the crystal. Moreover, for both desilicated samples of this series, the introduction of intracrystalline mesopores due to the attack of HO^- anions through the crystals could not have compensated the loss in the intercrystalline mesopores, for that we observe a decrease in the total mesopore volume. For the zeolites of series 2, the desilication in presence of NaOH alone was more effective in generating intracrystalline mesopores than the desilication in presence of TBAOH, which assumes that TBAOH played a negative role towards the increase of the mesoporous content in case of nanocrystals. This is due to the high protective effect on the zeolite surface which limits the attack of HO^- anions as shown with Abello et al. [280].

The mesopore volumes were shown to be increasing after desilication in case of microcrystals, a sign of the generation of intracrystalline mesopores through the bulk of the crystallite owing to the large sized crystals. If we look on the TEM images of this series (fig. 2), we see the intracrystalline mesopores are being formed starting from the surface of the crystal in the case of MC-D1. However, the use of the pore directing agents shows after desilication a hollow-like formation in the formed intracrystalline mesopores. This observation

is at the basis of a gradient in the distribution of these mesopores, where in the core of the crystal they exist less than near the surface. This observation is suggested to be due to attack of the HO^- anions through the bulk of the crystal, introducing however more intracrystalline mesopores near to the crystal surface than the core of it.

Concerning the pore size distributions, the BJH curves obtained are shown in Figure III.6. In series 1 zeolites, no change in the bimodal distribution of the sizes (where the peak at 2 nm reveals the microporous nature of the pores, and that at 5 nm reveals the mesoporous nature), except that there is an increase in the peaks' intensities on the desilicated zeolites, reflecting probably a more organized porosities. In series 2, it was evident according to our results (not all shown here), that the desilication with NaOH caused a preservation of the mesopore size diameter (at ca. 10 nm as was initially in P2), but was reduced in case of TBAOH company (to 4-5 nm). In series 3, all the zeolites possessed pore size of 2 nm, revealing the microporous nature of these zeolites, with a little upwards shifting of the BJH curves of the desilicated samples of this series in the region higher than 2 nm, reflecting the initial creation of mesopores.

2.5 Acidic properties

The hydroxyl groups spectra in parent and desilicated zeolites of the different series are presented in Figure III.9 of the supporting information (only for zeolites used in catalytic tests). The band 3608 cm^{-1} stands for the Si(OH)Al groups, band 3664 cm^{-1} for Al-OH groups, band 3740 cm^{-1} for Si-OH groups, and finally band 3782 cm^{-1} for the external framework aluminum.

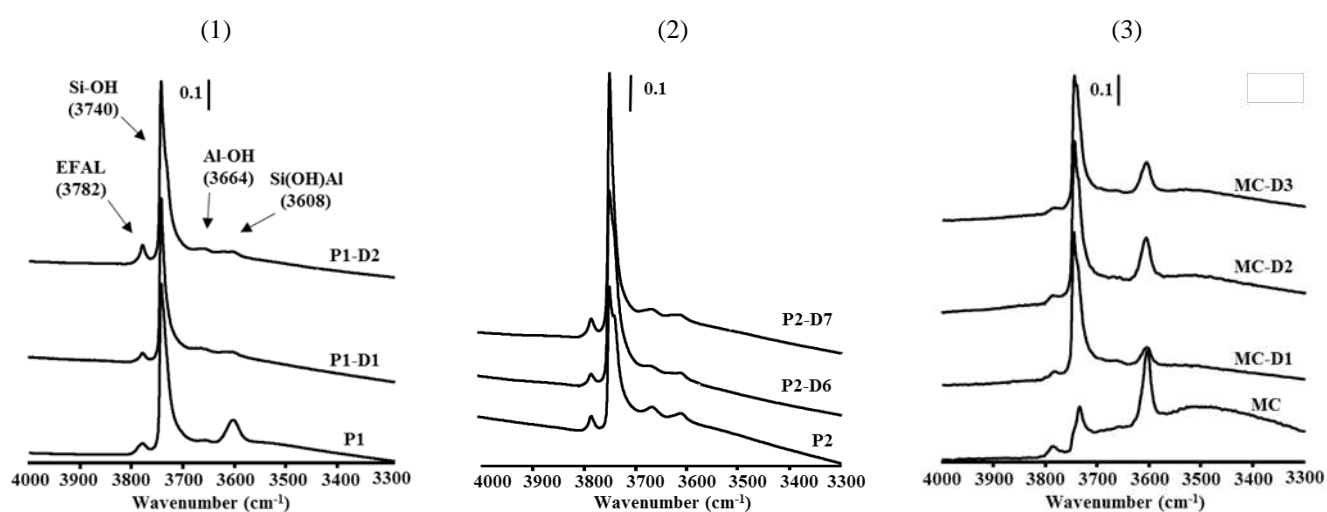


Figure III.9 Hydroxyl groups of the selected zeolites of series (1-3).

The distinct increase in the silanol groups (Si-OH) in the zeolites of series 2 and 3 desilicated zeolites reflects the increase (P2-D6 and P2-D7) or development (MC-D1, MC-D2 and MC-D3) of mesoporosity. The decrease in this band in P1-D1 is referred to the decrease in its mesopore volume (from 0.58 to 0.50). The shift of the Si(OH)Al bands to lower intensities signifies the decrease of the acidity of the zeolite [162]. This was seen on all the displayed zeolites, except in P2-D7, where this band seems to be the same after desilication (associated with a slight increase of its acidity from 346 to 365). The EFAL band at 3782 cm⁻¹ seems to decrease in all the desilicated samples except in D2 where there is a slight increase in comparison with the corresponding parent zeolite P1. In the MC parent zeolite, a broad band appears in the 3400-3550 cm⁻¹ range that corresponds to the hydroxyl nests typical for microporous solids, being referred to Si-OH defects bonded by hydrogen that is bonded to the oxygen in the framework [281]. As reported by Gil et al.[282] and Holm et al [283], the hierarchization of the zeolite by means of desilication leads to the disappearance of this band. This is confirmed in the other zeolites of series 1 and 2, where these hierarchical zeolites show no appearance of such a band. However, these Si atoms located in Si-OH defects, are bonded via oxygens to other three Si atoms and to the OH in defects, and are probably the least stable sites being the most incurred for the attack of the HO⁻ anions.

Table III.5 Acidic properties of the zeolites of series 1-3.

Sample	BAS (μmol/g)	LAS (μmol/g)	[H⁺]_{theor.} (μmol/g)	BAS/[H⁺]_{theor.}
P1	463	352	949	0.48
P1-D1	267	275	347	0.77
P1-D2	334	442	486	0.68
P2	346	349	677	0.48
P2-D1	339	323	730	0.46
P2-D2	396	369	1299	0.30
P2-D3	221	277	1944	0.11
P2-D4	407	394	875	0.47
P2-D5	370	425	847	0.44
P2-D6	295	446	659	0.45
P2-D7	365	422	549	0.66
MC	523	99	543	0.96

MC-D1	285	190	922	0.31
MC-D2	362	137	1063	0.34
MC-D3	431	168	941	0.46

The Brønsted $[\text{PyH}^+]$ acidities $[\text{PyH}^+]$ are reported in Table III.5 for all the zeolites before and after desilication, and are illustrated in the form of ratios between the acidities of the desilicated sample and its parent zeolite as a function of $[\text{HO}^-]_t$ (Figure III.10-a). Superior to the level of the parent Brønsted $[\text{PyH}^+]$ acidities, the curve in Figure III.10-a shows a continuous apparent decrease of the acidity with $[\text{HO}^-]_t$. However, taking into consideration the crystallinity of the samples, the normalized Brønsted acidities (with respect to their crystallinity) show always an increase with $[\text{HO}^-]_t$ in attribution to a probable recrystallization during desilication (Figure III.10-b). The Brønsted acidity determined by pyridine adsorption at 150 °C, is in fact affected by the Al content of the zeolite, the question that comes concerns the different locations of Al after desilication. The desilication treatments leads to dissolution of both Si and Al species, however, the realumination process that takes place during recrystallization could possess several expectations concerning “where” might be this realumination. In the majority of the represented zeolites, the theoretical acidity (Table III.5) calculated from the framework Si/Al ratio is always approximately the double that of the acidity determined by pyridine adsorption followed by FT-IR measurements (except that of MC). This indicates that there is no change of Al location during recrystallization. According to the two mentioned figures (Figure III.10-a-b), the desilication and realumination are said to be favored at high alkaline media provided by the HO^- anions, since as seen that high concentration cause a large increase in BAS (normalized), taking into consideration its crystallinity. Moreover, according to these curves, it seems that the pore directing agents have no important impacts on the Brønsted acidity; this means they were not important parameters for redistribution of Al species during recrystallization.

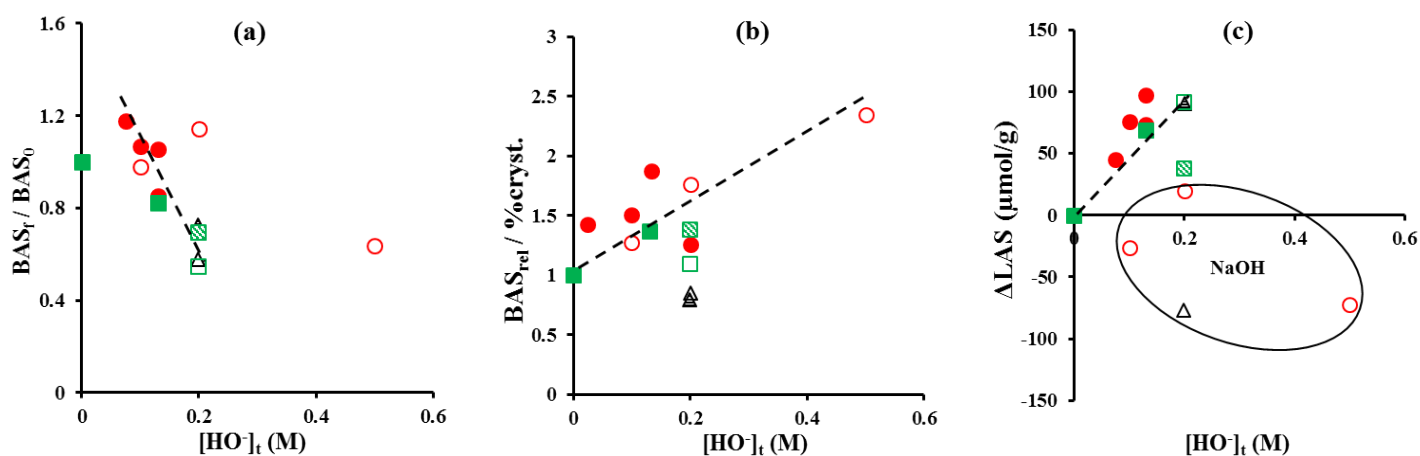


Figure III.10 Variation of acidic properties of the different zeolites as function total concentrations of hydroxyl anions.

Figure III.10-c that represents the difference between the Lewis acid sites of the desilicated sample and that of its parent zeolites, as a function of $[HO^-]_t$, shows two different trends. The first decreasing trend is referred to negative impact of NaOH alone no matter what was the starting material (nano- or microcrystal *BEA), where the difference in Lewis acidities falls in the negative region. Contrariwise, the company of the pore directing agents seem to have an influence on the redistribution of Al species mainly in the extra-framework positions during recrystallization, leading to an increasing trend of the Lewis acidities in the positive region of the graph.

3 Catalytic performance in n-hexane cracking

Recall that all catalysts were used under same operating conditions: temperature of 540 °C, atmospheric pressure, and the flow rate of n-hexane was fixed as well as the mass of the catalysts. Note that the colors used for the catalysts in this part will follow the same manner starting from Figure III.11 to Figure III.16.

- Series 1: ● P1, ● P1-D1, ● P1-D2;
- Series 2: ● P2, ● P2-D6, ● P2-D8;
- Series 3: ● MC, ● MC-D1, ● MC-D2, ● MC-D3.

Figure III.11 shows the change in the n-hexane conversion with time on stream (TOS) for all catalysts of series 1 and 3, but for only 3 catalysts of series 2 (the parent and two of the desilicated samples P2-D6 and P2-D7).

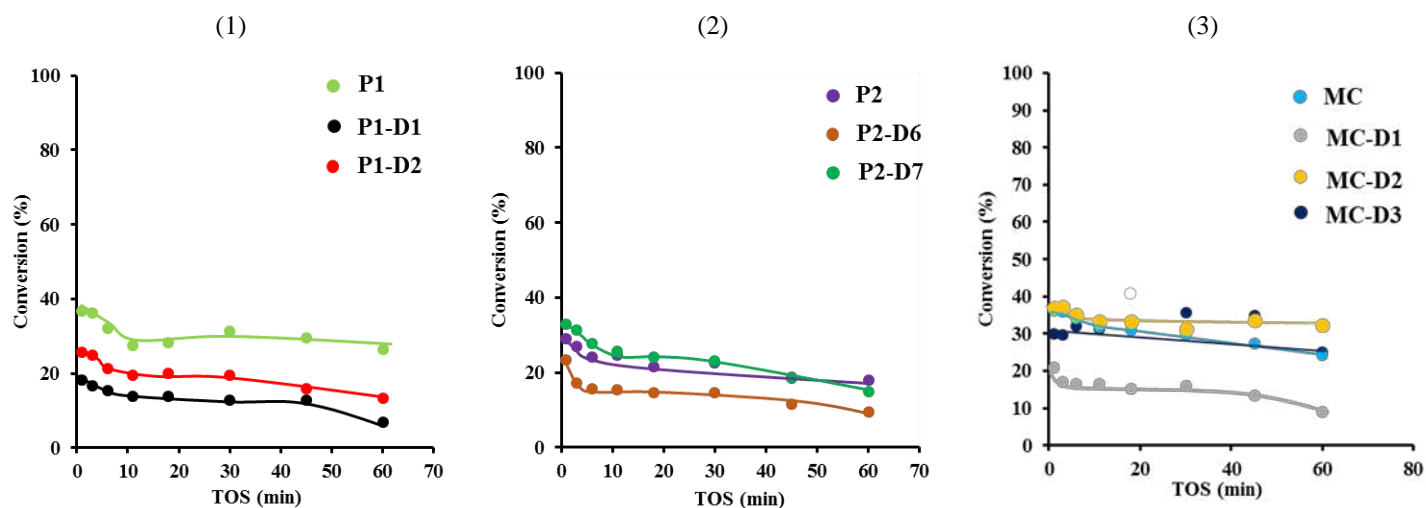


Figure III.11 n-hexane conversion as a function of time-on-stream for the various catalysts of series: (1-3).

As in Figure III.11, the three parent catalysts P1, P2 and MC showed initial conversions of 36.9, 29.1 and 37.1, respectively. Although both P1 and P2 represent nanocrystals *BEA zeolites with hierarchical porosity system, but the acidity in P1 is higher than that in P2, which accounts for the higher conversion in the former catalyst. The MC catalyst possess initial conversion similar to that of P1, knowing that this microcrystal *BEA is purely microporous zeolite, in which diffusional limitations may occur. However, the higher acidity of MC with respect to P1 might have compensated for the lack of a porous system that can favor better diffusion. All these parent catalysts possess slight deactivation at higher TOS due to coke formation. However, despite of the high coke formed on P1 catalyst, but it is assumed that the coke formed is not toxic being located in the mesopores where no probable diffusional limitations would occur (see Figure III.13).

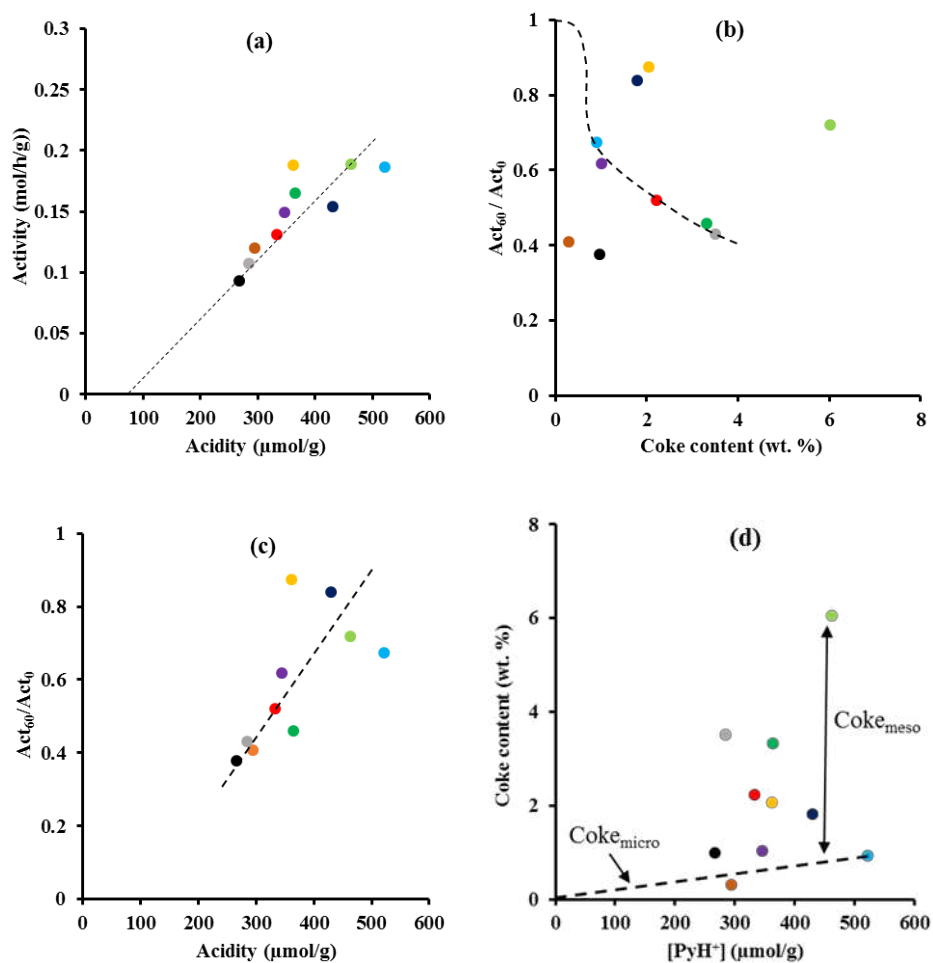


Figure III.12 Catalysts initial activities (a), ratios between final and initial activities (c), coke content (d) as a function of acidity, and ratios between final and initial activities as a function of coke content (b).

In series 1 catalysts, both desilicated samples of P1 seem to have worse initial conversion in comparison with P1, which may be due to the lower mesopore volumes and acidities as well. Similar deactivation behaviors were observed due to coke formation, but the coke content was still much lower than in P1 due to the lower acidity possessed (Figure III.13). In series 2 catalysts, the conversion of n-hexane was improved by the P2-D7 (ca. 33%) catalyst that possessed higher Brønsted acidity and mesoporous content after desilication, in contrary to the sample that possessed a lower acidity (P2-D6), attributing to the lower conversion as well (ca. 24%), despite of the slightly improved mesoporous content. In series 3 catalysts, although there was hierarchization in both MC-D1 and MC-D3 by generation of intracrystalline mesopores,

but still the conversions of n-hexane registered are lower than that in the parent MC catalyst, probably due to the lower acidity possessed in these two catalysts.

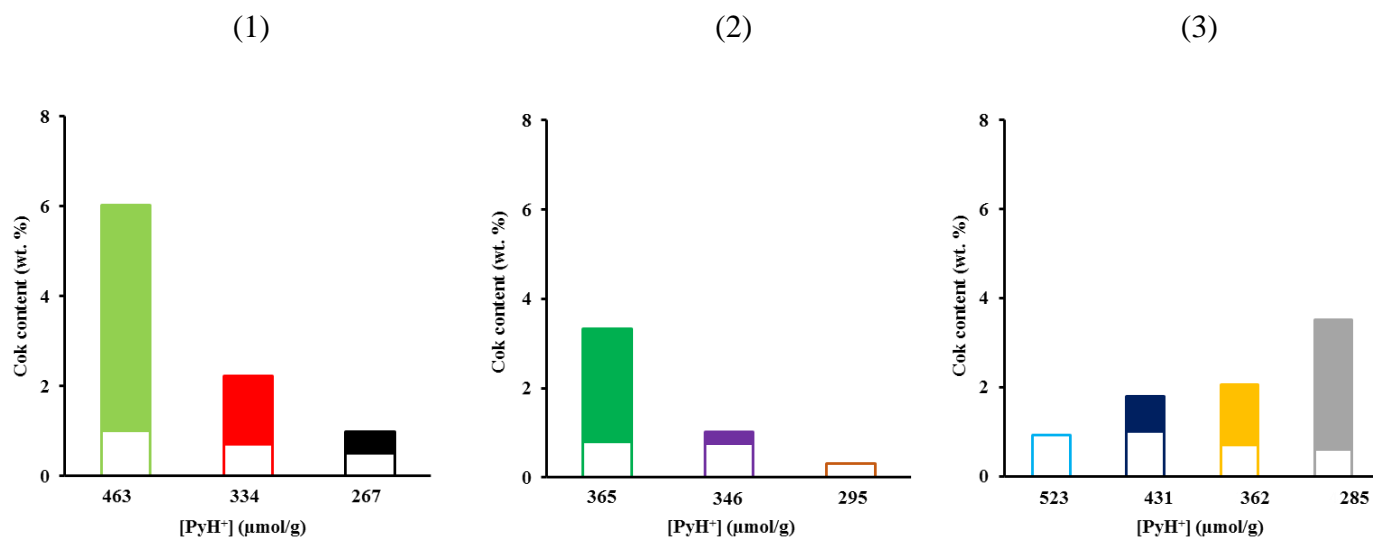


Figure III.13 Coke content as a function of acidity of the catalysts of the series: (1-3). The empty boxes correspond to the coke in the micropore, and the filled one in the mesopore.

The linear relation between the activity of the majority of the catalysts and their acidity in Figure III.12-a, shows that the higher the acidity, the higher the activity of the catalyst. This implies that this model reaction (cracking of n-hexane) is very acidity dependent, and as said in literature it can be used to characterize the acidic sites [284]. However, the points that are displaced from the line should account for different issues. Any point that is clearly above the line should account to an exaltation of the Brønsted acid sites by the Lewis acid ones. On the contrary, the points below the line attribute to diffusional limitations. Being all the points nearly on the curve without any significant deviation, implies that neither there exist exaltation nor diffusional limitations on any of the catalysts even the purely microporous zeolite (MC). Figure III.12-b shows a general decrease of the stability of the catalysts with the coke content with some exceptions of lower deactivation (points above the general trend of the curve line) that account for presence of the coke in the mesopores (non-toxic coke). Moreover, the stability of these catalysts seem to be recovered in the same time by their acidity, as Figure III.12-c shows an increase of the stability with acidity. Nonetheless, the coke content seems also to be formed more and more as the catalyst is more acidic (Figure III.12-d). So how could it be that

there is deactivation of the catalysts with the formation of coke, and in the same time recover of stability and increase of coke content with acidity? This is explained by the presence of the coke probably in in the micropores and the mesopores as well.

The light blue point in Figure III.12-d corresponds to the purely microporous zeolite (MC), which means that all the coke content formed is present in the micropores only. Consequently, any point that lies on this line will account the amount of coke present in the micropore. Moreover, for any point that is present above the line corresponds to the global amount of coke formed. As a result, the coke formed in the mesopores is then the difference between the global amount and the point that corresponds to the vertical projection of the global coke content on the dotted line of the microporous coke content as drawn on Figure III.12-d.

Figure III.13 shows clearly the decrease of the content found in the micropore with the acidity of the corresponding catalysts. However, the evolution of the global content is attributed to different suggestions. In series 1 catalysts, it is true that the mesopore coke content is decreasing with acidity, but this can be also due to the amount of intercrystalline mesopore volume possessed. As to say, as the crystal size of the desilicated samples of P1 was reduced, the intercrystalline mesopore volume was also reduced, so the accumulation of the coke right here is favored by larger intercrystalline mesopores. In series 2 catalysts, the decrease in the mesopore coke content is in relation to the amount of silanol groups possessed that are able to trap the precursors of the coke molecules [285]. With P2-D7 possessing significant increase in the silanol band at 3740 cm^{-1} (Figure III.9), coke was highly formed. In the microcrystal series (series 3) the observation is different concerning the global coke content where there is a decrease with acidity. This is suggested to be due to more accumulation of coke in the intracrystalline mesopores (formed after desilication). Moreover, between these formed hierarchical zeolites of series 3, more coke was formed in the mesopores generated upon NaOH treatment alone, than in presence of the pore directing agents. This is probably related to the shape of the mesopores generated upon the dissolution of the crystal starting from the surface as revealed in the TEM image of MC-D1, where the mesopores are probably formed in the form of ink-bottle shape, which favors more the accumulation of coke.

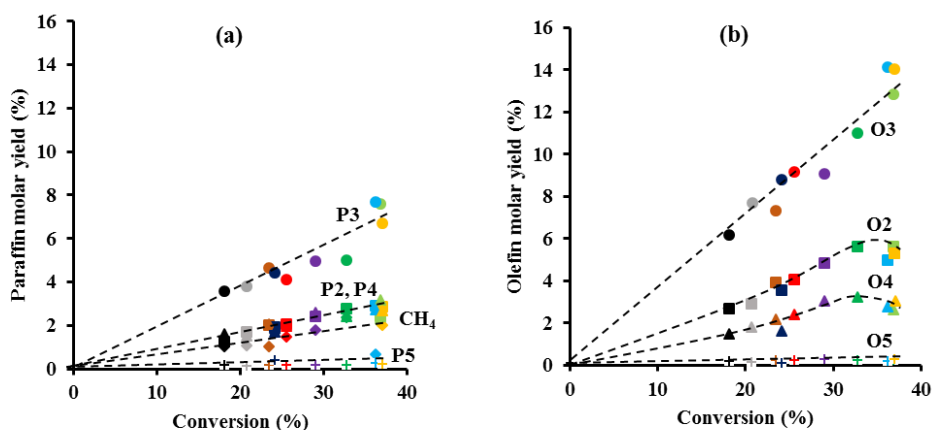


Figure III.14 Variation of paraffin (a) and olefin (b) products molar yield as a function of n-hexane conversion for all the selected catalysts.

Figure III.14 displays the variation of the reaction products with conversion. The passage of the curves through the origin indicates that the reaction mechanism taking place is the monomolecular one, knowing that it is operating at low pressure (atmospheric) and high temperature (540 °C) [286]. This mechanism usually takes place in the micropores of the zeolites; however, there was no change in the mechanism despite of presence of mesopores in all the corresponding catalysts. Figure III.14-a shows that all the paraffin products seem to be elevating with conversion no matter what catalyst is used. C₃ paraffin are always produced in the highest amount no matter what was the catalyst used, and it seems also to be more pronounced with increased conversion. Taking into consideration that the cracking of n-hexane will take place respecting the reactants and products stoichiometry, the production of C₃ paraffin and olefins should be equal. However, this not the case. If we compare the molar yields of C₃ paraffin Figure III.14-a to that of C₃ olefin in Figure III.14-b, the amount of olefins exceeds that of paraffin to almost the double, which assumes that the produced paraffin are undergoing hydrogenation over the strong Brønsted acid sites to form excess olefins and dihydrogen (H₂). C₅ paraffin are rarely seen, as well as their olefin form as in Figure III.14-b. Nonetheless, the production of the same amounts of paraffin and olefin C₅ suggests that all C₅ paraffin are dehydrogenated to form the alkene form of this carbon chain.

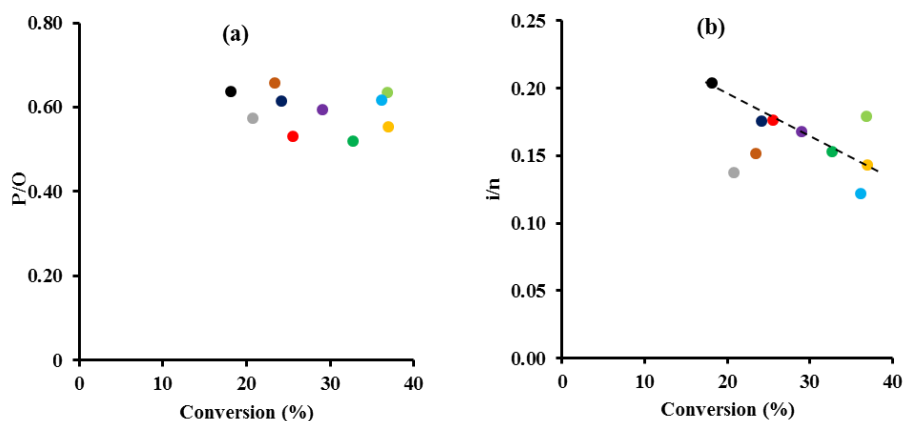


Figure III.15 Ratios of initial paraffin to olefin (a) and normal to isomers (b) molar yields products as a function of n-hexane conversion for all the selected catalysts.

Figure III.15-a points to previous observations that more olefins are produced than paraffin, owing to the ratio of paraffin to olefin products molar yields, which is less than 1. These observations were also seen by Nakao et al. [287], where they suggested also that the coke formation which was the origin of the deactivation of the catalysts used (HBEA), was due to the polymerization of the propylene olefins that exceeded the propane molecules.

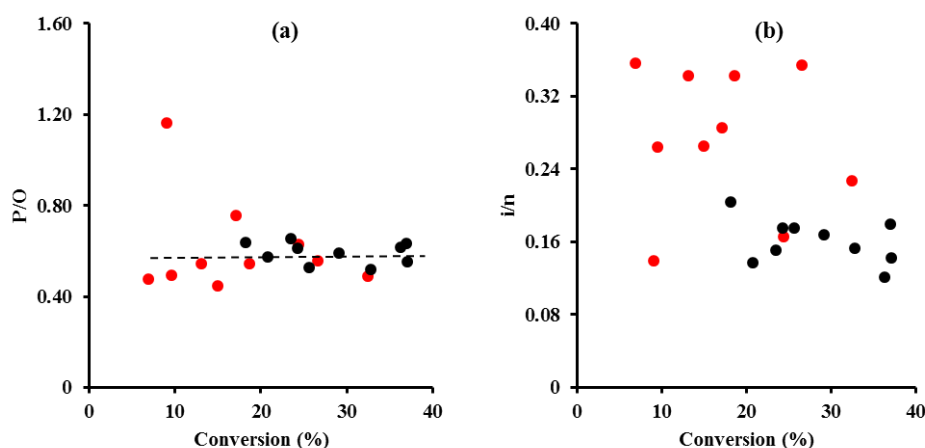


Figure III.16 Variation between initial (in black) and final (in red) “paraffin to olefin” (a) and “normal to isomers” (b) molar yields vs n-hexane conversion for all the selected catalysts.

Moreover, following the olefin to paraffin ratio also at the end of the reaction (TOS of 60 min) as in Figure III.16-a, the whole ratios still fluctuate in the same range as the values taken at initial conversion, despite of the deactivation of the catalysts (lower final conversions). This

observation provides our suggestion that probable dehydrogenation is taking place despite of the coke formed. The normal to isomers products molar yields ratios in Figure III.15-b which is smaller than 1 signifies in spite of coke formation on the acidic sites, isomers products are still produced. Figure III.16-b illustrates the comparison of this ratio at initial and final conversions, which also seem to be higher at the end despite of coke formed. This may signify that the strength of the acidic sites played a major role in the isomerization of the products even at higher TOS without being affected by the coke formed on them.

4 Conclusions

Three parent *BEA zeolites two of which are commercial nanocrystals zeolites (series 1 and 2) and one of which is a synthesized microcrystal zeolite (series 3), were subjected to different alkaline treatments in presence of NaOH alone, NaOH+TPABr, NaOH+TBAOH, seeking for improved textural properties for better diffusion of molecules within the channels of the zeolites. It was found for the three series that the mass yield, crystallinity and microporosity were seen to decrease continuously with $[\text{HO}^-]$. Particular cases for preservation of both crystallinity and microporosity were seen in the nanocrystals only (P1-D2 zeolite of series 1), as well as preservation of crystallites size (P2-D6 zeolite of series 2), attributing these observations to the protective effect played by the pore directing agents. The normalization of the microporosities of the samples with respect to their crystallinities revealed that the desilication treatments had a direct impact on the crystallinity and not the microporosity, and the *BEA characteristics are still preserved. A decrease in the mesoporous content was consistent with the decrease of the nanocrystal size. Moreover, the use of NaOH alone was more effective than the company of pore directing agents in the introduction of intracrystalline mesopores in case of nanocrystals, while in microcrystals the effect was comparable with a high sign of surface protection when pore directing agents were used. The increase of Brønsted acidity at lower HO^- concentrations was attributed to probable recrystallization and realumination, with a pronounced decrease at higher alkaline media. Negative impact of NaOH alone was observed on the Lewis acidity, while the company of the pore directing agents was seen to provoke the formation of new Lewis acid sites as referred to the redistribution of Al species in the extra framework positions.

Monomolecular mechanism of n-hexane cracking was always the observed mechanism in spite of the presence of mesopores. However, the improvement of the textural properties in

some of the catalysts did not influence positively their catalytic performance in the cracking of n-hexane. A loss in the catalytic activity was attributed mainly to the decrease in the Brønsted acidity of the desilicated catalysts. The fast deactivation of the catalysts is referred to the fast formation of coke. Highly formed coke may not influence negatively the performance of the catalyst being as non-toxic deposits in the mesopores. The higher olefin to paraffin molar weights are at the origin of dehydrogenation reactions taking place even though coke is formed. The formation of isomers products in high amounts at the end of the reaction signifies the strength of the Brønsted acid sites that was still pronounced in spite of coke formed.

\

Chapter IV

Impact of desilication of *BEA zeolites on the catalytic performance in hydroisomerization of $n\text{-C}_{10}$

This chapter is published under the following reference :

[Applied Catalysis A, General 551 \(2018\) 1–12.](#)

[DOI : 10.1016/j.apcata.2017.11.024.](#)

1 Introduction

It is of much importance for bifunctional redox-acid refining catalysts to possess a rational design that requires the definition of some parameters that govern their behavior as well as the knowledge of their quantitative effect. This has been seen to be achieved with the Pt-H-zeolites that catalyze the isomerization of alkane products [124–126,288]. As said before, the n-alkane hydroisomerization reaction requires the incorporation of the redox-acid bifunctional catalyst, in which a metal (Pt in our case) presents the redox part, and the H-zeolite support (H-*BEA) presents the acidic one. Seven successive steps are covered during the hydroisomerization reaction, 3 of which are chemical and 4 are physical [124–126]. However, drawbacks are observed in such types of catalytic transformation of hydrocarbons, due to diffusional limitations associated with non-convenient zeolites' pores sizes [19,82,149,154,155].

In this chapter will be shown how the hierarchization of synthetic micro- and commercial mesoporous *BEA zeolites, affects the zeolite's characteristics, and in turn with the catalytic bifunctional properties, how they improve or worsen the catalytic performance of the requested zeolites in the hydroisomerization of n-decane.

2 Catalysts characterizations

As discussed in chapter 3, the parent commercial *BEA zeolite P1 (CP811) was desilicated in presence of NaOH alone and NaOH+TPABr to yield P1-D1 and P1-D2 respectively, while the parent commercial *BEA zeolite P2 (CP814E) was desilicated in presence of NaOH+TBAOH to yield P2-D6. In addition, the synthesized microcrystal *BEA zeolite (MC) was desilicated in presence of NaOH alone, in presence of NaOH+TPABr, and in presence of NaOH+TBAOH to yield finally MC-D1, MC-D2 and MC-D3 respectively.

Table IV.1 Conditions of desilications on the different parent zeolites.

Zeolite	[NaOH] (M)	PDA	[PDA] (M)	[HO⁻]_t (M)	R	T (°C)	t (min)
P1	-	-	-	-	-	-	-
P1-D1	0.2	-	-	0.2	-	65	30
P1-D2	0.2	TPABr	0.2	0.2	-	65	30
P2	-	-	-	-	-	-	-

P2-D6	0.12	TBAOH	0.2	0.13	0.625	65	30
MC	-	-	-	-	-	-	-
MC-D1	0.2	-	-	0.2	-	65	30
MC-D2	0.2	TPABr	0.2	0.2	-	65	30
MC-D3	0.12	TBAOH	0.2	0.13	0.625	65	30

The desilication conditions of these zeolites are rereported in Table IV.1. All of these zeolites were transformed into their bifunctional form by the impregnation of Platinum. The bifunctional characteristics are shown in Table IV.4 and will be discussed in section 2.2 of this chapter.

2.1 Impact of desilication on zeolites' properties

A brief summary here about the important influenced properties of the zeolites requested in this chapter will be given. The main structural, elemental, textural, and acidic properties of these zeolites are reported in Table IV.2 and Table IV.3. The structural characteristics of the *BEA zeolite was totally preserved after desilication, with some differences in the relative crystallinities as was discussed in chapter 3. A decrease in the crystal size was observed in P1-D1 (13.5 nm) and P1-D2 (14.9 nm) in comparison with P1 (20 nm), while it was almost preserved in case of P2-D6 (19.6 nm) in comparison with P2 (20 nm). The textural properties of all the zeolites deduced from the nitrogen sorption isotherms showed a decrease in micropore volume in P1-D1 (0.16 cm³/g) and a preservation in P1-D2 (0.22 cm³/g). In addition to that, the mesopore volume has decreased in both P1-D1 and P1-D2 from 0.58 to 0.50 and 0.44 cm³/g respectively. It was suggested that the decrease of the crystal size enhances missing of some portion of the pores. In series 2, the micropore volume was preserved in P2-D6 (0.20 to 0.18 cm³/g), while an increase in the mesopore volume (0.54 to 0.61 cm³/g) was observed, owing to the strict orientation of the HO⁻ anions through the pores of the zeolite. In series 3 zeolites that was meant with desilicating a purely microporous *BEA zeolite, showed a clear decrease in the micropore volume which was consistent with the decrease in crystallinity to almost around the half, and a clear introduction of mesopores in the three desilicated samples.

Table IV.2 Structural, elemental and acidic properties of parent and desilicated zeolites.

Zeolites	% Cryst.	Si/Al		[PyH ⁺]	[PyL]
		Total	Framework	($\mu\text{mol/g}$)	($\mu\text{mol/g}$)
P1	100	12	15	463	352
P1-D1	68	7.6	33	267	275
P1-D2	91	8.9	26.4	334	442
P2	100	12	20	346	349
P2-D6	72	8.6	18	295	446
MC	100	36	23	523	99
MC-D1	50	26.8	16.3	285	190
MC-D2	60	2.8	14.5	362	137
MC-D3	50	29.1	16.2	431	168

Table IV.2 shows also the records of the Brønsted and Lewis acidities of all the zeolites, where there is a decrease to ca. 40% in P1-D1, to ca. 30% in P1-D2, and to ca. 15% in P2-D6, in comparison with the acidities of the parent zeolites. Similar loss in Brønsted acidity was observed in the desilicated forms of MC. In the contrary, an increase in the Lewis acidity was observed on all the zeolites in comparison with their parent ones, except in P1-D2 where there was a decrease up to 20%.

Table IV.3 Textural properties of the parent and desilicated zeolites.

Zeolites	Crystal size (nm)	Pore volume (cm^3/g)		Surface area (cm^2/g)	
		Micro	Meso	External	Specific
P1	20	0.22	0.58	254	577
P1-D1	13.5	0.16	0.50	253	401
P1-D2	14.9	0.22	0.44	297	576
P2	20	0.20	0.54	176	605
P2-D6	19.6	0.18	0.61	388	693
MC	780	0.21	0.02	125	502
MC-D1	-	0.15	0.25	274	573
MC-D2	-	0.16	0.29	276	618
MC-D3	-	0.16	0.38	330	655

2.2 Bifunctional characteristics of the catalysts

Table IV.4 represents the properties of the related zeolite catalysts. It is remarked in the table the platinum contents that varied from 0.44 to 1.5% wt. over P1 catalysts, and ca. 1.5% wt. on the others of series 1. This preceding gradual increase of Pt is done to study the impact of Pt content on activity of the related catalysts and their selectivity towards isomers products, where it was that 1.5% of Pt was the amount of impregnation needed to obtain the ideal bifunctional catalyst. Because of this finding, series 2 catalysts contained 1.5% wt. of Pt on P2 and P2-D6 catalysts. Finally, series 3 contained 0.75% wt. of Pt on the parent MC and 1.0 on the MC-D1, MC-D2 and MC-D3, in spite of the attempt to impregnate 1.5% of Pt to these zeolites, respecting all the calculations needed to impregnate this amount, but surprisingly, this series of microcrystal *BEA zeolites showed a strange response after impregnation. Several bifunctional characteristics could be further deduced from the amount of Pt content in each catalyst, e.g. dispersion of Pt, size of Pt, concentration of Pt, and final the balance between their concentration and the Brønsted acid concentration of the catalyst. Note that Table IV.4 includes also the values of the Brønsted acidities of the catalysts and not the related zeolites, i.e. the acidity was calculated after the impregnation of Pt.

Table IV.4 Bifunctional characteristic of all the catalysts.

Zeolites	Pt				[PyH ⁺] ($\mu\text{mol/g}$)	$n_{\text{Pt}} / n_{\text{H}^+}$
	Wt. (%)	D. (%)	d (nm)	n ($\mu\text{mol/g}$)		
P1	0.44	25	4.52	5.64	408	1.40
P1	0.98	48	2.35	24.1	371	6.50
P1	1.10	48	2.35	27.1	464	5.80
P1	1.50	33	3.42	24.2	489	5.00
P1-D1	1.38	9	12.5	6.40	219	2.92
P1-D2	1.60	55	2.05	45.1	253	17.8
P2	1.48	13	8.69	9.90	304	3.20
P2-D6	1.53	9	12.5	7.10	303	2.34
MC	0.75	15	7.53	5.60	372	1.50
MC-D1	1.00	56	2.01	29.2	294	9.93
MC-D2	1.00	46	2.45	23.6	286	8.25
MC-D3	1.00	41	2.75	21.0	365	5.75

The dispersion of Pt was found to vary from low to moderate values in the different catalysts. It was also possible to calculate the size of Pt particles (d_{Pt}) from the dispersion values (section), and was found that it differed from catalyst to another from 2 to 12.5 nm. The knowledge of the Pt particle size is of too much importance in order to determine if they were located inside or outside the pores, i.e. on the surface of the zeolite's crystallites. Consequently, some of the catalysts contained Pt particles that were located outside the pores (1.38P1-D1, 1.53P2-D6, and all series 3 catalysts), being larger than the pore aperture. The high temperature of the calcination program after the ion-exchange reaction (required to impregnate Pt), is responsible for the low dispersion of Pt, and consequently responsible for their location on the external surface. All the other catalysts contained Pt particles less than the pore aperture, i.e. the particles can be located inside the mesopores (being larger than micropore diameter and less than the mesopore diameter).

Concerning the catalysts acidities, the Pt impregnation caused a general decrease between a minimum of 10 to a maximum of 30% of the initial acidity, marking also a slight increase in 1.50P1 (5.6%), in 1.53P2-D6 (2.7%), and 1.00MC-D1 (3%), which can be referred to the error accompanied with the final measurements. It was also possible to determine the number (concentration) of accessible Pt atoms (n_{Pt}), and was found to be much lower than that of Brønsted acid sites (n_{H^+}). Consequently, the values of the ratios between the accessible Pt atoms and Brønsted acid sites (n_{Pt} / n_{H^+}) were very low in the range 0.014-0.178. As the size of Pt particle size knowledge was important, though was the knowledge of the metal to acid ratio. This ratio determines the value after which the performance of the catalyst is optimal, thus the catalyst can be considered a well-balanced catalyst [125].

3 Catalysts activities

In order to obtain a well-balanced catalyst that exhibits the highest activity, different platinum contents (0.44, 0.98, 1.1, & 1.5%wt. of Pt) were impregnated on the reference parent P1 *BEA zeolite of series 1. Regardless of the platinum content, all the P1 catalysts exhibited a stable activity (measured at 230 °C on all catalysts). It is well seen that as the Pt content increases a little from 0.98 to 1.1%wt. of P1, the activity was maintained constant at $0.4 \text{ g}_{C_{10}} \cdot \text{g}_{cat}^{-1} \cdot \text{h}^{-1}$ (reported in Table IV.5). Unexpectedly, the activity increased sharply (to $5 \text{ g}_{C_{10}} \cdot \text{g}_{cat}^{-1} \cdot \text{h}^{-1}$) over 1.50P1 due to the appearance of a very highly active catalyst at lower temperatures, where 1.50P1 starts conversion at 190 °C and the others (0.44, 0.98 and 1.10P1) start at higher

temperatures. This comparison was done between the different Pt content P1 catalysts, in order to quantify the best amount of Pt that allows to obtain the optimal activity, which was found to be 1.5% of Pt.

Table IV.5 Activities of the different Pt content P1 catalysts measured at 230 °C.

Catalyst	Activity ($\text{g}_{\text{C}_{10}} \cdot \text{g}_{\text{cat}}^{-1} \cdot \text{h}^{-1}$)
0.44P1	-
0.98P1	0.4
1.10P1	0.4
1.50P1	5.0

In the other hand, the activity comparison was further investigated between the highest Pt content P1 catalysts (1.50P1) and its desilicated forms, and between the catalysts of the other two series themselves (series 2 and 3). In accordance to a previous work [289] during the hydroisomerization of n-hexadecane, a plateau for the maximum activity per Brønsted acid sites (or the turnover frequency (TOF)), was obtained over 0.5, 1, & 1.5%Pt-H*BEA catalysts. Consequently, and according to this result, all the other catalysts (except series 3 catalysts), were impregnated by ca. 1.5% wt. of Pt to insure maximum activity of the catalysts for n-C₁₀ transformation.

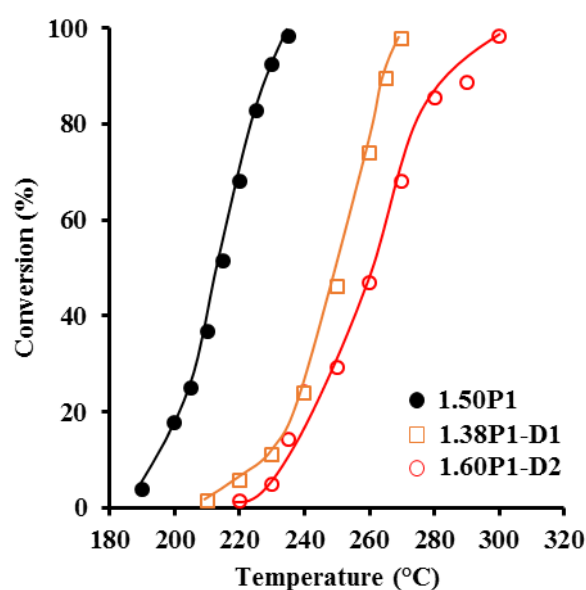


Figure IV.1 n-C₁₀ conversion as a function of temperature of the catalysts of series 1.

The comparison was done by plotting the curves of conversion of n-C₁₀ versus temperature as shown in Figure IV.1, where it clearly shows for series 1 the higher activity of 1.50P1 catalyst demonstrated by earlier conversion at lower temperatures, in comparison to 1.38P1-D1 and 1.60P1-D2 catalysts. These two catalysts 1.38P1-D1 and 1.60P1-D2 exhibit similar activities with a very small difference (Figure IV.1). This slight difference was reflected also by the slightly higher activity value for 1.38D1 ($0.5 > 0.3$) (Table IV.6).

Table IV.6 Activities of the different series 1 catalysts measured at 230 °C.

Catalyst	Activity (gC ₁₀ .g _{cat} ⁻¹ .h ⁻¹)
1.10P1	0.4
1.50P1	5.0
1.38P1-D1	0.5
1.60P1-D2	0.3

Series 2 conversion vs temperature curves show that 1.48P2 converts earlier n-C₁₀ than 1.53P2-D6 does (Figure IV.2). This implies that the parent zeolite catalyst is more active than its desilicated form. This aspect was reflected also in the activity values measured at 230 °C, where there was a drop down from 1.2 on 1.48P2 to 0.3 gC₁₀.g_{cat}⁻¹.h⁻¹ on 1.53P2-D6 catalyst.

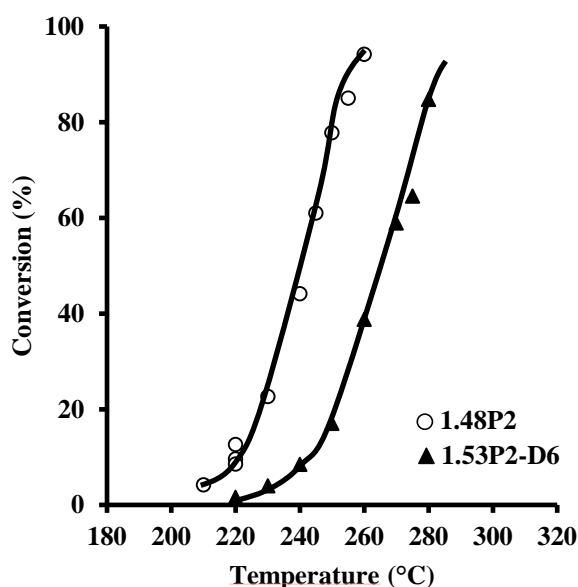


Figure IV.2 n-C₁₀ conversion as a function of temperature of the catalysts of series 2.

The values of the activities of series 2 catalysts are in the Table IV.7.

Table IV.7 Activities of the series 2 catalysts measured at 230 °C.

Catalyst	Activity (g _{C10} .g _{cat} ⁻¹ .h ⁻¹)
1.48P2	1.2
1.53P2-D6	0.3

In series 3 catalysts, the desilicated forms of MC show different aspects, where some register higher activity and the others lower one. As revealed in the conversion vs temperature curves in Figure IV.3, MC-D1 and MC-D3 converts n-C₁₀ in the same time but clearly earlier than MC, and the latter converts earlier than D5. This indicates that MC-D1 and MC-D3 are more active than MC, which in turn is more active than MC-D2.

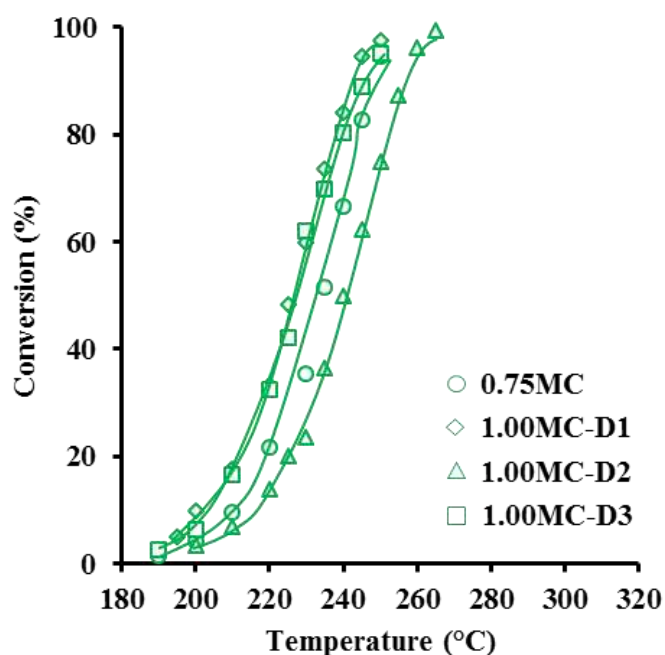


Figure IV.3 n-C₁₀ conversion as a function of temperature of the catalysts of series 3.

This was verified by the values of activities measured at 230 °C, where 1.00MC-D1 and 1.00MC-D3 catalysts exhibit higher activity than MC (4.7-4.8 > 1.9), and 1.00MC-D2 exhibits a very slightly lower activity to that of 0.75MC catalyst (1.8 g_{C10}.g_{cat}⁻¹.h⁻¹). The values of the activities measured are presented in Table IV.8.

Table IV.8 Activities of the series 3 catalysts measured at 230 °C.

Catalyst	Activity ($\text{g}_{\text{C10}} \cdot \text{g}_{\text{cat}}^{-1} \cdot \text{h}^{-1}$)
0.75MC	1.9
1.00 MC-D1	4.7
1.00 MC-D2	1.8
1.00 MC-D3	4.8

The $n_{\text{Pt}} / n_{\text{H}^+}$ ratios (ratio between number of accessible Pt atoms and the total number of protonic sites) of the catalysts varied in the range 0.014-0.178, which indicates that the rate of some reactions was limited by the metallic step (for $n_{\text{Pt}} / n_{\text{H}^+} < 0.03$), and the others by the acidic step (for $n_{\text{Pt}} / n_{\text{H}^+} > 0.03$) [290]. It can be seen in Table IV.9 that the values of the turnover frequencies (TOF), activity per Brønsted acid sites measured at 230 °C, are in the same range ($7\text{-}16 \text{ h}^{-1}$) in case of 0.98 & 1.10P1, and the desilicated forms of P1, 1.38P1-D1 & 1.60P1-D2. This value was found to be too much high on 1.50P1 (72 h^{-1}). In case of 1.48P2, the TOF value (28.5 h^{-1}) was much higher in comparison with all forms of P1 except 1.50P1, but unexpectedly it decreased to 6.9 h^{-1} over its desilicated form, 1.53P2-D6. Note that TOF value of 1.53P2-D6 is also less than those obtained with P1 catalysts and their desilicated forms as well. The TOF values registered for series 3 catalysts are in general considered higher than series 1 and 2 catalysts, but still the 0.75MC parent catalyst exhibit TOF value (36 h^{-1}) lower than 1.00MC-D2 (44 h^{-1}), 1.00MC-D2 lower than 1.00MC-D3 (92.4 h^{-1}), and the latter lower than 1.00MC-D1 (112 h^{-1}). The metal to acid ratios and the TOF values are presented in Table IV.9.

Table IV.9 Values of $n_{\text{Pt}} / n_{\text{H}^+}$ ratio and turnover frequencies for all the catalysts.

Catalyst	$n_{\text{Pt}} / n_{\text{H}^+} (\times 100)$	TOF (h^{-1})
0.44P1	1.40	-
0.98P1	6.50	8.2
1.10P1	5.80	7.0
1.50P1	5.00	72.2
1.38P1-D1	2.92	16.0
1.60P1-D2	17.8	8.6

1.48P2	3.20	28.5
1.53P2-D6	2.34	6.9
0.75MC	1.50	36.0
1.00 MC-D1	9.93	112.0
1.00 MC-D2	8.25	44.0
1.00 MC-D3	5.75	92.4

4 Reaction products and selectivity

During the completion of transformation of n-C₁₀ over all the catalysts, the products formed were the isomerization products I (monobranched isomers M and multibranched isomers B) and the cracking products C. However, the products distributions depended on the catalysts themselves and on degree of n-C₁₀ conversion (X). It was discussed in literature [291] that the isomers yield evolution is said to be unique due to the fact that the effects of the operating conditions on the isomerization or cracking are identical, or in a less way similar. To be more specific, Thybaut et al. [291] clarified that even upon varying the temperature under which the reaction is running to have complete conversion, the activation energies of the acid-catalyzed steps would be similar. This makes the isomers distribution unique and susceptible to comparison with each other.

The isomerization products were distributed into mono- and multibranched isomers. The monobranched isomers M were mainly methylnonanes, ethyl-branched isomers were rarely formed. Propyl-branched isomers were not observed as well. The mainly formed multibranched isomers were dimethyloctanes; 3-methyl-4-ethylheptane and small amounts of 3,4,5-trimethylheptane. 2,3-dimethyloctane was hard to be detected.

Figure IV.4 presents the yield into isomers (I) and cracking (C) for series 1 as a function of n-C₁₀ conversion. It is clearly shown that the Pt content favored positively the maximum isomers yield as the latter is increasing over P1 catalysts. The yield in isomers increased from ca. 30% over 0.44P1, to ca. 40% over 0.98P1, to 47% over 1.10P1, and finally to ca. 59% over 1.50P1. On the desilicated zeolites, the maximum yield observed over the highest Pt content P1 catalyst (59%), decreased over 1.38P1-D1 catalyst, to reach a maximum yield which is between that obtained by 0.98 and 1.10P1. However, a very slight increase was observed over 1.60P1-

D2 catalyst more than the highest P1 Pt content from 59 to 61%. The isomers evolutions are shown in Figure IV.4.

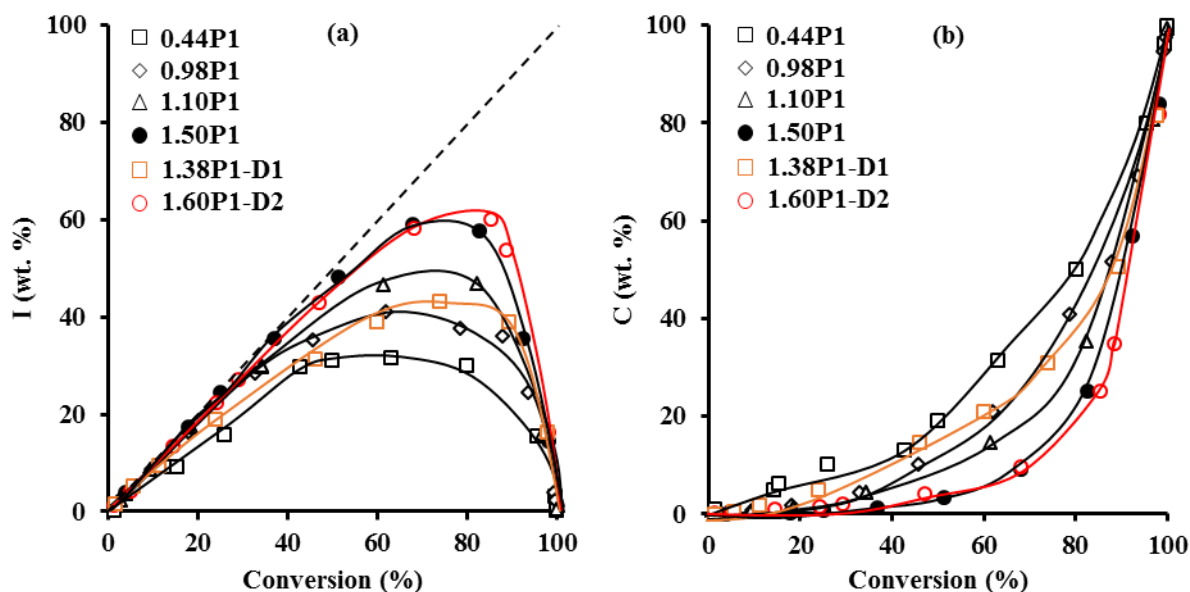


Figure IV.4 Yield in isomers (I) (a) and cracking (C) (b) products vs n-C₁₀ conversion obtained over series 1 catalysts.

The parent zeolite catalyst of series 2, 1.48P2 catalyst, yielded approximately around 45% of isomers products. This yield resembled that obtained over 0.98P1, 1.10P1, and 1.38P1-D1 catalysts. However, the desilicated form of this catalyst showed an unexpected decrease in the maximum isomers yield to ca. 13% over 1.53P2-D6 catalyst. The isomers yield evolution of this catalysts series is shown in Figure IV.5.

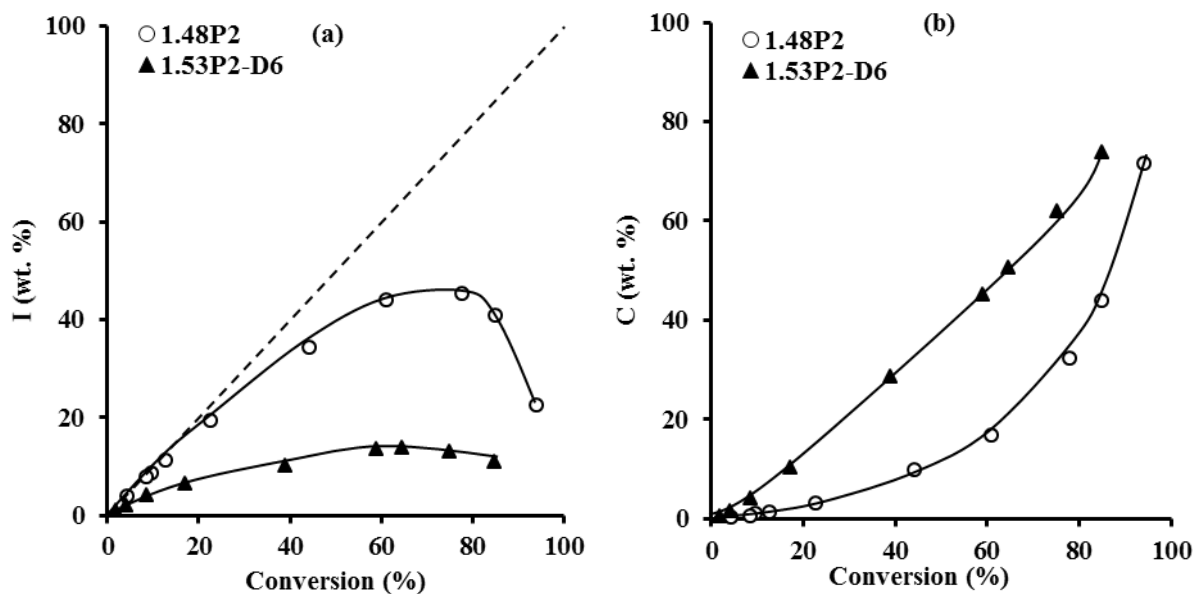


Figure IV.5 Yield in isomers (I) (a) and cracking (C) (b) products vs n-C₁₀ conversion obtained over series 2 catalysts.

With the lower Pt content of series 3 catalysts in comparison with other series, it has been seen that the maximum isomers yield is almost high (more than 54%) in comparison with the other series. The maximum yield obtained over the parent zeolite catalysts of this series (0.75MC) was ca. 54%. This yield increased over all its desilicated forms, to be 68% over MC-D1, 60% over MC-D2 and 67% over MC-D3 catalysts. The evolution of the isomers yield of this catalyst series is shown in Figure IV.6.

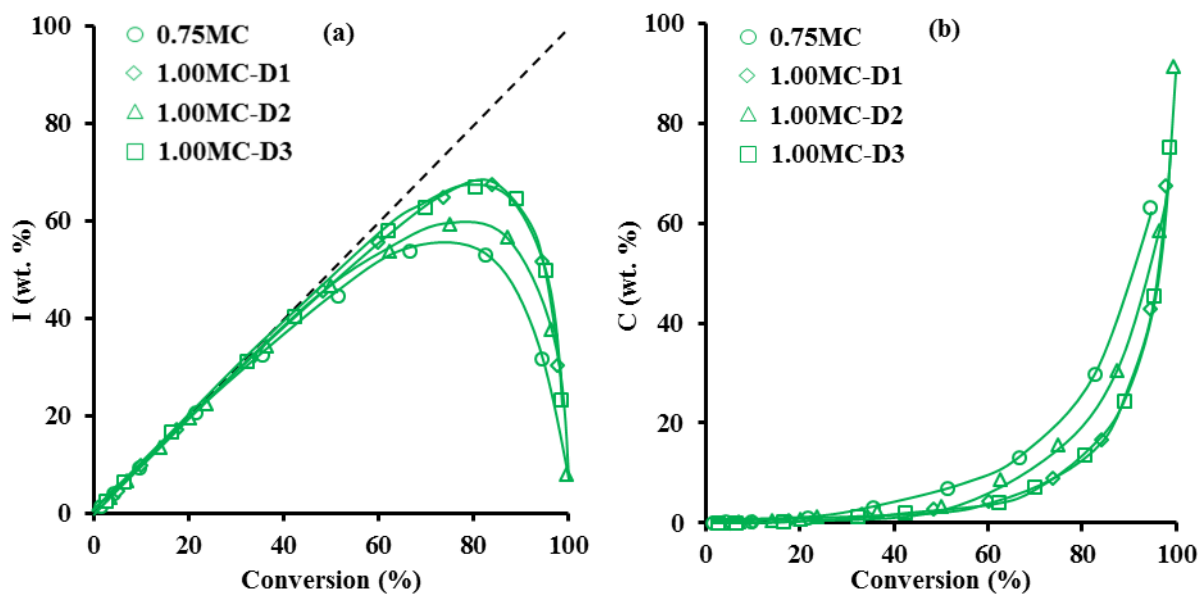


Figure IV.6 Yield in isomers (a) and cracking (C) (b) products vs n-C₁₀ conversion obtained over series 3 catalysts.

It is possible also to describe the transformation reaction of n-C₁₀ by the reaction scheme shown in Figure IV.7, in which every single step is considered irreversible, and follows a pseudo kinetic of order 1 [147]. This happens regardless of any of the characteristics of the tested catalysts, that is to say, the rate of reaction is proportional to the concentration of the n-C₁₀ reagent. The hydroconversion of n-C₁₀ occurs through following three reactions:

- isomerization, where k_1 and k_4 rate constants represent the isomerization of n-C₁₀ into monobranched isomers (M), then into multibranched isomers (B);
- cracking, where k_3 and k_5 rate constants represent M (monobranched) and B (multibranched) cracking, respectively;
- hydrogenolysis, represented by k_2 rate constant.

The values of the rate constants calculated by a software we possess that follows a classical simplex kinetic model that applies the Runge-Kutta method [292], are shown in Table IV.10. A rather good agreement between the experimental values and the theoretical curves was obtained for our catalysts (examples in Figure IV.8).

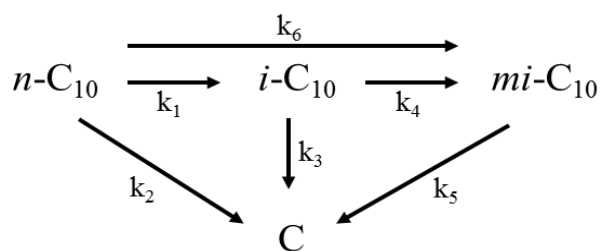


Figure IV.7 Reaction scheme of n-C₁₀ transformation.

According to this kinetic model, the low isomers yield in 0.44P1 and 1.53P2-D6 catalysts, is confirmed by the high value of k_2 (1.11 and 0.59 respectively) presented in Table IV.10, the kinetic constant responsible for direct transformation of n-C₁₀ to cracking products, in comparison with the other catalysts. Still these values are not high enough to say that the hydrogenolysis reaction is occurring on the Pt particles. For that, this side reaction is said to be neglected.

Table IV.10 Kinetic constants calculated by Runge-Kutta method.

Catalyst	k_1	k_2	k_3	k_4	k_5	k_6
0.44P1	1.00	1.11	0.00	1.35	2.28	0.33
0.98P1	1.00	0.05	0.00	1.54	3.39	0.13
1.10P1	1.00	0.04	0.15	1.05	1.65	0.12
1.50P1	1.00	0.04	0.00	1.99	1.96	0.00
1.38P1-D1	1.00	0.11	0.00	1.79	3.20	0.10
1.60P1-D2	1.00	0.05	0.00	0.93	3.49	0.10
1.48P2	1.00	0.10	0.00	1.68	3.32	0.10
1.53P2-D6	1.00	0.59	4.90	1.04	1.38	0.10
0.75MC	1.00	0.00	0.00	1.25	4.89	0.06
1.00 MC-D1	1.00	0.16	0.00	2.66	2.09	0.00
1.00 MC-D2	1.00	0.00	0.00	0.98	4.12	0.06
1.00 MC-D3	1.00	0.04	0.00	0.82	2.86	0.02

In addition to that, the high value of k_3 for 1.53P2-D6 catalyst, the kinetic constant responsible for transformation of monobranched isomers to cracking products before being transformed into multibranched isomers, confirms the high yield of cracking products

produced. This value was 4.9 on 1.53P2-D6 catalyst but was almost null on all the other catalysts. The high isomers yield in series 3 catalysts was also reflected by the very low k_2 and k_3 kinetic constants for these catalysts (almost zero values).

Figure IV.8 shows a good agreement between the experimental and theoretical data obtained for some catalysts for the hydroisomerization of n-C₁₀. The good agreement is shown by the fitting or partial fitting of the theoretical data to the experimental ones. However, for low isomers selective catalysts, the fitting is more pronounced on high isomers selective ones.

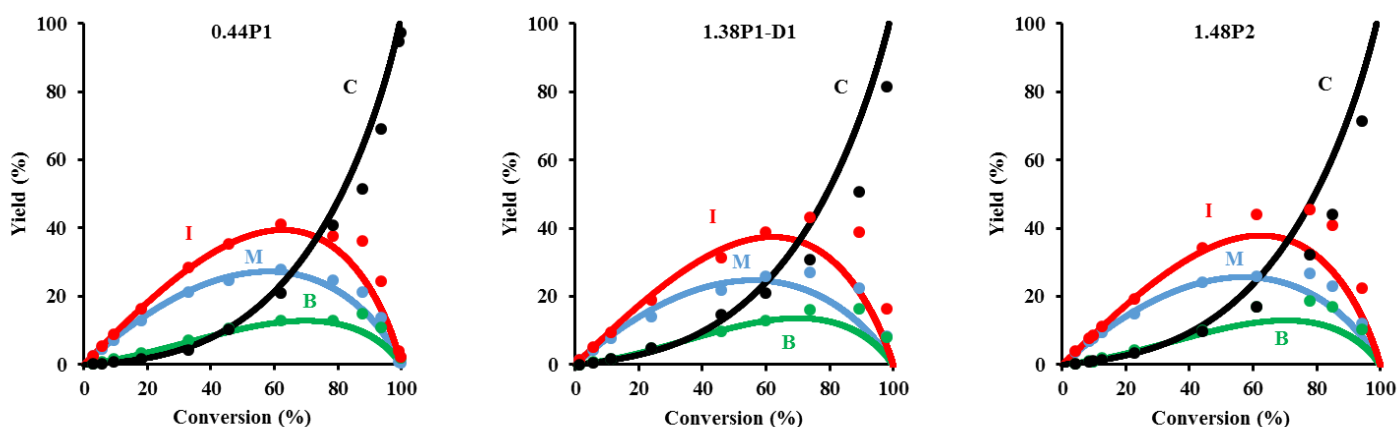


Figure IV.8 Yield into monobranched (M), multibranched (B), isomers (I) and cracking (C) products. Experimental points (points) and theoretical curves (continuous lines) obtained from the kinetic model.

The cracking products formed were mainly C₃ to C₇ molecules, as shown in Figure IV.9. The absence of methane (C₁) and presence of very low amounts C₂ and C₈ products allow to confirm that hydrogenolysis side reactions over Pt sites can be neglected. Let us consider C_{n-x} and C_x the cracking products formed by n-C₁₀, for example C₁ and C₉, C₂ and C₈, etc. As well seen in Figure IV.9, C₁ and C₉ products are not observed over any catalyst. In addition, the C₂/C₈ molar ratio is always close to unity over all the catalysts. The C₃/C₇ and C₄/C₆ molar ratios are also always close to unity, which gives finally a global symmetric distribution of the cracking products, and signifies that no secondary transformation of the cracking products had taken place over all the catalysts except in 0.44P1. The maximum C product produced over all catalysts was always C₅ product, except over 0.44P1 where it was C₃ product due to a possible secondary transformation of cracking products.

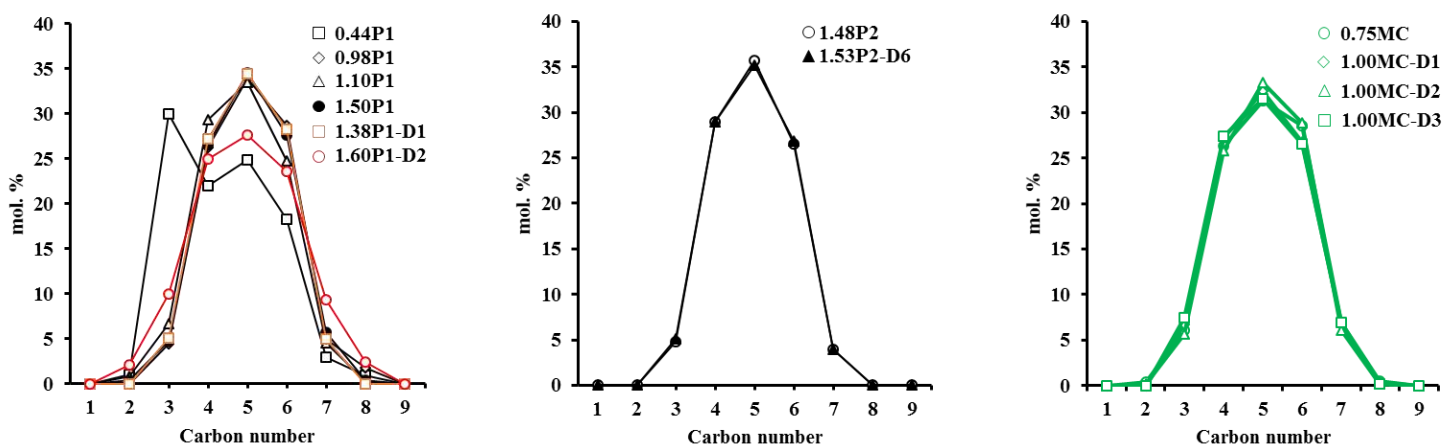


Figure IV.9 Cracking products distribution as a function of carbon number on the catalysts series: (1-3).

It is known that at low conversion (low X values), if the experimental curve follows the dotted line that bisects the two axes into equal parts, it means there is a total selective formation of isomers, i.e. only I products appear as primary ones and C products appear as a secondary transformation of isomers [289]. In this case, the scheme of transformation is then successive as follows: $n\text{-C}_{10} \rightleftharpoons \text{I} \rightarrow \text{C}$.

This aspect is observed at low X values on 0.98, 1.10P1, 1.38P1-D1 and 1.48P2 catalysts, and it was even more pronounced at higher X values on 1.50P1, 1.60P1-D2 and all series 3 catalysts. However, no points on the dotted line were detected for 0.44P1 and 1.53P2-D6 catalysts. In this case, some of the C products were directly transformed from the $n\text{-C}_{10}$. This is in agreement with the kinetic constants shown in Table IV.10, where k_2 is higher in 0.44P1 (1.11) and 1.53P2-D6 (0.59) catalysts, which signifies that this step is taking place on these catalysts but not in a well-observed extent (neglected hydrogenolysis). In contrast, all the other catalysts maintain this kinetic constant even lower than 0.1.

This significance can be quantitatively expressed also as well by the initial value of cracking/isomers (C/I) yield ratio drawn by the extrapolation at zero conversion of (C/I) vs conversion curve [289]. Table IV.11 provides information about the initial $(C/I)_0$ at zero X values for all the catalysts. This value is almost high in both 0.44P1 (0.45) and 1.53P2-D6 (0.5) catalysts. In contrast, in series 1, this value decreases as Pt content on P1 parent zeolite increases. The initial C/I ratio of D2 catalyst is similar to those obtained by 0.98 and 1.10P1

catalysts, but it increased to 0.1 on 1.38P1-D1 catalyst. P2 and all series 3 catalysts possessed low values, as 1.00MC-D1 and 1.00MC-D3 catalysts marked the lowest (0.005) amongst all.

Table IV.11 Initial multi- to mono-branched isomers ratios, initial cracking to isomers ratios, and number of acidic steps involved during n-C₁₀ transformation, on all the catalysts.

Catalyst	(B/M) ₀	(C/I) ₀	n _{a.s}
0.44P1	0.28	0.45	2.16
0.98P1	0.15	0.06	1.35
1.10P1	0.12	0.04	1.22
1.50P1	0.08	0.01	1.14
1.38P1-D1	0.20	0.10	1.50
1.60P1-D2	0.09	0.05	1.26
1.48P2	0.04	0.04	1.17
1.53P2-D6	0.36	0.50	2.26
0.75MC	0.02	0.03	1.11
1.00MC-D1	0.005	0.005	1.02
1.00MC-D2	0.01	0.018	1.07
1.00MC-D3	0.02	0.005	1.04

Figure IV.10 shows the variation of these ratios as a function of the ratio between the concentration of accessible Pt sites and the concentration of Brønsted acidic sites (n_{Pt} / n_{H^+}) for all the catalysts. It is clearly shown that the production of initial cracking products decreases sharply initially with a slight increase of n_{Pt} / n_{H^+} ratio, and then a very slightly decreasing curve is observed after a n_{Pt} / n_{H^+} value of ca. 0.03 (Figure IV.10-a). Another significance of this aspect can also be seen (Figure IV.10-b), where the majority of the maximum isomers yield on the catalysts seems to be increasing with the increase of n_{Pt} / n_{H^+} ratio starting also from ca. 0.03.

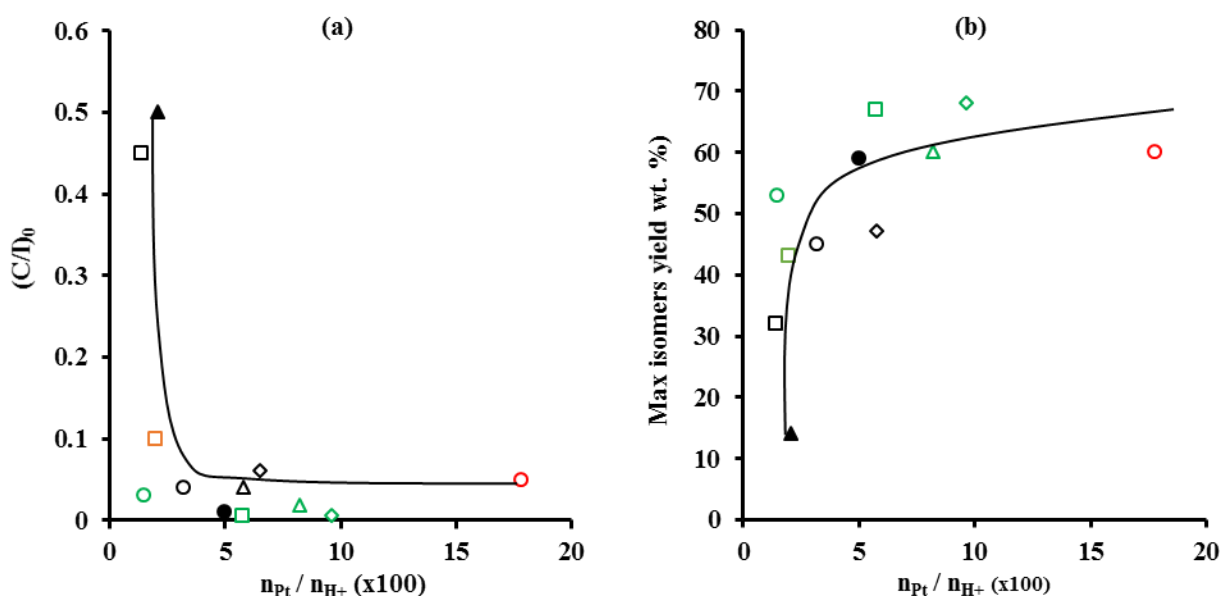


Figure IV.10 (a) Variation of initial C/I ratios, (b) variation of maximum isomers (I) yield; on the different catalysts as a function of n_{Pt} / n_{H^+} .

Table IV.11 provides another information about the number of acidic steps ($n_{a.s}$) responsible for the rearrangement and cracking of the olefin intermediates along their diffusion between Pt sites [289,293]. It was advanced that in order to obtain optimal catalytic characteristics, two conditions should be satisfied: n_{Pt} / n_{H^+} ratios high enough so that the rate of the reaction would be limited by the acidic steps, and the number of acidic steps ($n_{a.s}$) between two Pt sites low enough to catalyze one step of skeletal rearrangement or to crack the olefin intermediates [125]. The n_{Pt} / n_{H^+} ratio seems to be low in 0.44P1 and 1.53P2-D6 catalysts, and the number of acidic steps ($n_{a.s}$) involved is also higher than in the others. This implies that the optimal catalytic characteristics criterion are not satisfied for these two catalysts. This signifies the high number of cracking products produced initially and during the transformation of $n\text{-C}_{10}$.

As the $n_{a.s}$ number decreases, the maximum isomers yield increases, consequently, cracking decreases. This is what is clearly shown on all the catalysts, by comparing the number of acidic steps also to the earlier production of cracking products (C) as shown in the figures up (Figure IV.4, Figure IV.5 & Figure IV.6) for the three series, it is concluded that C products are produced more at lower X values as the number of the acidic steps involved is increasing. This is demonstrated by the shifting of the C curves left- and upwards. For example, in series 3 catalysts, Figure IV.6 shows that C products are produced earlier in 0.75MC and 1.00MC-D2

catalysts. These curves referring to series 3 catalysts are in agreement with the values of $n_{a,s}$ which are slightly higher in 0.75MC and 1.00MC-D2 than in 1.00MC-D1 and 1.00MC-D3. However, these series catalysts all preserve the $n_{a,s}$ value close to 1. This indicates that the olefin intermediates are undergoing only 1 step of rearrangement between two Pt sites.

5 Impact on the catalytic performance

After having a global overview on the characteristics of these zeolites before and after deislication in chapter 3, it is important to discuss how they impact, besides the bifunctional characteristics of the catalysts, the process of n -C₁₀ hydroconversion.

It is well known that the activity and selectivity of bifunctional catalysts depends significantly on ratio between the (de)hydrogenating and acidic sites. The increase in the (de)hydrogenating sites has a positive influence on: i) initial activity of the catalyst, ii) stability of the catalyst, iii) selectivity toward isomerization products [294]. In our work, the increase of the platinum content on the different P1 catalysts, increases clearly the yield in mono- and multibranched products, i.e. the total isomers yield ($I = M+B$). In addition, the activity was still maintained constant for the moderate Pt content, until the impregnation of the highest Pt content where there was a sharp increase in activity and TOF as well. This indicates that the increase in the Pt content serves in better feeding the acidic sites with the olefin intermediates and increases the activity of these sites at the highest Pt content [125,289,294]. It should be also noted that the ratio of n_{Pt} / n_{H^+} increases from 1.4 (lowest Pt content) to a range of 5-6 on the high ones (0.98, 1.1, and 1.5%Pt), but the yield in isomers (I) is still increasing in spite of a maintained balance between the accessible metallic and acid sites. The case reported in [294] demonstrates the increase in n_{Pt} / n_{H^+} ratio by increasing the Pt content while preserving acidity, i.e. a global increase in the ratio. In our work, the acidity was still being modified on the same support after impregnating different Pt contents, so the ratio was maintained constant even with high Pt contents. However, the same aspect was seen and the results were in agreement with the previous work [294].

The maximum isomers yield obtained by the 1.50P1 catalyst decreased again from 59 to 38% on the 1.38P1-D1 catalyst, but marks an unnoticeable increase to 61% on 1.60P1-D2 catalyst. In case of 1.38P1-D1 catalyst, the decrease in both the micro- and mesopore volume in P1-D1 (in spite of the appearance of a small hysteresis in the isotherm pattern), suggests to be ascribed to the contributions on inter-particle voids due to a disordered agglomeration of the

small crystals [214]. This allows the intermediates to suffer some diffusional limitations although a decrease in the crystal size was observed. This lead to their long-lasting contact with the acid sites, thus favoring their cracking. It seems that the crystal size here did not have a stronger impact than the volume of the mesopores. Moreover, the low metal to acid ratio ($n_{Pt} / n_{H^+} = 0.02$), can also attribute to the decrease in the isomerization yield noting that it is less than 0.03. This indicates that the acidic sites governed between two Pt sites are high enough to induce further cracking of the intermediates before being hydrogenated and exited from channels as well.

The case here between 1.50P1 and 1.60P1-D2 concerning the production of isomers is similar, but in every catalyst, a major factor is behind this observation. It is accepted that the value of the metal to acid balance in 1.50P1 is enough to induce isomerization ($0.05 > 0.03$), in addition to the high mesopore volume possessed ($0.58 \text{ cm}^3/\text{g}$). However, a decrease in the isomerization yield over 1.60P1-D2 was expected due to the decrease in the mesopore volume in 1.60D2, but the decrease of the crystal size that may favor easier diffusion of the intermediates (decrease of contact), in addition to the increase in the metal to acid ratio that was triple that of 1.50P1, removed this expectation. Therefore, it is suggested that it is not majorly the organization of the mesopore that increased slightly the yield, instead it is the diminish of the crystal size and the high metal to acid balance that permitted more isomerization steps to occur between Pt sites before cracking to take over.

Taking a look on the number of acidic steps involved in the olefin intermediates transformation on 1.50P1, 1.38P1-D1 and 1.60P1-D2 catalysts, it seems that it is less in 1.50P1 (1.14) and 1.60P1-D2 (1.26) in comparison to 1.38P1-D1 (1.5). These measurements confirm that the intermediates formed within the channels of 1.38P1-D1, were more trapped with the acidic sites, and subjected then to more acidic transformations. Nonetheless, the low mesopore volume, and the lack in the organization of these pores (unlike in P1-D2), would attribute to diffusional obstacles within this catalyst (1.38P1-D1). Therefore, the cracking of these molecules is then preferred over any other isomerization reactions, in order to decrease their size and facilitate their desorption and exit from the channels as well.

Moreover, an unexpected decrease in the maximum isomerization yield was seen from 45 to 13% on 1.53P2-D6 catalyst, in comparison with its parent 1.48P2 catalyst, in spite of an increase in the mesopore volume after the alkaline treatment by NaOH and TBAOH (0.54 to

0.61 cm³/g). However, the low n_{Pt} / n_{H^+} and the bad dispersion of Pt, together, allow us to assume that activity as well as the isomers selectivity will decrease. The decrease in activity is easily related to the idea that the number of Pt atoms is not enough to highly feed the acidic sites with the olefin intermediates. The aspect seen in the isomers selectivity decrease was seen by Martens et al. recently in 2015 [295]. They proposed another criterion to characterize the catalytic performance of a catalyst. The proposition says that the nanoscale intimacy between the metallic and the acidic sites of the support is better for the selectivity of the bifunctional catalysts towards isomers products [295]. In their work, the utilization of a large pore zeolite Y mixed with an alumina binder was chosen to investigate the effect of proximity between the metallic and acidic sites. Previously, it was suggested that having the metal functions as close as possible from the acidic functions, should prevent undesired secondary transformations [289]. However, the results with Martens et al. [295] contradicts the previous suggestion. It was found that when the Pt particles were in the closest position to the acidic sites, the feed components were obliged to diffuse into the micropores where the Pt particles are located. This leads to trap the olefin intermediates in the micropores due to their strong adsorption on the acidic sites and slow diffusion and longer residence time, which increases the probability of these intermediates to be cracked. In the contrary, in the same work reported, when the metal particles were located on the alumina binder, which means outside the zeolite crystals, the olefin intermediates formed were easily diffusing through the wide pores to the zeolite Y, where they undergo isomerization rather than cracking. Summing up these results with another ones [296,297], it is said that the optimal location for the metal function should not be in the micropores of the zeolites, but rather on the surface or in the mesopores of the zeolite.

According to these assumptions and taking into consideration large Pt particles in 1.53P2-D6 (12.5 nm) that are larger than the mesopore diameter (ca. 5 nm), makes them more probably located outside the mesopores, i.e. on the zeolite surface. However, since the Pt dispersion is very low, and though the number of Pt particles, it is suggested that the distance covered by the intermediates between every two Pt sites is long enough to induce the secondary transformations and favor cracking. This explains the low intimacy between the Pt and acidic sites.

In contrast, it was also expected that the microcrystal *BEA (MC) would have performed less efficient in comparison with all the other catalysts, due to the presence of large crystals which enhances long time contact of the intermediates with the acidic sites and, thus favors

their cracking. Moreover, the presence of only micropores in the structure should have enhanced the cracking of the olefin intermediates, due to their slow diffusion, long residence time and stronger adsorption with the acidic sites inside the micropores. However, in 0.75MC catalyst, the Pt size (7.53 nm) in fact is larger than the diameter of the pores, so the Pt is located on the zeolite's external surface, and the transformation is then occurring on the surface rather than inside the pores. According to the assumptions in [295–297], the presence of the metal particles on the zeolite surface induces high nanoscale intimacy between metallic and acidic functions, and thus favors isomerization and reduces their cracking.

Followed by desilication, 1.00MC-D1, 1.00MC-D2 and 1.00MC-D3 catalysts produced the highest isomers yield amongst all catalyst. Figure IV.6 shows that the yield increase up to 68% over 1.00MC-D1 in comparison with the parent MC, to 60% on 1.00MC-D2, and to 67% on 1.00MC-D2. The location of Pt particles (> 2 nm size) being more probably on the zeolite surface, with their high dispersion, suggests that the metal and acidic sites were at the intimacy that allows only one acidic transformation of the intermediates between two Pt sites, which is clearly revealed in the number of acidic steps involved ($n_{a,s}$ is ca. 1). Moreover, the increase in the mesopore volume could have also played a crucial role in the fast desorption of the intermediates from the acidic walls lowering their contact time with them and facilitating the fast diffusion of the molecules as they enter and exit the channels.

The very low initial B/M ratios in series 3 catalysts shown in Table IV.11, points to the aspect that the initially formed multibranched products were neglected, close to zero. In addition, the zero value of the k_3 kinetic constant responsible for direct transformation of mono to cracking products over these catalysts implies that no cracking took place for the monobranched products, and all cracking products were formed from multibranched products. This indicates the successive scheme followed in the $n\text{-C}_{10}$ transformation $n\text{-C}_{10} \rightleftharpoons M \rightarrow B \rightarrow C$.

6 Conclusions

The desilication of *BEA nanocrystal zeolites by NaOH alone and by NaOH incorporated with a low zeolite surface affinity pore directing agent (TPABr), caused a diminishing in the crystal size but a drawback in the textural properties, especially in presence of NaOH alone where no protection for the zeolite surface was provided. The use of TBAOH, which has stronger affinity to the zeolite surface, preserved the crystal size by total protection, and allowed

an improvement of the textural properties by orienting the attack of hydroxyl ions through the pores only. In the synthesized microcrystal *BEA series, the use of the three alkaline treatments caused an improvement of the textural properties.

The designation of an “ideal” bifunctional catalyst was achieved by increasing the Pt content and then testing in the hydroisomerization of n-C₁₀. In spite of the improvement of the textural properties by use of TBAOH in the nanocrystal *BEA (in 1.53P2-D6), there was a drop in activity due to the low Pt content that wasn't enough to feed well the acidic sites, and a drop in selectivity due to the large Pt particles located on the zeolite surface, that probably induced far distance between each two Pt sites, i.e. many acidic sites were accessible to wide range of rearrangement and cracking processes. In the other hand, the diminishing of crystal size caused by NaOH alone, and consequently the diminish of the diffusional path length, should have enhanced the catalytic performance of the 1.38P1-D1 catalyst. However, the drawback in the textural properties in this zeolite catalyst (P1-D1), in addition to the low bifunctional characteristics as Pt dispersion, did not improve its global catalytic performance. The use of TPABr that decreased the crystal size, in addition to the high Pt dispersion, and high metallic to acidic balance possessed with this catalyst (1.60P1-D2), preserved its activity and improved the selectivity.

The same alkaline treatments were applied on a synthesized microcrystal *BEA. It was found that there is an improvement in the catalytic performance in terms of activity and selectivity due to a probable high nanoscale intimacy between the Pt and acidic sites on the zeolite surface and not inside the micropores or the initially formed mesopores (Pt size larger than pore aperture, i.e. located on zeolites surface), in addition to the improved textural properties which enhances better diffusion through the channels of the zeolite.

Chapter V

**Impact of desilication of
*BEA zeolites on the
catalytic performance in
hydroisomerization of $n\text{-C}_{10}$,
 $n\text{-C}_{12}$ & $n\text{-C}_{14}$.**

1 Introduction

In the hydroisomerization of paraffin, it is not always evident that the pore structure is behind the expected catalytic performance, but rather the bifunctional characteristics might account for larger influence. For example, as reported in literature, the location of the hydro/dehydrogenation sites is of much interest when being inside the mesopore or on the external surface of the crystallites, hence an optimal nanoscale intimacy between them and the active sites might induce further isomerization instead of cracking [295,298,299]. In the previous chapter, it was found that in case of the microcrystals, higher selectivity to isomers products was obtained in spite of the lower textural properties comparable to nanocrystal hierarchical zeolites in the hydroisomerization of n-C₁₀. This was attributed to the bifunctional properties that were behind the observation of such an aspect.

Seeking for the factors that might further improve the catalytic performance in hydroisomerization reactions is continuous. However, it is also precious to find how might bulky molecules have an impact in such reactions. For example, it was stated by Marcilly that during the conversion of paraffin, the rate of cracking was increasing as the carbon number increased to reach a maximum with carbon number equal to 16, then a decrease was observed [300]. He also mentioned in his book that this was in contradiction with previous results observed by Vynckier and Froment where the carbon number of which maximum rate constant was reached and after decreased, was 9 [300]. Soualah et al. [301] reported that isomers were the main products produced over Pt/H-*BEA, while cracking is the main reaction to be observed over Pt/H-ZSM-5 and Pt/H-MCM-22, with bulky molecules as long chain paraffin. The large channels of *BEA zeolite contribute to such an aspect, and the blockage of intermediates in the other zeolites lead to extensive cracking. The isomerization yield was continuously decreasing in the investigated catalysts as the chain length was increasing from 10 to 14 and finally to 16 carbon number n-alkanes [301]. Konnov et al. [302] reported the results of hydroisomerization of different n-alkanes (n-hexane, n-octane and n-hexadecane) over Pt-MOR catalyst. They found that the activity, unlike the selectivity towards isomers products, increased with chain length.

Martens et al. [303] study showed that the isomerization yield of n-C₁₀ exceeded that of a tetra-branched paraffin (pristane i-C₁₉), but surprisingly was lower than the normal n-C₁₉ form by 20% of yield, over conventional and hierarchical Pt/ZSM-22 catalysts. Rossetti et al. jumped

to higher carbon number chains, and studied the difference between n-C₁₆ and n-C₂₈ over Pt/SiO₂-Al₂O₃ catalyst. It was found over this catalyst, that the activity of the bulkier molecules was slightly more active than the lower one, but the isomerization yields were highly comparable.

The objective in this chapter is to investigate if the chain length increase have an impact on the activity and isomers selectivity over only the nanocrystal *BEA series catalysts (series 1 & 2), in the hydroisomerization of n-C₁₀, n-C₁₂ and n-C₁₄, and to verify if the presence of inter- and intracrystalline mesopores have an impact on the chain length in the hydroisomerization reaction.

2 Catalysts activities and products selectivity

2.1 Catalysts of series 1

2.1.1 Catalysts activities

Figure V.1 shows that 1.50P1 catalyst is always more active than its desilicated forms in the three alkanes transformations. As reported in the previous chapter that was concerned in the hydroisomerization of only n-C₁₀ over the same catalysts, that the activity was shown to increase with Pt content, where its maximum was observed with 1.5% of Pt on P1 catalyst. Figure V.1 shows the evolution of the activity during the different n-alkanes transformations over the catalysts of this series (S1). As discussed previously, 1.38P1-D1 catalyst was more active than 1.60P1-D2 catalyst during n-C₁₀ transformation, but with increasing chain length, the latter becomes more and more active than the former catalyst, where the 1.60P1-D2 conversion curves shift leftwards to be leading that of 1.38P1-D1 in n-C₁₂ and n-C₁₄ transformations. In all cases, the 1.50P1 catalyst is more active than its desilicated forms.

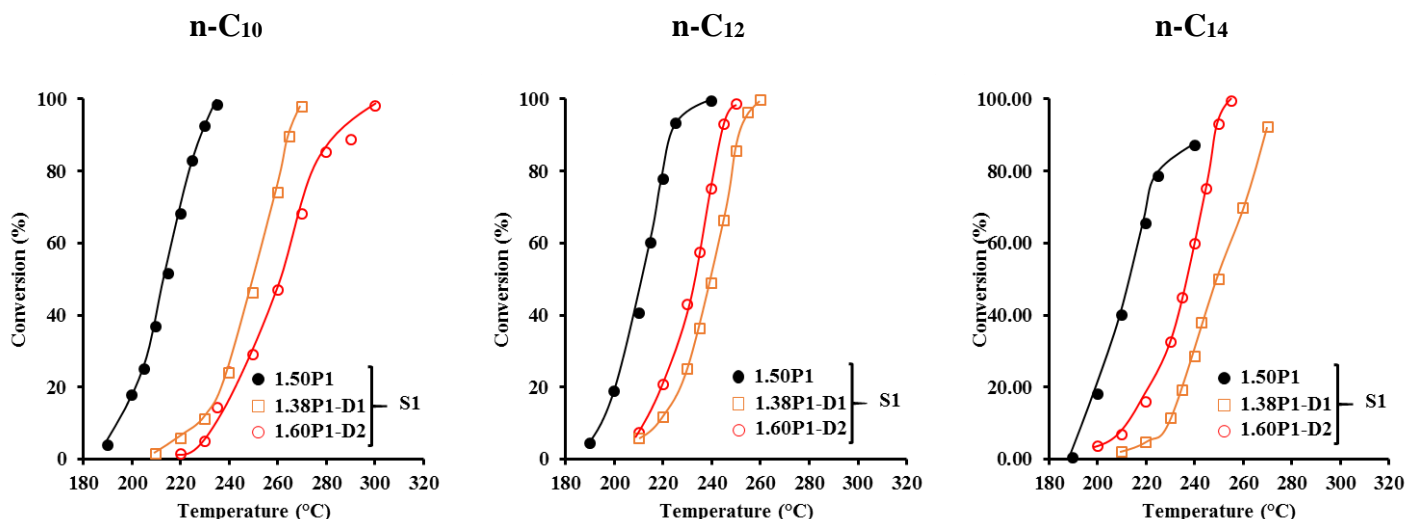


Figure V.1 n-alkanes conversions vs temperature over series 1 catalysts.

The TOF values (Table V.1) increased as well with the increase of chain length, especially in 1.50P1 and 1.60P1-D2. However, a remarkable increase was noticed in the TOF exhibited by 1.38P1-D1 on n-C₁₂, and in a lesser extent over 1.60P1-D2. The TOF values of 1.50P1 catalyst is always exceeding that of its desilicated forms, and 1.60P1-D2 always that of 1.38P1-D1 except on n-C₁₀ where they were similar.

Table V.1 The n_{Pt}/n_{H^+} ratios, activity and TOF values of series 1 catalysts.

Catalysts	n_{Pt}/n_{H^+}	n-C ₁₀		n-C ₁₂		n-C ₁₄	
		Activity (g _{C10} .g _{cat} ⁻¹ .h ⁻¹)	TOF (h ⁻¹)	Activity (g _{C12} .g _{cat} ⁻¹ .h ⁻¹)	TOF (h ⁻¹)	Activity (g _{C14} .g _{cat} ⁻¹ .h ⁻¹)	TOF (h ⁻¹)
1.10P1	5.8	0.4	7	0.75	9.5	0.8	10
1.50P1	5.0	5.0	72	8.0	97	9.4	97
1.38P1-D1	2.92	0.5	16	2.3	61	1.2	27
1.60P1-D2	17.8	0.3	9	3.2	75	3.5	69

2.1.2 Products selectivity

The increase of Pt content on the P1 catalyst influenced positively the selectivity towards isomers products. As shown in Figure V.2 for series 1 catalysts, the increase in Pt content caused an increase in the isomers yield from ca. 30% on the least Pt content (0.44P1) to 59% on the highest (1.50P1). However, this yield decreased over 0.44P1 as chain length increased,

but the decrease was more realized during n-C₁₂ transformation. Over 1.10P1, the decrease was very slightly observed even though there was, as chain length increase, with even more decrease during n-C₁₂ transformation. On the highest Pt content 1.50P1, the yield was maintained constant on n-C₁₀ and n-C₁₂ (59%), but decreased to ca. 40% on n-C₁₄. Note that during n-C₁₄ transformation, starting from ca. 1% wt. of Pt was needed to obtain a balanced catalyst where we see nearly similar selectivity to isomers as Pt exceeded 1% wt. The desilicated form 1.38P1-D1 was less selective towards isomers in comparison with 1.50P1 in n-C₁₀ hydroconversion. However, the selectivity of 1.38P1-D1 improved on n-C₁₂ but dropped again on n-C₁₄. No change in the yield was observed by increasing the n-alkane chain length over the 1.60P1-D2 catalyst (ca. 60%).

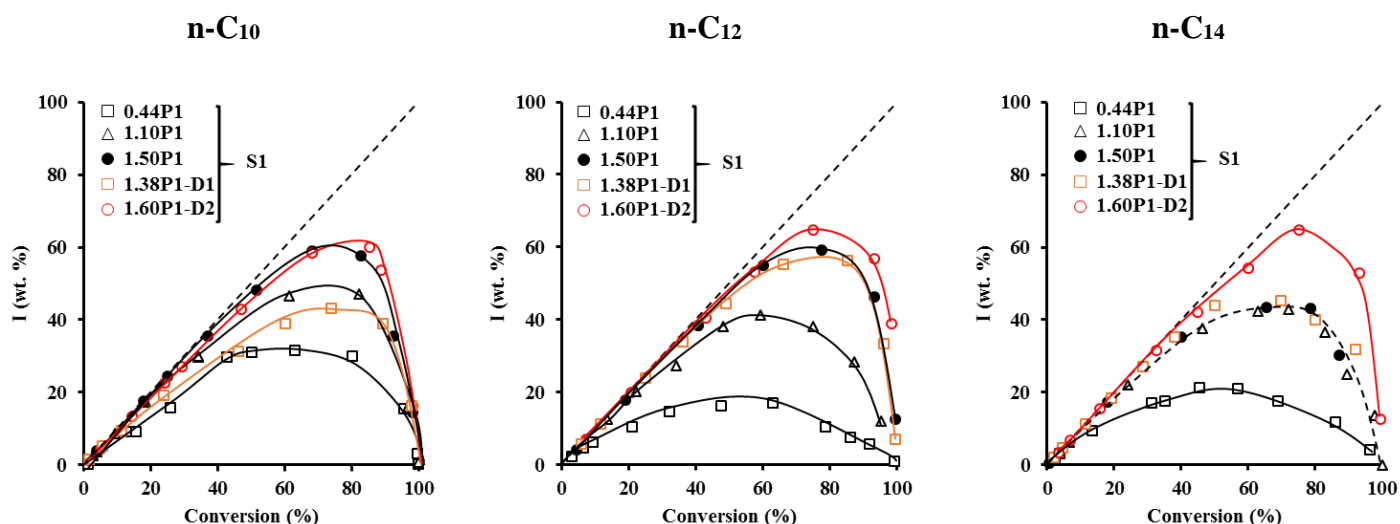


Figure V.2 Yield in isomers over series 1 catalysts in the three n-alkanes transformations.

Figure V.3 shows the cracking product distribution over the catalysts of the this series during the different n-alkanes transformations. The data of the cracking products were taken at 10-20% cracking yield. The cracking products formed were mainly C₃ to C₇, C₃ to C₉ and C₃ to C₁₁ molecules, on n-C₁₀, n-C₁₂ and n-C₁₄ respectively. The absence of methane (C₁) and presence of very low amounts ethane (C₂) and its corresponding second cracked product, i.e. C₈ on n-C₁₀, C₁₀ on n-C₁₂, and C₁₂ on n-C₁₄, allow us to consider that hydrogenolysis side reactions over Pt sites can be neglected. Let us consider C_{x-m} and C_m the cracking products formed by n-C_x, for example C₁ and C₉, C₂ and C₈ in case of n-C₁₀, with the same manner followed in n-C₁₂ and n-C₁₄.

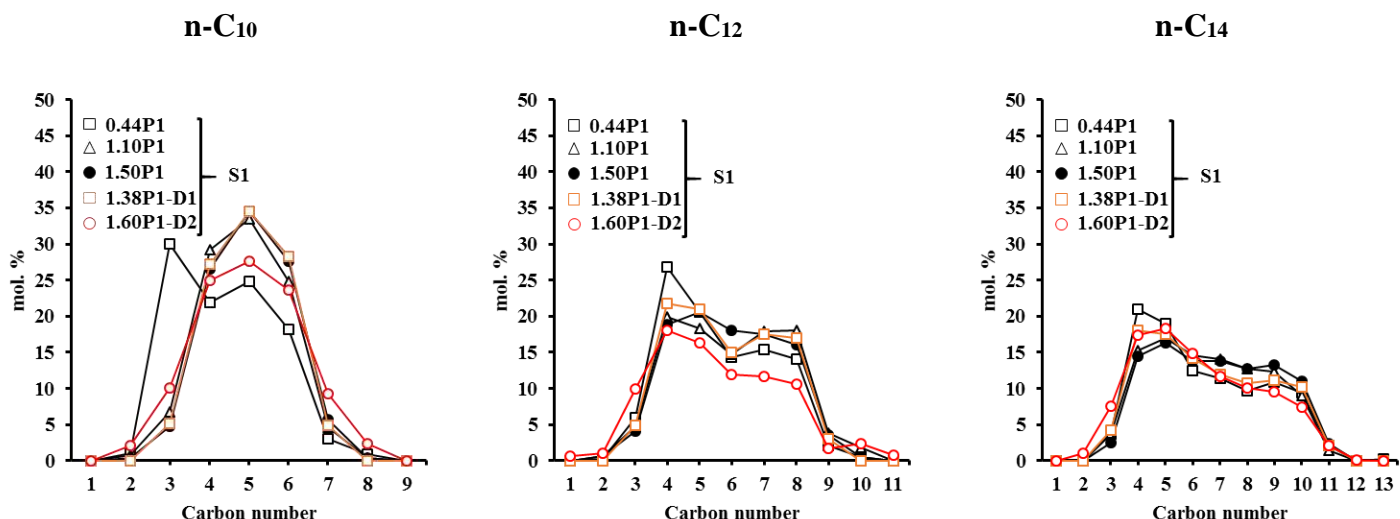


Figure V.3 Cracking products distribution over series 1 catalysts in the transformation of the three n-alkanes.

In the transformation of n-C₁₀, C₁ and C₉ products are not observed over any catalyst of this series. The molar ratios of C₂/C₈, C₃/C₇ and C₄/C₆ are always close to unity, which gives finally a global symmetric distribution of the cracking products, and signifies that no secondary transformation of the cracking products had taken place over all the catalysts. However, an asymmetrical distribution caused by high C₃/C₇ molar ratio was observed due to a possible such transformation over 0.44P1 (not well-balanced catalyst). The maximum C product produced over all catalysts was always C₅ product, except over 0.44P1 where it was C₃ product. The transformation of n-C₁₂ have shown asymmetrical distributions on the majority of the catalysts of series 1. However, increasing the Pt content over P1 catalysts was efficient to reach a near quasi plateau of distribution. The same aspect was observed on n-C₁₄ transformation, which indicates that 1.5% wt. of Pt was the best amount to obtain a well-balanced catalyst and not starting from 1% as mentioned above. Note that the molar ratios between the small and large cracking products of all catalysts of this series 1 (except 1.50P1) during n-C₁₂ and n-C₁₄ transformations were all higher than 1, which indicates that possible secondary transformation were observed on these catalysts.

2.2 Catalysts of series 2

2.2.1 Catalysts activities

In the catalysts of series 2, the 1.53P2-D6 catalyst, the desilicated form of 1.48P2 catalyst, is always less active no matter what the chain length was. This was displayed in the activity curves where 1.48P2 catalyst always converts the three n-alkanes at earlier temperatures than 1.53P2-D6 catalyst does (Figure V.4).

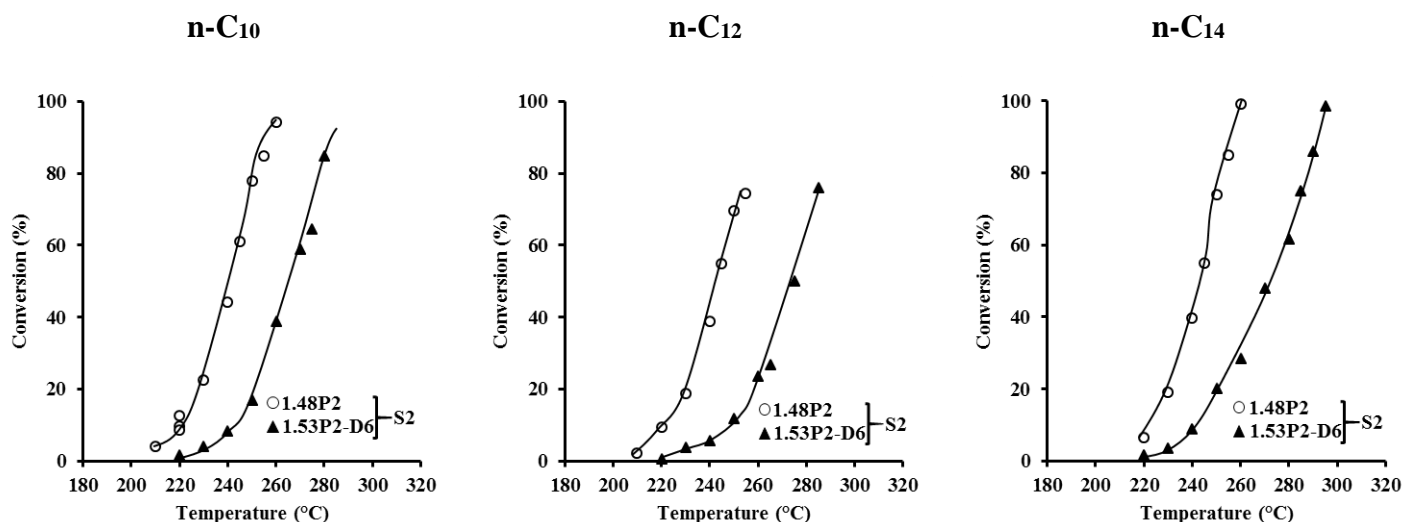


Figure V.4 n-alkanes conversions vs temperature over series 2 catalysts.

Similarly, the TOF values (Table V.2) exhibited for the desilicated samples are always less than the parent ones, marking always the highest value during n-C₁₂ transformation. The lower activity and TOF values exhibited in 1.53P2-D6 catalyst is due to the low number of Pt atoms unable to feed enough the acidic sites with the olefin intermediates, knowing that the metallic to acidic ratio is low (0.023).

Table V.2 The n_{Pt}/n_{H^+} ratios, activity and TOF values of series 2 catalysts.

Catalysts	n_{Pt}/n_{H^+}	n-C ₁₀		n-C ₁₂		n-C ₁₄	
		Activity (gC ₁₀ .g _{cat} ⁻¹ .h ⁻¹)	TOF (h ⁻¹)	Activity (gC ₁₂ .g _{cat} ⁻¹ .h ⁻¹)	TOF (h ⁻¹)	Activity (gC ₁₄ .g _{cat} ⁻¹ .h ⁻¹)	TOF (h ⁻¹)
1.48P2	3.20	1.2	29	1.7	33	1.6	27
1.53P2-D6	2.34	0.28	6.9	0.35	9.4	0.25	5.7

2.2.2 Products selectivity

The isomers yield on 1.48P2 decreased more on n-C₁₂ than on n-C₁₄ in comparison with n-C₁₀ (Figure V.5). The 1.53P2-D6 catalyst have also shown dramatically a decrease in this yield to around 13% without a remarkable change with chain length. Note that the mesopore volume and pore size diameter for these two catalysts are the highest among all catalysts of this work, but surprisingly the yield was not though.

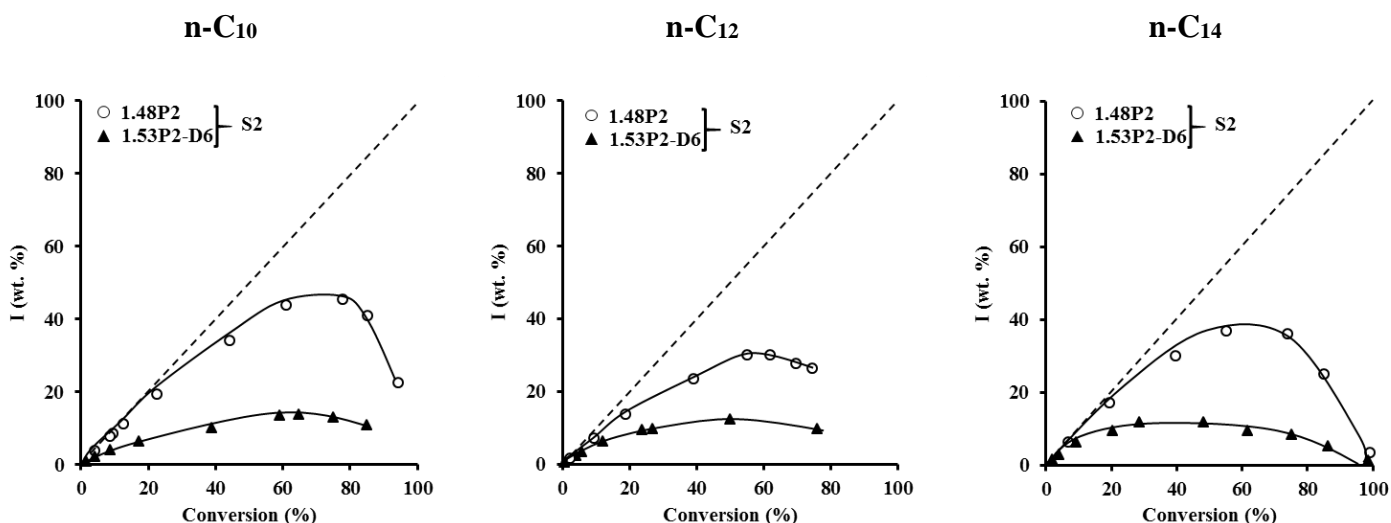


Figure V.5 Yield in isomers over series 2 catalysts in the three n-alkanes transformations.

The aspects of the cracking product distributions revealed over the catalysts of this series are similar to those observed over series 1 catalysts, with no particular catalyst of the two catalysts of this series is showing an asymmetrical distribution of cracking products in n-C₁₀ transformation. Figure V.6 shows the distribution of the cracking products on the three n-alkanes. Note that on n-C₁₂ and n-C₁₄ the shape obtained did not reach a plateau, signifying the non-well balanced catalysts of this series.

n-C₁₀

n-C₁₂

n-C₁₄

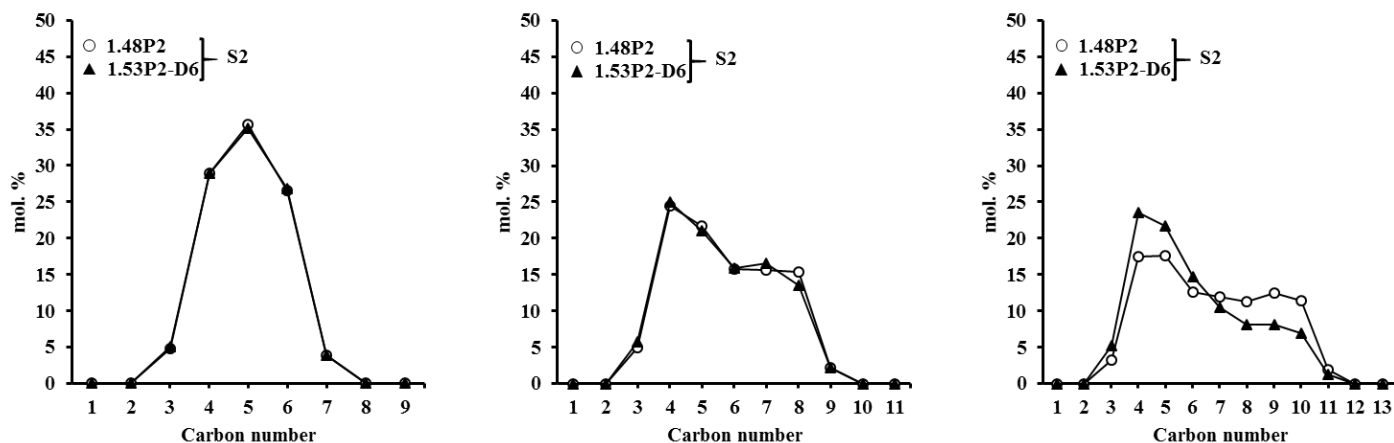


Figure V.6 Cracking products distribution over series 2 catalysts.

3 Catalytic performance

The nanocrystal catalysts series were investigated in the transformation of different n-alkanes to study the impact of chain length in the hydroisomerization reaction. It was meant at the beginning to study the effect of Pt content (in P1) on catalysts activity and isomers selectivity. The well-balanced P1 catalyst (1.50P1) was observed to have stable activity and selectivity to isomers during n-C₁₀ and n-C₁₂ transformations, whereas a decrease in isomers selectivity only was observed during that of n-C₁₄. To explain the evolution of the catalysts performance during n-C₁₄ in specific, it is good to rely on either the textural or the bifunctional characteristics, and sometimes we might rely on both. No doubt that the textural and bifunctional characteristics should account for the increase and decrease of the isomers yield after 1.50P1. However, in the cases to be reported, one of the characteristics would dominate over the other. It was expected as in 1.50P1 that the 1.60P1-D2 would be less selective to isomers as we reach to n-C₁₄, however the result was not though. The porous system of P1 zeolite is better than that of P1-D2, but the hysteresis loop obtained for P1-D2 catalyst (Figure III.6; chapter III), suggests the appearance of organized inter- and intracrystalline mesopores, which helps the diffusion of the intermediates to be more facile, and reduces the risk of being trapped inside to induce further cracking. Nonetheless, the majority of the crystallites in P1-D2 zeolite are smaller than that possessed in P1 (Figure III.3 and Figure III.4; chapter III) which may account to a facilitated diffusion of the molecules no matter what the chain length was. Moreover, the metallic to acidic ratio of 1.60P1-D2 is ca. 3 times that of

1.50P1 catalyst, that might be also an additional parameter that enhanced the maintained isomers yield in n-C₁₄ over 1.60P1-D2 and not over 1.50P1.

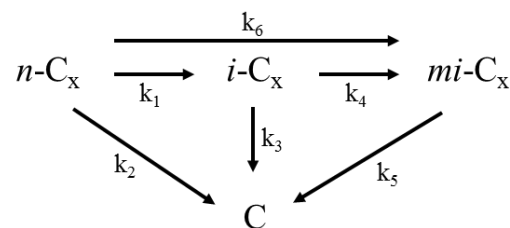
Over the catalysts of series 2, the dispersion of Pt seems to be low on the catalysts, consequently, the concentration of Pt sites will be low, and large Pt sizes will be obtained. However, still the Pt size in P2 catalyst is less than the pore diameter, so it is assumed to be located inside the mesopores, in opposition to the location of Pt particles on P2-D6, assumed to be more probably on the surface being larger than the pore diameter. However, the low dispersion exhibited in 1.53P2-D6 catalyst, causes higher distance between the metallic and acidic sites, and suggests more cracking steps to be induced. This is reflected in the number of acidic steps involved where it was always high (ca. 2). Comparing P2 catalyst with series 1 catalysts, the higher textural properties of P2 didn't mark an influence in this case, but rather the bifunctional characteristics. According to Martens et al. [295], the optimal location for the metal particle shouldn't be in the micropores, but rather in the mesopores or on the surface of the zeolite. However, in spite of the Pt presence inside the mesopores, but their low dispersion in P2 catalysts was low, which makes the distance between them and acidic sites larger, causing in more acid steps, and thus reduces the isomers yield. As a summary, the low bifunctional characteristic of this series dominated the influence of the high textural properties possessed within both catalysts. Moreover, still the 1.53P2-D6 catalyst possesses lower bifunctional characteristics, highly reflected in the low activity and selectivity to isomers products.

Similarly as for n-C₁₀ different steps transformations in chapter 4, the values of the rate constants of the different occurring steps for n-C₁₂ and n-C₁₄ transformations, calculated using the classical simplex kinetic model provided by Runge-Kutta method [292], are shown in Table V.3. Note at the beginning that the values of k_2 are the lowest in comparison to all of the other rate constants. This confirms the ignorable side reactions as hydrogenolysis to be taking place. Moreover, the value of k_3 is found to be also near to zero over all the catalysts except on 0.44P1 and 1.53P2-D6, the lowest isomers yielding catalysts (most cracking yielding ones), which indicates that the formed monobranched isomers are being cracked in high extent over these two catalysts. The value of this rate constant (k_3) is noticed to be increasing with chain length, which is also confirmed by the decrease of isomers yield (increase in cracking yield) with chain length increase. However, the second hydrocracking step occurring (cracking of B products), exhibit rate constants (k_5) higher than those (k_3) in the first hydrocracking step

(cracking of M products). This is behind the fact that β -scission becomes more favorable as the branching degree of the carbon chain increases [147].

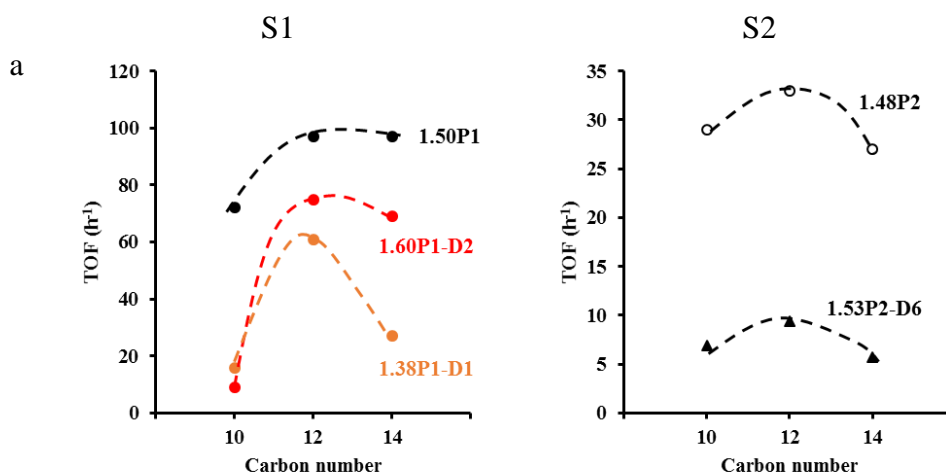
Globally, summing up the overall behavior of the rate constants, it is noticed that there is an increase in the values of the majority as chain length increases, except in hydrogenolysis rate constant k_2 where there is a decrease, suggesting that it is more and more pronounced for hydrogenolysis to disappear as chain length increases.

Table V.3 The corresponding kinetic constants of the different reaction steps during n-C₁₀, n-C₁₂ and n-C₁₄ transformations, calculated by Runge-Kutta method.



Catalysts	n-C ₁₀						n-C ₁₂						n-C ₁₄					
	k ₁	k ₂	k ₃	k ₄	k ₅	k ₆	k ₁	k ₂	k ₃	k ₄	k ₅	k ₆	k ₁	k ₂	k ₃	k ₄	k ₅	k ₆
0.44P1	1.00	1.11	0.00	1.35	2.28	0.33	1.00	0.45	3.99	3.36	4.33	0.29	1.00	0.19	3.59	4.60	4.10	0.42
1.10P1	1.00	0.04	0.15	1.05	1.65	0.12	1.00	0.00	1.02	1.54	1.46	0.33	1.00	0.00	0.28	1.81	1.9	0.33
1.50P1	1.00	0.04	0.00	1.99	1.96	0.00	1.00	0.01	0.00	0.70	1.53	0.14	1.00	0.07	0.00	1.81	3.41	0.21
1.38P1-D1	1.00	0.11	0.00	1.79	3.20	0.10	1.00	0.00	0.00	0.88	1.47	0.13	1.00	0.00	0.68	1.07	1.43	0.28
1.60P1-D2	1.00	0.05	0.00	0.93	3.49	0.10	1.00	0.02	0.00	0.6	3.02	0.18	1.00	0.00	0.00	0.42	2.3	0.45
1.48P2	1.00	0.10	0.00	1.68	3.32	0.10	1.00	0.37	0.49	2.26	4.26	0.74	1.00	0.00	1.28	1.17	1.98	0.56
1.53P2-D6	1.00	0.59	4.90	1.04	1.38	0.10	1.00	0.41	12.0	0.00	16.5	0.98	1.00	0.20	7.84	5.74	11.6	0.78

No dense information about the impact of chain length on the activity per Brønsted acid sites (TOF) in the hydroisomerization reactions. Nevertheless, some researchers reported the constant evolution of the TOF with chain length, that was in the 30-40 h⁻¹ range with n-C₁₀, n-C₁₄ and n-C₁₆ over Pt-*BEA catalysts [301]. Other researchers reported recently in 2013 the enhanced activity as chain increased (n-C₆, n-C₈ and n-C₁₆) over Pt-MOR catalysts [302]. However, it is expected in our work to have an increasing trend of TOF values with chain length, but as we see in Figure V.7-a, the shape of the TOF change is resembling a parabola behavior, with a maximum obtained during n-C₁₂ hydroconversion. In the beginnings of 1970's, R. L. Goring [304] measured the diffusivities of n-paraffin ranging from ethane to n-tetradecane, and found that the diffusion of n-dodecane was faster than that of n-decane and n-tetradecane. This phenomenon was termed the “window effect”. However according to the results we have, the selectivity to isomers products obtained is not always in agreement with this “window effect” assumption as it is not reliable to say that the diffusion of n-C₁₂ is more rapid than the other two n-alkanes. This is because despite of the maximum TOF observed during n-C₁₂ transformation, no improvement of isomers selectivity was shown on the majority of the catalysts but rather a decrease in comparison to n-C₁₀ and n-C₁₄, as Figure V.7-b illustrates that more acidic steps are involved during n-C₁₂ transformation, i.e. higher selectivity to cracking.



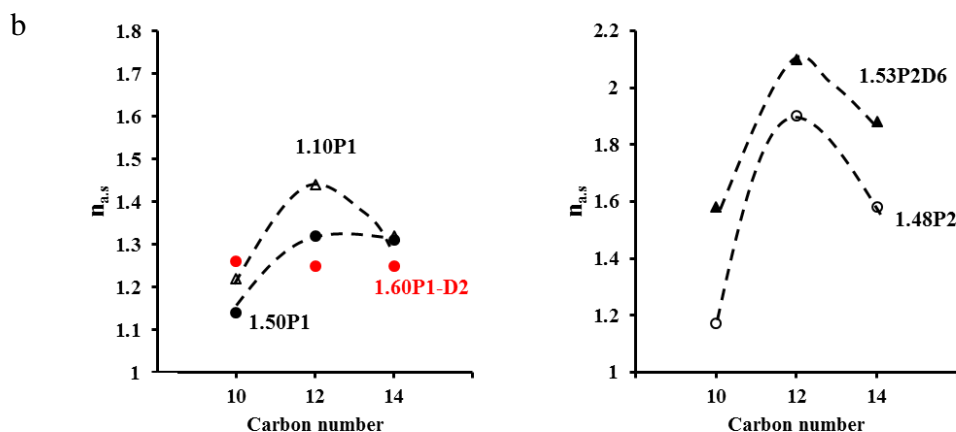


Figure V.7 TOF values (a) and $n_{a,s}$ (b) vs carbon number for catalysts of series 1 and 2.

The higher TOF exhibited in case of n-C₁₂ transformation with the associated higher selectivity to cracking products means that the apparent strength of the acidic sites might be higher. This indicates that the interaction of these molecules with the zeolite is changing in case of n-C₁₂ and seems to be different from that with n-C₁₀ and n-C₁₄. In the late 1980's, Derouane [305] described the confinement effect in zeolites in which interactions between the sorbate and the walls of the zeolite play a major role in the sorption and catalytic activation, that is to say that adsorption and catalytic properties of zeolites are strongly influenced by the confinement effect [306]. Moreover, as reported recently in 2014 by Iglesia et al. [307], that the combined effects of confinement and acidic strength on the reactivity of the Brønsted acid sites were seen, and as stated in literature that it accounts for the stability of the adsorbed intermediates that further determine the reactivity and selectivity in acid catalysts [218,308,309]. This effect that depends also on the size of the molecule traversing the channels, seems to be more pronounced with n-C₁₂ molecules than the other n-alkanes. According to what was advanced, the more confined molecules in the channels of the zeolite will lead to higher interaction with the acidic sites, and will consequently provoke higher activity and selectivity towards cracking products. This phenomenon appeared to be dominant on the hydroisomerization of n-C₁₂ molecules over the used *BEA zeolites based catalysts.

4 Conclusions

In studying the impact of chain length on the catalytic performance of the requested commercial and desilicated *BEA zeolites in the hydroisomerization of n-C₁₀, n-C₁₂ and n-C₁₄, it was seen that the textural and bifunctional characteristics can be behind the positive or negative influence either together or separately as one might dominate over the other. A special

phenomenon appeared with the increased TOF values during n-C₁₂ transformation. The high selectivity to cracking products in case of n-C₁₂ as a result of the apparent higher strength of the acidic sites, was said to be due the confinement effect and the stronger interactions of the n-C₁₂ molecules with the zeolite's acidic sites (higher TOF values) than the other two alkanes.

General Conclusions

General Conclusions

Zeolites are the most important molecular sieves used in most of refining and petrochemical industry. However, diffusional limitations may rise due to the small size of the zeolite's micropores possessed. The hierarchization of these zeolites by post synthetic procedures is the most common recent strategy to favor the fast diffusion of large molecules inside the zeolite channels by targeting the pore system of the zeolites. Seeking for improved diffusion of molecules inside the zeolitic pore systems of *BEA zeolites, we tend to subject commercial nanocrystal *BEA zeolites and synthesized microcrystal one to several alkaline treatments by NaOH alone and by NaOH mixed with pore directing agents as tetrapropylammonium bromide (TPABr) and tetrabutylammonium hydroxide (TBAOH).

It was found the mass yield, crystallinity and microporosity were seen to decrease continuously with total concentrations of HO⁻ anions. Particular cases for preservation of both crystallinity, microporosity and crystallites size in case of nanocrystals, attributing these observations to the protective effect played by the pore directing agents. The normalization of the microporosities of the samples with respect to their crystallinities revealed that the desilication treatments had a direct impact on the crystallinity and not the microporosity. The mesoporous content was seen to elevate more upon use of NaOH alone especially in the nanocrystals, while the contrary was seen in case of microcrystals where the company of the pore directing agents served in introducing more mesopores. The increase of Brønsted acidity at lower HO⁻ concentrations was attributed to probable recrystallization and realumination, with a pronounced decrease at higher alkaline media. Negative impact of NaOH alone was observed on the Lewis acidity, while the company of the pore directing agents was seen to provoke the formation of new Lewis acid sites as referred to the redistribution of Al species in the extra framework positions.

In the catalytic cracking of n-hexane, a monomolecular mechanism was always the observed mechanism in spite of the presence of mesopores. However, the improvement of the textural properties in some of the catalysts did not influence positively their catalytic performance in the cracking of n-hexane. However, the loss in the catalytic activity was attributed to even the diffusional limitations occurring within the microcrystal zeolite or even due to the decrease in the Brønsted acidity of some the desilicated catalysts. The fast deactivation of the catalysts was referred to the fast formation of coke. Highly formed coke may

not influence negatively the performance of the catalyst being considered as non-toxic deposits in the mesopores. The higher olefin to paraffin molar weights are at the origin of dehydrogenation reactions taking place even though coke is formed. The formation of isomers products in high amounts at the end of the reaction signifies the strength of the acidic that was still pronounced in spite of coke formed.

In the hydroisomerization of n-alkanes, prior to any test on the hydroisomerization of n-C₁₀, the designation of an “ideal” bifunctional catalyst was achieved by increasing the Pt content, where the catalysts activity and isomers selectivity were seen to relate with Pt content. The catalytic performance of the catalysts was seen to be improved sometimes and sometimes not despite of the high textural properties possessed in the majority of the catalysts (except for the microcrystal. However, the bifunctional characteristics was always an additional parameter to the textural properties behind the catalytic performance of the catalyst. Possessing high textural and bifunctional characteristics was evident in increasing the catalysts activity and isomers selectivity. Nonetheless, in spite of the high textural possessed within a catalyst, but the low bifunctional properties might account for a worse performance. This was explained by the large Pt-H⁺ distance as a result of low dispersion and non-well balanced catalyst as well. The large Pt-H⁺ distance enhances several acidic steps to take place between two Pt sites, namely cracking, thus lowering the isomerization yield.

In the other hand, despite that the microcrystal *BEA zeolite comprise no high textural property, but the catalytic performance was high. The size of the Pt particles dispersed on the microcrystal *BEA zeolite was larger than the pore aperture, which means they are located on the surface of the crystals. In this case the n-alkanes molecules are not obliged to diffuse into the micropores to perform the reacting but rather it will perform on the crystallite surface, i.e. no diffusional limitations will be suffered and the catalyst's activity and isomers selectivity will elevate. Moreover, the desilication of this microcrystal *BEA zeolite with the different alkaline media resulted in hierarchical zeolites that have shown to improve more and more the catalytic performance in comparison with all the other catalysts. This was on the basis of the synergy between the improved textural properties and the high bifunctional characteristics (high metal to acid ratio, high dispersion), that assumes that the Pt-H⁺ distance was short enough to induce more isomerization rather than cracking.

The impact of chain length on the catalytic performance of the requested commercial and desilicated nanocrystal *BEA zeolites in the hydroisomerization of n-C₁₂ and n-C₁₄ was

also studied. It was seen as in the case of n-C₁₀ transformation that the textural and bifunctional characteristics can be behind the positive or negative influence either together or separately as one might dominate over the other. However, a special phenomenon appeared during n-C₁₂ transformation. The TOF was seen to elevate more on the majority of the catalysts, which was assumed to be due to the window effect that says that n-C₁₂ molecules diffuse faster than the lower and higher carbon number molecules. However, the faster diffusion would have also favored the isomerization steps rather than cracking, but surprisingly, the aspect was not though. This led us to refuse the suggestion that it might be the windows effect phenomenon appearing right here. It was assumed finally that these molecules are probably being more confined in the zeolite channels, leading to stronger interactions with the acidic sites of the zeolite, increasing apparently their strength. This increase in the acidic strength increases the activity of the catalyst per Brønsted acid site, but non-interestingly, favors cracking. This phenomenon was evident to appear more during n-C₁₂ transformation rather than n-C₁₀ and n-C₁₄ transformations.

Perspectives

The work developed during this Ph. D. allowed to answer several questions concerning the impact of desilication of *BEA zeolites on their various properties, and the impact of desilication on the catalytic performance in the hydroisomerization of n-alkanes and cracking of n-hexane. Nonetheless, research is always in progress and much more remains to do. In this section, several suggestions will be made to continue the studies made on the performed studies developed during this thesis.

1. Desilication

As was seen that the desilication of the nanocrystal *BEA zeolites was interesting in terms of crystal size reduction but rarely in the creation of additional mesopores except in case of desilication of CP814E *BEA zeolite with NaOH. It is important to try to multiple the potential toward wide range of pore directing agents in order to see which might target in an optimized way the textural properties without having an important negative impact on structure, crystallinity, acidity and so on. It is important also to study the effect of temperature and time change of the desilication reactions.

2. Hydroisomerization reactions

2.1. Impact of chain length

Intense experiments on the hydroisomerization reactions of higher carbon number n-alkanes chains (> 14), should be done in order to investigate whether the confinement effect that appeared is particular to n-C₁₂ or still can be observed with other higher (or lower) carbon number chains. It is interesting to further investigate also if the new desilicated *BEA zeolites have a positive impact on the catalytic performance of higher carbon number chains.

2.2. Proximity between active sites

As discussed in the thesis that Martens et al. have studied the impact of the proximity between the metallic and acidic functions within extrudates of zeolite Y and alumina binder, and it was found the optimum proximity between the both is when the metal particles are not in the micropores but even on the binder or on the surface/in the mesopores of the zeolite. Being the *BEA zeolites one of the most catalysts effective in such reactions, it is important to study where could be the optimized proximity on such zeolites, and is the presence of binders

important in this case and plays a major role ? Could the nanoscale intimacy in the closest positions be more effective in the presence of binders ?

Annex

1. Catalytic performance of series 3 catalysts (impact of chain length)

1.1. Catalysts activities

The catalysts of this series were not tested on $n\text{-C}_{12}$. Remarkably, these catalysts have marked globally the highest activity among all series on both $n\text{-C}_{10}$ and $n\text{-C}_{14}$ transformations. Always, and on the two n -alkanes, the parent MC seems to be more active than its desilicated form 1.00MC-D2, but less active than 1.00MC-D1 and 1.00MC-D3 catalysts, as seen in figure 1.

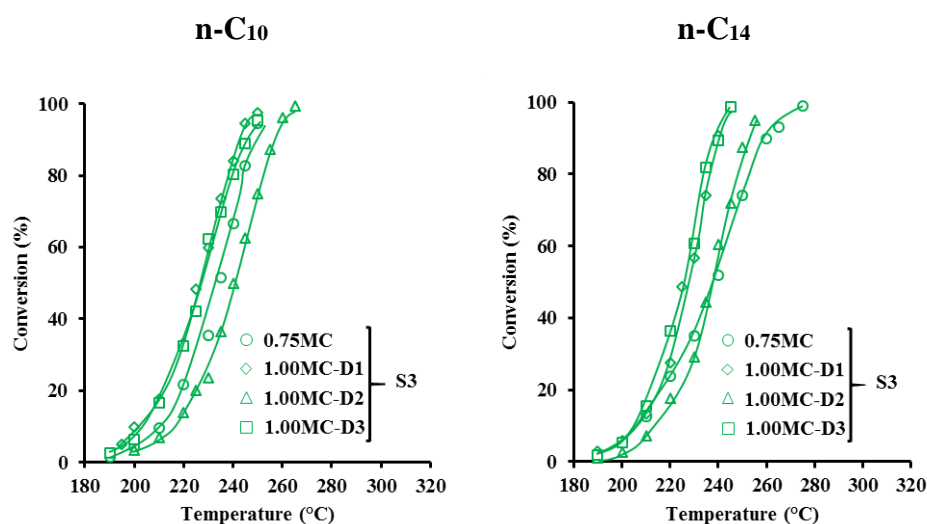


Figure 1. n -alkanes conversions vs temperature over series 3 catalysts.

The quantitative analysis of the activities of series 3 catalysts measured at $230\text{ }^{\circ}\text{C}$, are reported in (table 1). The activities seemed to be 1.5 times higher during $n\text{-C}_{14}$ transformation than that in $n\text{-C}_{10}$. No clear difference was observed in the TOF values on both n -alkanes. The better activity exhibited on the desilicated zeolites may be attributed to the increase in their external surface area with respect to their parent zeolite (MC) (Table III.4; chapter III). An increase in this area was observed to be more than the double on the desilicated forms, and as much as the surface area increases, as much as the interaction with its components will be, namely the acidic sites, knowing also that the transformation is taking place on the surface and not inside the pores ($d_{\text{Pt}} > d_{\text{pore}}$).

Table 1. The n_{Pt} / n_{H^+} ratios, activity and TOF values of series 3 catalysts.

Catalysts	n_{Pt} / n_{H^+}	n-C ₁₀		n-C ₁₄	
		Activity (g _{C10} .g _{cat} ⁻¹ .h ⁻¹)	TOF (h ⁻¹)	Activity (g _{C14} .g _{cat} ⁻¹ .h ⁻¹)	TOF (h ⁻¹)
0.75MC	1.50	1.9	36	3.2	50
1.00MC-D1	9.93	4.7	112	6.2	106
1.00MC-D2	8.25	1.8	44	3.1	55
1.00MC-D3	5.75	4.8	92	6.8	95

1.2. Products selectivity

In this series, the desilication of the parent 0.75MC have shown an improved selectivity toward isomers during n-C₁₀ transformation (figure 2). It was found that the size of Pt particles amongst all the samples of this series was always higher than the micropore diameter, and in the desilicated forms less than the initially formed mesopores diameters. This suggests that Pt sites are not located inside the micropores, but more probably on the surface of the zeolite in case of MC, and probably inside the initially formed mesopores in the desilicated forms. This is also in agreement with Marten's [295] and other researchers proposition [296,297], that when the location of the Pt particles is inside the mesopores or on the surface of the crystallites, the isomerization reactions will be dominating over any other acidic transformation (namely cracking). Furthermore, besides the optimal location of the Pt particles possessed, the slightly improved textural properties, i.e. the initial formation of the mesopores, have played a crucial role in making the catalysts more selective to isomers during n-C₁₀ conversion, by facilitating their diffusion through the channels of these zeolites, making their contact time with the acidic sites lower. However, the increase in chain length (n-C₁₄) made a step backward, where there was a decrease in the isomers yield from 54-70% to be around 40% over all the catalysts of this series. This suggests that the n-C₁₄ paraffin are suffering some diffusional limitations within this series, in spite of the advantageous bifunctional properties possessed. This indicates that the effect of chain length increase is more pronounced in the case of microcrystals.

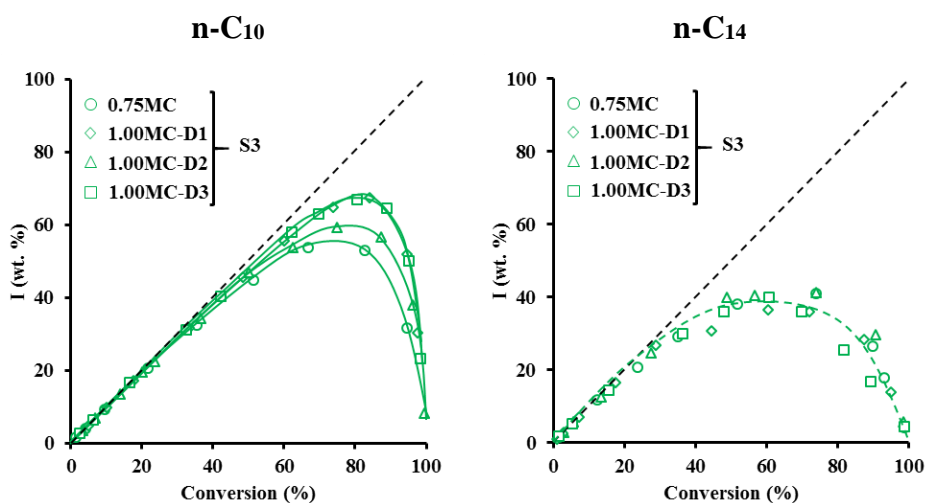


Figure 2. Yield in isomers over series 3 catalysts in the transformations of n-C₁₀ and n-C₁₄.

As in series 1 and 2, the cracking products distribution over n-C₁₀ and n-C₁₄ are resembling those of all the previous catalysts of series 1 and 2.

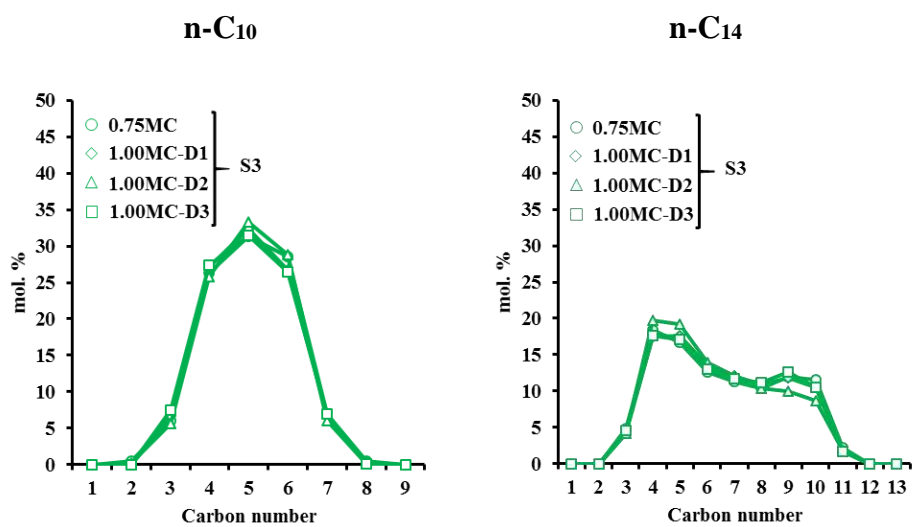


Figure 3. Cracking products distribution of catalysts of series 3 in the transformation of the n-C₁₀ and n-C₁₄.

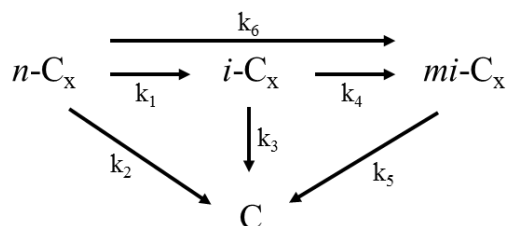
2. Table of ratios of multi to monobranched isoemrs, cracking to isomers, and n_{a.s.}

Table 2. Ratios of multi- to monobranched isomers, cracking to isomers, and n_{a.s.} of the different Pt-*BEA catalysts for transformation of n-C₁₀, n-C₁₂ and n-C₁₄.

Catalysts	n-C ₁₀			n-C ₁₂			n-C ₁₄		
	(B/M) ₀	(C/I) ₀	n _{a.s.}	(B/M) ₀	(C/I) ₀	n _{a.s.}	(B/M) ₀	(C/I) ₀	n _{a.s.}
0.44P1	0.28	0.45	2.16	0.36	0.30	2.00	0.41	0.15	1.80
1.10P1	0.12	0.04	1.22	0.32	0.03	1.44	0.22	0.02	1.32
1.50P1	0.08	0.01	1.14	0.14	0.05	1.32	0.24	0.01	1.31
1.38P1-D1	0.20	0.10	1.50	0.16	0.02	1.26	0.24	0.01	1.32
1.60P1-D2	0.09	0.05	1.26	0.1	0.04	1.25	0.15	0.02	1.25
1.48P2	0.04	0.04	1.17	0.60	0.20	1.9	0.60	0.01	1.58
1.53P2-D6	0.36	0.50	2.26	0.50	0.30	2.1	0.80	0.10	1.88
0.75MC	0.02	0.03	1.11	-	-	-	0.24	0.03	1.32
1.00MC-D1	0.005	0.005	1.02	-	-	-	0.3	0.02	1.35
1.00MC-D2	0.01	0.018	1.07	-	-	-	0.2	0.01	1.39
1.00MC-D3	0.02	0.005	1.04	-	-	-	0.3	0.01	1.30

3. Table of kinetic constants of catalysts of series 3 in the transformation of the n-C₁₀ and n-C₁₄.

Table 2. The corresponding kinetic constants of the different reaction steps during n-C₁₀ and n-C₁₄ transformations, calculated by Runge-Kutta method, for catalysts of series 3.



Catalysts	n-C ₁₀						n-C ₁₄					
	k ₁	k ₂	k ₃	k ₄	k ₅	k ₆	k ₁	k ₂	k ₃	k ₄	k ₅	k ₆
0.75MC	1.00	0.00	0.00	1.25	4.89	0.06	1.00	0.01	0.87	1.42	1.69	0.32
1.00MC-D1	1.00	0.16	0.00	2.66	2.09	0.00	1.00	0.00	0.99	1.89	1.96	0.25
1.00MC-D2	1.00	0.00	0.00	0.98	4.12	0.06	1.00	0.03	0.04	2.73	2.72	0.28
1.00MC-D3	1.00	0.04	0.00	0.82	2.86	0.02	1.00	0.05	0.13	2.21	2.55	0.27

Bibliographic references

- [1] A.F. Cronstedt, in: *Akademibokhandeln Stockholm*, 1756: p. 120.
- [2] A. Dwyer, *An Introduction to Zeolite Molecular Sieves*, John Wiley & Sons, Chichester, 1988.
- [3] S.T. Wilson, B.M. Lok, C.A. Messina, T.R. Cannan, E.M. Flanigen, Aluminophosphate molecular sieves: a new class of microporous crystalline inorganic solids, *J. Am. Chem. Soc.* 104 (1982) 1146–1147. doi:10.1021/ja00368a062.
- [4] M. Taramasso, G. Perego, B. Notari, Preparation of porous crystalline synthetic material comprised of silicon and titanium oxides, (1983). <https://www.google.com/patents/US4410501>.
- [5] S. Inagaki, Y. Fukushima, K. Kuroda, Synthesis of highly ordered mesoporous materials from a layered polysilicate, *J. Chem. Soc. Chem. Commun.* (1993) 680–682. doi:10.1039/C39930000680.
- [6] C.T. Kresge, M.E. Leonowicz, W.J. Roth, J.C. Vartuli, J.S. Beck, Ordered mesoporous molecular sieves synthesized by a liquid-crystal template mechanism, *Nature*. 359 (1992) 710–712. doi:10.1038/359710a0.
- [7] B.. Schoeman, J. Sterte, J.-E. Otterstedt, Colloidal zeolite suspensions, *Zeolites*. 14 (1994) 110–116. doi:10.1016/0144-2449(94)90004-3.
- [8] A. Corma, V. Fornés, Delaminated zeolites as active catalysts for processing large molecules, *Zeolites Mesoporous Mater. Dawn 21st Century*. 135 (2001) 73–82. doi:10.1016/S0167-2991(01)81187-3.
- [9] T. Maesen, B. Marcus, Chapter 1 The zeolite scene—An overview, *Introd. Zeolite Sci. Pract.* 137 (2001) 1–9. doi:10.1016/S0167-2991(01)80242-1.
- [10] J.A. Tossell, A theoretical study of the molecular basis of the Al avoidance rule and of the spectral characteristics of Al-O-Al linkages, *Am. Mineral.* 78 (1993) 911.
- [11] W. Lowenstein, The distribution of aluminium in the tetrahedra of silicates and aluminates, *Am. Mineral.* 39 (1954) 92–96.
- [12] A. Corma, A. Martinez, Zeolites and Zeotypes as catalysts, *Adv. Mater.* 7 (1995) 137–144. doi:10.1002/adma.19950070206.
- [13] A. Thangaraj, M.J. Eapen, S. Sivasanker, P. Ratnasamy, Studies on the synthesis of titanium silicalite, TS-1, *Zeolites*. 12 (1992) 943–950. doi:10.1016/0144-2449(92)90159-M.
- [14] C. Baerlocher, L.B. McCusker, D.H. Olson, *Atlas of Zeolite Framework Types*, 6th edition, Elsevier, 2007.
- [15] M.E. Davis, Ordered porous materials for emerging applications, *Nature*. 417 (2002) 813–821. doi:10.1038/nature00785.
- [16] K.E. Christensen, C. Bonneau, M. Gustafsson, L. Shi, Sun, J. Grins, K. Jansson, I. Sibile, B.-L. Su, Zou, An Open-Framework Silicogermanate with 26-Ring Channels Built from Seven-Coordinated (Ge,Si)10(O,OH)28 Clusters, *J. Am. Chem. Soc.* 130 (2008) 3758–3759. doi:10.1021/ja8002556.
- [17] H.O. Pastore, S. Coluccia, L. Marchese, POROUS ALUMINOPHOSPHATES :From Molecular Sieves to Designed Acid Catalysts, *Annu. Rev. Mater. Res.* 35 (2005) 351–395. doi:10.1146/annurev.matsci.35.103103.120732.
- [18] D.W. Breck, *Zeolite Molecular Sieves: Structure, Chemistry, and Use*, in: John Wiley & Sons, 1974: p. 634.
- [19] M. Guisnet, F.R. Ribeiro, *Les zéolithes un nanomonde au service de la catalyse*, 6th ed., 2006.
- [20] A. Corma, *Inorganic Solid Acids and Their Use in Acid-Catalyzed Hydrocarbon Reactions*, *Chem. Rev.* 95 (1995) 559–614. doi:10.1021/cr00035a006.
- [21] J.T. Fermann, C. Blanco, S. Auerbach, Modeling proton mobility in acidic zeolite clusters. I. Convergence of transition state parameters from quantum chemistry, *J. Chem. Phys.* 112 (2000) 6779–6786. doi:10.1063/1.481253.
- [22] J.A. Ryder, A.K. Chakraborty, A.T. Bell, Density Functional Theory Study of Proton Mobility in Zeolites: Proton Migration and Hydrogen Exchange in ZSM-5, *J. Phys. Chem. B*. 104 (2000) 6998–7011. doi:10.1021/jp9943427.
- [23] M. Guisnet, Influence of zeolite composition on catalytic activity, in: D.C. Sherrington, A.P. Kybett (Eds.), *Support. Catal. Their Appl.*, The Royal Society of Chemistry, 2001: pp. 55–67. doi:10.1039/9781847551962-00055.
- [24] M. Guisnet, J.-P. Gilson, *Zeolites for cleaner technologies*, (2002). <http://site.ebrary.com/id/10713390>.
- [25] M. Elanany, M. Koyama, M. Kubo, E. Broclawik, A. Miyamoto, Periodic density functional investigation of Lewis acid sites in zeolites: relative strength order as revealed from NH₃ adsorption, *Appl. Surf. Sci.* 246 (2005) 96–101. doi:10.1016/j.apsusc.2004.10.052.
- [26] A. Corma, H. García, *Lewis Acids as Catalysts in Oxidation Reactions: From Homogeneous to Heterogeneous Systems*, *Chem. Rev.* 102 (2002) 3837–3892. doi:10.1021/cr010333u.
- [27] T. Chen, A. Men, P. Sun, J. Zhou, Z. Yuan, Z. Guo, J. Wang, D. Ding, H. Li, Lewis acid sites on dehydroxylated zeolite HZSM-5 studied by NMR and EPR, *Proc. 1st Glob. Conf. Young Chin. Sci. Catal. Sci. Technol.* 30 (1996) 189–192. doi:10.1016/0920-5861(96)00011-9.
- [28] C. Marilly, *Catalyse acido-basique. Application au raffinage et à la pétrochimie*, 2002.

-
- [29] L. Oswaldo Almanza, T. Narbeshuber, P. d'Araujo, C. Naccache, Y. Ben Taarit, On the influence of the mordenite acidity in the hydroconversion of linear alkanes over Pt-mordenite catalysts, *Appl. Catal. Gen.* 178 (1999) 39–47. doi:10.1016/S0926-860X(98)00283-X.
- [30] A. Lugstein, A. Jentys, H. Vinek, Hydroisomerization and cracking of n-octane and C8 isomers on Ni-containing zeolites, *Appl. Catal. Gen.* 176 (1999) 119–128. doi:10.1016/S0926-860X(98)00231-2.
- [31] J.A. Martens, G. Vanbutsele, P.A. Jacobs, J. Denayer, R. Ocaakoglu, G. Baron, J.A. Muñoz Arroyo, J. Thybaut, G.B. Marin, Evidences for pore mouth and key–lock catalysis in hydroisomerization of long n-alkanes over 10-ring tubular pore bifunctional zeolites, *Catalysis Refin. Fuels Reformul.* 65 (2001) 111–116. doi:10.1016/S0920-5861(00)00577-0.
- [32] P.B. Weisz, Molecular shape selective catalysis, *Pure Appl. Chem.* 52 (1980) 2091–2103.
- [33] B. Chen, W. Garwood, F. Dwyer, *Shape Selective Catalysis in Industrial Applications*, Marcel Dekker, Inc., New York, 1989.
- [34] T.F. Degnan, The implications of the fundamentals of shape selectivity for the development of catalysts for the petroleum and petrochemical industries, 40th Anniv. Commem. Issue. 216 (2003) 32–46. doi:10.1016/S0021-9517(02)00105-7.
- [35] S.M. Csicsery, Catalysis by shape selective zeolites-science and technology, *Pure Appl. Chem.* 58 (1986) 841–856.
- [36] J. Buchanan, The chemistry of olefins production by ZSM-5 addition to catalytic cracking units, *Catal. Today.* 55 (2000) 207–212. doi:10.1016/S0920-5861(99)00248-5.
- [37] J.A. Martens, R. Parton, L. Uytterhoeven, P.A. Jacobs, G.F. Froment, Selective conversion of decane into branched isomers, *Appl. Catal.* 76 (1991) 95–116. doi:10.1016/0166-9834(91)80007-J.
- [38] S.J. Miller, New molecular sieve process for lube dewaxing by wax isomerization, *Microporous Mater.* 2 (1994) 439–449. doi:10.1016/0927-6513(94)00016-6.
- [39] M.C. Claude, J.A. Martens, Monomethyl-Branching of Long n-Alkanes in the Range from Decane to Tetracosane on Pt/H-ZSM-22 Bifunctional Catalyst, *J. Catal.* 190 (2000) 39–48. doi:10.1006/jcat.1999.2714.
- [40] W. Souverijns, J.A. Martens, G.F. Froment, P.A. Jacobs, Hydrocracking of Isoheptadecanes on Pt/H-ZSM-22: An Example of Pore Mouth Catalysis, *J. Catal.* 174 (1998) 177–184. doi:10.1006/jcat.1998.1959.
- [41] E.G. Derouane, Z. Gabelica, A novel effect of shape selectivity: Molecular traffic control in zeolite ZSM-5, *J. Catal.* 65 (1980) 486–489. doi:10.1016/0021-9517(80)90328-0.
- [42] E.G. Derouane, New Aspects of Molecular Shape-Selectivity: Catalysis by Zeolite ZSM - 5, *Catal. Zeolites.* 5 (1980) 5–18. doi:10.1016/S0167-2991(08)64860-0.
- [43] C. Nai Y., T. F. Degnan, C.M. Smith, *Molecular Transport and Reaction Zeolites: Design and Application of Shape Selective Catalysis*, 1994.
- [44] D.S. Santilli, T.V. Harris, S.I. Zones, Inverse shape selectivity in molecular sieves: Observations, modelling, and predictions, *Microporous Mater.* 1 (1993) 329–341. doi:10.1016/0927-6513(93)80049-Z.
- [45] M. Schenk, S. Calero, T.L.M. Maesen, L.L. van Benthem, M.G. Verbeek, B. Smit, Understanding Zeolite Catalysis: Inverse Shape Selectivity Revised, *Angew. Chem. Int. Ed.* 41 (2002) 2499–2502. doi:10.1002/1521-3773(20020715)41:14<2499::AID-ANIE2499>3.0.CO;2-T.
- [46] T.F. Degnan, C.M. Smith, C.R. Venkat, Alkylation of aromatics with ethylene and propylene: recent developments in commercial processes, *Hoelderich Spec. Issue.* 221 (2001) 283–294. doi:10.1016/S0926-860X(01)00807-9.
- [47] R.L. Goring, Diffusion of normal paraffins in zeolite T, *J. Catal.* 31 (1973) 13–26. doi:10.1016/0021-9517(73)90265-0.
- [48] N.Y. Chen, S.J. Lucki, E.B. Mower, Cage effect on product distribution from cracking over crystalline aluminosilicate zeolites, *J. Catal.* 13 (1969) 329–332. doi:10.1016/0021-9517(69)90409-6.
- [49] N.M.R. Batalha, Optimization of the balance between activity and selectivity on a hydroisomerization catalyst, *Universite de Poitiers*, 2012.
- [50] L.B. Young, S.A. Butter, W.W. Kaeding, Shape selective reactions with zeolite catalysts, *J. Catal.* 76 (1982) 418–432. doi:10.1016/0021-9517(82)90271-8.
- [51] W.W. Kaeding, C. Chu, L.B. Young, S.A. Butter, Shape-selective reactions with zeolite catalysts, *J. Catal.* 69 (1981) 392–398. doi:10.1016/0021-9517(81)90174-3.
- [52] R. Roque-Malherbe, V. Ivanov, Codiffusion and counterdiffusion of para-xylene and ortho-xylene in a zeolite with 10 MR/12 MR interconnected channels. An example of molecular traffic control, *J. Mol. Catal. Chem.* 313 (2009) 7–13. doi:10.1016/j.molcata.2009.07.015.
- [53] N. Viswanadham, G. Murali Dhar, T.S. Prasad Rao, Pore size analysis of ZSM-5 catalysts used in n-heptane aromatization reaction: an evidence for molecular traffic control (MTC) mechanism, *J. Mol. Catal. Chem.* 125 (1997) L87–L90. doi:10.1016/S1381-1169(97)00128-3.
- [54] R.L. Goring, Diffusion of normal paraffins in zeolite T, *J. Catal.* 31 (1973) 13–26. doi:10.1016/0021-9517(73)90265-0.
- [55] G. Mirth, J. Cejka, J.A. Lercher, Transport and Isomerization of Xylenes over HZSM-5 Zeolites, *J. Catal.* 139 (1993) 24–33. doi:10.1006/jcat.1993.1003.
-

-
- [56] A.N.C. van laak, L. Zhang, A.N. Parvulescu, P.C.A. Bruijninx, B.M. Weckhuysen, K.P. de Jong, P.E. de Jongh, Alkaline treatment of template containing zeolites: Introducing mesoporosity while preserving acidity, *Catal. Today*. 168 (2011) 48–56. doi:10.1016/j.cattod.2010.10.101.
- [57] Y. Wang, Y. Sun, C. Lancelot, C. Lamonier, J.-C. Morin, B. Revel, L. Delevoye, A. Rives, Effect of post treatment on the local structure of hierarchical Beta prepared by desilication and the catalytic performance in Friedel–Crafts alkylation, *Microporous Mesoporous Mater.* 206 (2015) 42–51. doi:10.1016/j.micromeso.2014.12.017.
- [58] J. Qi, T. Zhao, X. Xu, F. Li, G. Sun, C. Miao, H. Wang, Study of cracking of large molecules over a novel mesoporous beta, *Catal. Commun.* 10 (2009) 1523–1528. doi:10.1016/j.catcom.2009.04.008.
- [59] K. Tarach, K. Góra-Marek, J. Tekla, K. Brylowska, J. Datka, K. Mlekodaj, W. Makowski, M.C. Iguada López, J. Martínez Triguero, F. Rey, Catalytic cracking performance of alkaline-treated zeolite Beta in the terms of acid sites properties and their accessibility, *J. Catal.* 312 (2014) 46–57. doi:10.1016/j.jcat.2014.01.009.
- [60] V. Rac, V. Rakić, D. Stošić, O. Otman, A. Auroux, Hierarchical ZSM-5, Beta and USY zeolites: Acidity assessment by gas and aqueous phase calorimetry and catalytic activity in fructose dehydration reaction, *Microporous Mesoporous Mater.* 194 (2014) 126–134. doi:10.1016/j.micromeso.2014.04.003.
- [61] V. Calemma, S. Peratello, C. Perego, Hydroisomerization and hydrocracking of long chain n-alkanes on Pt/amorphous SiO₂–Al₂O₃ catalyst, *Appl. Catal. Gen.* 190 (2000) 207–218. doi:10.1016/S0926-860X(99)00292-6.
- [62] S. Rajagopal, J.A. Marzari, R. Miranda, Silica-Alumina-Supported Mo Oxide Catalysts: Genesis and Demise of Brønsted-Lewis Acidity, *J. Catal.* 151 (1995) 192–203. doi:10.1006/jcat.1995.1021.
- [63] C. Marcilly, *Catalyse acido-basique. Application au raffinage et à la pétrochimie*, TECHNIP, 2003.
- [64] C. Bouchy, G. Hastoy, E. Guillon, J.A. Martens, Fischer-Tropsch Waxes Upgrading via Hydrocracking and Selective Hydroisomerization, *Oil Gas Sci. Technol. - Rev IFP*. 64 (2009) 91–112. doi:10.2516/ogst/2008047.
- [65] S.P. Elangovan, C. Bischof, M. Hartmann, Isomerization and Hydrocracking of n-Decane over Bimetallic Pt–Pd Clusters Supported on Mesoporous MCM-41 Catalysts, *Catal. Lett.* 80 (2002) 35–40. doi:10.1023/A:1015366408242.
- [66] K. Fang, W. Wei, J. Ren, Y. Sun, n-Dodecane Hydroconversion over Ni/AlMCM-41 Catalysts, *Catal. Lett.* 93 (2004) 235–242. doi:10.1023/B:CATL.0000017082.44599.86.
- [67] S. Lin, H. Ning, S. Wan-Fu, L. Wei-Min, X. Qun-Ji, Preparation of Pd/Al-MCM-41 Catalyst and Its Hydroisomerization Properties for long chain alkane compounds, *Nanoporous Mater. III*. 141 (2002) 517–524. doi:10.1016/S0167-2991(02)80584-5.
- [68] F. Alvarez, F.R. Ribeiro, G. Perot, C. Thomazeau, M. Guisnet, Hydroisomerization and Hydrocracking of Alkanes, *J. Catal.* 162 (1996) 179–189. doi:10.1006/jcat.1996.0275.
- [69] J. Zecevic, G. Vanbutsele, K.P. de Jong, J.A. Martens, Nanoscale intimacy in bifunctional catalysts for selective conversion of hydrocarbons, *Nature*. 528 (2015) 245–248.
- [70] M. Guisnet, N.S. Gnep, Aromatization of propane over GaHMF1 catalysts. Reaction scheme, nature of the dehydrogenating species and mode of coke formation, *Gallium-Loaded Zeolites Relat. Syst.* 31 (1996) 275–292. doi:10.1016/S0920-5861(96)00018-1.
- [71] H. Deldari, Suitable catalysts for hydroisomerization of long-chain normal paraffins, *Appl. Catal. Gen.* 293 (2005) 1–10. doi:10.1016/j.apcata.2005.07.008.
- [72] J.A. Martens, M. Tielen, P.A. Jacobs, Relation Between Paraffin Isomerisation Capability and Pore Architecture of Large-Pore Bifunctional Zeolites, *Zeolites Catal. Sorbents Deterg. Build.* 46 (1989) 49–60. doi:10.1016/S0167-2991(08)60966-0.
- [73] C.S. Laxmi Narasimhan, J.W. Thybaut, G.B. Marin, P.A. Jacobs, J.A. Martens, J.F. Denayer, G.V. Baron, Kinetic modeling of pore mouth catalysis in the hydroconversion of n-octane on Pt-H-ZSM-22, *J. Catal.* 220 (2003) 399–413. doi:10.1016/S0021-9517(03)00281-1.
- [74] I. Roy Choudhury, J.W. Thybaut, P. Balasubramanian, J.F.M. Denayer, J.A. Martens, G.B. Marin, Synergy between shape selective and non-shape selective bifunctional zeolites modelled via the Single-Event MicroKinetic (SEMK) methodology, 20th Int. Symp. Chem. React. Eng. Chem. React. Eng. Sustain. Future. 65 (2010) 174–178. doi:10.1016/j.ces.2009.08.020.
- [75] R. Merabti, 2011.
- [76] R. Merabti, L. Pinard, J.L. Lemberon, P. Magnoux, A. Barama, K. Moljord, Effect of Na exchange of a HBEA zeolite on the activity and the selectivity of a bifunctional Pt-HBEA catalyst for n-hexadecane hydroisomerization. Comparison with a Pt-HZSM-22 catalyst, *React. Kinet. Mech. Catal.* 100 (2010) 1–9. doi:10.1007/s11144-010-0183-1.
- [77] F.R. Ribeiro, F. Alvarez, C. Henriques, F. Lemos, J.M. Lopes, M.F. Ribeiro, Structure-activity relationship in zeolites, *J. Mol. Catal. Chem.* 96 (1995) 245–270. doi:10.1016/1381-1169(94)00058-1.
- [78] A. Soualah, J.L. Lemberon, L. Pinard, M. Chater, P. Magnoux, K. Moljord, Hydroisomerization of long-chain n-alkanes on bifunctional Pt/zeolite catalysts: Effect of the zeolite structure on the product selectivity and on the reaction mechanism, *Spec. Issue Dedic. Prof. Jean Sommer His 70th Birthd.* 336 (2008) 23–28. doi:10.1016/j.apcata.2007.09.038.
- [79] M.J. Ramos, A. de Lucas, V. Jiménez, P. Sánchez, J.L. Valverde, Hydroisomerization of different refinery naphtha streams by using a beta zeolite catalyst, *Fuel Process. Technol.* 89 (2008) 721–727. doi:10.1016/j.fuproc.2008.01.008.
- [80] Z.-W. Liu, X. Li, K. Asami, K. Fujimoto, Iso-paraffins synthesis from modified Fischer–Tropsch reaction—Insights into Pd/beta and Pt/beta catalysts, *Catal. Ultra-Clean Fuels Prod.* 104 (2005) 41–47. doi:10.1016/j.cattod.2005.03.030.
-

-
- [81] N. Batalha, S. Morisset, L. Pinard, I. Maupin, J.L. Leberthon, F. Lemos, Y. Pouilloux, BEA zeolite nanocrystals dispersed over alumina for n-hexadecane hydroisomerization, *Innov. Zeolites Ordered Porous Solids Sel. Pap. Invit. Lect. 5th Int. FEZA Conf. FEZA-2011 July 3-7 2011*. 166 (2013) 161–166. doi:10.1016/j.micromeso.2012.04.041.
- [82] N. Batalha, L. Pinard, C. Bouchy, E. Guillon, M. Guisnet, n-Hexadecane hydroisomerization over Pt-HBEA catalysts. Quantification and effect of the intimacy between metal and protonic sites, *J. Catal.* 307 (2013) 122–131. doi:10.1016/j.jcat.2013.07.014.
- [83] R. Nakao, Y. Kubota, N. Katada, N. Nishiyama, K. Kunimori, K. Tomishige, Performance and characterization of BEA catalysts for catalytic cracking, *Appl. Catal. Gen.* 273 (2004) 63–73. doi:10.1016/j.apcata.2004.06.013.
- [84] R.M. Mihályi, F. Lónyi, H.K. Beyer, Á. Szegedi, M. Kollár, G. Pál-Borbély, J. Valyon, n-Heptane hydroconversion over nickel-loaded aluminum- and/or boron-containing BEA zeolites prepared by recrystallization of magadiite varieties, *J. Mol. Catal. Chem.* 367 (2013) 77–88. doi:10.1016/j.molcata.2012.09.030.
- [85] P. Sazama, D. Kaucky, J. Moravkova, R. Pilar, P. Klein, J. Pastvova, E. Tabor, S. Sklenak, I. Jakubec, L. Mokrzycki, Superior activity of non-interacting close acidic protons in Al-rich Pt/H-*BEA zeolite in isomerization of n-hexane, *Appl. Catal. Gen.* 533 (2017) 28–37. doi:10.1016/j.apcata.2016.12.016.
- [86] S.K. Saxena, N. Viswanadham, M.O. Garg, Porosity and acidity patterns of steam treated BEA zeolite material for enhanced catalytic isomerization of naphtha, *J. Ind. Eng. Chem.* 20 (2014) 3875–3883. doi:10.1016/j.jiec.2013.12.093.
- [87] K. Föttinger, G. Kinger, H. Vinek, 1-Pentene isomerization over FER and BEA, *Appl. Catal. Gen.* 249 (2003) 205–212. doi:10.1016/S0926-860X(03)00192-3.
- [88] P. Gallezot, B. Blanc, D. Barthomeuf, M.I. País da Silva, Selective hydrogenation of cinnamaldehyde controlled by host/guest interactions in beta zeolite, *Zeolites Relat. Microporous Mater. State Art 1994 - Proc. 10th Int. Zeolite Conf. Garm.-Partenkirch. Ger. 17-22 July 1994*. 84 (1994) 1433–1439. doi:10.1016/S0167-2991(08)63685-X.
- [89] P.R. Hari Prasad Rao, P. Massiani, D. Barthomeuf, Alkylation of aniline with methanol of Beta and EMT zeolites exchanged with alkaline cations, *Zeolites Relat. Microporous Mater. State Art 1994 - Proc. 10th Int. Zeolite Conf. Garm.-Partenkirch. Ger. 17-22 July 1994*. 84 (1994) 1449–1455. doi:10.1016/S0167-2991(08)63687-3.
- [90] R.L. Wadlinger, G.T. Kerr, E.J. Rosinski, Catalytic composition of a crystalline zeolite, (1967). <https://www.google.com/patents/US3308069>.
- [91] M.M.J. Treacy, J.M. Newsam, Two new three-dimensional twelve-ring zeolite frameworks of which zeolite beta is a disordered intergrowth, *Nature*. 332 (1988) 249–251. doi:10.1038/332249a0.
- [92] J.A. Martens, M. Tielen, P.A. Jacobs, J. Weitkamp, Estimation of the void structure and pore dimensions of molecular sieve zeolites using the hydroconversion of n-decane, *Zeolites*. 4 (1984) 98–107. doi:10.1016/0144-2449(84)90044-7.
- [93] J.V. Smith, J.J. Pluth, R.C. Boggs, D.G. Howard, Tschernichite, the mineral analogue of zeolite Beta, *J. Chem. Soc. Chem. Commun.* (1991) 363–364. doi:10.1039/C39910000363.
- [94] J.M. Newsam, M.M.J. Treacy, W.T. Koetsier, C.B.D. Gruyter, Structural Characterization of Zeolite Beta, *Proc. R. Soc. Lond. Math. Phys. Sci.* 420 (1988) 375. doi:10.1098/rspa.1988.0131.
- [95] J.B. Higgins, R.B. LaPierre, J.L. Schlenker, A.C. Rohrman, J.D. Wood, G.T. Kerr, W.J. Rohrbaugh, The framework topology of zeolite beta, *Zeolites*. 8 (1988) 446–452. doi:10.1016/S0144-2449(88)80219-7.
- [96] C. Baerlocher, W.M. Meier, D.H. Olson, *Atlas of Zeolite Framework Types*, 5th edition, Elsevier, Amsterdam, 2001.
- [97] M.A. Cambor, P.A. Barrett, M.-J. Díaz-Cabañas, L.A. Villaescusa, M. Puche, T. Boix, E. Pérez, H. Koller, High silica zeolites with three-dimensional systems of large pore channels, *Microporous Mesoporous Mater.* 48 (2001) 11–22. doi:10.1016/S1387-1811(01)00325-0.
- [98] T. Ohsuna, O. Terasaki, V. Alfredsson, J.-O. Bovin, D. Watanabe, S.W. Carr, M.W. Anderson, Observations on the Role of Crown Ether Templates in the Formation of Hexagonal and Cubic Polymorphs of Zeolite Y, *Proc. R. Soc. Lond. Ser. Math. Phys. Eng. Sci.* 452 (1996) 715. doi:10.1098/rspa.1996.0036.
- [99] L.A. Villaescusa, W. Zhou, R.E. Morris, P.A. Barrett, Synthesis, characterization and control of faulting in STF/SFF topologies, a new family of intergrowth zeolites, *J. Mater. Chem.* 14 (2004) 1982–1987. doi:10.1039/B315643E.
- [100] A. Corma, A. Martínez, Transformation of Alkanes on Solid Acid and Bifunctional Catalysts, in: E.G. Derouane, J. Haber, F. Lemos, F.R. Ribeiro, M. Guisnet (Eds.), *Catal. Act. Funct. Light Alkanes Adv. Chall.*, Springer Netherlands, Dordrecht, 1998: pp. 35–74. doi:10.1007/978-94-017-0982-8_2.
- [101] G.W. Huber, P. O'Connor, A. Corma, Processing biomass in conventional oil refineries: Production of high quality diesel by hydrotreating vegetable oils in heavy vacuum oil mixtures, *Appl. Catal. Gen.* 329 (2007) 120–129. doi:10.1016/j.apcata.2007.07.002.
- [102] T. Kalnes, T. Marker, D.R. Shonnard, Green Diesel: A Second Generation Biofuel, *Int. J. Chem. React. Eng.* 5 (2007). doi:https://doi.org/10.2202/1542-6580.1554.
- [103] J. Weitkamp, Catalytic Hydrocracking—Mechanisms and Versatility of the Process, *ChemCatChem*. 4 (2012) 292–306. doi:10.1002/cctc.201100315.
- [104] G. Ertl, H. Knözinger, J. Weitkamp, *Handbook of Heterogeneous Catalysis*, Wiley, VCH, Weinheim, 1997.
- [105] C. Vollhardt, N. Schore, *Traite De Chimie Organique*, 2nd edition, De Boeck Universite, Bruxelles, 1995.
- [106] S.R. Blaszkowski, R.A. van Santen, Quantum chemical studies of zeolite proton catalyzed reactions, *Top. Catal.* 4 (1997) 145–156. doi:10.1023/A:1019123818998.
-

-
- [107] B.S. Greensfelder, H.H. Voge, G.M. Good, Catalytic and Thermal Cracking of Pure Hydrocarbons: Mechanisms of Reaction, *Ind. Eng. Chem.* 41 (1949) 2573–2584. doi:10.1021/ie50479a043.
- [108] W.F. Pansing, The Catalytic Cracking of Hexadecane—Effects of Impurities, Olefins, and Steam, *J. Phys. Chem.* 69 (1965) 392–399. doi:10.1021/j100886a006.
- [109] S.E. Tung, E. McIninch, Zeolitic aluminosilicate, *J. Catal.* 10 (1968) 166–174. doi:10.1016/0021-9517(68)90169-3.
- [110] D.M. Nace, Catalytic Cracking over Crystalline Aluminosilicates. II. Application of Microreactor Technique to Investigation of Structural Effects of Hydrocarbon Reactants, *Prod. RD.* 8 (1969) 31–38. doi:10.1021/i360029a005.
- [111] A. Borodzinski, A. Corma, B.W. Wojciechowski, The nature of the active sites in the catalytic cracking of gas—oil, *Can. J. Chem. Eng.* 58 (1980) 219–229. doi:10.1002/cjce.5450580213.
- [112] V.B. Kazansky, Adsorbed carbocations as transition states in heterogeneous acid catalyzed transformations of hydrocarbons, *Catal. Today.* 51 (1999) 419–434. doi:10.1016/S0920-5861(99)00031-0.
- [113] F.C. Whitmore, Mechanism of the Polymerization of Olefins by Acid Catalysts, *Ind. Eng. Chem.* 26 (1934) 94–95. doi:10.1021/ie50289a023.
- [114] A. McNaught, A. Wilkinson, *IUPAC Compendium of Chemical Terminology*, 2nd ed., Blackwell Science, Boston, 1997.
- [115] D.M. Brouwer, H. Hogeveen, Electrophilic Substitutions at Alkanes and in Alkylcarbonium Ions, in: *Prog. Phys. Org. Chem.*, John Wiley & Sons, Inc., 1972: pp. 179–240. doi:10.1002/9780470171882.ch4.
- [116] F.C. Jentoft, B.C. Gates, Solid-acid-catalyzed alkane cracking mechanisms: evidence from reactions of small probe molecules, *Top. Catal.* 4 (1997) 1–13. doi:10.1023/A:1019184004885.
- [117] G. Caeiro, R.H. Carvalho, X. Wang, M.A.N.D.A. Lemos, F. Lemos, M. Guisnet, F. Ramôa Ribeiro, Activation of C2–C4 alkanes over acid and bifunctional zeolite catalysts, *J. Mol. Catal. Chem.* 255 (2006) 131–158. doi:10.1016/j.molcata.2006.03.068.
- [118] A. Corma, A.V. Orchillés, Current views on the mechanism of catalytic cracking, *Microporous Mesoporous Mater.* 35 (2000) 21–30. doi:10.1016/S1387-1811(99)00205-X.
- [119] S. Kotrel, H. Knözinger, B.C. Gates, The Haag–Dessau mechanism of protolytic cracking of alkanes, *Microporous Mesoporous Mater.* 35 (2000) 11–20. doi:10.1016/S1387-1811(99)00204-8.
- [120] J.A. Martens, M. Tielen, P.A. Jacobs, Attempts to rationalize the distribution of hydrocracked products. III. mechanistic aspects of isomerization and hydrocracking of branched alkanes on ideal bifunctional large-pore zeolite catalysts, *HYDROCRACKING Sci. Technol.* 1 (1987) 435–453. doi:10.1016/0920-5861(87)80008-1.
- [121] P. Weisz, *Science.* 123 (1956) 887–888.
- [122] P. Weisz, *Science.* 126 (1957) 31–32.
- [123] P.B. Weisz, Polyfunctional Heterogeneous Catalysis, *Adv. Catal.* 13 (1962) 137–190. doi:10.1016/S0360-0564(08)60287-4.
- [124] J. Weitkamp, Catalytic Hydrocracking—Mechanisms and Versatility of the Process, *ChemCatChem.* 4 (2012) 292–306. doi:10.1002/cctc.201100315.
- [125] M. Guisnet, “Ideal” bifunctional catalysis over Pt-acid zeolites, *Catal. Today.* 218–219 (2013) 123–134. doi:10.1016/j.cattod.2013.04.028.
- [126] C. Bouchy, G. Hastoy, E. Guillon, J.A. Martens, Fischer-Tropsch Waxes Upgrading via Hydrocracking and Selective Hydroisomerization, *Oil Gas Sci. Technol. - Rev IFP.* 64 (2009) 91–112. doi:10.2516/ogst/2008047.
- [127] M. Steijns, G.F. Froment, Hydroisomerization and hydrocracking. 3. Kinetic analysis of rate data for n-decane and n-dodecane, *Ind. Eng. Chem. Prod. Res. Dev.* 20 (1981) 660–668. doi:10.1021/i300004a014.
- [128] J. WEITKAMP, The Influence of Chain Length in Hydrocracking and Hydroisomerization of n-Alkanes, in: *Hydrocracking Hydrotreating*, AMERICAN CHEMICAL SOCIETY, 1975: pp. 1–27. doi:10.1021/bk-1975-0020.ch001.
- [129] M. Guisnet, F. Alvarez, G. Giannetto, G. Perot, Hydroisomerization and hydrocracking of n-heptane on Pth zeolites. Effect of the porosity and of the distribution of metallic and acid sites., *HYDROCRACKING Sci. Technol.* 1 (1987) 415–433. doi:10.1016/0920-5861(87)80007-X.
- [130] M.C. Claude, G. Vanbutsele, J.A. Martens, Dimethyl Branching of Long n-Alkanes in the Range from Decane to Tetracosane on Pt/H-ZSM-22 Bifunctional Catalyst, *J. Catal.* 203 (2001) 213–231. doi:10.1006/jcat.2001.3325.
- [131] R.J. Taylor, R.H. Petty, Selective hydroisomerization of long chain normal paraffins, *Appl. Catal. Gen.* 119 (1994) 121–138. doi:10.1016/0926-860X(94)85029-1.
- [132] M.A. Cambor, A. Corma, S. Valencia, Characterization of nanocrystalline zeolite Beta, *Microporous Mesoporous Mater.* 25 (1998) 59–74. doi:10.1016/S1387-1811(98)00172-3.
- [133] M.V. Landau, L. Vradman, V. Valtchev, J. Lezervant, E. Liubich, M. Talianker, Hydrocracking of Heavy Vacuum Gas Oil with a Pt/H-beta-Al₂O₃ Catalyst: Effect of Zeolite Crystal Size in the Nanoscale Range, *Ind. Eng. Chem. Res.* 42 (2003) 2773–2782. doi:10.1021/ie020899o.
- [134] M. Farcasiu, T.F. Degnan, The role of external surface activity in the effectiveness of zeolites, *Ind. Eng. Chem. Res.* 27 (1988) 45–47. doi:10.1021/ie00073a010.
-

-
- [135] S. Melson, F. Schüth, The Influence of the External Acidity of H-ZSM-5 on Its Shape Selective Properties in the Disproportionation of Ethylbenzene, *J. Catal.* 170 (1997) 46–53. doi:10.1006/jcat.1997.1715.
- [136] M. Arribas, A. Martínez, Simultaneous isomerization of n-heptane and saturation of benzene over Pt/Beta catalysts, *Cataysis Refin. Fuels Reformul.* 65 (2001) 117–122. doi:10.1016/S0920-5861(00)00576-9.
- [137] A. Chica, A. Corma, Hydroisomerization of Pentane, Hexane, and Heptane for Improving the Octane Number of Gasoline, *J. Catal.* 187 (1999) 167–176. doi:10.1006/jcat.1999.2601.
- [138] A. Corma, A. Martínez, The Chemistry of Catalytic Processes, in: *Zeolites Clean. Technol.*, 2002: pp. 29–55. doi:10.1142/9781860949555_0002.
- [139] R. Merabti, J.G. Abreu, L. Pinard, B. Leroux, J.L. Lemberton, P. Magnoux, A. Barama, F.R. Ribeiro, K. Moljord, Hydroisomerization of n-hexadecane on Pt/HBEA bifunctional catalysts: effect of the zeolite crystallites size on the reaction scheme, in: A. Gédéon, P. Massiani, F. Babonneau (Eds.), *Stud. Surf. Sci. Catal.*, Elsevier, 2008: pp. 1107–1110. doi:10.1016/S0167-2991(08)80079-1.
- [140] J. Kim, W. Kim, Y. Seo, J.-C. Kim, R. Ryoo, n-Heptane hydroisomerization over Pt/MFI zeolite nanosheets: Effects of zeolite crystal thickness and platinum location, *J. Catal.* 301 (2013) 187–197. doi:10.1016/j.jcat.2013.02.015.
- [141] E. Verheyen, C. Jo, M. Kurttepel, G. Vanbutsele, E. Gobechiya, T.I. Korányi, S. Bals, G. Van Tendeloo, R. Ryoo, C.E.A. Kirschhock, J.A. Martens, Molecular shape-selectivity of MFI zeolite nanosheets in n-decane isomerization and hydrocracking, *J. Catal.* 300 (2013) 70–80. doi:10.1016/j.jcat.2012.12.017.
- [142] A. Astafan, Y. Pouilloux, J. Patarin, N. Bats, C. Bouchy, T. Jean Daou, L. Pinard, Impact of extreme downsizing of *BEA-type zeolite crystals on n-hexadecane hydroisomerization, *New J. Chem.* 40 (2016) 4335–4343. doi:10.1039/C5NJ02837J.
- [143] K.-C. Park, S.-K. Ihm, Comparison of Pt/zeolite catalysts for n-hexadecane hydroisomerization, *Appl. Catal. Gen.* 203 (2000) 201–209. doi:10.1016/S0926-860X(00)00490-7.
- [144] A. Carati, C. Flego, V. Calemma, EP 635556A1, 1994.
- [145] M.R. Apelian, W.S. Borghard, T.F. Degnan, R.T. Hanlon, M.K. Rubin, Wax hydroisomerization process, US 5885438 A, 1999. <https://www.google.com/patents/US5885438>.
- [146] M.R. Apelian, C.L. Baker, T.F. Degnan, D.O. Marler, D.N. Mazzone, D.E. Walsh, Production of high viscosity index lubricants, US 5358628 A, 1994. <https://www.google.sr/patents/US5358628>.
- [147] R. Merabti, L. Pinard, J.L. Lemberton, P. Magnoux, A. Barama, K. Moljord, Effect of Na exchange of a HBEA zeolite on the activity and the selectivity of a bifunctional Pt-HBEA catalyst for n-hexadecane hydroisomerization. Comparison with a Pt-HZSM-22 catalyst, *React. Kinet. Mech. Catal.* 100 (2010) 1–9. doi:10.1007/s11144-010-0183-1.
- [148] R.A. Keogh, R. Srinivasan, B.H. Davis, The effect of Pt concentration on the activity and selectivity of SO₄²⁻-ZrO₂ catalysts for the hydrocracking and hydroisomerization of n-hexadecane, *Appl. Catal. Gen.* 140 (1996) 47–57. doi:10.1016/0926-860X(96)00016-6.
- [149] N. Batalha, L. Pinard, Y. Pouilloux, M. Guisnet, Bifunctional Hydrogenating/Acid Catalysis: Quantification of the Intimacy Criterion, *Catal. Lett.* 143 (2013) 587–591. doi:10.1007/s10562-013-1003-9.
- [150] G.E. Giannetto, G.R. Perot, M.R. Guisnet, Hydroisomerization and hydrocracking of n-alkanes. 1. Ideal hydroisomerization PtHY catalysts, *Ind. Eng. Chem. Prod. Res. Dev.* 25 (1986) 481–490. doi:10.1021/i300023a021.
- [151] J. Francis, E. Guillon, N. Bats, C. Pichon, A. Corma, L.J. Simon, Design of improved hydrocracking catalysts by increasing the proximity between acid and metallic sites, *Appl. Catal. Gen.* 409 (2011) 140–147. doi:10.1016/j.apcata.2011.09.040.
- [152] E. Iglesia, D.G. Barton, J.A. Biscardi, M.J.L. Gines, S.L. Soled, Bifunctional pathways in catalysis by solid acids and bases, *Acid-Base Catal.* 38 (1997) 339–360. doi:10.1016/S0920-5861(97)81503-7.
- [153] V. Calemma, S. Peratello, F. Stroppa, R. Giardino, C. Perego, Hydrocracking and Hydroisomerization of Long-Chain n-Paraffins. Reactivity and Reaction Pathway for Base Oil Formation, *Ind. Eng. Chem. Res.* 43 (2004) 934–940. doi:10.1021/ie0304309.
- [154] F. Ngoye, L. Lakiss, Z. Qin, S. Laforge, C. Canaff, M. Tarighi, V. Valtchev, K. Thomas, A. Vicente, J.P. Gilson, Y. Pouilloux, C. Fernandez, L. Pinard, Mitigating coking during methylcyclohexane transformation on HZSM-5 zeolites with additional porosity, *J. Catal.* 320 (2014) 118–126. doi:10.1016/j.jcat.2014.10.001.
- [155] M. Guisnet, P. Magnoux, Deactivation by coking of zeolite catalysts. Prevention of deactivation. Optimal conditions for regeneration, *Interact. Ind. Fundam. Res. Catal.* 36 (1997) 477–483. doi:10.1016/S0920-5861(96)00238-6.
- [156] P. Magnoux, P. Cartraud, S. Mignard, M. Guisnet, Coking, aging, and regeneration of zeolites, *J. Catal.* 106 (1987) 242–250. doi:10.1016/0021-9517(87)90228-4.
- [157] E. Koohsaryan, M. Anbia, Nanosized and hierarchical zeolites: A short review, *Chin. J. Catal.* 37 (2016) 447–467. doi:10.1016/S1872-2067(15)61038-5.
- [158] W. Song, R.E. Justice, C.A. Jones, V.H. Grassian, S.C. Larsen, Size-Dependent Properties of Nanocrystalline Silicalite Synthesized with Systematically Varied Crystal Sizes, *Langmuir.* 20 (2004) 4696–4702. doi:10.1021/la049817m.
- [159] G.-T. Vuong, T.-O. Do, A New Route for the Synthesis of Uniform Nanozeolites with Hydrophobic External Surface in Organic Solvent Medium, *J. Am. Chem. Soc.* 129 (2007) 3810–3811. doi:10.1021/ja069058p.
- [160] X. Chen, K. Wendell, J. Zhu, J. Li, X. Yu, Z. Zhang, Synthesis of nano-zeolite from coal fly ash and its potential for nutrient sequestration from anaerobically digested swine wastewater, *Bioresour. Technol.* 110 (2012) 79–85. doi:10.1016/j.biortech.2012.01.096.
-

-
- [161] R. Chal, C. Gérardin, M. Bulut, S. van Donk, Overview and Industrial Assessment of Synthesis Strategies towards Zeolites with Mesopores, *ChemCatChem*. 3 (2011) 67–81. doi:10.1002/cctc.201000158.
- [162] K. Tarach, K. Góra-Marek, J. Tekla, K. Brylewska, J. Datka, K. Mlekodaj, W. Makowski, M.C. Igualada López, J. Martínez Triguero, F. Rey, Catalytic cracking performance of alkaline-treated zeolite Beta in the terms of acid sites properties and their accessibility, *J. Catal.* 312 (2014) 46–57. doi:10.1016/j.jcat.2014.01.009.
- [163] Y. Wang, Y. Sun, C. Lancelot, C. Lamonier, J.-C. Morin, B. Revel, L. Delevoye, A. Rives, Effect of post treatment on the local structure of hierarchical Beta prepared by desilication and the catalytic performance in Friedel–Crafts alkylation, *Microporous Mesoporous Mater.* 206 (2015) 42–51. doi:10.1016/j.micromeso.2014.12.017.
- [164] V. Rac, V. Rakić, D. Stošić, O. Otman, A. Auroux, Hierarchical ZSM-5, Beta and USY zeolites: Acidity assessment by gas and aqueous phase calorimetry and catalytic activity in fructose dehydration reaction, *Microporous Mesoporous Mater.* 194 (2014) 126–134. doi:10.1016/j.micromeso.2014.04.003.
- [165] J. Qi, T. Zhao, X. Xu, F. Li, G. Sun, C. Miao, H. Wang, Study of cracking of large molecules over a novel mesoporous beta, *Catal. Commun.* 10 (2009) 1523–1528. doi:10.1016/j.catcom.2009.04.008.
- [166] K. Egeblad, C.H. Christensen, M. Kustova, C.H. Christensen, Templating Mesoporous Zeolites, *Chem. Mater.* 20 (2008) 946–960. doi:10.1021/cm702224p.
- [167] J. Perez-Ramirez, C.H. Christensen, K. Egeblad, C.H. Christensen, J.C. Groen, Hierarchical zeolites: enhanced utilisation of microporous crystals in catalysis by advances in materials design, *Chem. Soc. Rev.* 37 (2008) 2530–2542. doi:10.1039/B809030K.
- [168] Z. LIU, Y. WANG, Z. XIE, Thoughts on the Future Development of Zeolitic Catalysts from an Industrial Point of View, *Chin. J. Catal.* 33 (2012) 22–38. doi:10.1016/S1872-2067(10)60299-9.
- [169] D. Verboekend, A.M. Chabaneix, K. Thomas, J.-P. Gilson, J. Perez-Ramirez, Mesoporous ZSM-22 zeolite obtained by desilication: peculiarities associated with crystal morphology and aluminium distribution, *CrystEngComm*. 13 (2011) 3408–3416. doi:10.1039/C0CE00966K.
- [170] P. Matias, C. Sá Couto, I. Graça, J.M. Lopes, A.P. Carvalho, F. Ramôa Ribeiro, M. Guisnet, Desilication of a TON zeolite with NaOH: Influence on porosity, acidity and catalytic properties, *Appl. Catal. Gen.* 399 (2011) 100–109. doi:10.1016/j.apcata.2011.03.049.
- [171] W. Schmidt, Solid Catalysts on the Nanoscale: Design of Complex Morphologies and Pore Structures, *ChemCatChem*. 1 (2009) 53–67. doi:10.1002/cctc.200900125.
- [172] C.J.H. Jacobsen, J. Houžvicka, A. Carlsson, I. Schmidt, 03-O-02-Mesoporous zeolites, *Zeolites Mesoporous Mater. Dawn 21st Century*. 135 (2001) 167. doi:10.1016/S0167-2991(01)81295-7.
- [173] J. Čejka, S. Mintova, Perspectives of Micro/Mesoporous Composites in Catalysis, *Catal. Rev.* 49 (2007) 457–509. doi:10.1080/01614940701583240.
- [174] S. Moreno, G. Poncelet, Dealumination of small- and large-pore mordenites: A comparative study, *Microporous Mater.* 12 (1997) 197–222. doi:10.1016/S0927-6513(97)00067-9.
- [175] M. Müller, G. Harvey, R. Prins, Comparison of the dealumination of zeolites beta, mordenite, ZSM-5 and ferrierite by thermal treatment, leaching with oxalic acid and treatment with SiCl₄ by ¹H, ²⁹Si and ²⁷Al MAS NMR, *Microporous Mesoporous Mater.* 34 (2000) 135–147. doi:10.1016/S1387-1811(99)00167-5.
- [176] Y. Hong, J.J. Fripiat, Microporous characteristics of H⁺Y, H-ZSM-5 and H-mordenite dealuminated by calcination, *Microporous Mater.* 4 (1995) 323–334. doi:10.1016/0927-6513(95)00038-B.
- [177] R. Giudici, H. Kouwenhoven, R. Prins, Comparison of nitric and oxalic acid in the dealumination of mordenite, *Appl. Catal. Gen.* 203 (2000) 101–110. doi:10.1016/S0926-860X(00)00470-1.
- [178] A.W. O'Donovan, C.T. O'Connor, K.R. Koch, Effect of acid and steam treatment of Na- and H-mordenite on their structural, acidic and catalytic properties, *Microporous Mater.* 5 (1995) 185–202. doi:10.1016/0927-6513(95)00052-6.
- [179] A. Corma, M.J. Diaz-Cabanas, J. Martínez-Triguero, F. Rey, J. Rius, A large-cavity zeolite with wide pore windows and potential as an oil refining catalyst, *Nature*. 418 (2002) 514–517. doi:10.1038/nature00924.
- [180] A.H. Janssen, A.J. Koster, K.P. de Jong, On the Shape of the Mesopores in Zeolite Y: A Three-Dimensional Transmission Electron Microscopy Study Combined with Texture Analysis, *J. Phys. Chem. B*. 106 (2002) 11905–11909. doi:10.1021/jp025971a.
- [181] L. Teyssier, M. Thomas, C. Bouchy, J.A. Martens, E. Guillon, Liquid chromatography method for quantification of surface connected mesoporosity in ultrastable Y zeolites, *Microporous Mesoporous Mater.* 100 (2007) 6–11. doi:10.1016/j.micromeso.2006.09.044.
- [182] R.A. Beyerlein, C. Choi-Feng, J.B. Hall, B.J. Huggins, G.J. Ray, Effect of steaming on the defect structure and acid catalysis of protonated zeolites, *Top. Catal.* 4 (1997) 27–42. doi:10.1023/A:1019188105794.
- [183] D. Tzoulaki, A. Jentys, J. Pérez-Ramírez, K. Egeblad, J.A. Lercher, On the location, strength and accessibility of Brønsted acid sites in hierarchical ZSM-5 particles, *Spec. Issue Dedic. Paul Ratnasamy Occas. His 70th Birthd.* 198 (2012) 3–11. doi:10.1016/j.cattod.2012.03.078.
- [184] F. Schmidt, M.R. Lohe, B. Büchner, F. Giordanino, F. Bonino, S. Kaskel, Improved catalytic performance of hierarchical ZSM-5 synthesized by desilication with surfactants, *Microporous Mesoporous Mater.* 165 (2013) 148–157. doi:10.1016/j.micromeso.2012.07.045.

-
- [185] D. Verboekend, J. Perez-Ramirez, Design of hierarchical zeolite catalysts by desilication, *Catal. Sci. Technol.* 1 (2011) 879–890. doi:10.1039/C1CY00150G.
- [186] R.M. Dessau, E.W. Valyocsik, N.H. Goeke, Aluminum zoning in ZSM-5 as revealed by selective silica removal, *Zeolites*. 12 (1992) 776–779. doi:10.1016/0144-2449(92)90049-U.
- [187] G. Lietz, K.H. Schnabel, C. Peuker, T. Gross, W. Storek, J. Volter, Modifications of H-ZSM-5 Catalysts by NaOH Treatment, *J. Catal.* 148 (1994) 562–568. doi:10.1006/jcat.1994.1242.
- [188] M. Ogura, S. Shinomiya, J. Tateno, Y. Nara, E. Kikuchi, M. Matsukata, Formation of Uniform Mesopores in ZSM-5 Zeolite through Treatment in Alkaline Solution, *Chem. Lett.* 29 (2000) 882–883. doi:http://doi.org/10.1246/cl.2000.882.
- [189] A. Čížmek, B. Subotić, R. Aiello, F. Crea, A. Nastro, C. Tuoto, Dissolution of high-silica zeolites in alkaline solutions I. Dissolution of silicalite-1 and ZSM-5 with different aluminum content, *Microporous Mater.* 4 (1995) 159–168. doi:10.1016/0927-6513(94)00096-E.
- [190] J.C. Groen, J.C. Jansen, J.A. Moulijn, J. Pérez-Ramírez, Optimal Aluminum-Assisted Mesoporosity Development in MFI Zeolites by Desilication, *J. Phys. Chem. B*. 108 (2004) 13062–13065. doi:10.1021/jp047194f.
- [191] S. Abelló, A. Bonilla, J. Pérez-Ramírez, Mesoporous ZSM-5 zeolite catalysts prepared by desilication with organic hydroxides and comparison with NaOH leaching, *Appl. Catal. Gen.* 364 (2009) 191–198. doi:10.1016/j.apcata.2009.05.055.
- [192] J.C. Groen, J.A. Moulijn, J. Perez-Ramirez, Desilication: on the controlled generation of mesoporosity in MFI zeolites, *J. Mater. Chem.* 16 (2006) 2121–2131. doi:10.1039/B517510K.
- [193] J.C. Groen, L.A.A. Peffer, J.A. Moulijn, J. Pérez-Ramírez, Mechanism of Hierarchical Porosity Development in MFI Zeolites by Desilication: The Role of Aluminium as a Pore-Directing Agent, *Chem. – Eur. J.* 11 (2005) 4983–4994. doi:10.1002/chem.200500045.
- [194] J.C. Groen, W. Zhu, S. Brouwer, S.J. Huynink, F. Kapteijn, J.A. Moulijn, J. Pérez-Ramírez, Direct Demonstration of Enhanced Diffusion in Mesoporous ZSM-5 Zeolite Obtained via Controlled Desilication, *J. Am. Chem. Soc.* 129 (2007) 355–360. doi:10.1021/ja065737o.
- [195] M.S. Holm, M.K. Hansen, C.H. Christensen, “One-Pot” Ion-Exchange and Mesopore Formation During Desilication, *Eur. J. Inorg. Chem.* 2009 (2009) 1194–1198. doi:10.1002/ejic.200801194.
- [196] D. Verboekend, G. Vilé, J. Pérez-Ramírez, Hierarchical Y and USY Zeolites Designed by Post-Synthetic Strategies, *Adv. Funct. Mater.* 22 (2012) 916–928. doi:10.1002/adfm.201102411.
- [197] J. Pérez-Ramírez, D. Verboekend, A. Bonilla, S. Abelló, Zeolite Catalysts with Tunable Hierarchy Factor by Pore-Growth Moderators, *Adv. Funct. Mater.* 19 (2009) 3972–3979. doi:10.1002/adfm.200901394.
- [198] R. Le Van Mao, S. Xiao, A. Ramsaran, J. Yao, Selective removal of silicon from zeolite frameworks using sodium carbonate, *J. Mater. Chem.* 4 (1994) 605–610. doi:10.1039/JM9940400605.
- [199] L. Zhao, J. Gao, C. Xu, B. Shen, Alkali-treatment of ZSM-5 zeolites with different SiO₂/Al₂O₃ ratios and light olefin production by heavy oil cracking, *Fuel Process. Technol.* 92 (2011) 414–420. doi:10.1016/j.fuproc.2010.10.003.
- [200] A.N.C. van laak, R.W. Gosselink, S.L. Sagala, J.D. Meeldijk, P.E. de Jongh, K.P. de Jong, Alkaline treatment on commercially available aluminum rich mordenite, *Appl. Catal. Gen.* 382 (2010) 65–72. doi:10.1016/j.apcata.2010.04.023.
- [201] J.C. Groen, T. Sano, J.A. Moulijn, J. Pérez-Ramírez, Alkaline-mediated mesoporous mordenite zeolites for acid-catalyzed conversions, *J. Catal.* 251 (2007) 21–27. doi:10.1016/j.jcat.2007.07.020.
- [202] V. Paixão, A.P. Carvalho, J. Rocha, A. Fernandes, A. Martins, Modification of MOR by desilication treatments: Structural, textural and acidic characterization, *Microporous Mesoporous Mater.* 131 (2010) 350–357. doi:10.1016/j.micromeso.2010.01.013.
- [203] B. Gil, L. Mokrzycki, B. Sulikowski, Z. Olejniczak, S. Walas, Desilication of ZSM-5 and ZSM-12 zeolites: Impact on textural, acidic and catalytic properties, *Catal. Acids Bases New Mater. Surf. Stud. ABC-6 6th World Congr. Catal. Acids Bases Genova Italy May 10-14 2009*. 152 (2010) 24–32. doi:10.1016/j.cattod.2010.01.059.
- [204] X. Wei, P.G. Smirniotis, Development and characterization of mesoporosity in ZSM-12 by desilication, *Microporous Mesoporous Mater.* 97 (2006) 97–106. doi:10.1016/j.micromeso.2006.01.024.
- [205] D. Verboekend, L.A. Villaescusa, K. Thomas, I. Stan, J. Pérez-Ramírez, Acidity and accessibility studies on mesoporous ITQ-4 zeolite, *Catal. Acids Bases New Mater. Surf. Stud. ABC-6 6th World Congr. Catal. Acids Bases Genova Italy May 10-14 2009*. 152 (2010) 11–16. doi:10.1016/j.cattod.2010.02.004.
- [206] D. Verboekend, J.C. Groen, J. Pérez-Ramírez, Interplay of Properties and Functions upon Introduction of Mesoporosity in ITQ-4 Zeolite, *Adv. Funct. Mater.* 20 (2010) 1441–1450. doi:10.1002/adfm.200902205.
- [207] J.C. Groen, L.A.A. Peffer, J.A. Moulijn, J. Pérez-Ramírez, On the introduction of intracrystalline mesoporosity in zeolites upon desilication in alkaline medium, *Microporous Mesoporous Mater.* 69 (2004) 29–34. doi:10.1016/j.micromeso.2004.01.002.
- [208] J.C. Groen, S. Abelló, L.A. Villaescusa, J. Pérez-Ramírez, Mesoporous beta zeolite obtained by desilication, *Microporous Mesoporous Mater.* 114 (2008) 93–102. doi:10.1016/j.micromeso.2007.12.025.
- [209] J. Pérez-Ramírez, S. Abelló, A. Bonilla, J.C. Groen, Tailored Mesoporosity Development in Zeolite Crystals by Partial Detemplation and Desilication, *Adv. Funct. Mater.* 19 (2009) 164–172. doi:10.1002/adfm.200800871.
- [210] M.S. Holm, M.K. Hansen, C.H. Christensen, “One-Pot” Ion-Exchange and Mesopore Formation During Desilication, *Eur. J. Inorg. Chem.* 2009 (2009) 1194–1198. doi:10.1002/ejic.200801194.
-

-
- [211] J.A. Martens, D. Verboekend, K. Thomas, G. Vanbutsele, J. Pérez-Ramírez, J.-P. Gilson, Hydroisomerization and hydrocracking of linear and multibranched long model alkanes on hierarchical Pt/ZSM-22 zeolite, *Catal. Act. Sites Process.* 218 (2013) 135–142. doi:10.1016/j.cattod.2013.03.041.
- [212] L. Sommer, D. Mores, S. Svelle, M. Stöcker, B.M. Weckhuysen, U. Olsbye, Mesopore formation in zeolite H-SSZ-13 by desilication with NaOH, *Microporous Mesoporous Mater.* 132 (2010) 384–394. doi:10.1016/j.micromeso.2010.03.017.
- [213] M. Guisnet, L. Costa, F.R. Ribeiro, Prevention of zeolite deactivation by coking, *Mem. Eric Derouane.* 305 (2009) 69–83. doi:10.1016/j.molcata.2008.11.012.
- [214] F. Tian, Y. Wu, Q. Shen, X. Li, Y. Chen, C. Meng, Effect of Si/Al ratio on mesopore formation for zeolite beta via NaOH treatment and the catalytic performance in α -pinene isomerization and benzylation of naphthalene, *Microporous Mesoporous Mater.* 173 (2013) 129–138. doi:10.1016/j.micromeso.2013.02.021.
- [215] K. Sadowska, A. Wach, Z. Olejniczak, P. Kuśtrowski, J. Datka, Hierarchic zeolites: Zeolite ZSM-5 desilicated with NaOH and NaOH/tetrabutylamine hydroxide, *Microporous Mesoporous Mater.* 167 (2013) 82–88. doi:10.1016/j.micromeso.2012.03.045.
- [216] D. Verboekend, G. Vilé, J. Pérez-Ramírez, Mesopore Formation in USY and Beta Zeolites by Base Leaching: Selection Criteria and Optimization of Pore-Directing Agents, *Cryst. Growth Des.* 12 (2012) 3123–3132. doi:10.1021/cg3003228.
- [217] K.S.W. Sing, Reporting physisorption data for gas/solid systems with special reference to the determination of surface area and porosity (Recommendations 1984), *Pure Appl. Chem.* 57 (2009) 603–619. doi:10.1351/pac198557040603.
- [218] E.G. Derouane, On the physical state of molecules in microporous solids, *Spec. Issue Dedic. Late Lovat Rees Apprec. His Outst. Contrib. Zeolite Sci.* 104 (2007) 46–51. doi:10.1016/j.micromeso.2007.01.003.
- [219] M.S. Holm, S. Svelle, F. Joensen, P. Beato, C.H. Christensen, S. Bordiga, M. Bjørgen, Assessing the acid properties of desilicated ZSM-5 by FTIR using CO and 2,4,6-trimethylpyridine (collidine) as molecular probes, *Appl. Catal. Gen.* 356 (2009) 23–30. doi:10.1016/j.apcata.2008.11.033.
- [220] J. Marques, I. Gener, P. Ayrault, J. Bordado, J. Lopes, F. Ramôa Ribeiro, M. Guisnet, Infrared spectroscopic study of the acid properties of dealuminated BEA zeolites, *Microporous Mesoporous Mater.* 60 (2003) 251–262. doi:10.1016/S1387-1811(03)00382-2.
- [221] K. Sadowska, K. Góra-Marek, J. Datka, Hierarchic zeolites studied by IR spectroscopy: Acid properties of zeolite ZSM-5 desilicated with NaOH and NaOH/tetrabutylamine hydroxide, *Vib. Spectrosc.* 63 (2012) 418–425. doi:10.1016/j.vibspec.2012.09.007.
- [222] C. Bertrand-Drira, X. Cheng, T. Cacciaguerra, P. Trens, G. Melinte, O. Ersen, D. Minoux, A. Finiels, F. Fajula, C. Gerardin, Mesoporous mordenites obtained by desilication: Mechanistic considerations and evaluation in catalytic oligomerization of pentene, *Microporous Mesoporous Mater.* 213 (2015) 142–149. doi:10.1016/j.micromeso.2015.02.015.
- [223] Z. Liu, X. Dong, Y. Zhu, A.-H. Emwas, D. Zhang, Q. Tian, Y. Han, Investigating the Influence of Mesoporosity in Zeolite Beta on Its Catalytic Performance for the Conversion of Methanol to Hydrocarbons, *ACS Catal.* 5 (2015) 5837–5845. doi:10.1021/acscatal.5b01350.
- [224] R. Kore, R. Srivastava, B. Satpati, Synthesis of industrially important aromatic and heterocyclic ketones using hierarchical ZSM-5 and Beta zeolites, *Appl. Catal. Gen.* 493 (2015) 129–141. doi:10.1016/j.apcata.2015.01.002.
- [225] Ł. Mokrzycki, B. Sulikowski, Desilication of ZSM-12 and MCM-22 type zeolites and their performance in isomerization of α -pinene, *Zeolites Relat. Mater. Trends Targets Chall.* 174 (2008) 1231–1234. doi:10.1016/S0167-2991(08)80110-3.
- [226] Ł. Mokrzycki, B. Sulikowski, Z. Olejniczak, Properties of Desilicated ZSM-5, ZSM-12, MCM-22 and ZSM-12/MCM-41 Derivatives in Isomerization of α -Pinene, *Catal. Lett.* 127 (2008) 296. doi:10.1007/s10562-008-9678-z.
- [227] M. A. Cambor, A. Corma, S. Valencia, Synthesis in fluoride media and characterisation of aluminosilicate zeolite beta, *J. Mater. Chem.* 8 (1998) 2137–2145. doi:10.1039/A804457K.
- [228] A.L. Patterson, The Scherrer Formula for X-Ray Particle Size Determination, *Phys. Rev.* 56 (1939) 978–982. doi:10.1103/PhysRev.56.978.
- [229] S. Brunauer, P.H. Emmett, E. Teller, Adsorption of Gases in Multimolecular Layers, *J. Am. Chem. Soc.* 60 (1938) 309–319. doi:10.1021/ja01269a023.
- [230] I. Langmuir, THE CONSTITUTION AND FUNDAMENTAL PROPERTIES OF SOLIDS AND LIQUIDS. PART I. SOLIDS., *J. Am. Chem. Soc.* 38 (1916) 2221–2295. doi:10.1021/ja02268a002.
- [231] M.M. Dubinin, The Potential Theory of Adsorption of Gases and Vapors for Adsorbents with Energetically Nonuniform Surfaces., *Chem. Rev.* 60 (1960) 235–241. doi:10.1021/cr60204a006.
- [232] G. Leofanti, M. Padovan, G. Tozzola, B. Venturelli, Surface area and pore texture of catalysts, *Catal. Today.* 41 (1998) 207–219. doi:10.1016/S0920-5861(98)00050-9.
- [233] B.C. Lippens, J.H. de Boer, Studies on pore systems in catalysts, *J. Catal.* 4 (1965) 319–323. doi:10.1016/0021-9517(65)90307-6.
- [234] S. Storck, H. Bretinger, W.F. Maier, Characterization of micro- and mesoporous solids by physisorption methods and pore-size analysis, *Appl. Catal. Gen.* 174 (1998) 137–146. doi:10.1016/S0926-860X(98)00164-1.
- [235] P. Hudec, A. Smiešková, Z. Idek, P. Schneider, O. Šolcová, Determination of microporous structure of zeolites by t-plot method—State-of-the-art, *Impact Zeolites Porous Mater. New Technol. Begin. New Millenn.* 142 (2002) 1587–1594. doi:10.1016/S0167-2991(02)80328-7.

-
- [236] E.P. Barrett, L.G. Joyner, P.P. Halenda, The Determination of Pore Volume and Area Distributions in Porous Substances. I. Computations from Nitrogen Isotherms, *J. Am. Chem. Soc.* 73 (1951) 373–380. doi:10.1021/ja01145a126.
- [237] F. Thibault-starzyk, Groupe français des zéolithes., *Les Matériaux micro et mésoporeux : Caractérisation*, EDP Sciences, Les Ulis, France, 2004.
- [238] A. Vimont, F. Thibault-Starzyk, J.C. Lavalley, Infrared Spectroscopic Study of the Acidobasic Properties of Beta Zeolite, *J. Phys. Chem. B.* 104 (2000) 286–291. doi:10.1021/jp992550t.
- [239] M. Maache, A. Janin, J.C. Lavalley, J.F. Joly, E. Benazzi, Acidity of zeolites Beta dealuminated by acid leaching: An FTi.r. study using different probe molecules (pyridine, carbon monoxide), *Zeolites.* 13 (1993) 419–426. doi:10.1016/0144-2449(93)90114-I.
- [240] M.T. Aronson, R.J. Gorte, W.E. Farneth, An infrared spectroscopy study of simple alcohols adsorbed on H-ZSM-5, *J. Catal.* 105 (1987) 455–468. doi:10.1016/0021-9517(87)90073-X.
- [241] J. Marques, I. Gener, P. Ayrault, J. Bordado, J. Lopes, F. Ramôa Ribeiro, M. Guisnet, Infrared spectroscopic study of the acid properties of dealuminated BEA zeolites, *Microporous Mesoporous Mater.* 60 (2003) 251–262. doi:10.1016/S1387-1811(03)00382-2.
- [242] S.G. Hegde, R. Kumar, R.N. Bhat, P. Ratnasamy, Characterization of the acidity of zeolite Beta by FTi.r. spectroscopy and t.p.d. of NH₃, *Zeolites.* 9 (1989) 231–237. doi:10.1016/0144-2449(89)90031-6.
- [243] E. Loeffler, U. Lohse, C. Peuker, G. Oehlmann, L.M. Kustov, V.L. Zhlobenko, V.B. Kazansky, Study of different states of nonframework aluminum in hydrothermally dealuminated HZSM-5 zeolites using diffuse reflectance i.r. spectroscopy, *Zeolites.* 10 (1990) 266–271. <http://www.sciencedirect.com/science/article/pii/0144244994901384> (accessed May 1, 1990).
- [244] E.P. Parry, An infrared study of pyridine adsorbed on acidic solids. Characterization of surface acidity, *J. Catal.* 2 (1963) 371–379. doi:10.1016/0021-9517(63)90102-7.
- [245] H. Knözinger, Specific Poisoning and Characterization of Catalytically Active Oxide Surfaces, *Adv. Catal.* 25 (1976) 184–271. doi:10.1016/S0360-0564(08)60315-6.
- [246] F. Bauer, H.G. Karge, *Characterization II*, 1st ed., Springer-Verlag Berlin Heidelberg, 2007.
- [247] M. Guisnet, P. Ayrault, C. Coutanceau, M. Fernanda Alvarez, J. Datka, Acid properties of dealuminated beta zeolites studied by IR spectroscopy, *J. Chem. Soc. Faraday Trans.* 93 (1997) 1661–1665. doi:10.1039/A607609B.
- [248] R. Merabti, Ph. D. Thesis, Université des sciences et de la technologie Houari Boumediene, 2011.
- [249] J. Perez-Ramirez, C.H. Christensen, K. Egeblad, C.H. Christensen, J.C. Groen, Hierarchical zeolites: enhanced utilisation of microporous crystals in catalysis by advances in materials design, *Chem. Soc. Rev.* 37 (2008) 2530–2542. doi:10.1039/B809030K.
- [250] W. Schmidt, Solid Catalysts on the Nanoscale: Design of Complex Morphologies and Pore Structures, *ChemCatChem.* 1 (2009) 53–67. doi:10.1002/cctc.200900125.
- [251] R. Chal, C. Gérardin, M. Bulut, S. van Donk, Overview and Industrial Assessment of Synthesis Strategies towards Zeolites with Mesopores, *ChemCatChem.* 3 (2011) 67–81. doi:10.1002/cctc.201000158.
- [252] K. Egeblad, C.H. Christensen, M. Kustova, C.H. Christensen, Templating Mesoporous Zeolites, *Chem. Mater.* 20 (2008) 946–960. doi:10.1021/cm702224p.
- [253] H. Wang, T.J. Pinnavaia, MFI Zeolite with Small and Uniform Intracrystal Mesopores, *Angew. Chem. Int. Ed.* 45 (2006) 7603–7606. doi:10.1002/anie.200602595.
- [254] D.P. Serrano, J. Aguado, J.M. Escola, J.M. Rodríguez, Á. Peral, Hierarchical Zeolites with Enhanced Textural and Catalytic Properties Synthesized from Organofunctionalized Seeds, *Chem. Mater.* 18 (2006) 2462–2464. doi:10.1021/cm060080r.
- [255] L. Tosheva, V.P. Valchev, Nanozeolites: Synthesis, Crystallization Mechanism, and Applications, *Chem. Mater.* 17 (2005) 2494–2513. doi:10.1021/cm047908z.
- [256] R. Srivastava, M. Choi, R. Ryoo, Mesoporous materials with zeolite framework: remarkable effect of the hierarchical structure for retardation of catalyst deactivation, *Chem. Commun.* (2006) 4489–4491. doi:10.1039/B612116K.
- [257] J. Liu, L. Cui, L. Wang, X. Ni, S. Zhang, Y. Jin, Alkaline–acid treated mordenite and beta zeolites featuring mesoporous dimensional uniformity, *Mater. Lett.* 132 (2014) 78–81. doi:10.1016/j.matlet.2014.06.027.
- [258] D. Verboekend, G. Vilé, J. Pérez-Ramírez, Mesopore Formation in USY and Beta Zeolites by Base Leaching: Selection Criteria and Optimization of Pore-Directing Agents, *Cryst. Growth Des.* 12 (2012) 3123–3132. doi:10.1021/cg3003228.
- [259] D. Verboekend, S. Mitchell, M. Milina, J.C. Groen, J. Pérez-Ramírez, Full Compositional Flexibility in the Preparation of Mesoporous MFI Zeolites by Desilication, *J. Phys. Chem. C.* 115 (2011) 14193–14203. doi:10.1021/jp201671s.
- [260] Z. Qin, B. Shen, X. Gao, F. Lin, B. Wang, C. Xu, Mesoporous Y zeolite with homogeneous aluminum distribution obtained by sequential desilication–dealumination and its performance in the catalytic cracking of cumene and 1,3,5-triisopropylbenzene, *J. Catal.* 278 (2011) 266–275. doi:10.1016/j.jcat.2010.12.013.
- [261] J.C. Groen, S. Abelló, L.A. Villaescusa, J. Pérez-Ramírez, Mesoporous beta zeolite obtained by desilication, *Microporous Mesoporous Mater.* 114 (2008) 93–102. doi:10.1016/j.micromeso.2007.12.025.
- [262] D. Verboekend, J. Pérez-Ramírez, Desilication Mechanism Revisited: Highly Mesoporous All-Silica Zeolites Enabled Through Pore-Directing Agents, *Chem. – Eur. J.* 17 (2011) 1137–1147. doi:10.1002/chem.201002589.
-

- [263] O. Bortnovsky, P. Szama, B. Wichterlova, Cracking of pentenes to C2–C4 light olefins over zeolites and zeotypes: Role of topology and acid site strength and concentration, *Appl. Catal. Gen.* 287 (2005) 203–213. doi:10.1016/j.apcata.2005.03.037.
- [264] X. Li, A. Kant, Y. He, H.V. Thakkar, M.A. Atanga, F. Rezaei, D.K. Ludlow, A.A. Rownaghi, Light olefins from renewable resources: Selective catalytic dehydration of bioethanol to propylene over zeolite and transition metal oxide catalysts, 8th Sino-US Jt. Conf. Chem. Eng. 12-16 Oct 2015 Shanghai China. 276 (2016) 62–77. doi:10.1016/j.cattod.2016.01.038.
- [265] X. Hu, T. Xu, C. Li, C. Yang, Catalytic cracking of n-heptane under activation of lattice oxygen in a circulating fluidized bed unit, *Chem. Eng. J.* 172 (2011) 410–417. doi:10.1016/j.cej.2011.05.085.
- [266] S. Inagaki, S. Shinoda, Y. Kaneko, K. Takechi, R. Komatsu, Y. Tsuboi, H. Yamazaki, J.N. Kondo, Y. Kubota, Facile Fabrication of ZSM-5 Zeolite Catalyst with High Durability to Coke Formation during Catalytic Cracking of Paraffins, *ACS Catal.* 3 (2013) 74–78. doi:10.1021/cs300426k.
- [267] J. Jin, C. Peng, J. Wang, H. Liu, X. Gao, H. Liu, C. Xu, Facile Synthesis of Mesoporous Zeolite Y with Improved Catalytic Performance for Heavy Oil Fluid Catalytic Cracking, *Ind. Eng. Chem. Res.* 53 (2014) 3406–3411. doi:10.1021/ie403486x.
- [268] J. Zhao, G. Wang, L. Qin, H. Li, Y. Chen, B. Liu, Synthesis and catalytic cracking performance of mesoporous zeolite Y, *Catal. Commun.* 73 (2016) 98–102. doi:10.1016/j.catcom.2015.10.020.
- [269] P.G. Smirniotis, E. Ruckenstein, Comparison of the Performance of ZSM-5, .beta. Zeolite, Y, USY, and Their Composites in the Catalytic Cracking of n-Octane, 2,2,4-Trimethylpentane, and 1-Octene, *Ind. Eng. Chem. Res.* 33 (1994) 800–813. doi:10.1021/ie00028a004.
- [270] J. Liu, G. Jiang, Y. Liu, J. Di, Y. Wang, Z. Zhao, Q. Sun, C. Xu, J. Gao, A. Duan, J. Liu, Y. Wei, Y. Zhao, L. Jiang, Hierarchical Macro-meso-microporous ZSM-5 Zeolite Hollow Fibers With Highly Efficient Catalytic Cracking Capability, 4 (2014) 7276. <http://dx.doi.org/10.1038/srep07276>.
- [271] A. Corma, From Microporous to Mesoporous Molecular Sieve Materials and Their Use in Catalysis, *Chem. Rev.* 97 (1997) 2373–2420. doi:10.1021/cr960406n.
- [272] G. Bellussi, A. Carati, C. Rizzo, R. Millini, New trends in the synthesis of crystalline microporous materials, *Catal. Sci. Technol.* 3 (2013) 833–857. doi:10.1039/C2CY20510F.
- [273] D. Liu, A. Bhan, M. Tsapatsis, S. Al Hashimi, Catalytic Behavior of Brønsted Acid Sites in MWW and MFI Zeolites with Dual Meso- and Microporosity, *ACS Catal.* 1 (2011) 7–17. doi:10.1021/cs100042r.
- [274] D. Verboekend, S. Mitchell, M. Milina, J.C. Groen, J. Pérez-Ramírez, Full Compositional Flexibility in the Preparation of Mesoporous MFI Zeolites by Desilication, *J. Phys. Chem. C.* 115 (2011) 14193–14203. doi:10.1021/jp201671s.
- [275] M.M. Helmkamp, M.E. Davis, Synthesis of Porous Silicates, *Annu. Rev. Mater. Sci.* 25 (1995) 161–192. doi:10.1146/annurev.ms.25.080195.001113.
- [276] X. Li, D.F. Shantz, PFG NMR Investigations of Tetraalkylammonium–Silica Mixtures, *J. Phys. Chem. C.* 114 (2010) 8449–8458. doi:10.1021/jp101006f.
- [277] J.C. Groen, L.A.A. Peffer, J.A. Moulijn, J. Pérez-Ramírez, Mechanism of Hierarchical Porosity Development in MFI Zeolites by Desilication: The Role of Aluminium as a Pore-Directing Agent, *Chem. – Eur. J.* 11 (2005) 4983–4994. doi:10.1002/chem.200500045.
- [278] H. Sammouy, J. Toufaily, K. Cherry, T. Hamieh, Y. Pouilloux, L. Pinard, Impact of desilication of *BEA zeolites on the catalytic performance in hydroisomerization of n-C10, *Appl. Catal. Gen.* 551 (2018) 1–12. doi:10.1016/j.apcata.2017.11.024.
- [279] C. Bertrand-Drira, X. Cheng, T. Cacciaguerra, P. Trens, G. Melinte, O. Ersen, D. Minoux, A. Finiels, F. Fajula, C. Gerardin, Mesoporous mordenites obtained by desilication: Mechanistic considerations and evaluation in catalytic oligomerization of pentene, *Microporous Mesoporous Mater.* 213 (2015) 142–149. doi:10.1016/j.micromeso.2015.02.015.
- [280] S. Abelló, A. Bonilla, J. Pérez-Ramírez, Mesoporous ZSM-5 zeolite catalysts prepared by desilication with organic hydroxides and comparison with NaOH leaching, *Appl. Catal. Gen.* 364 (2009) 191–198. doi:10.1016/j.apcata.2009.05.055.
- [281] K. Sadowska, A. Wach, Z. Olejniczak, P. Kuśtrowski, J. Datka, Hierarchic zeolites: Zeolite ZSM-5 desilicated with NaOH and NaOH/tetrabutylamine hydroxide, *Microporous Mesoporous Mater.* 167 (2013) 82–88. doi:10.1016/j.micromeso.2012.03.045.
- [282] B. Gil, Ł. Mokrzycki, B. Sulikowski, Z. Olejniczak, S. Walas, Desilication of ZSM-5 and ZSM-12 zeolites: Impact on textural, acidic and catalytic properties, *Catal. Acids Bases New Mater. Surf. Stud. ABC-6 6th World Congr. Catal. Acids Bases Genova Italy May 10-14 2009.* 152 (2010) 24–32. doi:10.1016/j.cattod.2010.01.059.
- [283] M.S. Holm, S. Svelle, F. Joensen, P. Beato, C.H. Christensen, S. Bordiga, M. Bjørgen, Assessing the acid properties of desilicated ZSM-5 by FTIR using CO and 2,4,6-trimethylpyridine (collidine) as molecular probes, *Appl. Catal. Gen.* 356 (2009) 23–30. doi:10.1016/j.apcata.2008.11.033.
- [284] W.O. Haag, R.M. Dessau, R.M. Lago, Kinetics and Mechanism of Paraffin Cracking with Zeolite Catalysts, in: T. Inui, S. Namba, T. Tatsumi (Eds.), *Stud. Surf. Sci. Catal.*, Elsevier, 1991: pp. 255–265. doi:10.1016/S0167-2991(08)61903-5.
- [285] B. Liu, D. Slocombe, M. AlKinany, H. AlMegren, J. Wang, J. Arden, A. Vai, S. Gonzalez-Cortes, T. Xiao, V. Kuznetsov, P.P. Edwards, Advances in the study of coke formation over zeolite catalysts in the methanol-to-hydrocarbon process, *Appl. Petrochem. Res.* 6 (2016) 209–215. doi:10.1007/s13203-016-0156-z.
- [286] J. Luo, B.V. Bhaskar, Y.-H. Yeh, R.J. Gorte, n-Hexane cracking at high pressures on H-ZSM-5, H-BEA, H-MOR, and USY for endothermic reforming, *Appl. Catal. Gen.* 478 (2014) 228–233. doi:10.1016/j.apcata.2014.04.010.

-
- [287] R. Nakao, Y. Kubota, N. Katada, N. Nishiyama, K. Kunimori, K. Tomishige, Performance and characterization of BEA catalysts for catalytic cracking, *Appl. Catal. Gen.* 273 (2004) 63–73. doi:10.1016/j.apcata.2004.06.013.
- [288] P.B. Weisz, Polyfunctional Heterogeneous Catalysis, in: P.W.S. D.D. Eley Paul B. Weisz, A.A. Balandin, J.H. De Boer, P.J. Debye, P.H. Emmett, J. Horiuti, W. Jost, G. Natta, E.K. Rideal and H.S. Taylor (Ed.), *Adv. Catal.*, Academic Press, 1962: pp. 137–190. doi:10.1016/S0360-0564(08)60287-4.
- [289] N. Batalha, L. Pinard, C. Bouchy, E. Guillon, M. Guisnet, n-Hexadecane hydroisomerization over Pt-HBEA catalysts. Quantification and effect of the intimacy between metal and protonic sites, *J. Catal.* 307 (2013) 122–131. doi:10.1016/j.jcat.2013.07.014.
- [290] F. Alvarez, G. Giannetto, M. Guisnet, G. Perot, Hydroisomerization and hydrocracking of n-Alkanes. 2. n-Heptane transformation on a Pt-dealuminated Y zeolite - comparison with a Pt-Y zeolite, *Appl. Catal.* 34 (1987) 353–365. doi:10.1016/S0166-9834(00)82468-9.
- [291] J.W. Thybaut, C.S. Laxmi Narasimhan, J.F. Denayer, G.V. Baron, P.A. Jacobs, J.A. Martens, G.B. Marin, Acid–Metal Balance of a Hydrocracking Catalyst: Ideal versus Nonideal Behavior, *Ind. Eng. Chem. Res.* 44 (2005) 5159–5169. doi:10.1021/ie049375+.
- [292] W.H. Press, S.A. Teukolsky, W.T. Vetterling, B.P. Flannery, *Numerical Recipes in C++: the art of scientific computing*, Second Edition, 2002.
- [293] N. Batalha, L. Pinard, Y. Pouilloux, M. Guisnet, Bifunctional Hydrogenating/Acid Catalysis: Quantification of the Intimacy Criterion, *Catal. Lett.* 143 (2013) 587–591. doi:10.1007/s10562-013-1003-9.
- [294] F. Alvarez, F.R. Ribeiro, G. Perot, C. Thomazeau, M. Guisnet, Hydroisomerization and Hydrocracking of Alkanes, *J. Catal.* 162 (1996) 179–189. doi:10.1006/jcat.1996.0275.
- [295] J. Zecevic, G. Vanbutsele, K.P. de Jong, J.A. Martens, Nanoscale intimacy in bifunctional catalysts for selective conversion of hydrocarbons, *Nature*. 528 (2015) 245. <http://dx.doi.org/10.1038/nature16173>.
- [296] J. Francis, E. Guillon, N. Bats, C. Pichon, A. Corma, L.J. Simon, Design of improved hydrocracking catalysts by increasing the proximity between acid and metallic sites, *Appl. Catal. Gen.* 409 (2011) 140–147. doi:10.1016/j.apcata.2011.09.040.
- [297] M.V. Landau, L. Vradman, V. Valtchev, J. Lezervant, E. Liubich, M. Talianker, Hydrocracking of Heavy Vacuum Gas Oil with a Pt/H-beta–Al₂O₃ Catalyst: Effect of Zeolite Crystal Size in the Nanoscale Range, *Ind. Eng. Chem. Res.* 42 (2003) 2773–2782. doi:10.1021/ie020899o.
- [298] M.V. Landau, L. Vradman, V. Valtchev, J. Lezervant, E. Liubich, M. Talianker, Hydrocracking of Heavy Vacuum Gas Oil with a Pt/H-beta–Al₂O₃ Catalyst: Effect of Zeolite Crystal Size in the Nanoscale Range, *Ind. Eng. Chem. Res.* 42 (2003) 2773–2782. doi:10.1021/ie020899o.
- [299] J. Francis, E. Guillon, N. Bats, C. Pichon, A. Corma, L.J. Simon, Design of improved hydrocracking catalysts by increasing the proximity between acid and metallic sites, *Appl. Catal. Gen.* 409 (2011) 140–147. doi:10.1016/j.apcata.2011.09.040.
- [300] Christian Marcilly, *Acido-basic catalysis, application to refining and petrochemistry*, 2002.
- [301] A. Soualah, J.L. Lemberton, L. Pinard, M. Chater, P. Magnoux, K. Moljord, Hydroisomerization of long-chain n-alkanes on bifunctional Pt/zeolite catalysts: Effect of the zeolite structure on the product selectivity and on the reaction mechanism, *Spec. Issue Dedic. Profr. Jean Sommer His 70th BirthdaySpecial Issue Dedic. Profr. Jean Sommer*. 336 (2008) 23–28. doi:10.1016/j.apcata.2007.09.038.
- [302] S.V. Konnov, I.I. Ivanova, O.A. Ponomareva, V.I. Zaikovskii, Hydroisomerization of n-alkanes over Pt-modified micro/mesoporous materials obtained by mordenite recrystallization, *Microporous Mesoporous Mater.* 164 (2012) 222–231. doi:10.1016/j.micromeso.2012.08.017.
- [303] J.A. Martens, D. Verboekend, K. Thomas, G. Vanbutsele, J. Pérez-Ramírez, J.-P. Gilson, Hydroisomerization and hydrocracking of linear and multibranch long model alkanes on hierarchical Pt/ZSM-22 zeolite, *Catal. Act. Sites Process.* 218 (2013) 135–142. doi:10.1016/j.cattod.2013.03.041.
- [304] R.L. Goring, Diffusion of normal paraffins in zeolite T: Occurrence of window effect, *J. Catal.* 31 (1973) 13–26. doi:10.1016/0021-9517(73)90265-0.
- [305] E.G. Derouane, J.B. Nagy, C. Fernandez, Z. Gabelica, E. Laurent, P. Maljean, Diffusion of alkanes in molecular sieves evidence for confinement effects, *Appl. Catal.* 40 (1988) L1–L10. doi:10.1016/S0166-9834(00)80420-0.
- [306] M. Pera-Titus, J. Llorens, Evaluation of confinement effects in zeolites under Henry’s adsorption regime, *Seventh Int. Symp. Eff. Surf. Heterog. Adsorpt. Catal. Solids - ISSHAC-7*. 256 (2010) 5305–5310. doi:10.1016/j.apsusc.2009.12.067.
- [307] A.J. Jones, R.T. Carr, S.I. Zones, E. Iglesia, Acid strength and solvation in catalysis by MFI zeolites and effects of the identity, concentration and location of framework heteroatoms, *J. Catal.* 312 (2014) 58–68. doi:10.1016/j.jcat.2014.01.007.
- [308] A.J. Jones, E. Iglesia, The Strength of Brønsted Acid Sites in Microporous Aluminosilicates, *ACS Catal.* 5 (2015) 5741–5755. doi:10.1021/acscatal.5b01133.
- [309] A.J. Jones, S.I. Zones, E. Iglesia, Implications of Transition State Confinement within Small Voids for Acid Catalysis, *J. Phys. Chem. C*. 118 (2014) 17787–17800. doi:10.1021/jp5050095.